Small Molecule Derived Nanotheranostics for Alzheimer's Disease

Manju Sharma

A thesis submitted for the partial fulfillment of the degree of Doctor of Philosophy

Institute of Nano Science and Technology (INST)
Knowledge City, Sector-81, SAS Nagar, Mohali-140306, Punjab, India
Indian Institute of Science Education and Research (IISER) Mohali
Knowledge City, Sector 81, SAS Nagar, Mohali, P.O. 140306
Punjab, India.

December, 2022

Dedicated to my beloved parents, Shri. Mohan Lal Sharma and Smt. Kamla Sharma for their unconditional love, support, endless guidance, and encouragement every step of the way.

Declaration

The work presented in this thesis has been carried out by me under the guidance of Dr. Jiban Jyoti Panda at the Institute of Nano Science and Technology, Mohali. This work has not been submitted in part or in full for a degree, a diploma, or a fellowship to any other university or institute. Whenever contributions of others are involved, every effort is made to indicate this clearly, with due acknowledgment of collaborative research and discussions. This thesis is a bonafide record of original work done by me and all sources listed within have been detailed in the bibliography.

Manju Sharma

In my capacity as the supervisor of the candidate's thesis work, I certify that the above statements by the candidate are true to the best of my knowledge.

Dr. Jiban Jyoti Panda

Acknowledgments

First and foremost, praises and thanks to the Almighty God, the supreme power who has given me strength, knowledge, and encouragement throughout all the challenging moments of completing this task. Thank you, ***my Lord, Shiv Ji*** for showering countless blessings during this journey and giving me this opportunity to acknowledge all the people who have contributed in some way to accomplish the research work described in this thesis.

I would take the opportunity to express my sincere gratitude to my ***Ph.D. supervisor Dr. Jiban Jyoti Panda*** for her wisdom, invaluable guidance, continuous support, motivation, and patience throughout my Ph.D. tenure. I would like to thank her for giving me the intellectual freedom to work in my own way. I always admire her for her perfectionism and never-ending enthusiasm. She has been a living role model to me, taking up new challenges every day, tackling them with all her grit and determination, and always thriving to come out victorious. Ma'am, I am fortunate to have worked with you. I will always be indebted for the conviction you showed in my abilities and for your invaluable support.

My profound gratitude is due for ***Prof. Ashok Kumar Ganguli (founding director of INST)***, ***Prof. Hirendra N. Ghosh***, and ***Dr. Priyanka*** who impacted and inspired me and also for giving me the opportunity to pursue my doctoral degree.

My sincere and heartfelt thanks to ***Prof. Amitava Patra, Director, INST*** Mohali for providing outstanding research facilities along with a congenial/competitive environment for the students to work.

I am extremely grateful to my doctoral committee members, ***Dr. Dipankar Mandal and Dr. Asifkhan Shanavas*** for their valuable feedback, suggestions, encouragement, and insightful comments for this thesis.

I am also thankful to all faculty members and staff of INST Mohali for their direct and indirect support. My special words of thanks go to ***Dr. Bhanu Praksah, Dr. Manish Singh, Dr. Jibanandan Mishra, and Dr. Shubha Shukla,*** our collaborators for always being so kind, helpful, and for constantly motivating me in my scientific endeavors.

Now, I would like to thank those people with whom I have spent most of my time over these five years. I have great pleasure in acknowledging my labmates ***Dr. Taru Dube, Dr. Sonika Chibh, Dr. Imocha Rajkumar, Avneet kour, Farheen Khanam, Nidhi Aggarwal, Samraggi Chaudhary, Aman Kumar, Himanshu Panda, and Swapnil*** for their encouragement, support, and all the fun we have had in the last five years. Thank you all for your cooperation and wonderful patience in bearing with me during my time here. Further, I would like to especially thank both ***Dr. Sonika Chibh and Avneet Kour*** for being my caring labmates like sisters. Thank you for your unconditional support, and constant encouragement, for cheering me up, you stood by me through the good and bad times. I am also thankful to ***Himanshu, Nidhi and Samraggi*** for always being helpful, and supportive throughout my research work. I would like to thank ***Virendra Tiwari*** and his wife ***Swati Chaturvedi*** for helping me in animal experimentation and being a constant source of encouragement and help.

I would like to acknowledge all the teachers I learnt from since my childhood, I would not

have been here without their guidance, blessing and support.

The thesis could not have been completed without the endless love, sacrifice and blessings of my Family. ***Mummy and Papa***, I can't imagine myself on this stage without your unconditional love, trust, time encouragement, guidance, patience, and support. It was just your love that raised me up again when I got weary. I am grateful to have ***Anju di, Arti, and Kartick*** as my dearest sisters and brother who have a deep love and desire for the best for me

always. I am heartily thankful to my jiju, ***Shri Sushil Kumar Sharma,*** and my cute nephew, ***Shiven Sharma*** (my little angel) for their blessings, love, and continuous encouragement.

I would like to express my gratitude to my parents-in-law ***Shri Hemant Kaushik*** and ***Smt. Nisha Kaushik*** for their unfailing emotional support. I am extremely grateful to my soulmate, ***Nishant Kaushik*** for always being there when I really needed someone by my side. I am truly thankful to you for your motivation, patience, love, support, boosting words, and extreme faith in me throughout this entire experience.

Finally, I also would like to thank my son, ***Kiyansh,*** baby this endeavor would not have been possible without you. Thank you maamla, for giving me unlimited happiness and pleasure and cooperating with me to complete this journey.

There are many more who have directly or indirectly contributed to making this journey successful, I thank them all.

Manju Sharma

LIST OF CONTENTS

LIST OF FIGURES

recorded after 48 h. Data were measured by one-way ANOVA and turkey multiple comparison test (* $p < 0.05$; ** $p < 0.01$; *** $p < 0.001$). Confocal microscopic images aimed to detect FF and Aβ42 peptide fibrils in cells. (E) ThT and DAPI-stained control SH-SY5Y cells without treatment (scale bar ~10μm). The intracellular fibrils of FF were assessed by ThT staining in SH-SY5Y cells (F) and (G) in the presence of TNPs (scale bar ~5 μm). (H) The intracellular fibrils of Aβ42 peptide were assessed by ThT staining in SH-SY5Y cells and (I) in the presence of TNPs (scale bar ~10 μm).

2.14 **Effect of TNPs on behavioural performance of ICV-STZ induced rat model.** TNPs treatment improved STZ induced memory and learning deficits in AD rats and also reduced the expression of Aβ42 peptide in both cortex and hippocampus area of rats' brain. Spatial memory and learning behaviours were determined by using MWM study. (A) Bar graph representing escape latency time (in sec). (B) Bar graph showing average path length represented in cm. (C) Graph showing swim speed (in cm) of the animals after TNPs treatment. (D) Graph showing time spent by the animals in the target quadrant. (E) The track plot representing the path travelled by rat of each group**.** Data are plotted as the mean ± SE of n = 6 animals/group. Data were calculated by repeated-measures two-way ANOVA and bonferroni post hoc analysis [*p < 0.05, **p < 0.01, ***p < 0.001 (* Session 1 vs Session 2, and* control *vs* STZ); #p < 0.05, ##p < 0.01, ###p < 0.001 ($^{\#}$ Session 1 vs Session 3, and $^{\#}$ STZ *vs* STZ+TNPs)]. (F) Bar graph showing numbers of Aβ42 oligomers in both regions. Data were measured by two-way ANOVA and Bonferroni multiple comparison test [*P < 0.05, **P < 0.01, ***P < 0.001 (*Control vs STZ); $^{\#}$P < 0.05, $^{\#\#}$P < 0.01, $^{\#\#\#}$P < 0.001 ($^{\#}$STZ vs STZ+ TNPs)]. (G and H) Immunostaining based photomicrographs displaying expression of Aβ42 oligomers in both cortex and hippocampus areas of the brain. **97**

2.15 *In vitro* serum stability of TNPs after 2 hours of incubation. Data are presented as the mean ± SE of n = 3. **98**

2.16 The pharmacokinetic profile of TNPs determined in brain and serum after their intravenous administration to SD rats at a dose of 5mg/kg body weight of the animal. Data presented as the mean ± SE of n = 3. **99**

3.1 (A) DLS size distribution profile of DTNPs. (B) UV absorbance spectra of DTNPs. (C) ATR-FTIR of DTNPs. (D) SEM images of DTNPs. (E) AFM image of DTNPs. (F) Fluorescence emission spectra of DTNPs taken at different excitation wavelengths ranging from 340 nm to 460 nm. (G-I) Confocal images of DTNPs. (J) Photostability of DTNPs, FITC and curcumin irradiated with 365 nm UV light at various time points. **128**

3.2 ThT assay showing concentration dependent aggregation of (A) FF; (B) Aβ; SEM images showing morphological changes of (C) FF fibrils after 24 h of incubation; (D) FF fibrils after 48 h of incubation; (E) FF fibrils after 72 h of incubation. Confocal microscopic images showing **130**

showing neuroprotective effects of non-activated (without exposure to acoustic stimulus) PVDF and DPVDF nanospheres (a = 0.4 mg/mL, b = 0.6 mg/mL, c = 0.8 mg/mL) against FF fibrils (12mM) induced toxicity in SH-SY5Y cells. (D) MTT results showing neuroprotective effects of sono-activated (placed under acoustic stimulus) PVDF and DPVDF (a = 0.4 mg/mL, b = 0.6 mg/mL, c = 0.8 mg/mL) nanospheres against FF fibrils (12mM) induced toxicity in SH-SY5Y cells. One-way analysis of variance (ANOVA) followed by Tukey's multiple comparison test were used to analyse the significant difference between the mean values of controls and treated samples; results are presented as mean ± SD. *p < 0.05, **p < 0.01, ***p < 0.001, and ****p < 0.0001 when nanospheres treated cells were compared with control groups.

5.14 (A) Data showing generation of ROS using NBT assay, where 'a' represents the ROS generated by non-activated nanospheres after 30 min and 1 h and 'b' represents ROS generated by activated nanospheres after 30 min and 1 h of exposure to the acoustic stimuli. (B) TMB assay results, where 'a' represents ROS generated by TMB and H_2O_2 solution without nanospheres, 'b' represents ROS generated by only TMB solution and nanospheres, 'c; represents ROS generated by TMB, H_2O_2 solution and nanospheres in the absence of acoustic stimulus, and 'd' represents ROS generated by TMB, H_2O_2 solution and nanospheres after 30 min and 1h exposure of the acoustic stimulus. (C) Confocal images showing ROS produced by different concentrations of PVDF nanospheres under acoustic stimulus and non-stimulus conditions (scale bar 50 μm). Two-way analysis of variance (ANOVA) followed by Tukey's multiple comparisons were used to analyse the significant difference between the mean values of controls and treated samples; results are presented as mean ± SD. *p < 0.05, **p < 0.01, ***p < 0.001, and ****p < 0.0001 when treated samples were compared with control groups. **206**

5.15 *In vivo* fluorescence images of ICG-labeled DPVDF nanospheres obtained in Balb/c mice. (A) *In-vivo* fluorescence imaging of ICG-DPVDF nanospheres-treated mice demonstrated that the particles can reach and stay in the brain tissues from the nasal cavity after1,2, 3, and 4h of nanospheres administration. (B) *In-vivo* fluorescence imaging of PBS treated **209**

LIST OF SCHEMES

LIST OF TABLES

ABBREVIATIONS

Abbreviations	Long Form
AD	Alzheimer Disease
Aβ	Amyloid beta
NPs	Nanoparticles
TNPs	Tryptophan Nanoparticles
FF	Diphenylalanine
ThT	Thioflavin T
CD	Circular Dichroism
SH-SY5Y	Human neuroblastoma cell line
PAMPA	Parallel artificial membrane permeability assay
BBB	Blood-brain barrier
ICV	Intracerebroventricular
STZ	Streptozotocin
MWM	Morris Water Maze
L-Trp	L-Tryptophan
UV-Vis	Ultraviolet-Visible
DLS	Dynamic light scattering
ATR-FTIR	Attenuated total reflection-Fourier transform infrared
AFM	Atomic force microscopy
QY	Quantum yield
DTNPs	Dopamine tryptophan nanoparticles
SEM	Scanning electron microscopic
TEM	Transmission electron microscopic
RTDNPs	Resveratrol tryptophan nanoparticles loaded polydopamine core nanoparticles
Ac-PHF6	tau-derived hexapeptide
PVDF	Polyvinylidene fluoride
DPVDF	Dopamine coated polyvinylidene fluoride
Bis-ANS	4,4'-Dianilino-1,1'-Binaphthyl-5,5'-Disulfonic Acid, Dipotassium Salt
L929	fibroblast cell line
ROS	Reactive oxygen species
APP	Amyloid precursor protein
NMR	Nuclear magnetic resonance
TGA	Thermogravimetric analysis
DAPI	4',6-diamidino-2-phenylindole

FACS	Fluorescence-activated cell sorting
PI	Propidium Iodide
FESEM	Field emission scanning electron microscopy
XPS	X-ray photoelectron spectroscopy
MTT	(3-(4, 5-dimethylthiazolyl-2)-2, 5-diphenyltetrazolium bromide)
NBT	Nitroblue tetrazolium test
TMB	3,3′,5,5′-Tetramethylbenzidine
H_2O_2	Hydrogen peroxide
ICG	Indocyanine green
LCMS	Liquid chromatography–mass spectrometry
NIR	Near infrared radiation
HFIP	Hexafluoro isopropyl alcohol
DCFH-DA	Dichlorodihydrofluorescein diacetate

ABSTRACT

Brain, being the center of control for the body, is capable of causing major threat to life in case of any malfunctioning. Other than cardiovascular and pulmonary disorders/diseases, steep rise in global burden of neuronal disorders especially Alzheimer's disease (AD) is one of the major public health concern in today's world. The aggregation and accumulation of neurotoxic amyloid-β (Aβ) and hyper-phosphorylated tau proteins are the major neuropathological hallmarks of Alzheimer's disease (AD). Inhibiting their aggregation is one of the most viable approaches for controlling the progression of this deadly disease. Currently available anti-AD drugs have many limitations such as their limited ability to pass through the blood−brain barrier (BBB), low bioavailability in the central nervous system (CNS). Their several physicochemical characteristics like low lipophilicity, high molecular weight (MW), and higher polar surface area, also hinder their successful brain delivery. Therefore, it becomes imperative to look for more efficient and disease modifying anti-AD drugs. New generation theranostic nanomedicines can serve as cutting-edge and safer solutions to overcome these existing limitations and improve current treatment stratagems for the disease with potential clinical success.

In this regard, the present thesis is focused on the development of small molecule derived nanotheranostics for imaging and potential therapy of Alzheimer's disease. In the very first study, we developed self-fluorescent solo tryptophan nanoparticles (TNPs) from a single amino acid, L-tryptophan by a simple hydrothermal reaction. We demonstrated that TNPs could significantly inhibit as well as disrupt the fibrils formed by Aβ42 peptide, and a reductionist approach based amyloid model dipeptide, phenylalanine-phenylalanine (FF). More importantly, these nanoparticles were non-toxic to neuronal cells and could protect the neurons from Aβ42 peptide and FF aggregates induced cytotoxicity. In addition, efficacy

studies performed in animal models further revealed that the TNPs could rescue spatial and learning memory in intracerebroventricular (ICV) STZ administration induced AD phenotype in rats. Moreover, pharmacokinetics studies further established the BBB permeability and brain delivery potency of TNPs. Inherent excellent fluorescent properties of these nanoparticles could further be exploited to use them as imaging modalities for tagging and detecting FF and Aβ42 peptide fibrils. Thus, the biocompatible and utterly simple and fluorescent tryptophan nanoparticles synthesized here could serve as potent nanotheranostic agents for treating and diagnosing AD.

Stepping forward, we next tried to explore the anti-amyloid propensity of theranostic tryptophan nanocomposite with another anti-amyloidogenic and neuroactive molecule, dopamine. The nanocomposite (DTNPs) was developed by following a simple hydrothermal reaction. Interestingly, the designed multimodal theranostic system carried triple advantages: (a) amyloid recognition and binding capacity owing to the presence of the aromatic moiety specifically tryptophan, (b) Aβ-polypeptide fibril disaggregation propensity contributed by the presence of both tryptophan and dopamine, and (c) inherent BBB permeability by means of tryptophan. Further, the DTNPs showed synergistic neuroprotective effects against both in neuroblastoma cells and in animal model (ICV-STZ) of dementia. In addition, DTNPs exhibited excellent fluorescent properties and light up the cytoplasm of neuroblastoma cells when being incubated with cells, confirming their ability to serve as an intracellular bioimaging agent. Thus, our overall results of this study signify the potency of the DTNPs as promising multifunctional theranostic agents for treating AD.

Despite the promising anti-amyloid potency of both solo tryptophan and nanocomposite of tryptophan toward both FF-derived amyloid fibrils and preformed Aβ-peptide fibers, the anti-aggregation property of nanosystems against tau protein were not explored. Thus, in our next study we have tried to develop a dual functional fluorescent resveratrol and L-tryptophan

(Res- Trp) loaded dopamine (dopa) core nanotheranostic system as a dual anti-amyloid agent. The nanosystem demonstrated dual anti-amyloidogenic activity against both Aβ42 peptide, and the hexapeptide Ac-PHF6 (VQIVYK) derived from tau protein. Additionally, Res-Trp loaded Dopa core showed remarkable neuroprotective effect in neuroblastoma cells against both FF amyloid fibrils and hexapeptide Ac-PHF6 fibrils induced toxicity under the NIR laser irradiation. Our dual functional nanosystems thus serve as new class of theranostic systems for combating the AD.

In addition to simple small molecule based nanotheranostic systems for treating and diagnosing AD, we tried to explore dopamine coated piezoelectric polyvinylidene fluoride (DPVDF) nanospheres as acoustic stimulus (sonication) triggered anti-fibrillizing agents towards FF, as well as Aβ42-polypeptide fibrils. DPVDF nanospheres represent a class of biocompatible piezoelectric materials with piezo-catalytic property triggered in response to acoustic stimulus. The acoustic stimulus-activated DPVDF nanospheres produced piezo-induced oxidative stress, under both in vitro and in cellular conditions, which successfully destabilized FF and Aβ42 fibrils. In vitro studies also revealed that the stimulus-activated DPVDF nanospheres could efficiently alleviate the neuro-toxicity of FF fibrils as exemplified in the neuroblastoma, SHSY5Y cells. Thus, these acoustic stimuli activated nanospheres could serve as novel class of disease modifying nanomaterials for non-invasive electro-chemotherapy of AD.

Overall, this thesis demonstrates the development of different small molecule derived nanotheranostic systems, capable of transversing the BBB to serve as simultaneous amyloid inhibitors and aggregate detecting agents under one roof. Such multifunctional nanosystem are not only interesting but also superior to many other reported anti-amyloid nanostructures in terms of their biocompatibility and ease of fabrication.

SYNOPSIS

Chapter 1. Introduction

Brain, being the centre of control for the body, can cause major threat to life in case of any malfunctioning. Other than cardiovascular and pulmonary disorders/diseases, steep rise in global burden of neuronal disorders especially Alzheimer's disease (AD) is one of the major public health concern in today's world. According to World Alzheimer's reports, AD accounts for one of the leading causes of dementia and the 7th leading cause of death globally affecting approximately 55 million people worldwide, and the number will gradually rise to about 139 million cases by 2050. There are approximately 10 million new cases of dementia rising per year globally (one new case in every 3 seconds) according to WHO (2019) and Alzheimer's Disease International (ADI) reports, and most of the cases are rising in developing countries. Despite many years of intensive research, various clinical trials on available disease-modifying therapies for the treatment of AD have shown unsatisfactory results and suffer from several limitations. Current AD therapies though help to reduce the disease symptoms to some extent and improve the patient's quality of life, but these medications neither slow the progression of the disease nor can cure it. Moreover, the available treatment strategies are not able to detect the disease at its earliest stage. Additionally, the major limitation of these therapies is the low bioavailability of these drugs in the central nervous system (CNS) due to their meagre access to the brain because of the blood-brain barrier (BBB). Moreover, most of these medicines have various side effects and cause vomiting, allergic reactions, loss of appetite, and diarrhea to the person taking them. To overcome all these issues and to achieve effective therapy, there is a pressing need for the development of advanced methods which possess high sensitivity, high resolution, deep penetration power, and the ability to facilitate real-time monitoring of disease progression along with biosafety. These days nanotechnology-based drug delivery approaches have gained significant advantages over traditionally used strategies. Moreover, many recent advancements in the field of nanomedicine have led to the development of nanotheranostics,

a novel approach which integrates both diagnostic as well as therapeutic functions in one system. This chapter introduces the fundamental concepts of nanotheranostics systems for the treatment of AD **(Scheme 1)**. Currently, different multifunctional nanoparticles such as inorganic NPs, polymeric NPs, protein-based NPs, and carbonaceous nanostructures are widely used as nanotheranostics agents due to the inherent theranostic properties of these nanoparticles that can offer real-time, rapid and sensitive diagnostics as well as therapeutic platforms for AD. Among them, fluorescent nanostructures based on π-conjugated, self-assembled oligomers have been rated to be suitable for theranostic applications based on their unique photo-physical properties and drug-loading capabilities. They possessed well-defined shapes and sizes, attained stable architectures in an aqueous environment, and sometimes boosted fluorescence quantum yield as well. Thus, these NPs carry inherent theranostic features that can offer rapid, real-time, and sensitive diagnosis, as well as therapeutic platforms for AD. In this regard, we ventured into developing small molecule-derived fluorescent nanotheranostics for AD. The designed auto-fluorescent nanoparticles could act as potential amyloid inhibitors and neuroprotective agents. In addition, owing to their inherent fluorescent and biocompatible nature as well as based on their ability to interact with amyloid aggregates, these NPs can also contribute towards AD imaging and diagnosis.

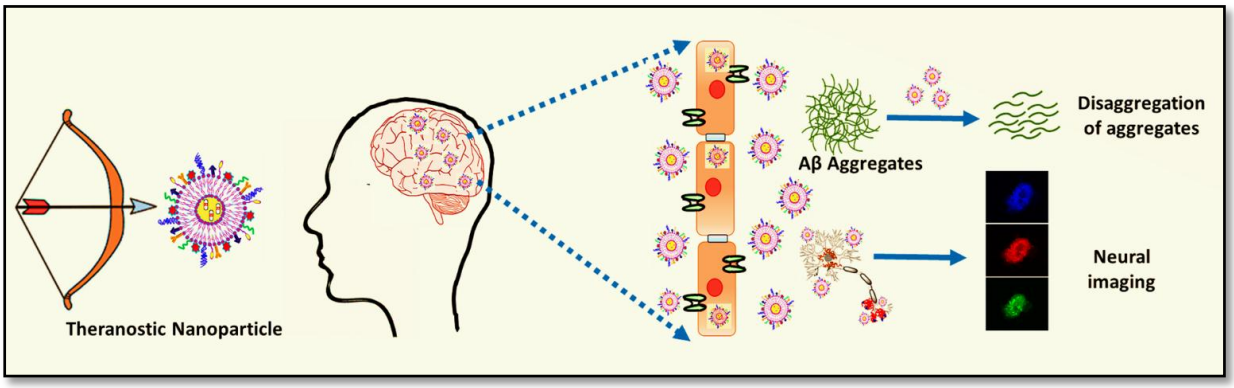

Scheme 1. A schematic presentation showing multimodal nanotheranostics as an anti-amyloid theranostic inhibitor and biocompatible neural cell imaging agent for early diagnosis and therapy of AD.

Chapter 2. Self-Fluorescent Lone Tryptophan Nanoparticles as Theranostic Agents for Alzheimer's Disease

Aggregation of β-amyloid (Aβ42) peptide in neural extracellular space leads to cellular dysfunction resulting in Alzheimer's disease (AD) pathology. The amyloidogenic Aβ42 peptide contains aromatic amino acids in its hydrophobic core that play an important role in its self-assembly. Hence, targeting these hydrophobic aromatic core residues by potent small molecules may be a promising approach against amyloid aggregation. Herein in this chapter, we have developed self-fluorescent solo tryptophan nanoparticles (TNPs) as nanotheranostic systems against AD. We demonstrated that TNPs could significantly inhibit as well as disrupt the fibrils formed by Aβ42 peptide, and a reductionist approach based amyloid model dipeptide, phenylalanine-phenylalanine (FF). More importantly, these nanoparticles were non-toxic to neuronal cells and could protect the neurons from Aβ42 peptide and FF aggregates induced cytotoxicity. In addition, efficacy studies performed in animal models further revealed that the TNPs could rescue spatial and learning memory in intracerebroventricular (ICV) STZ induced AD phenotype in rats. Moreover, pharmacokinetics study further established the BBB permeability and brain delivery potency of TNPs. The inherent excellent fluorescent properties of these nanoparticles could further be exploited to practically use them as imaging modalities for tagging and detecting FF and Aβ42 peptide fibrils **(Scheme 2)**. Overall, our results clearly illustrated that the solo TNPs could serve as promising nanotheranostic agents for AD therapy.

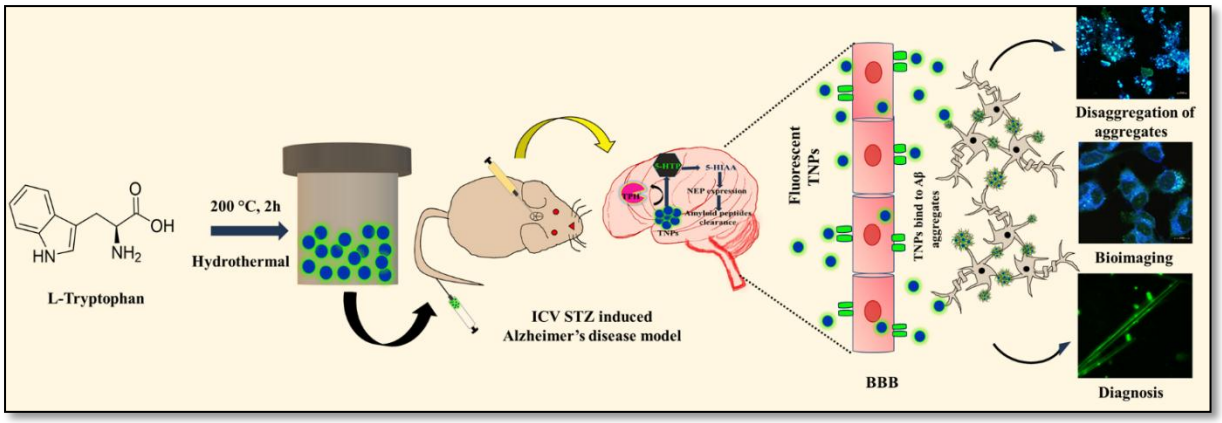

Scheme 2. A schematic presentation depicting self-fluorescent tryptophan nanoparticles synthesis along with their anti-amyloidogenic activity and amyloid aggregates detecting potential.

Chapter 3. Fluorescent Dopamine-tryptophan nanocomposites as dual imaging and anti-aggregation agents: New generation of amyloid theranostics with trimeric effects

Moving a step ahead in the direction of finding a potent anti-AD therapeutics, in this chapter, we developed inherently fluorescent theranostic dopamine tryptophan-nanocomposites (DTNPs) and investigated their amyloid inhibition propensity along with their ability to act as a cellular bioimaging agent in neuronal cells. The anti-aggregation potency of the nanocomposites was further investigated against an in vitro established reductionist amyloid aggregation model consisting of a mere dipeptide, phenylalanine-phenylalanine (FF). As opposed to large peptide/protein derived robust and high molecular weight amyloid aggregation models of Alzheimer's disease, our dipeptide based amyloid model provides an edge over other systems in the row in terms of the ease of their handling, synthesis and cost-effectiveness. Results demonstrated positive anti-aggregation behaviour of the DTNPs towards both FF derived amyloid fibrils and preformed Aβ-peptide fibers by means of electron microscopic and circular dichroism-based studies. Our results further pointed towards the neuroprotective effects exhibited by the DTNPs in neuroblastoma cells against FF amyloid fibrils induced toxicity and also significantly suppressed the accumulation of Aβ42 oligomers in both cortex and hippocampus regions and improved cognitive impairment

in intracerebroventricular streptozotocin **(**ICV-STZ) induced animal model of dementia. Besides, DTNPs also exhibited excellent fluorescent properties and lit up the cytoplasm of neuroblastoma cells upon cellular uptake confirming their ability to serve as an-intracellular bioimaging agent **(Scheme 3)**. Overall, these results signify the potency of the DTNPs as promising multifunctional theranostic agents for treating AD.

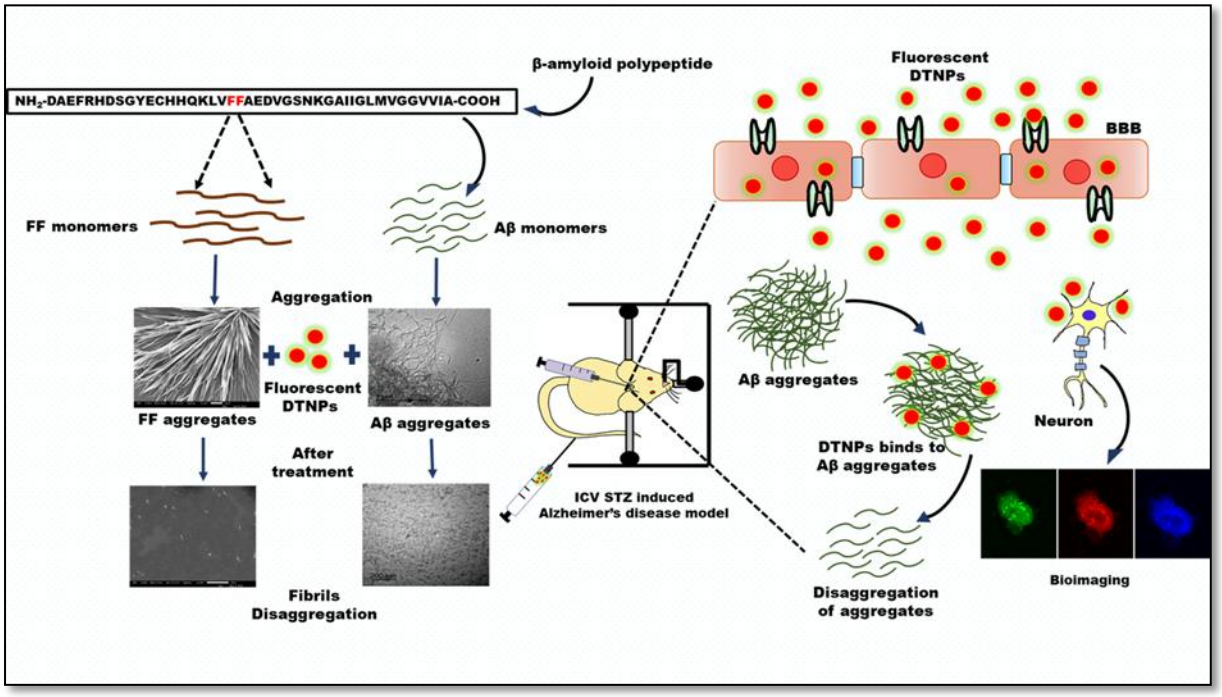

Scheme 3: Overall scheme showing self-fluorescent dopamine tryptophan nanocomposites as anti-amyloid theranostic inhibitor and biocompatible neural cell imaging agent for early diagnosis and therapy of AD.

Chapter 4. Dual functional resveratrol tryptophan nanoparticles loaded polydopamine core (RTDNPs) for Alzheimer's treatment

Inhibiting the aggregation of neurotoxic amyloid aggregates is one of the most viable approach to control the progression of Alzheimer's disease (AD). Despite the promising anti-amyloid potency of both solo tryptophan and nanocomposite of tryptophan toward both FF-derived amyloid fibrils and preformed Aβ-peptide fibers as described in our previous chapters, the anti-aggregation property of nanosystems against tau protein were not explored. Tau pathology is also the common cause of neurodegeneration in Alzheimer's disease (AD) and prevention of aggregated form of hyperphosphorylated tau is one of the targets for AD

treatment. Thus, in this chapter, we have tried to develop a self–fluorescent dual functional resveratrol and L-tryptophan (Res-Trp) loaded polydopamine core (RTDNPs) nanotheranostic system as a dual anti-amyloid agent. The nanosystem demonstrated dual anti-amyloidogenic activity against both FF amyloid fibrils, and the hexapeptide Ac-PHF6 (VQIVYK) derived from the tau protein. Additionally, RTDNPs exhibited a significant neuroprotective effect in neuroblastoma cells against both FF and Ac-PHF6 fibrils-induced toxicity under the NIR laser irradiation (**Scheme 4**). Moreover, RTDNPs also demonstrated remarkable fluorescent properties and lit up the cytoplasm of neural cells confirming their capability to serve as bioimaging agent. Overall, the results of this work clearly illustrate that our dual functional nanosystems can serve as a new class of theranostic systems for combating AD.

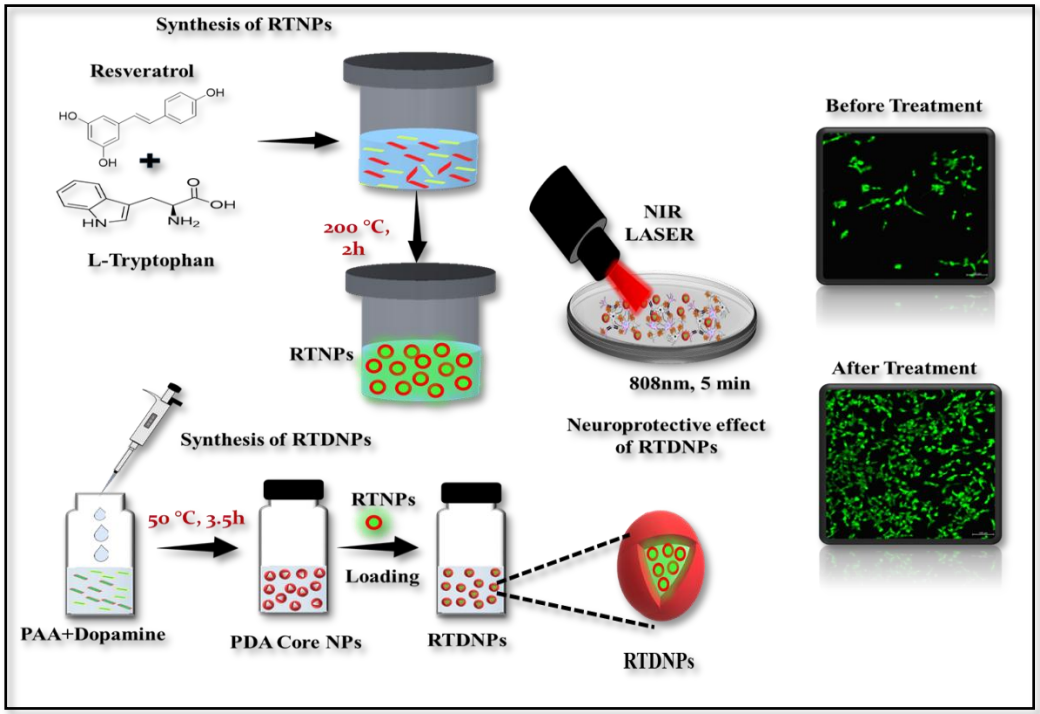

Scheme 4: Overall scheme showing the synthesis of self–fluorescent dual functional resveratrol and L-tryptophan (Res-Trp) loaded polydopamine core (RTDNPs) nanotheranostic nanoparticles and their neuroprotective effect in neuroblastoma cells against both FF amyloid fibrils and hexapeptide Ac-PHF6 fibrils-induced toxicity under the NIR laser irradiation.

Chapter 5. Anti-amyloidogenic potency of acoustic stimulus activated piezoelectric polydopamine-PVDF nanospheres, a futuristic approach towards Alzheimer's therapy

The degeneration of neurons due to the accumulation of misfolded amyloid aggregates in the central nervous system (CNS) is a fundamental neuropathology of Alzheimer's disease (AD). Dislodging/clearing these amyloid aggregates from the neuronal tissues is considered a viable strategy for finding a potential cure for AD. In this chapter, we explored biocompatible polydopamine-coated piezoelectric polyvinylidene fluoride (DPVDF) nanospheres as acoustic stimulus-triggered anti-fibrillating agents against two model amyloidogenic peptides, which includes the reductionist model-based amyloidogenic dipeptide, diphenylalanine, and the amyloid polypeptide, Aβ42. Our results revealed that DPVDF nanospheres could effectively disassemble the model peptide-derived amyloid fibrils, under suitable acoustic stimulation. In vitro studies also revealed that stimulus-activated DPVDF nanospheres could efficiently alleviate the neurotoxicity of FF fibrils as exemplified in neuroblastoma, SHSY5Y cells (**Scheme 5**). Thus, these acoustic stimuli-activated nanospheres could serve as a novel class of disease-modifying nanomaterials for non-invasive electro-chemotherapy of Alzheimer's disease.

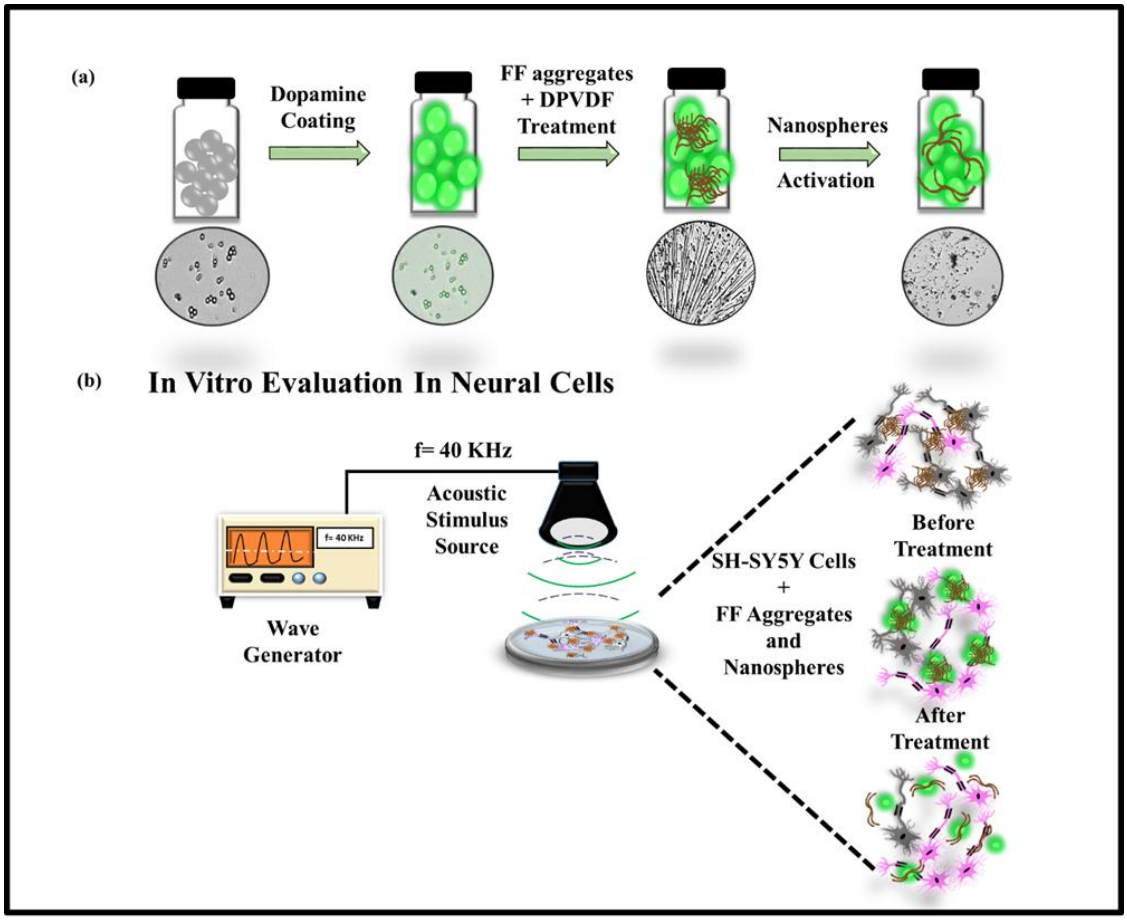

Scheme 5: (a) Overall schematic representation showing the formation of polydopamine-coated PVDF nanospheres. (b) Amyloid fibril disaggregation ability and neuroprotective effects exhibited by acoustic stimulus activated DPVDF nanospheres in neural cells.

CHAPTER 1
INTRODUCTION

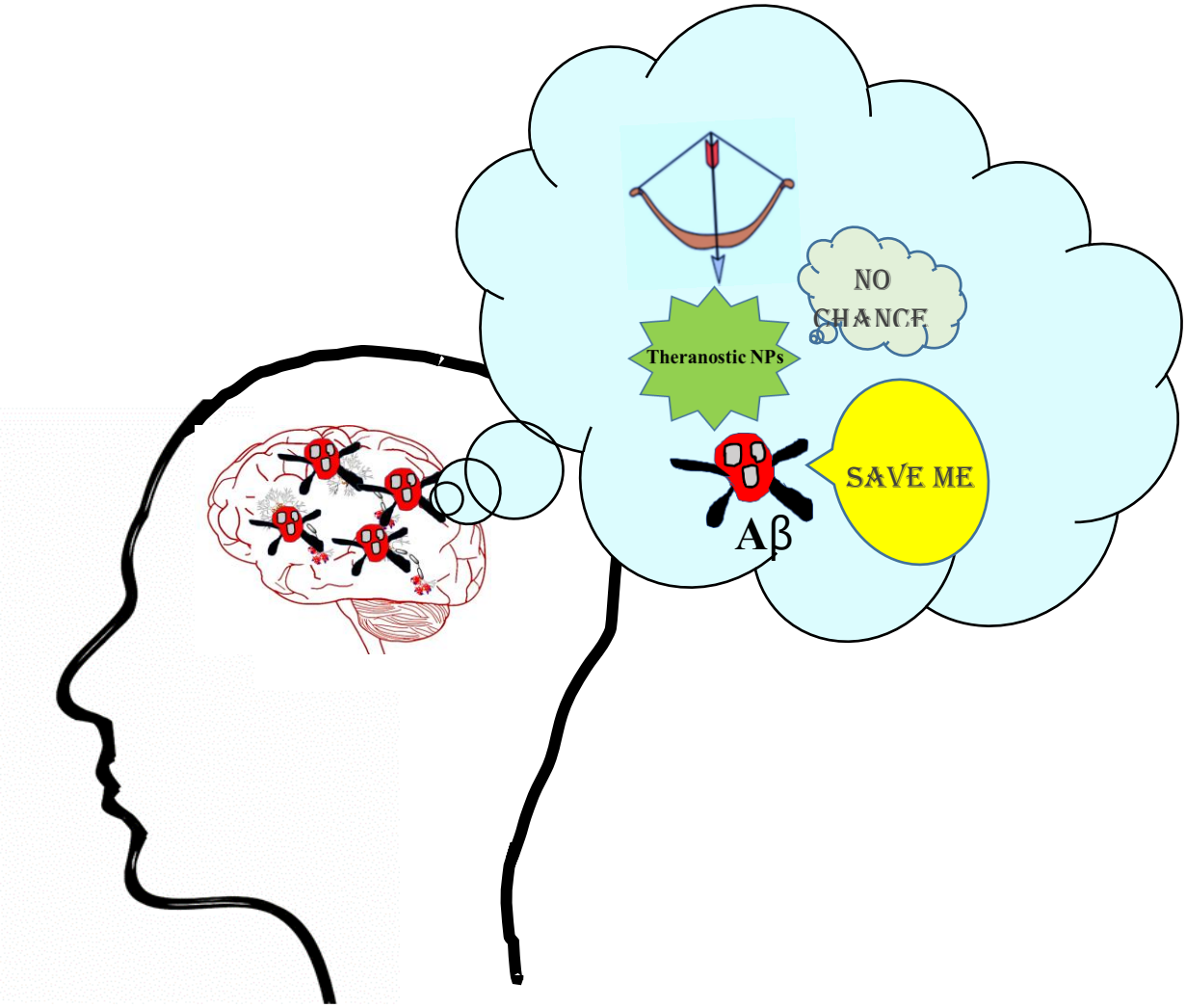

INTRODUCTION

1.1.Background:

Brain, being the centre of control for the body, can cause major threat to life in case of any malfunctioning.[1] Other than cardiovascular and pulmonary disorders/diseases, a steep rise in global burden of neuronal disorders especially Alzheimer's disease (AD) is one of the major public health concerns in today's world. [2] In 1906, AD is first described by Dr. Alois Alzheimer and is named after his name. He examined the brain of his patient named Auguste Deter after her death and found different types of abnormal plaques and tangles of fibers in the cerebral cortex of her brain.[3] AD is a lethal, irreversible and progressive degenerative brain disorder that deteriorates learning, memory and cognition in patients carrying the disorder.[4] Patients with AD show several behavioural issues including anxiety, depression, agitation, and delusion.[5] Pathological characteristics of AD include Aβ42 neuritic plaques, neurofibrillary tangles (NFTs), and neuronal, and synaptic loss.[6] Aβ42 peptide is produced via enzymatic cleavage of the transmembrane amyloid precursor protein (APP) by β and γ-secretase.[7] Aβ42 peptide gets first deposited inside neurons and subsequently, gets released into the neuropil-forming neuritic plaques.[8] The intraneuronal deposition of Aβ42 peptide could indicate a pathologically crucial event of the initiation of neurodegenerative process in AD.[9] Thus, deposition of these intraneuronal Aβ plaques represent a predictive biomarker for the detection of AD pathology **(Figure 1.1).**

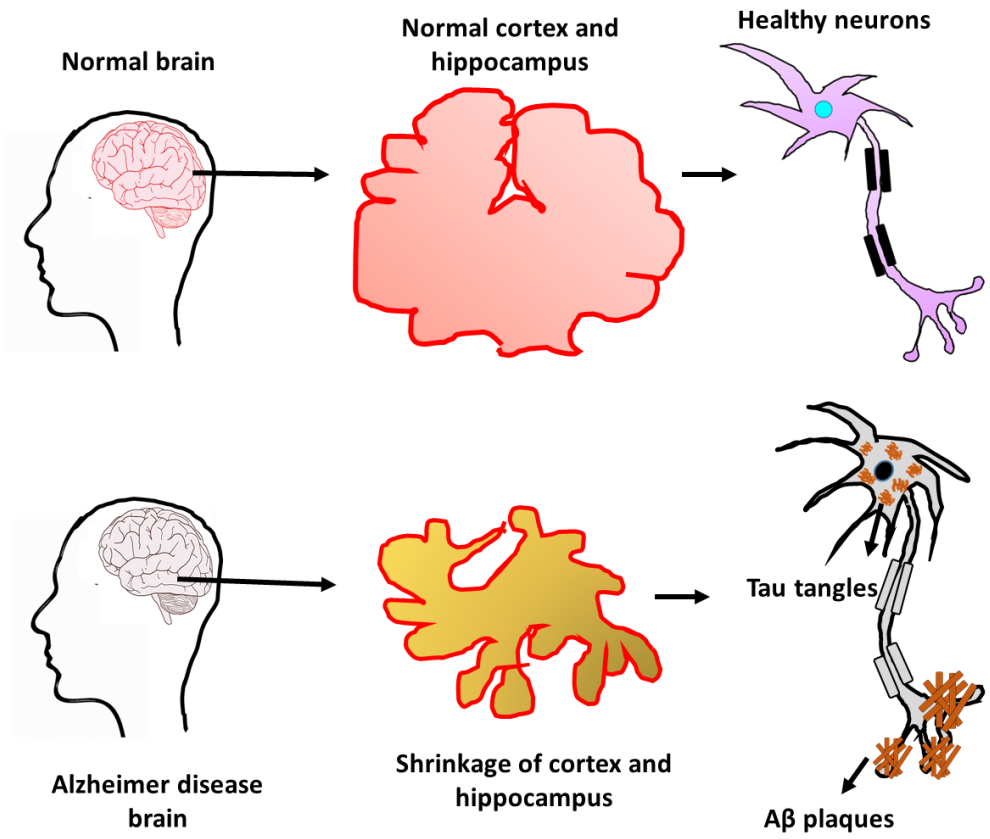

Figure 1.1: A comparison of a normal brain with Alzheimer's disease affected brain.

1.1.1. Alzheimer's cases and global health:

According to World Alzheimer's reports, AD accounts for one of the leading causes of dementia and the 7th leading cause of death globally affecting approximately 55 million people worldwide, and the number will gradually rise to about 139 million cases by 2050. [10] There are approximately 10 million new cases of dementia rising per year globally (one new case in every 3 seconds) according to WHO (2019) report and most of the cases are rising in developing countries.[11,12] According to the Alzheimer's and Related Disorders Society of India (ARDSI) 2020 report, approximately 5.3 million Indians aged >60 years had dementia, and the number will gradually rise to about 14 million cases by 2050. [13] Moreover, the statistics also disclose that > 122,000 people died in the year 2018 from AD, an increase in the number of deaths by ~146% from the year 2000, as compared to other major diseases

such as cancer, HIV, and heart diseases.[14,15] It is the fifth leading cause of mortality among adults aged >65 years.[16] In 2020, the total estimated healthcare costs are accounted for around $305 billion for the treatment of AD and it will rise to more than $1 trillion by 2050.[17] Thus, this neuropathology is ultimately turning out to be a terrible medical, economic, and social burden. [18]

1.1.2. AD Pathogenesis Hypotheses:

AD is a complex multifactorial disease.[19] Thus, its pathogenesis is explained by various hypotheses such as amyloid cascade, tau hyperphosphorylation, cholinergic hypothesis, oxidative stress, genetic hypothesis, etc.[20] But insoluble extracellular plaques of β-amyloid peptide (Aβ) and intraneuronal neurofibrillary tau tangles (NFT) are considered to be the main neuropathological hallmark of AD. Thus, the amyloid cascade hypothesis and tau hyperphosphorylation are two fundamental hypotheses of AD as described below.[21]

Amyloid cascade hypothesis

The amyloid cascade hypothesis is considered to be the most commonly accepted AD etiology.[22] According to this, amyloidogenic Aβ plaques form due to an imbalance of Aβ protein production and clearance in the brain and also act as a trigger for a cascade of events that involves neuritic injury, neurofibrillary tangles formations that ultimately leads to abnormal functioning of neurons and finally cell death.[7] The pathogenic mutation of the amyloid precursor protein (APP) gene located on chromosome 21 leads to AD.[23] Majorly, two important APP processing pathways are involved: a non-amyloidogenic, α-secretase mediated pathway and an amyloidogenic pathway.[24] The Proteolytic cleavage of APP by the α-secretase enzyme at 16-17 residues of the Aβ domain generates a soluble large molecule, sAPPα, that has neuroprotective effects.[25] An amyloidogenic pathway involved sequential cleavage of the amyloid-β protein precursor (AβPP) by β/γ secretase generates short amyloid-

β (Aβ) peptides (Aβ 40 and Aβ 42), which further aggregate into insoluble self-aggregates, senile plaques, and neurotoxic oligomers.[26] These neurotoxic oligomers interfere with cholinergic, dopaminergic, serotonergic, and noradrenergic neurons' functioning and also favour insoluble Aβ peptide accumulation.[27,28] Furthermore, Aβ aggregate deposition damage the plasma membrane of neurons and induces misfolded Aβ peptide internalization into the healthy neurons which cause axonal and dendritic atrophy.[29] Moreover, this also leads to the activation of local microglial cells, release of cytokine, multi-protein inflammatory response, and reactive astrocytosis (**Figure 1.2)**.[30-32]

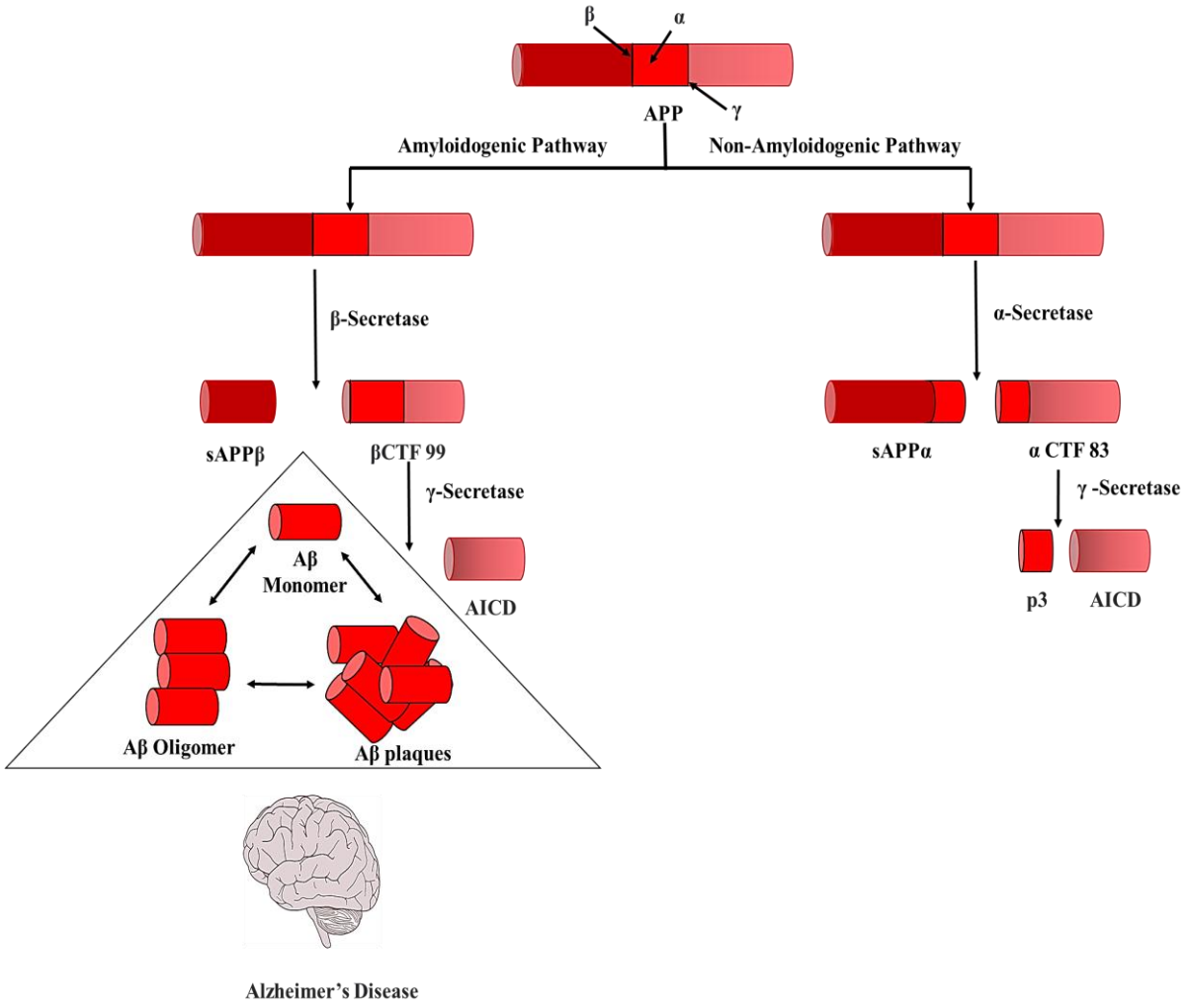

Figure 1.2: Non-amyloidogenic and an amyloidogenic pathway of APP processing that leads to the generation of AD-associated Aβ peptides (APP-amyloid precursor protein, sAPPβ-

soluble APP beta, αCTF 83-alpha C-terminal fragment 83, AICD-APP intracellular domain, sAPPα-soluble APP alpha, βCTF 99-beta C-terminal fragment 99).

Tau Hypothesis

Tau pathology is also a common cause of neurodegeneration in AD. According to the tau hypothesis, excessive or abnormal phosphorylation of the tau protein results in its transformation into PHF-tau (paired helical filament) and NFTs.[33] Tau protein, is a soluble microtubule-associated protein (MAP), majorly present in neurons, and constitute of six isoforms, ranging from 352 and 441 amino-acid residues, which are mainly derived through alternative splicing of a single gene situated on the long arm of chromosome 17.[34,35] The longest isoform of tau protein contains four repeats (R1, R2, R3, and R4) whereas the shortest isoform contains three repeats (R1, R3, and R4).[36] The most important characteristic of the tau protein is microtubule-binding domain (MTBD) which is comprised of extremely conserved three or four repeats of 18 amino acid residues placed in the carboxy-terminal (C-terminal) half of the tau protein. [37] This MTBD is ultimately involved in polymerization and stabilization of microtubules.[38] The amino terminus (N-terminal) (residues 172-251) comprises of mainly acidic amino acids followed by a basic proline-rich region which is usually referred to as the projection domain. The projection domain interacts with the cytoskeleton element and plasma membrane.[39] The dysregulation of the kinase and phosphatase enzymes activities leads to hyperphosphorylation of the tau protein.[40] The hyperphosphorylation of tau also decreases its affinity toward microtubules.[41] The hyperphosphorylated tau proteins further polymerize into PHF and straight NFT in the cytosol of neurons that ultimately impair the axonal functions, degeneration of neuronal cells, and finally lead to cell death.[42,43] In addition, Aβ peptide deposition also causes hyperphosphorylation of tau protein by the generation of proinflammatory cytokines that stimulate the phosphorylation of tau protein **(Figure 1.3)**.[44]

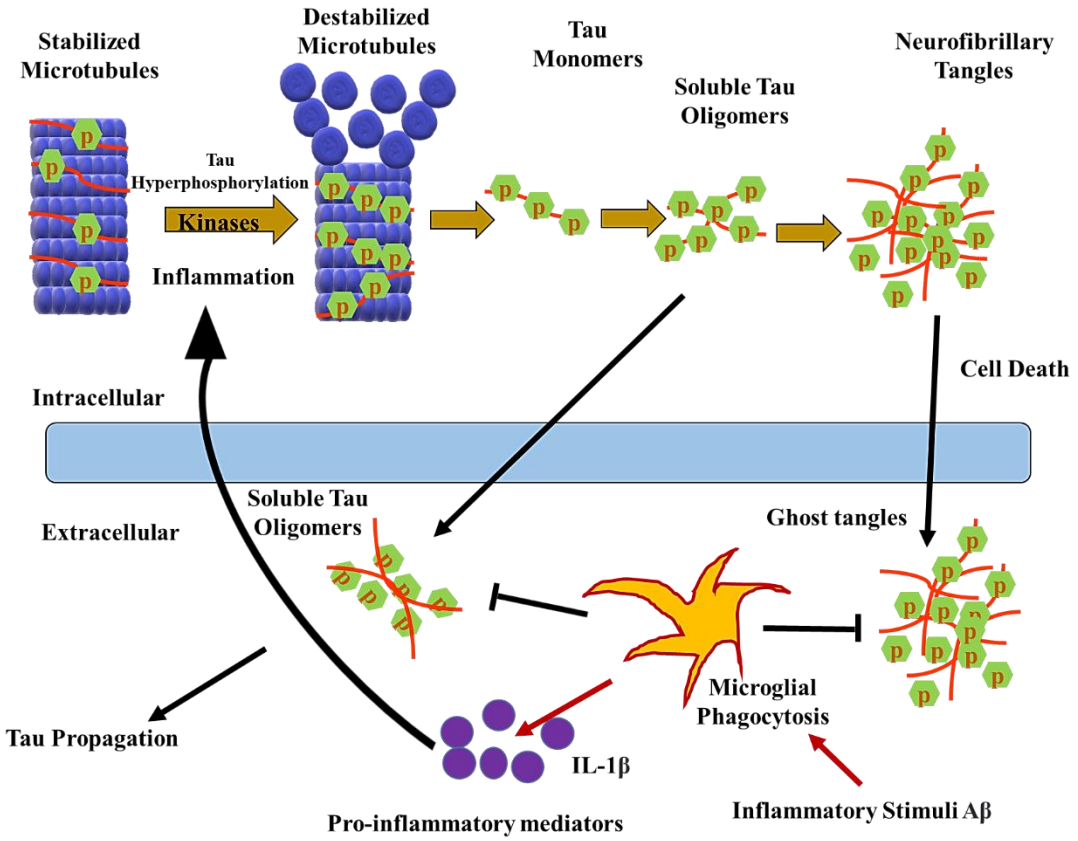

Figure 1.3: Progression of tau neuropathology in AD brain.

1.2. Conventional Treatment of AD:

1.2.1. Acetylcholinesterase inhibitors:

Acetylcholinesterase inhibitors (ACEIs) are the first USFDA-approved drugs for AD treatment. [45] These drugs enhance the levels of acetylcholine (a neurotransmitter in the brain) that helps establish communication of nerve cells with each other, and these are the only drugs currently prescribed by neurologists. [46] Rivastigmine, galantamine, tacrine, para-aminobenzoic acid, coumarin, donepezil, xanthostigmine, and flavonoid have been developed for AD treatment. All these ACEIs promote higher levels of ACh and inhibit the enzyme acetylcholinesterase to degrade the ACh. [47] Memantine is an N-methyl D-aspartate (NMDA) glutamate receptor antagonist which blocks the NMDA glutamate receptors to regulate the glutamatergic system and improves cognitive and memory problems. It is approved by the

food and drug administration (FDA) in 2003 and is also recommended for moderate-to-severe treatment of AD when an ACEI doesn't work.[48]

1.2.2 Secretase inhibitors for AD:

Secretases inhibitors are a class of drugs that thwart the development of abnormal senile plaques.[49] β-secretase inhibitors (BACEI) such as (atabecestat, BI1181181, elenbecestat, LY2886721, LY3202626, lanabecestat, PF-06751979, RG7129, umibecestat, verubecestat) and γ secretase inhibitors (GSI) such as avagacestat, EVP0015962, PF-06648671, semagacestat are in different phases of clinical trials for AD.[50] Aduhelm is the first medicine approved by the USFDA to target and remove amyloid senile plaques in the brain for the treatment of AD (FDA,2021). [51]

1.2.3 Aβ fibril inhibitors:

Aβ plaques represent a promising and predictive amyloid biomarker for the early detection of amyloid pathology in AD and also serve as a viable therapeutic target. [52] Scylloinositol (phase II), tramiprosate (phase III), epigallocatechin-3-gallate (phase II/III), and clioquinol (phase II) are currently available small molecule inhibitors against aggregation of Aβ in clinical trials.[53] Also, β-sulfonylproline, β-proline, 3-phenyl azetidine-2-carboxylic acid, and azetidine-2-carboxylic acid are synthetic β-sheet breaker peptides that prevent the fibril formation and modulate the cell damage due to the exposure of Aβ. [54] Similarly, Stemazole has been exhibited in vitro neuroprotective effect against Aβ induced cytotoxicity in SH-SY5Y cells. [55] Likewise, SK-PC-B70M, curcumin, and T718MA are other compounds that protect neuronal cells from A*β*-mediated cytotoxicity.[56]

1.2.4. Aβ therapeutic antibodies:

Among anti- Aβ treatment strategies, passive immunization of anti-amyloid monoclonal antibodies (anti-Aβ mAbs) is the most extensively developed therapy for AD treatment.[57]

Currently, exogenous monoclonal antibodies in different phases of clinical trials for the disease are solanezumab (LY2062430), a humanized monoclonal antibody (IgG1) that targets and removes neurotoxic Aβ aggregates in mild-to-moderate AD brains,[58] aducanumab (BI-IB037) is also human IgG1 monoclonal antibody that targets Aβ oligomers and insoluble plaques,[59] Genentech and Roche's crenezumab (MABT5102A, RG7412) are humanized IgG4 monoclonal antibody that targets multiple forms of Aβ aggregates such as oligomers, fibrils, and insoluble plaques,[60] and gantenerumab (RO4909832, RG14502) is a type of IgG1 monoclonal antibody that targets and binds the fibrils of Aβ at subnanomolar scale.[61]

1.2.5. Tau Therapies:

Tau pathology is also the common cause of neurodegeneration in Alzheimer's disease (AD) and prevention of aggregated form of hyperphosphorylated tau is one of the targets for AD treatment.[62] Currently, humanized antibodies such as 8E12 and BIIB092 are being investigated at different phases of clinical trials for the treatment of AD.[63] Like passive tau immunotherapy, two active tau vaccines that have been investigated in human clinical trials for AD are AADvac1(Axon Neuroscience SE), and ACI-35M, a liposomal-based vaccine. [64]

Instead of immunotherapy and vaccines, various other molecules also act as potent inhibitors of tau aggregation and are being investigated in clinical trials. Among these drugs, azure A and azure B, metabolites of methylene blue (MB) and MB itself are able to inhibit the activity of caspase-1 and caspase-3 and promote degradation of protein.[65,66] Similarly, methylthioninium chloride (MTC) (phase II clinical trial) and leucomethylthioninium (LMTX) (phase III clinical trial) have been found effective to reduce aggregation of tau and reverse behavioral ailments in the transgenic model of mice and to slow the disease progression in AD patients.[67] Other promising tau aggregation inhibitors are phenothiazines,

N-phenylamines, rhodanines, anthraquinones, benzothiazoles, and phenylthiazolyl-hydrazides.[68]

In addition to all these therapies, different types of therapeutic agents in clinical trials for AD[69] treatments are also represented in **Figure 1.4**.

Figure 1.4: Therapeutic agents in clinical trials for treatment of AD. The inner ring represents agents in Phase 3, middle ring shows Phase 2 and outer ring comprises phase 1 agents. [Reproduced with permission from (69) under creative commons licenses 4.0 (https://creativecommons.org/licenses/by-nc-nd/4.0/)][69]

1.2.6. Limitations:

Despite many years of intensive research, various clinical trials on available disease-modifying therapies for the treatment of AD have shown unsatisfactory results and also have

several limitations. The current AD therapies help to reduce the symptoms and improve the patient's quality of life but these medications neither slow the progression of the disease nor cure it. Moreover, the available treatment strategies are not able to detect the disease at its earliest stage. [70] Additionally, the major limitation of these therapies is the low bioavailability of the potent CNS drugs in the central nervous system (CNS) due to their meagre access to the brain because of the blood-brain barrier (BBB).[71] Moreover, most of these medicines have various side effects such as vomiting, allergic reactions, loss of appetite, and diarrhea. To overcome all these issues and to achieve effective therapy, there is a pressing need for the development of advanced methods which possess high sensitivity, high resolution, deep penetration power, and the ability to facilitate real-time monitoring of disease progression along with biosafety. In this context, ultrasmall multimodal nanotheranostics can show great potential for biomedical imaging and disease therapy.

1.3. Nanotheranostics:

The term 'theranostics' defined as the combination of diagnosis and therapy, is an emerging and promising field of medicine believed to hold great potential to cure many difficult to treat diseases.[72] The motive behind its development has hailed from the fact that all existing treatment modalities for fatal diseases are only capable of treating limited patient subpopulations and only at selective stages of disease development. Therefore, an integration of diagnosis and therapeutic approach could offer a superior therapeutic regimen which is not only specific to the subjects but at the same time offer improved prognosis. [73] Nanotheranostics is an advanced form of theranostic system which involves 'nanotechnology' for diagnosis and therapy of different diseases with gloomy prognosis.[74]

Treatment of different dreaded diseases can be effective if diagnosed at a very early stage. Whereas, as a matter of concern, existing diagnosis approaches are usually incompetent in

diagnosing neural disorders at their primary stages. Therefore, nanotheranostics comprising of nanocarriers, carrying both therapeutic and/or diagnostic moieties can be game changing in revolutionizing and personalizing neuromedicine. [75] The diagnostic agents, which are often used in nanotheranostics, are quantum dots or fluorescent dyes for optical imaging, iron oxides for magnetic resonance imaging (MRI), radionuclides for nuclear imaging and heavy metals for computed tomography (CT).[73] In addition to diagnostic agents, therapeutic agents can be hydrophobic organic drugs, proteins, peptides and genetic materials.[76] Besides, the imaging or diagnostic agents, nanocarriers are the major components of a nanotheranostic system. Nanocarriers foster pharmacokinetics, enhance biodistribution of the loaded therapeutic and diagnostic moieties at the target tissues,[77] and increase drug efficacy along with lessening toxicity due to reduced non-specific biodistribution.[78,79] These nanocarriers have been discerned to be functionalized with biomarkers or other targeting ligands for achieving target-specific treatments and also to achieve diagnostic ability in real time. Further, therapeutic entities such as small sized hydrophobic molecules, peptide drugs as well as oligonucleotides have been shown to exhibit enhanced stability when being loaded into nanocarriers.[80]

1.3.1. Nanotheranostics for AD:

Currently, different multifunctional nanoparticles such as inorganic NPs, polymeric NPs, protein-based NPs, and carbonaceous nanostructures are widely used as nanotheranostics agents due to the inherent theranostic properties of these nanoparticles that can offer real-time, rapid and sensitive diagnostics as well as therapeutic platforms for AD.[81] Zhang and group reported a nanotheranostics system (congo red/rutin-MNPs) based on magnetic iron oxide NPs (MNPs) with ultrasmall size to realize in vivo imaging of amyloid plaques along with targeted delivery and H_2O_2 triggered release of therapeutic agent rutin. congo red/ rutin-MNPs theranostic system when co-administered with mannitol was able to breach and cross

BBB of the APPswe/PS1dE9 transgenic mouse and specifically bind to amyloid plaques, allowing the recognition of amyloid plaques by MRI along with targeted, and stimuli-responsive delivery of rutin via the Aβ-induced production of H_2O_2. Rutin is a powerful antioxidant which prevents oxidative stress, interferes with Aβ aggregation, and reduces amyloid plaques and neuronal loss.[82] In another report, researchers have developed a novel tau targeted multifunctional nanocomposite, ceria nanocrystals (CeNC) and iron oxide nanocrystals (IONCs) onto the surface of mesoporous silica nanoparticles (MSNs) functionalized with amino-T807 (PET tau tracer), an amino substituent of T807 and methylene blue (CeNC/IONC/MSNT807-MB) for AD theranostics. They focused on an alternative tau targeting approach for treating AD instead of amyloid-β (Aβ) targeted therapy. The CeNC/IONC/MSN-T807-MB nanocomposite was formed by the controlled assembly of ultrasmall ceria nanocrystals (CeNCs), as tau hyperphosphorylation inhibitor and iron oxide nanocrystals (IONCs), as MRI agent, on the surface of uniform mesoporous silica NPs (MSNPs). Further, the surface of MSN was functionalized with amino-T807, via 1,4,7-triazacyclononane1,4,7-triacetic acid (NOTA), for active targeting of tau protein. Methylene blue (MB), a small inhibitor for tau aggregation was further loaded into the pores of MSNs. In vitro and in vivo studies of CeNC/IONC/MSN-T807-MB nanocomposite formulations using SH-SY5Y cells and AD rat models demonstrated significant suppression of tau hyperphosphorylation and protection of neural death.[83] Similarly, Li et. al. have reported novel multifunctional peptide conjugated gold (Au) nanorods for diagnosis and treatment of AD. They combined unique high NIR absorption property of AuNRs with two Aβ inhibitors, Aβ15–20 (Aβ-targeted peptide inhibitor) and polyoxometalates (POMs) for effective inhibition of Aβ aggregation and also dissociation of amyloid deposits by NIR irradiation. Additionally, shape and size-dependent optical properties of gold nanorods were used as effective diagnostic probes for the detection of Aβ aggregates. Thus, this study exemplifies a

multifunctional theranostic nanosystem containing various components such as a targeting ligand, a reporter, and inhibitors in one system for treating AD.[84] Cui et. al. have reported a novel smart UCNP based nanoprobe that can simultaneously serve the purpose for accurate diagnosis and effective therapy of AD. UCNPs nanoprobe consists of two major components: UCNPs for detection and imaging, the chelator 8-hydroxyquinoline-2-carboxylic acid (HQC) for capturing of Cu^{2+}, and therapy of AD. These multifunctional UCNPs were capable of detecting and capturing Cu^{2+} both in vitro and in vivo. Fascinatingly, this system has also shown the unique ability to inhibit as well as transform toxic Aβ intermediates into nontoxic fibers.[85] Recently, Pedro et. al. reported the synthesis of functionalized CNTs (f-CNTs) and used them as theranostic carriers for brain delivery of amyloid-targeting drugs/compounds that efficiently cross the BBB. Importantly, attractive intrinsic optical, thermal properties, and the ability to cross biological barriers by both energy-dependent and independent mechanisms of functionalized CNTs (f-CNTs), bestows them as useful tools towards brain targeting theranostic applications.[86] Functionalized multi-walled carbon nanotubes (f-MWNTs) capable of crossing an intact BBB have already been demonstrated by Kafa and group.[87-89] They functionalized MWNTs with two PiB derivative Gd^{3+} complexes ,Gd (L2) and Gd(L3). PiB is an Aβ-binding molecule and used as a PET imaging agent. In vivo biodistribution results demonstrated considerable uptake and accumulation of f-MWNTs in the brain as compared to free metal complexes. Thus, this report claims that f-MWNTs could be used as carriers in theranostic applications involving brain delivery of BBB impermeable compounds.[90]

1.3.2. Fluorescent Nanoparticles as AD Theranostic agents:

Among different theranostics nanostructures, fluorescent nanostructures based on π-conjugated, self-assembled oligomers have been rated to be suitable for theranostic applications based on their unique photo-physical properties and drug loading capabilities.

They possessed well-defined shape and sizes, attained stable architectures in an aqueous environment and sometimes boosted fluorescence quantum yield as well.[91] Thus, these NPs carry inherent theranostic features that can offer rapid, real-time, and sensitive diagnosis, as well as therapeutic platforms for AD. [92] In recent years, a large amount of newly-developed fluorescent theranostic nanostructures have been designed and used for AD treatment. Zhi Du et. al. developed a 'sense and treat system' to target amyloid aggregates related to AD, which is one of the best examples to illustrate 'image-guided therapy' of Alzheimer's by simultaneous diagnosis and treatment. They used magnetic NPs (MNPs) whose surface was modified with two moieties, firstly, by napthalimide based fluorescent probe (NFP) which was an oligomer-specific fluorescent probe designed against the exposed hydrophobic regions on Aβ oligomer surface and secondly, by Aβ-target peptide, KLVFF. The complex (MNP@NFP-pep) monitored the changes in Aβ morphology resulting from the disaggregation of Aβ aggregates by the local heat generated by MNPs that could be sensed by the fluorescence probe. Therefore, it can be used as a real-time, 'sense and treat' system for the treatment of AD.[93] Li and group showed the theranostic effect of (E)-4-(4-(dibutylamino)styryl)-1-(2-hydroxyethyl) quinolin-1-ium chloride (DBA-SLOH) NIR dye which accomplished AD diagnostics via NIR based in vivo imaging of Aβ plaques in APP/PS1 transgenic (Tg) mouse over-expressing Aβ. Concomitantly therapeutics were achieved by inhibiting Aβ monomers to self-aggregate. This group developed three cationic NIR dyes and confirmed their activity to inhibit Aβ peptide aggregation by ThT fluorescence assays, CD spectroscopy, in vitro fluorescence staining of Aβ plaques in brain slices, and in vivo NIR imaging in animal model. Among them, DBASLOH showed highest BBB permeability, excellent selectivity and binding affinity to Aβ peptides, and intense enhancement of fluorescence signal in the NIR window upon binding to Aβ aggregates. The developed theranostic design with excellent BBB permeability integrating both NIR imaging

of Aβ species and inhibition of Aβ aggregation in vivo for the diagnosis and therapy of AD may open up a new avenue in AD treatment.[94] In another study, Zhang and group developed dual functional pegylated poly (lactic acid) NPs (PEG-PLA NPs) based targeted delivery system for the early diagnosis and treatment of AD. To achieve dual targeting, a 12-amino acid peptide, TGN (targeting ligand for BBB), D-enantiomeric peptide, QSH (targeting ligand for Aβ42 deposits in the brain), were surface functionalized over the NPs. Dual targeting of the designed system was confirmed via brain distribution studies of NPs using a near-infrared dye, DiR, as a probe and ex vivo imaging studies. T3Q3-NP showed precise and improved targeted delivery towards amyloid plaque in the brains of AD mice model pointing towards a valuable theranostic system for AD diagnosis and therapy.[95]

Likewise, we ventured into developing small molecule-derived fluorescent nanotheranostics for AD. Initially, we started with single amino acid based solo tryptophan nanoparticles (TNPs) and explored their antiamyloidogenic, neuroprotective and auto-fluorescent properties for AD diagnosis and treatment. Next we tried to explore the anti-amyloid propensity of theranostic tryptophan nanocomposite with another anti-amyloidogenic and neuroactive molecule, dopamine (DTNPs). Both solo TNPs and DTNPs exhibited neuroprotective effect in neuroblastoma cells against FF amyloid fibrils induced toxicity and also significantly suppressed the accumulation of Aβ42 oligomers in both cortex and hippocampus regions and improved cognitive impairment in intracerebroventricular streptozotocin **(**ICV-STZ) induced animal model of dementia. Besides, they also exhibited excellent fluorescent properties and light up the cytoplasm of neuroblastoma cells when being co-incubated with cells confirming their ability to serve as an-intracellular bioimaging agent.
Despite the promising anti-amyloid potency of both solo tryptophan and nanocomposite of tryptophan toward both FF-derived amyloid fibrils and preformed Aβ-peptide fibers, we have tried to explore anti-amyloidogenic property of a nanosystem against tau protein and

developed a dual functional fluorescent resveratrol and L-tryptophan (Res- Trp) loaded dopamine (dopa) core nanotheranostic system as a dual anti-amyloid agent. The nanosystem demonstrated dual anti-amyloidogenic activity against both FF peptide aggregates, and the hexapeptide Ac-PHF6 (VQIVYK) derived from tau protein.

In addition to simple small molecule based nanotheranostic systems for treating and diagnosing AD, we have also tried to explore dopamine coated piezoelectric polyvinylidene fluoride (DPVDF) nanospheres as acoustic stimulus (sonication) triggered anti-fibrillizing agents towards FF, as well as Aβ42-polypeptide fibrils. DPVDF nanospheres represent a class of biocompatible piezoelectric materials with piezo-catalytic properties triggered in response to acoustic stimulus. The acoustic stimulus-activated DPVDF nanospheres produced piezo-induced oxidative stress, under both in vitro and in cellular conditions, which successfully destabilized FF and Aβ42 fibrils.

Thus, these different auto-fluorescent small molecule-derived nanotheranostic systems, could act as potential amyloid inhibitors and neuroprotective agents. In addition, owing to their inherent fluorescent and biocompatible nature as well as based on their ability to interact with amyloid aggregates, these NPs can also contribute towards AD imaging and diagnosis **(Scheme 1.1)**.

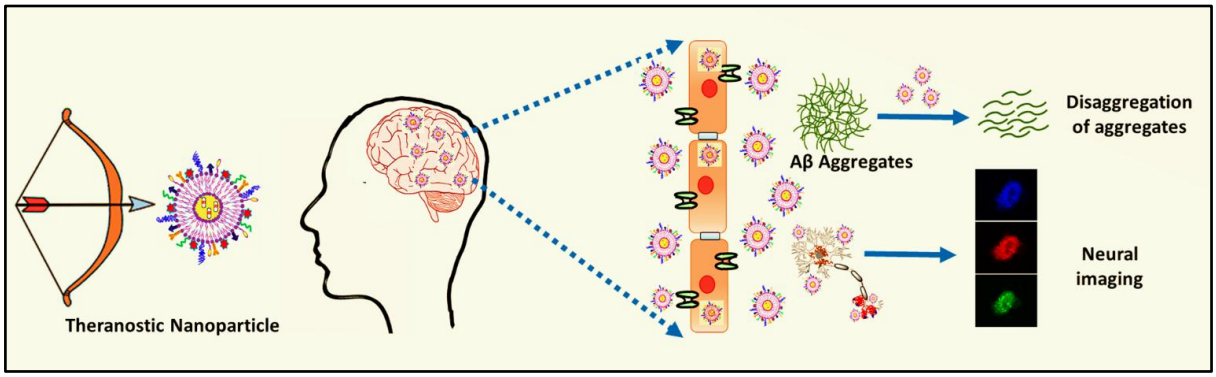

Scheme 1.1: A schematic presentation showing multimodal nanotheranostics as an anti-amyloid theranostic inhibitor and biocompatible neural cell imaging agent for early diagnosis and therapy of AD.

1.4. References:

(1) Cieza, A.; Anczewska, M.; Ayuso-Mateos, J. L.; Baker, M.; Bickenbach, J.; Chatterji, S.; Hartley, S.; Leonardi, M.; Pitkänen, T.; PARADISE Consortium. Understanding the Impact of Brain Disorders: Towards a "Horizontal Epidemiology" of Psychosocial Difficulties and Their Determinants. *PLoS One* **2015**, *10* (9), e0136271.

(2) Collaborators, G. 2016 N. Global, Regional, and National Burden of Neurological Disorders, 1990–2016: A Systematic Analysis for the Global Burden of Disease Study 2016. *The Lancet. Neurology* **2019**, *18* (5), 459.

(3) Alzheimer, A.; Stelzmann, R. A.; Schnitzlein, H. N.; Murtagh, F. R. An English Translation of Alzheimer's 1907 Paper, "Uber Eine Eigenartige Erkankung Der Hirnrinde." *Clin Anat* **1995**, *8* (6), 429–431.

(4) Castellani, R. J.; Rolston, R. K.; Smith, M. A. Alzheimer Disease. *Dis Mon* **2010**, *56* (9), 484–546.

(5) Cerejeira, J.; Lagarto, L.; Mukaetova-Ladinska, E. B. Behavioral and Psychological Symptoms of Dementia. *Front Neurol* **2012**, *3*, 73.

(6) Serrano-Pozo, A.; Frosch, M. P.; Masliah, E.; Hyman, B. T. Neuropathological Alterations in Alzheimer Disease. *Cold Spring Harb Perspect Med* **2011**, *1* (1), a006189.

(7) O'Brien, R. J.; Wong, P. C. Amyloid Precursor Protein Processing and Alzheimer's Disease. *Annu Rev Neurosci* **2011**, *34*, 185–204.

(8) Murphy, M. P.; LeVine, H. Alzheimer's Disease and the β-Amyloid Peptide. *J Alzheimers Dis* **2010**, *19* (1), 311.

(9) DeTure, M. A.; Dickson, D. W. The Neuropathological Diagnosis of Alzheimer's Disease. *Molecular Neurodegeneration* **2019**, *14* (1), 32.

(10) Breijyeh, Z.; Karaman, R. Comprehensive Review on Alzheimer's Disease: Causes and Treatment. *Molecules* **2020**, *25* (24), 5789.

(11) International, A. D. World Alzheimer Report 2019: Attitudes to Dementia. **2019**.

(12) International, A. D.; Guerchet, M.; Prince, M.; Prina, M. Numbers of People with Dementia Worldwide: An Update to the Estimates in the World Alzheimer Report 2015. **2020**.

(13) Kumar, CTS.; Shaji, KS.; Varghese, M.; Nair, MKC.Dementia in India: Alzheimer's and Related Disorders Society of India (ARDSI). **2020**.

(14) Alzheimer's Association. 2020 Alzheimer's disease facts and figures. *Alzheimer's Dementia*, 2020, **16**, 391.

(15) Alzheimer's Association. Neuroscience Next 2020 Abstracts. *Alzheimers Dement* **2020**, *16 Suppl 12*, e12278.

(16) 2021 Alzheimer's disease facts and figures. Alzheimers Dement 2021 ,17(3),327-406.

(17) Wong, W. Economic Burden of Alzheimer Disease and Managed Care Considerations. *Am J Manag Care* **2020**, *26* (8 Suppl), S177–S183.

(18) W, W. Economic Burden of Alzheimer Disease and Managed Care Considerations. *The American journal of managed care* **2020**, *26* (8 Suppl).

(19) Iqbal, K.; Grundke-Iqbal, I. Alzheimer Disease, a Multifactorial Disorder Seeking Multi-Therapies. *Alzheimers Dement* **2010**, *6* (5), 420–424.

(20) Du, X.; Wang, X.; Geng, M. Alzheimer's Disease Hypothesis and Related Therapies. *Transl Neurodegener* **2018**, *7*, 2.

(21) Bloom, G. S. Amyloid-β and Tau: The Trigger and Bullet in Alzheimer Disease Pathogenesis. *JAMA Neurol* **2014**, *71* (4), 505–508.

(22) Ricciarelli, R.; Fedele, E. The Amyloid Cascade Hypothesis in Alzheimer's Disease: It's Time to Change Our Mind. *Curr Neuropharmacol* **2017**, *15* (6), 926–935.

(23) TCW, J.; Goate, A. M. Genetics of β-Amyloid Precursor Protein in Alzheimer's Disease. *Cold Spring Harb Perspect Med* **2017**, *7* (6), a024539.

(24) Haass, C.; Kaether, C.; Thinakaran, G.; Sisodia, S. Trafficking and Proteolytic Processing of APP. *Cold Spring Harb Perspect Med* **2012**, *2* (5), a006270.

(25) Nhan, H. S.; Chiang, K.; Koo, E. H. The Multifaceted Nature of Amyloid Precursor Protein and Its Proteolytic Fragments: Friends and Foes. *Acta Neuropathol* **2015**, *129* (1), 1–19.

(26) Hampel, H.; Hardy, J.; Blennow, K.; Chen, C.; Perry, G.; Kim, S. H.; Villemagne, V. L.; Aisen, P.; Vendruscolo, M.; Iwatsubo, T.; Masters, C. L.; Cho, M.; Lannfelt, L.; Cummings, J. L.; Vergallo, A. The Amyloid-β Pathway in Alzheimer's Disease. *Mol Psychiatry* **2021**, *26* (10), 5481–5503.

(27) Kar, S.; Slowikowski, S. P. M.; Westaway, D.; Mount, H. T. J. Interactions between β-Amyloid and Central Cholinergic Neurons: Implications for Alzheimer's Disease. *J Psychiatry Neurosci* **2004**, *29* (6), 427–441.

(28) Rajmohan, R.; Reddy, P. H. Amyloid Beta and Phosphorylated Tau Accumulations Cause Abnormalities at Synapses of Alzheimer's Disease Neurons. *J Alzheimers Dis* **2017**, *57* (4), 975–999.

(29) Sadigh-Eteghad, S.; Sabermarouf, B.; Majdi, A.; Talebi, M.; Farhoudi, M.; Mahmoudi, J. Amyloid-Beta: A Crucial Factor in Alzheimer's Disease. *Med Princ Pract* **2015**, *24* (1), 1–10.

(30) Mandrekar, S.; Landreth, G. E. Microglia and Inflammation in Alzheimer's Disease. *CNS Neurol Disord Drug Targets* **2010**, *9* (2), 156–167.

(31) Wang, W.-Y.; Tan, M.-S.; Yu, J.-T.; Tan, L. Role of Pro-Inflammatory Cytokines Released from Microglia in Alzheimer's Disease. *Ann Transl Med* **2015**, *3* (10), 136.

(32) Bamberger, M. E.; Landreth, G. E. Microglial Interaction with β-Amyloid: Implications for the Pathogenesis of Alzheimer's Disease. *Microscopy Research and Technique* **2001**, *54* (2), 59–70.

(33) Iqbal, K.; Liu, F.; Gong, C.-X.; Grundke-Iqbal, I. Tau in Alzheimer Disease and Related Tauopathies. *Current Alzheimer research* **2010**, *7* (8), 656.

(34) Gong, C.-X.; Iqbal, K. Hyperphosphorylation of Microtubule-Associated Protein Tau: A Promising Therapeutic Target for Alzheimer Disease. *Curr Med Chem* **2008**, *15* (23), 2321–2328.

(35) Goedert, M.; Spillantini, M. G.; Jakes, R.; Rutherford, D.; Crowther, R. A. Multiple Isoforms of Human Microtubule-Associated Protein Tau: Sequences and Localization in Neurofibrillary Tangles of Alzheimer's Disease. *Neuron* **1989**, *3* (4), 519–526.

(36) Goode, B. L.; Chau, M.; Denis, P. E.; Feinstein, S. C. Structural and Functional Differences between 3-Repeat and 4-Repeat Tau Isoforms: IMPLICATIONS FOR NORMAL TAU FUNCTION AND THE ONSET OF NEURODEGENERATIVE DISEASE*. *Journal of Biological Chemistry* **2000**, *275* (49), 38182–38189.

(37) Lee, G.; Neve, R. L.; Kosik, K. S. The Microtubule Binding Domain of Tau Protein. *Neuron* **1989**, *2* (6), 1615–1624.

(38) Goode, B. L.; Feinstein, S. C. Identification of a Novel Microtubule Binding and Assembly Domain in the Developmentally Regulated Inter-Repeat Region of Tau. *J Cell Biol* **1994**, *124* (5), 769–782.

(39) Mandelkow, E.-M.; Mandelkow, E. Biochemistry and Cell Biology of Tau Protein in Neurofibrillary Degeneration. *Cold Spring Harb Perspect Med* **2012**, *2* (7), a006247.

(40) Gong, C.-X.; Liu, F.; Grundke-Iqbal, I.; Iqbal, K. Dysregulation of Protein Phosphorylation/Dephosphorylation in Alzheimer's Disease: A Therapeutic Target. *J Biomed Biotechnol* **2006**, *2006*, 31825.

(41) Alonso, A. D.; Cohen, L. S.; Corbo, C.; Morozova, V.; ElIdrissi, A.; Phillips, G.; Kleiman, F. E. Hyperphosphorylation of Tau Associates With Changes in Its Function Beyond Microtubule Stability. *Frontiers in Cellular Neuroscience* **2018**, *12*.

(42) Crespo-Biel, N.; Theunis, C.; Van Leuven, F. Protein Tau: Prime Cause of Synaptic and Neuronal Degeneration in Alzheimer's Disease. *International Journal of Alzheimer's Disease* **2012**, *2012*, e251426.

(43) Gendron, T. F.; Petrucelli, L. The Role of Tau in Neurodegeneration. *Mol Neurodegener* **2009**, *4*, 13.

(44) Mohamed Asik, R.; Suganthy, N.; Aarifa, M. A.; Kumar, A.; Szigeti, K.; Mathe, D.; Gulyás, B.; Archunan, G.; Padmanabhan, P. Alzheimer's Disease: A Molecular View of β-Amyloid Induced Morbific Events. *Biomedicines* **2021**, *9* (9), 1126.

(45) Sharma, K. Cholinesterase Inhibitors as Alzheimer's Therapeutics. *Mol Med Rep* **2019**, *20* (2), 1479–1487.

(46) Čolović, M. B.; Krstić, D. Z.; Lazarević-Pašti, T. D.; Bondžić, A. M.; Vasić, V. M. Acetylcholinesterase Inhibitors: Pharmacology and Toxicology. *Curr Neuropharmacol* **2013**, *11* (3), 315–335.

(47) Bezerra da Silva, C.; Pott, A.; Elifio-Esposito, S.; Dalarmi, L.; Fialho do Nascimento, K.; Moura Burci, L.; de Oliveira, M.; de Fátima Gaspari Dias, J.; Maria Warumby Zanin, S.; Gomes Miguel, O.; Dallarmi Miguel, M. Effect of Donepezil, Tacrine, Galantamine and Rivastigmine on Acetylcholinesterase Inhibition in Dugesia Tigrina. *Molecules* **2016**, *21* (1), 53.

(48) Parsons, C. G.; Stöffler, A.; Danysz, W. Memantine: A NMDA Receptor Antagonist That Improves Memory by Restoration of Homeostasis in the Glutamatergic System--Too Little Activation Is Bad, Too Much Is Even Worse. *Neuropharmacology* **2007**, *53* (6), 699–723.

(49) Kumar, D.; Ganeshpurkar, A.; Kumar, D.; Modi, G.; Gupta, S. K.; Singh, S. K. Secretase Inhibitors for the Treatment of Alzheimer's Disease: Long Road Ahead. *Eur J Med Chem* **2018**, *148*, 436–452.

(50) Menting, K. W.; Claassen, J. A. H. R. β-Secretase Inhibitor; a Promising Novel Therapeutic Drug in Alzheimer's Disease. *Front Aging Neurosci* **2014**, *6*, 165.

(51) Esang, M.; Gupta, M. Aducanumab as a Novel Treatment for Alzheimer's Disease: A Decade of Hope, Controversies, and the Future. *Cureus 13* (8), e17591.

(52) Stockmann, J.; Verberk, I. M. W.; Timmesfeld, N.; Denz, R.; Budde, B.; Lange-Leifhelm, J.; Scheltens, P.; van der Flier, W. M.; Nabers, A.; Teunissen, C. E.; Gerwert, K. Amyloid-β Misfolding as a Plasma Biomarker Indicates Risk for Future Clinical Alzheimer's Disease in Individuals with Subjective Cognitive Decline. *Alzheimer's Research & Therapy* **2020**, *12* (1), 169.

(53) Yao, W.; Yang, H.; Yang, J. Small-Molecule Drugs Development for Alzheimer's Disease. *Frontiers in Aging Neuroscience* **2022**, *14*.

(54) Francioso, A.; Punzi, P.; Boffi, A.; Lori, C.; Martire, S.; Giordano, C.; D'Erme, M.; Mosca, L. β-Sheet Interfering Molecules Acting against β-Amyloid Aggregation and Fibrillogenesis. *Bioorg Med Chem* **2015**, *23* (8), 1671–1683.

(55) Han, M.; Liu, Y.; Tan, Q.; Zhang, B.; Wang, W.; Liu, J.; Zhang, X.-J.; Wang, Y.-Y.; Zhang, J.-M. Therapeutic Efficacy of Stemazole in a Beta-Amyloid Injection Rat Model of Alzheimer's Disease. *Eur J Pharmacol* **2011**, *657* (1–3), 104–110.

(56) Chainoglou, E.; Hadjipavlou-Litina, D. Curcumin in Health and Diseases: Alzheimer's Disease and Curcumin Analogues, Derivatives, and Hybrids. *Int J Mol Sci* **2020**, *21* (6), 1975.

(57) van Dyck, C. H. Anti-Amyloid-β Monoclonal Antibodies for Alzheimer's Disease: Pitfalls and Promise. *Biol Psychiatry* **2018**, *83* (4), 311–319.

(58) Imbimbo, B. P.; Ottonello, S.; Frisardi, V.; Solfrizzi, V.; Greco, A.; Seripa, D.; Pilotto, A.; Panza, F. Solanezumab for the Treatment of Mild-to-Moderate Alzheimer's Disease. *Expert Rev Clin Immunol* **2012**, *8* (2), 135–149.

(59) S, B. H.; J, O.; P, C.; T, B.; P, von R.; Y, T.; Y, Z.; C, von H.; S, G.; L, S.; T, C.; A, S. Clinical Development of Aducanumab, an Anti-Aβ Human Monoclonal Antibody Being Investigated for the Treatment of Early Alzheimer's Disease. *The journal of prevention of Alzheimer's disease* **2017**, *4* (4).

(60) Ostrowitzki, S.; Bittner, T.; Sink, K. M.; Mackey, H.; Rabe, C.; Honig, L. S.; Cassetta, E.; Woodward, M.; Boada, M.; van Dyck, C. H.; Grimmer, T.; Selkoe, D. J.; Schneider, A.; Blondeau, K.; Hu, N.; Quartino, A.; Clayton, D.; Dolton, M.; Dang, Y.; Ostaszewski, B.; Sanabria-Bohórquez, S. M.; Rabbia, M.; Toth, B.; Eichenlaub, U.; Smith, J.; Honigberg, L. A.; Doody, R. S. Evaluating the Safety and Efficacy of Crenezumab vs Placebo in Adults With Early Alzheimer Disease: Two Phase 3 Randomized Placebo-Controlled Trials. *JAMA Neurology* **2022**, *79* (11), 1113–1121.

(61) Bohrmann, B.; Baumann, K.; Benz, J.; Gerber, F.; Huber, W.; Knoflach, F.; Messer, J.; Oroszlan, K.; Rauchenberger, R.; Richter, W. F.; Rothe, C.; Urban, M.; Bardroff, M.; Winter, M.; Nordstedt, C.; Loetscher, H. Gantenerumab: A Novel Human Anti-Aβ Antibody Demonstrates Sustained Cerebral Amyloid-β Binding and Elicits Cell-Mediated Removal of Human Amyloid-β. *J Alzheimers Dis* **2012**, *28* (1), 49–69.

(62) Boutajangout, A.; Sigurdsson, E. M.; Krishnamurthy, P. K. Tau as a Therapeutic Target for Alzheimer's Disease. *Curr Alzheimer Res* **2011**, *8* (6), 666–677.

(63) Ji, C.; Sigurdsson, E. M. Current Status of Clinical Trials on Tau Immunotherapies. *Drugs* **2021**, *81* (10), 1135–1152.

(64) Plotkin, S. S.; Cashman, N. R. Passive Immunotherapies Targeting Aβ and Tau in Alzheimer's Disease. *Neurobiology of Disease* **2020**, *144*, 105010.

(65) Soeda, Y.; Takashima, A. New Insights Into Drug Discovery Targeting Tau Protein. *Frontiers in Molecular Neuroscience* **2020**, *13*.

(66) Stack, C.; Jainuddin, S.; Elipenahli, C.; Gerges, M.; Starkova, N.; Starkov, A. A.; Jové, M.; Portero-Otin, M.; Launay, N.; Pujol, A.; Kaidery, N. A.; Thomas, B.; Tampellini, D.; Beal, M. F.; Dumont, M. Methylene Blue Upregulates Nrf2/ARE Genes and Prevents Tau-Related Neurotoxicity. *Human Molecular Genetics* **2014**, *23* (14), 3716–3732.

(67) Wischik, C. M.; Harrington, C. R.; Storey, J. M. D. Tau-Aggregation Inhibitor Therapy for Alzheimer's Disease. *Biochemical Pharmacology* **2014**, *88* (4), 529–539.

(68) Panza, F.; Solfrizzi, V.; Seripa, D.; Imbimbo, B. P.; Lozupone, M.; Santamato, A.; Zecca, C.; Barulli, M. R.; Bellomo, A.; Pilotto, A.; Daniele, A.; Greco, A.; Logroscino, G. Tau-Centric Targets and Drugs in Clinical Development for the Treatment of Alzheimer's Disease. *Biomed Res Int* **2016**, *2016*, 3245935.

(69) Cummings, J.; Lee, G.; Nahed, P.; Kambar, M. E. Z. N.; Zhong, K.; Fonseca, J.; Taghva, K. Alzheimer's Disease Drug Development Pipeline: 2022. *Alzheimer's & Dementia: Translational Research & Clinical Interventions* **2022**, *8* (1), e12295.

(70) Schneider, L. S. The Potential and Limits for Clinical Trials for Early Alzheimer's Disease and Some Recommendations. *The journal of nutrition, health & aging* **2010**, *14* (4), 295.

(71) Cummings, J. Lessons Learned from Alzheimer Disease: Clinical Trials with Negative Outcomes. *Clinical and Translational Science* **2018**, *11* (2), 147–152.

(72) Sumer, B.; Gao, J. Theranostic Nanomedicine for Cancer. *Nanomedicine (Lond)* **2008**, *3* (2), 137–140.

(73) Janib, S. M.; Moses, A. S.; MacKay, J. A. Imaging and Drug Delivery Using Theranostic Nanoparticles. *Adv Drug Deliv Rev* **2010**, *62* (11), 1052–1063.

(74) Sharma, M.; Dube, T.; Chibh, S.; Kour, A.; Mishra, J.; Panda, J. J. Nanotheranostics, a Future Remedy of Neurological Disorders. *Expert Opin Drug Deliv* **2019**, *16* (2), 113–128.

(75) Kim, T. H.; Lee, S.; Chen, X. Nanotheranostics for Personalized Medicine. *Expert Rev Mol Diagn* **2013**, *13* (3), 257–269.

(76) Kim, J.-Y.; Lee, J. Y.; Park, H. Y.; Kim, H.; Kang, J. H.; Kim, H. J.; Jeong, W.-J. Combination of Peptides with Biological, Organic, and Inorganic Materials for Synergistically Enhanced Diagnostics and Therapeutics. *Peptide Science* **2022**, *114* (3), e24233.

(77) Jo, S. D.; Ku, S. H.; Won, Y.-Y.; Kim, S. H.; Kwon, I. C. Targeted Nanotheranostics for Future Personalized Medicine: Recent Progress in Cancer Therapy. *Theranostics* **2016**, *6* (9), 1362–1377.

(78) Kawasaki, E. S.; Player, A. Nanotechnology, Nanomedicine, and the Development of New, Effective Therapies for Cancer. *Nanomedicine* **2005**, *1* (2), 101–109.

(79) Bhojani, M. S.; Van Dort, M.; Rehemtulla, A.; Ross, B. D. Targeted Imaging and Therapy of Brain Cancer Using Theranostic Nanoparticles. *Mol Pharm* **2010**, *7* (6), 1921–1929.

(80) Muthu, M. S.; Mei, L.; Feng, S.-S. Nanotheranostics: Advanced Nanomedicine for the Integration of Diagnosis and Therapy. *Nanomedicine (Lond)* **2014**, *9* (9), 1277–1280.

(81) Kumar, A.; Chaudhary, R. K.; Singh, R.; Singh, S. P.; Wang, S.-Y.; Hoe, Z.-Y.; Pan, C.-T.; Shiue, Y.-L.; Wei, D.-Q.; Kaushik, A. C.; Dai, X. Nanotheranostic Applications for Detection and Targeting Neurodegenerative Diseases. *Front Neurosci* **2020**, *14*, 305.

(82) Hu, B.; Dai, F.; Fan, Z.; Ma, G.; Tang, Q.; Zhang, X. Nanotheranostics: Congo Red/Rutin-MNPs with Enhanced Magnetic Resonance Imaging and H2O2-Responsive Therapy of Alzheimer's Disease in APPswe/PS1dE9 Transgenic Mice. *Adv Mater* **2015**, *27* (37), 5499–5505.

(83) Chen, Q.; Du, Y.; Zhang, K.; Liang, Z.; Li, J.; Yu, H.; Ren, R.; Feng, J.; Jin, Z.; Li, F.; Sun, J.; Zhou, M.; He, Q.; Sun, X.; Zhang, H.; Tian, M.; Ling, D. Tau-Targeted Multifunctional Nanocomposite for Combinational Therapy of Alzheimer's Disease. *ACS Nano* **2018**, *12* (2), 1321–1338.

(84) Li, M.; Guan, Y.; Zhao, A.; Ren, J.; Qu, X. Using Multifunctional Peptide Conjugated Au Nanorods for Monitoring β-Amyloid Aggregation and Chemo-Photothermal Treatment of Alzheimer's Disease. *Theranostics* **2017**, *7* (12), 2996–3006.

(85) Cui, Z.; Bu, W.; Fan, W.; Zhang, J.; Ni, D.; Liu, Y.; Wang, J.; Liu, J.; Yao, Z.; Shi, J. Sensitive Imaging and Effective Capture of Cu(2+): Towards Highly Efficient Theranostics of Alzheimer's Disease. *Biomaterials* **2016**, *104*, 158–167.

(86) Costa, P. M.; Bourgognon, M.; Wang, J. T.-W.; Al-Jamal, K. T. Functionalised Carbon Nanotubes: From Intracellular Uptake and Cell-Related Toxicity to Systemic Brain Delivery. *J Control Release* **2016**, *241*, 200–219.

(87) Kafa, H.; Wang, J. T.-W.; Rubio, N.; Venner, K.; Anderson, G.; Pach, E.; Ballesteros, B.; Preston, J. E.; Abbott, N. J.; Al-Jamal, K. T. The Interaction of Carbon Nanotubes with an in Vitro Blood-Brain Barrier Model and Mouse Brain in Vivo. *Biomaterials* **2015**, *53*, 437–452.

(88) Kafa, H.; Wang, J. T.-W.; Rubio, N.; Klippstein, R.; Costa, P. M.; Hassan, H. A. F. M.; Sosabowski, J. K.; Bansal, S. S.; Preston, J. E.; Abbott, N. J.; Al-Jamal, K. T. Translocation of LRP1 Targeted Carbon Nanotubes of Different Diameters across the Blood-Brain Barrier in Vitro and in Vivo. *J Control Release* **2016**, *225*, 217–229.

(89) Wang, J. T.-W.; Rubio, N.; Kafa, H.; Venturelli, E.; Fabbro, C.; Ménard-Moyon, C.; Da Ros, T.; Sosabowski, J. K.; Lawson, A. D.; Robinson, M. K.; Prato, M.; Bianco, A.; Festy, F.; Preston, J. E.; Kostarelos, K.; Al-Jamal, K. T. Kinetics of Functionalised Carbon Nanotube Distribution in Mouse Brain after Systemic Injection: Spatial to Ultra-Structural Analyses. *J Control Release* **2016**, *224*, 22–32.

(90) Costa, P. M.; Wang, J. T.-W.; Morfin, J.-F.; Khanum, T.; To, W.; Sosabowski, J.; Tóth, E.; Al-Jamal, K. T. Functionalised Carbon Nanotubes Enhance Brain Delivery of Amyloid-Targeting Pittsburgh Compound B (PiB)-Derived Ligands. *Nanotheranostics* **2018**, *2* (2), 168–183.

(91) Schill, J.; Schenning, A. P. H. J.; Brunsveld, L. Self-Assembled Fluorescent Nanoparticles from π-Conjugated Small Molecules: En Route to Biological Applications. Macromol. Rapid Commun. 2015, 36, 1306−1321.

(92) Kim, J.; Jeong, M.; Stiles, W. R.; Choi, H. S. Neuroimaging Modalities in Alzheimer's Disease: Diagnosis and Clinical Features. *Int J Mol Sci* **2022**, *23* (11), 6079.

(93) Du, Z.; Gao, N.; Guan, Y.; Ding, C.; Sun, Y.; Ren, J.; Qu, X. Rational Design of a "Sense and Treat" System to Target Amyloid Aggregates Related to Alzheimer's Disease. *Nano Res.* **2018**, *11* (4), 1987–1997.

(94) Li, Y.; Xu, D.; Ho, S.-L.; Li, H.-W.; Yang, R.; Wong, M. S. A Theranostic Agent for in Vivo Near-Infrared Imaging of β-Amyloid Species and Inhibition of β-Amyloid Aggregation. *Biomaterials* **2016**, *94*, 84–92.

(95) Zhang, C.; Wan, X.; Zheng, X.; Shao, X.; Liu, Q.; Zhang, Q.; Qian, Y. Dual-Functional Nanoparticles Targeting Amyloid Plaques in the Brains of Alzheimer's Disease Mice. *Biomaterials* **2014**, *35* (1), 456–465.

CHAPTER 2

SELF-FLUORESCENT LONE TRYPTOPHAN NANOPARTICLES AS THERANOSTIC AGENTS FOR ALZHEIMER'S DISEASE

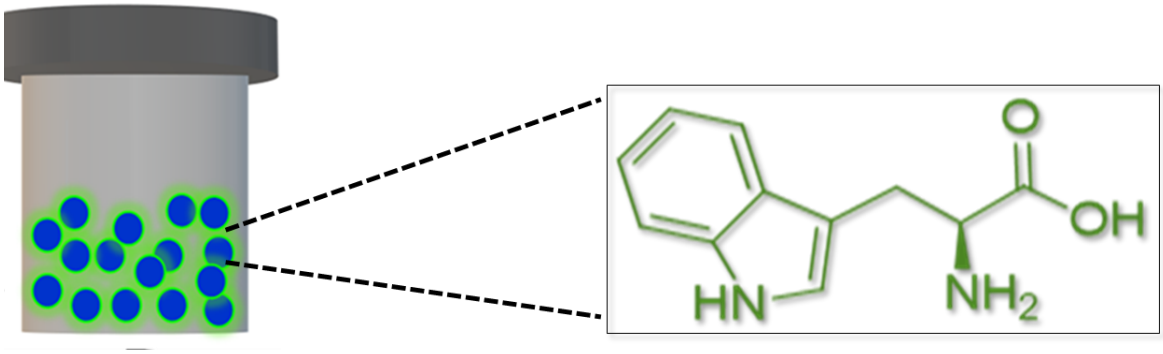

L-Tryptophan

SELF-FLUORESCENT LONE TRYPTOPHAN NANOPARTICLES AS THERANOSTIC AGENTS FOR ALZHEIMER'S DISEASE

Abstract

Aggregation of β-amyloid (Aβ42) peptide in neural extracellular space leads to cellular dysfunction resulting in Alzheimer's disease (AD) pathology. The hydrophobic core of the amyloidogenic Aβ42 contains aromatic residues that play an important role in the aggregation and self-assembly of the peptide. Hence, targeting these hydrophobic core residues by potent low molecular agents can be a promising therapeutic approach towards AD. In the current work, we have developed self-fluorescent solo tryptophan nanoparticles (TNPs) as nanotheranostic systems against AD. We demonstrated that TNPs could significantly inhibit as well as disrupt the fibrils formed by Aβ42 peptide, and a reductionist approach based amyloid model dipeptide, phenylalanine-phenylalanine (FF). More importantly, these nanostructures were non-toxic to neural cells and could protect the neurons from Aβ42 peptide and FF aggregates induced cytotoxicity. In addition, efficacy studies performed in animal models further revealed that the TNPs could rescue spatial and learning memory in intracerebroventricular (ICV) STZ administration induced AD phenotype in rats. Moreover, pharmacokinetics study further established the BBB permeability and brain delivery potency of TNPs. The inherent excellent fluorescent properties of these nanoparticles could further be exploited to further use them as imaging modalities for tagging and detecting FF and Aβ42 peptide fibrils. Overall, our results described in this chapter, clearly illustrated that the solo TNPs could serve as promising nanotheranostic agents for AD therapy.

2.1. Introduction:

Alzheimer's disease (AD) is a lethal neurodegenerative disorder that deteriorates learning, memory and cognition in patients carrying the disorder.[1] Patients with AD show several behavioural issues including anxiety, depression, agitation, and delusion.[2] Pathological characteristics of AD consist of Aβ42 neuritic plaques, neurofibrillary tangles (NFTs), and neuronal, and synaptic loss.[3] Aβ42 peptide is produced via sequential proteolysis of amyloid precursor protein (APP).[4] Aβ42 peptide gets first deposited inside neurons and subsequently, gets released into the neuropil-forming neuritic plaques.[5] The intraneuronal deposition of Aβ42 peptide could indicate a pathologically crucial event of the initiation of neurodegenerative process in AD.[6] Thus, deposition of these intraneuronal amyloid plaques serve as a promising target for achieving successful therapy and diagnosis of AD.[7,8] Currently, various anti-AD drugs are being developed for the therapy of AD but these drugs could not gain much success because of their inability to traverse the Blood-brain barrier (BBB).[9]

These days nanotechnology- based drug delivery approaches have recently gained significant advantages over traditionally used strategies. Various nanoparticle (NP) formulations including protein-based NPs, inorganic NPs, polymeric NPs and carbonaceous nanostructures are widely used in the AD diagnosis and effective therapy.[10,11] In this context, the application of tetrahedral DNA nanostructures (TDNs), a three- dimensional framework of nucleic acids (tFNA) have emerged as an effective treatment strategy for tackling neurodegenerative diseases. Notably, the TDNs can pass through the BBB partially and inhibit apoptosis in both cellular and animal model of AD.[12,13]

Additionally, carbon-based nanomaterials, especially carbon dots, have emerged as promising drug nanocarrier systems to treat various CNS diseases because of their capability to traverse

the BBB. For example, Y-CDs, GQDs, glycine-proline-glutamate loaded CDs and branched PEI-loaded CDs have been recently explored and investigated as amyloid inhibitors.[14] The inhibitory mechanisms of amyloid proteins by various carbon-based nanostructures and carbon dots have also been investigated through different experimental and computational studies. Interestingly, it has been found that chirality, aromaticity and hydrophobicity of carbon dots played an important role in causing the inhibition of amyloid proteins.[15.16] Malishev et al. demonstrated chiral modulation of Aβ fibrillation by enantiomeric carbon dots of L-Lys and D-Lys. It was observed that L-Lys carbon dots exhibited stronger inhibition of A□42 fibrils and mitigated their cytotoxicity.[16] Likewise, Xie et al. also reported that the C_{180} strongly inhibited formation of β-sheet by the peptide, due to robust aromatic and hydrophobic interactions taking place among the C_{180} and Phe rings of the Aβ42 peptide.[17]

Moreover, many recent advancements in the area of nanomedicine have brought about the development of nanotheranostics, a novel approach which integrates both diagnostic as well as therapeutic functions in one system. Currently, different multifunctional nanoparticles are widely used as nanotheranostics agents due to the inherent theranostic properties of these nanoparticles that may serve as real time, rapid and sensitive platforms for achieving effective diagnosis as well as therapy of AD.[18-20]

It is well known that AD is a very progressive neurodegenerative disorder and its progression affects various neurotransmitter systems including cholinergic,[21] glutamatergic,[22] and serotonergic (5-HT) systems.[23] Among them, 5-HT neurotransmitter system is the focus of much scientific interest due to its important pathophysiological role in AD.[24] 5-HT neurons are located in the dorsal (DR) and medial raphe (MR) nuclei.[25] The DR and MR raphe nuclei are comprised of greater number of 5-HT neurons and therefore play an imperative role in memory and cognition.[26] AD is the outcome of certain perturbations in 5-HT pathways and mainly the 5-HT raphe nuclei demonstrate initial pathological changes leading to AD.[27]

Patients with AD display lowered 5-HT neurotransmission, which can be directly associated with the disease severity.[28] In this context, treatment with precise 5-HT reuptake inhibitors like SSRI enhances neurotransmission of 5-HT which ultimately ameliorates memory and cognition in AD affected people and mitigates behavioural ailments related to AD. [29] Furthermore, many cell based studies also reported that 5-HT activation enhances APP metabolite processing (APPS) towards non-amyloidogenic mode.[30] Similarly, SSRI treatment enhanced 5-HT neurotransmission, decreased APP translation and reduced pathogenic Aβ42 peptide secretion causing decreased Aβ42 deposition in AD.[31] Likewise, SSRI treatment also retarded the development of both the Aβ and NFT neuropathology in 3xTg-AD animals (a triple transgenic AD mouse model).[32] Thus, targeting the serotonergic system by means of suitable molecules can be a suitable strategy to enhance cognitive performance in AD.

By now, it is well known that 5-HT synthesis as well as its availability are directly controlled by the intake of L-tryptophan (TrP), that acts as a precursor in the 5-HT synthesis. [33] Higher TrP intake has also been linked with enhanced memory and reduced accumulation of intraneuronal Aβ42 peptide in 3xTg-AD animals' brains.[34] Moreover, an important 5-HT metabolite, 5-HIAA is also synthesized in the brain from TrP which ultimately induces neprilysin (NEP), a proteolytic enzyme that is able to disaggregate pathologic Aβ42 peptide.[35]

Furthermore, change in alimentary TrP is often utilised as a non-invasive strategy to play with systemic concentrations of TrP and ultimately with central 5-HT neurotransmission.[36] Likewise, it has been also reported that alteration in nutritive TrP amounts, changes the level of basal extra-cellular 5-HT in different regions of brains; lowers TrP intake ultimately alleviates learning and memory.[37] Moreover, studies report that lowered TrP intake also worsens cognitive function in AD patients.[38] Interestingly, the oral administration of TrP has

been shown to enhance 5-HT neurotransmission and also improves behavioural illnesses in rodents.[39] Remarkably, daily 5-hydroxytryptophane (5-HTP) injections also improved spatial memory in aged rats.[40] Furthermore, the beneficial effects of TrP have also been noticed against depression in an experimental model of AD.[41]

In addition to the potential role played by TrP as a 5-HT precursor and besides its involvement in other AD regulating metabolic pathways, the molecule has also been shown to inhibit /disrupt fibrillar aggregates of amyloidogenic proteins/peptides.[42] It has been attributed that TrP caused disaggregation and inhibition of amyloid fibrils by intercalating between the fibrillar aggregates of the amyloid proteins and peptides that ultimately inhibited the process of aggregation. Several TrP conjugates have been explored and are investigated as anti-amyloid agents. For example, quinone-tryptophan hybrid, naphthoquinone–tryptophan hybrid, tryptophan-galactosylamine conjugates and fluorescent dopamine−tryptophan nanocomposites have been found to exhibit inhibitory effects towards amyloid aggregates of various peptides/proteins, including IAPP, α-Syn, Aβ42 peptide, Tau. [42-45] However, there is hardly any report that systematically studied the anti-amyloidogenic potential of solo TrP or its nanoformulation. Thus, in order to bridge this gap, here we have developed solo tryptophan nanoparticles (TNPs) and studied their capability to inhibit as well as disrupt the aggregation of two amyloidogenic peptides, Aβ42 peptide and the dipeptide FF. Moreover, TrP nanostructures can potentially cross the BBB via LAT1 transporters [46,47] and this would eliminate the necessity for any other surface conjugation of the nanostructures with potential molecules capable of targeting the BBB **(Scheme 2.1).** We further tried to decipher the ability of the TNPs as neuroprotective agents both under cellular conditions (neural cells) and in ICV STZ injection induced amyloid animal models.

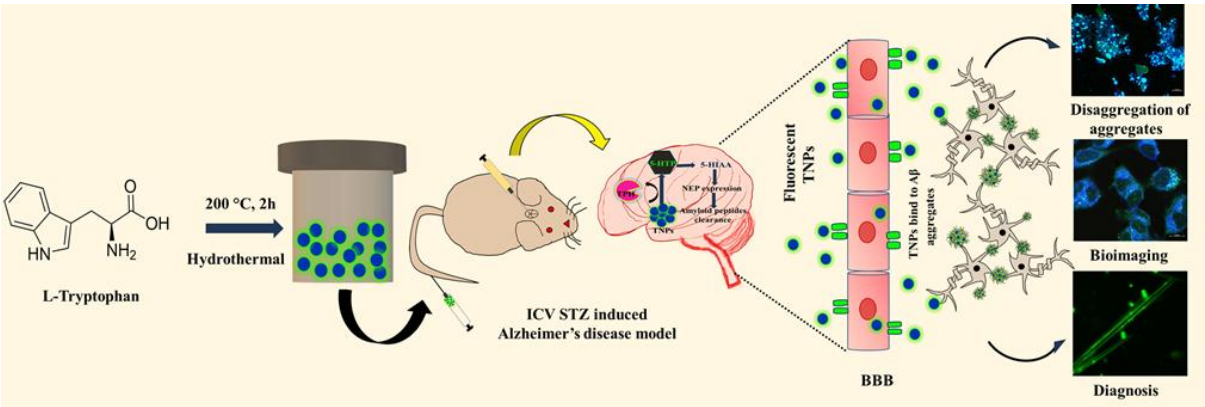

Scheme 2.1: Schematic presentation depicting self-fluorescent tryptophan nanoparticles synthesis along with their anti-amyloidogenic activity and amyloid aggregates detecting potential.

2.2. Materials and Methods:

2.2.1. Materials:

L-tryptophan (99%), D-tryptophan (99%), L-phenylalanine (99%), Boc-Phe-OH, isobutyl chloroformate (>99.8%), sodium chloride (99.9%), sodium sulfate (>99.0%), N-methyl morpholine (99%), tetrahydrofuran (>99.9%), sodium hydroxide, sodium acetate (>99%), acetic anhydride (98%), citric acid (>99.5%), sodium bicarbonate, and 3-(4,5-Dimethyl-2-thiazolyl)-2,5-diphenyltetrazolium bromide (MTT) (Sisco Research Laboratories, TCI Chemicals, and HiMedia Laboratories Pvt. Ltd., India**).** Thioflavin-T (ThT), 1,1,1,3,3,3-Hexafluro-2-propanol (HFIP) (> 99%), Aβ42 peptide (>95%), Methanol (MeOH) (99.8%), 4′,6-diamidino-2-phenylindole (DAPI)(>98%), and dichloromethane (DCM) (>99.8%), 4,4′-Dianilino-1,1′-binaphthyl-5,5′-disulfonic acid dipotassium salt (Bis-ANS) (Sigma Aldrich Munich Germany), fetal bovine serum (FBS), *Calcein AM, Propidium iodide* (*PI*), dulbecco's modified eagle medium (DMEM/F12), Phosphate buffer saline (PBS), trypsin EDTA solution (1X), and antibiotic antimycotic solution (100×) were obtained from Gibco, Thermo Fisher Scientific Inc., NY, USA.

2.2.2. Synthesis of fluorescent TNPs:

TNPs were synthesized by dissolving TrP in ultrapure water (at a concentration of 20 mM). Next, the solution was added into a hydrothermal container (made up of Teflon lined stainless steel hydrothermal reactor with 25 ml volume) and kept at 200 degrees Celsius (°C) in hot air oven for 2 h. After 2 h, the obtained light yellow coloured sample was centrifuged thrice (for 25 min at 14000 rpm) and finally pure fluorescent nanoparticles (NPs) were obtained.

2.2.3. Characterization of TNPs:

Different biophysical characterization of the TNPs were done by using various techniques as detailed below. In brief, the NPs were characterised for their particle size by using a Malvern Zetasizer Nano ZSP Instrument.

Next, the UV-vis spectral properties of TNPs were determined (using Shimadzu UV-2600 spectrophotometer). The TNPs solution (1 mg mL^{-1}) were taken in a quartz cell and diluted with ultrapure water for the spectral measurements.

Attenuated total reflection-Fourier transform infrared (ATR-FTIR) spectra of solid NPs samples were obtained using a Bruker VERTEX70 instrument (32 scans). Scans were carried out from 4000− 400 cm^{-1}.

Scanning electron microscopic **(**SEM**)** studies were also performed to investigate the morphology and structure of TNPs. Samples were prepared by drop casting the NPs solution (100 μg mL^{-1}) onto cleaned silicon wafers. They were then air-dried at 25 °C followed by gold coating for 90 s. The gold coated samples were analysed using SEM (JEOL JEM SEM, Tokyo, Japan).

Transmission electron microscopic (TEM) studies of the TNPs were also carried out to decipher their overall morphology. The sample was prepared following a previously reported protocol.[45]

Atomic force microscopic (AFM) studies of TNPs were carried out by depositing the TNPs solution (100 μg mL^{-1}) onto a cleaned silicon substrate. Tapping mode was used to capture AFM images of TNPs by an AFM instrument (Bruker Nanoscope-V).

Thermal stability of L-Trp and TNPs were also analysed using a Mettler Toledo TGA/DSC 1 instrument. Stability was determined between 25 °C and 500 °C with a heating rate of 10 °C/min under N2 atmosphere.

A confocal microscope was used to study the fluorescence properties of the TNPs and to determine the intracellular uptake of fluorescent TNPs.

Further, structural integrity of the Trp in TNPs with reference to L- Trp was also determined by ^{1}H and ^{13}C NMR [NMR instrument (Bruker 400 MHz)]. Chemical shifts are represented in ppm relative to Residual Deuterium Oxide downfield from an internal standard.

2.2.4. Formation of FF and Aβ42 peptide fibrillar aggregates in vitro:

Synthesis of dipeptide (FF), was performed using solution phase peptide synthesis protocols as described earlier.[45,48] Briefly, Boc-Phe-OH (5 mM) was dissolved in anhydrous tetrahydrofuran (THF), the solution was then stirred in an ice-salt mixture for 10 min and chilled to −20 °C. Next, IBCF (5 mM) was mixed to the solution followed by N-methyl morpholine (NMM) (5 mM) and stirred for 20 min. Afterwards, a pre chilled mixture of L-phenylalanine (6 mM) and sodium hydroxide (6 mM) in distilled-water was added. Reaction mixture was stirred at room temperature overnight and was concentrated in a rotary

evaporator. Finally, the residual reactant solution was acidified with concentrated chilled citric acid solution. The resultant oil was also extracted using ethyl acetate (3 × 15 ml) followed by washing with water (3 × 15 ml) and subsequent saturation with sodium chloride (1 × 10 ml). The extract was then dried on anhydrous sodium sulfate, and evaporated to obtain the compound Boc-Phe-Phe-COOH. Deprotection of the Boc group was achieved by treating Boc-Phe-Phe-COOH with anhydrous TFA and DCM at 1:1 ration v/v, on ice for 30 min. Following deprotection, excess solvent was removed by air-drying and precipitated using cold diethyl ether, subsequently dried and lyophilised using freeze drier to obtain dry powder. After lyophilization, the dried dipeptide was purified using a preparatory reverse phase C18 column running on a linear gradient of 5-95% of acetonitrile to water and also analyzed by mass spectrometry (Waters Q-TOF Microma (Q-TOF). Mass spectrum showed the expected mass (313 Da) for FF. FF fibers were formed at a concentration of 4 mg/ml, following a protocol mentioned earlier with little modification. [45] Typically, 4 mg FF was dissolved in 50 µl of HFIP to remove any preformed aggregated fibrils before the initiation of self-assembly and the sample was diluted to 4 mg/ml in ddH_2O to obtain the fibrils.

Aβ42 peptide was procured from Sigma Aldrich Munich Germany. Aβ (1-42) peptide fibrils were prepared as detailed in the literature.[49,50] In brief, powdered Aβ peptide was first monomerized by dissolving it in HFIP at a concentration of 1 mg/ml. Further, the prepared solution was mixed on a shaker for 2 h at 4 °C for proper dissolution of the polypeptide. Before the initiation of fibrillogenesis, HFIP was evaporated on a SpeedVac and a dried and thin clear film of Aβ peptide was obtained. The thin film of peptide was then dissolved in phosphate-buffered saline (PBS; 10 mM, pH 7.4) and briefly sonicated for 1 min. To induce aggregation and formation of fibrils, the Aβ polypeptide solution was kept in incubation at 37 °C for 3 days to obtain higher fibril concentration.

2.2.5. Thioflavin T (ThT) fluorescence assay to monitor the fibrillization of FF and Aβ42 peptides:

ThT assay was performed to monitor the amyloidogenesis of dipeptide and Aβ42 peptide. In brief, preformed FF/Aβ42 peptide fibrils of various concentrations were added to ThT buffer solution (20 μM) and ThT fluorescence intensity spectra (Ex 420 and Em-450 nm) were taken using MPlex 200 pro, Tecan after suitable incubation.

2.2.6. Inhibition and disaggregation studies of FF and Aβ42 peptide fibrils by TNPs:

To examine the inhibitory potential of TNPs towards the formation of FF aggregates, the NPs (100 μg mL^{-1}) were coincubated with the monomer solution of FF (12 mM) for 24 h and 48 h. After incubations, samples (90 μL) were stained with 10 μL of ThT solution (1 mM). After ThT staining, samples were drop-casted on a glass slide, air-dried, and then imaged using a confocal microscope. Similarly, for determining the inhibitory potential of TNPs towards the formation of Aβ42 aggregates, the NPs (100 μg mL^{-1}) were coincubated with the monomer solution of Aβ42 (20 μM) for 24, 48 and 72 h. After incubations, the ability of TNPs to cease or inhibit the formation of Aβ42 peptide aggregates was examined using TEM. Further, FF and Aβ42 peptide fibrils disaggregation by the TNPs was next determined by performing DLS, confocal, SEM, TEM and Bis-ANS assay. For disaggregation studies, FF fibrils (12 mM) and Aβ42 peptide fibrils (20 μM) were incubated with TNPs (100 μg mL^{-1}) for 24 and 48 h. After incubation, the disaggregation of FF aggregates was analysed by DLS, confocal, and SEM analysis whereas, Aβ42 peptide aggregates were examined using TEM. The quantitative disaggregation analysis of both FF and Aβ42 peptide aggregates was also examined by Bis-ANS dye (50 μM). In brief, FF (12mM) and Aβ42 peptide aggregates (20 μM) were incubated with TNPs (100 μg mL^{-1}) for 24 and 48 h. After incubations, Bis-ANS solution (50 μM) were added to all treated and control samples and fluorescence intensity

spectra (Ex 405 and Em-440 nm) were taken using a multimode plate reader following half an hour incubation with Bis-ANS dye.

2.2.7. Determination of in vitro disaggregation efficiency of TNPs:

Next, the disaggregation efficiency of TNPs towards FF aggregates in comparison to L-Trp and D-Trp was also carried out using SEM and confocal microscopy. Briefly, FF fibrils (12 mM) were incubated with similar concentrations of TNPs, L-Trp and D-Trp (100 μg mL^{-1}) for a period of 48 h. After incubations, fibrils disaggregation was analysed by both SEM and confocal microscopy.

2.2.8. Circular Dichroism (CD) analysis of TNPs-treated FF fibrils:

CD analysis was performed to determine the secondary structure of dipeptide assemblies. FF fibrils (4 mg/mL) were prepared as described above and CD analysis was performed after suitable dilution at 0.04 mg/mL. For disaggregation studies, FF fibrils (4 mg/mL) were treated with TNPs (100 μg mL^{-1}) on a rotary shaker for 24 and 48 h and CD measurements of the treated and neat FF samples were carried out (using JASCO J-1500 CD instrument). Scans were taken in a wavelength range from 190− 290 nm.

2.2.9. Cellular uptake study of the TNPs carried out in Human neuroblastoma cell line (SH-SY5Y):

Cellular uptake study of fluorescent TNPs (100 μg mL^{-1}) in SH-SY5Y cells was determined using confocal microscopy as described earlier.[45] Further quantification of fluorescent TNPs uptake in SH-SY5Y cells were carried out using fluorescence activated cell sorting analysis (FACS). In brief, 50000 cells/well were seeded in 6 well plates. Next, cell media were changed with TNPs (100 μg mL^{-1}) containing media and cells were incubated overnight. After treatment, cells were rinsed with PBS and trypsinized. Afterward, cells were centrifuged (1500 rpm for 5 min), pellet obtained was rinsed with PBS twice and finally

resuspended in PBS to be analysed by flow cytometry (BD, Aria Fusion) at corresponding wavelengths.

2.2.10. Live/Dead assay to test the neuroprotective effect of TNPs against FF and Aβ42 induced cytotoxicity:

The neuroprotective effect of different concentrations of TNPs (50 and 100 μg mL^{-1}) against FF (12 mM) and Aβ42 fibrils (20 μM) for 48 h was tested by Live/dead assay as described previously.[51] Briefly, for the live/dead assay, SH-SY5Y cells were plated in 6-well plates for 24 h. After incubation, cells were exposed to TNPs (50 and 100 μg mL^{-1}) and FF (12 mM) and Aβ42 fibrils (20 μM) for 48 h. After treatment, cells were gently rinsed with PBS twice and subsequently stained with live/dead viability assay reagents carrying 2 μL mL^{-1} of calcein AM (1mg mL^{-1}) and 2 μL mL^{-1} of propidium iodide (1mg mL^{-1}) for 15 min at 37 °C in the dark. Afterward, cells were then rinsed with PBS gently to remove extra stains and analyzed by a ZEISS LSM 880 confocal microscope with Airyscan. The viable cells were stained by calcein AM and emitted green light, whereas dead cells were stained by propidium iodide and emitted red light. Fluorescence intensity of calcein AM was also recorded after 48 h to measure the protective effect of TNPs using a multimode plate reader (MPlex 200 pro, Tecan).

2.2.11. Intracellular Aβ42 peptide and FF aggregates detection and inhibition by TNPs:

To examine whether the TNPs could inhibit aggregation of FF and Aβ42 peptide fibrils inside SH-SY5Y cells, intracellular peptide aggregation inhibition assay was conducted. In brief, cells were grown on coverslips, and then treated with either Aβ42 peptide (20 μM) or FF aggregates (12 mM) for 24 h. Afterwards, treated cells were further incubated for 24 h with TNPs (100 μg mL^{-1}) and later fixed in 4% (v/v) PFA for 15 min. Finally, cells were labeled with ThT (0.05% solution) and DAPI (1 μg mL^{-1}) and rinsed with PBS three times to

remove unnecessary stain. Samples were then observed by a ZEISS LSM 880 confocal microscope with Airyscan.

2.2.12. Interaction of TNPs with intracellular Aβ42 peptide and FF Aggregates:

Intracellular interaction of TNPs with amyloid fibrils was carried out by using confocal microscopy. Briefly, both FF and Aβ42 peptide fibrils were stained with ANS dye in 1:2 peptide to dye ratio for half an hour. After staining, stained fibrils were incubated with TNPs in SH-SY5Y cells for 6 h. After treatment, cells were gently rinsed with PBS and then fixed in 4% PFA for 15 min. Following this, cells were next labeled with DAPI (1 μg mL^{-1}) and analyzed by a ZEISS LSM 880 with Airyscan.

2.2.13 Parallel artificial membrane permeability assay (PAMPA) to examine the BBB permeability of TNPs:

The BBB permeability of different concentrations of TNPs (500 μg and 1mg mL^{-1}) was performed as previously described PAMPA assay with some modifications.[51] In brief, PAMPA assay was performed to examine the BBB permeability of TNPs. The property of TNPs to diffuse from a donor (lower) plate into an acceptor (upper) plate carrying a sandwiched membrane coated with brain polar lipids was evaluated. To do so, the membrane filters on the bottom of acceptor wells were gently coated with BBB-1 lipid solution (5 μL; P/N 110672). After application of artificial BBB membrane, TNPs (500 μg and 1mg mL^{-1}) were dissolved in prisma HT buffer (P/N 110151) (7.4 pH) and 180 μL of the prepared TNPs solutions were added in donor plate wells, and 200 μL of brain sink buffer (BSB) was added in the upper acceptor plate wells. Afterward, both the acceptor and donor plates were assembled carefully in a manner that the bottom of the filter membrane was in direct contact with the sample solution in the donor plate. The sandwich plate was next shaken for 18 h at

room temperature. After incubation, the sandwich was disassembled and the amount of TNPs in both the donor and acceptor wells was monitored by measuring fluorescence intensity (Ex 420 and Em-450 nm), using MPlex 200 pro,Tecan. The percentage BBB permeation ability of TNPs was calculated from TNPs standard curve.

2.2.14. Efficacy studies of TNPs performed in ICV-STZ induced rat model:

2.2.14.1. Animals:

Sprague-Dawley (SD) rats (adult males) were obtained from the in-house animal facility. Animals were housed under pathogen free and standard environment maintained at 23-25 ^{0} C and a relative humidity of 60-65%; with standard 12 h light-dark cycles with free access to standard diet and water. All interventions were carried out in accordance with the institutional animal ethics committee (IAEC) guidelines.

2.2.14.2. Dosage regimen and treatment schedule:

Stereotaxic injection of STZ

Animals were administered with STZ following **s**tereotaxic surgery as described in our previous reports.[45,52,53] Briefly, **S**tereotaxic surgery was performed using intraperitoneal injection of pentobarbitone sodium at a dose of 40 mg kg^{-1} to anaesthetize the rats before surgery. The rats were fixed on the stereotaxic apparatus (Stoelting Co. USA). Afterwards, bregma was located carefully to make a small burr hole by a drill followed by infusing STZ (dissolved in artificial cerebrospinal fluid; aCSF) at a dose of 1 mg kg^{-1} (10 µl) in each lateral ventricle following specific coordinates [-0.8 mm anteroposterior (AP), ±1.5 mediolateral (ML), -3.6 mm dorsoventrally (DV)] from bregma with Hamilton syringes at a rate of 0.5 µl min^{-1}. After injection, the syringe was left at the place of injection for complete diffusion and minimize backflow for 5 min. Control group animals were given an equal amount of aCSF in lateral ventricles.

TNPs treatment

Animals were divided indiscriminately into 4 groups containing 6 rats in each group. (**Scheme 2.2** depicts schematic representation of treatment schedule)

Group I: 10 µl of aCSF was stereotaxically infused into both the lateral ventricles of rats, constituting the control group.

Group II: STZ (10 µl; 1 mg kg^{-1}) was administered in this group of rats within each ventricle via stereotaxic surgery and this group was designated as STZ toxin group.

Group III: This group of rats were administered with STZ (10 µl; 1 mg kg^{-1}) in each ventricle via stereotaxic surgery and TNPs [5 mg kg^{-1}*(i.v.)*] were given to the animals every third day starting from 7-days post STZ injection and was continued till next 26 days.

Group IV: This group of animals were administered with TNPs, 5 mg kg^{-1} (i.v.) for 26 days on every alternate day.

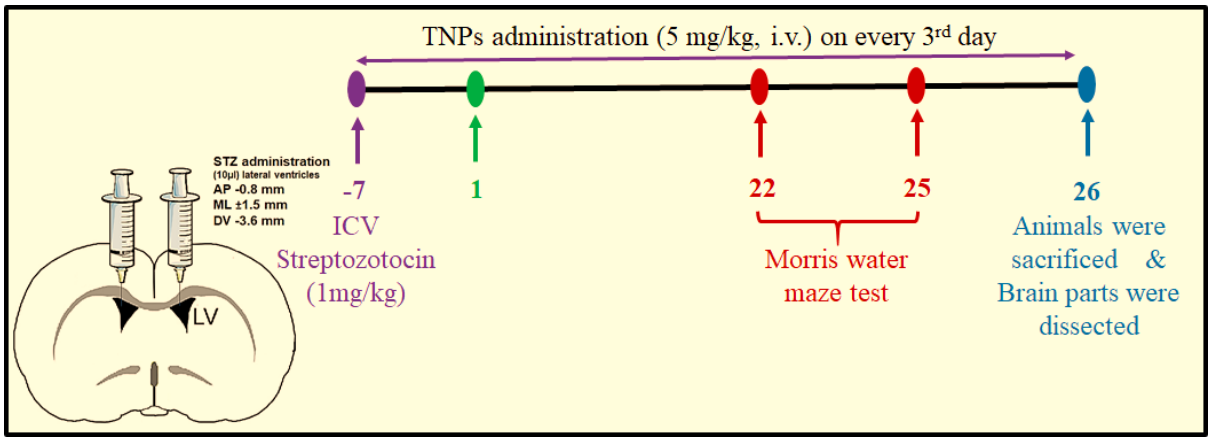

Scheme 2.2: Representing dosage regimen and treatment schedule of STZ and TNPs.

2.2.14.3. Morris Water Maze test:

Morris Water Maze (MWM) assay was performed to monitor spatial memory and learning functional alterations in the model rats, following a similar procedure as reported earlier.[45] Briefly, 3 weeks post STZ lesioning, animals were trained in MWM apparatus, thrice a day for consecutive three days/sessions to determine typical cognitive functions, and

subsequently a probe trial on the last day. MWM apparatus consists of a black water tank (1.32 m diameter/75 cm height) maintained at 25 ± 2°C temperature. Afterward, the tank was hypothetically divided into four similar quadrants with a large black platform submerged 1 cm below the water surface at the centre of the pre-planned quadrant. The spatial memory and learning task were conducted with the rats performing three trials in one session (1, 2, 3 & 4 day) of 2 min each duration. The trial was stopped when either rat finds the platform within 2 min or they are guided to the platform. Animals were allowed to rest for 20 s between each trial and each test trial was carried out to monitor the learning and memory alterations pre and post administration of the NPs. The behavioural activities of animals were recorded by a video camera fixed above the centre of the tank. The recordings were analysed in terms of latency time as well as mean path length using ANY-maze video tracking software (ver. 4.73; Stoelting, USA). After the last trial of training, rats were assessed for probe trials after removing the platform from the pool, for validation of memory retention. The time spent by rats in the target quadrant was measured using the same software.

2.2.14.4. Immunohistochemical analysis:

Immunohistochemical analysis was also performed to observe the expression of Aβ42 oligomers in the cortex and hippocampal brain regions of model rats of different treatment groups, following a similar procedure as reported earlier.[45] Animals were first euthanized using sodium pentobarbital (40 mg kg^{-1}, i.p.) injection and then slowly perfused with cold PBS, and later fixed in 4% PFA. The perfusion fixed sections were processed as reported earlier. Sections were rinsed thrice with tris-buffered saline (TBS) followed by tissue penetration using TBST at room temperature. Brain slices were blocked with 5% BSA in TBST for a period of 2 h at 25 °C, following incubation with mouse anti-amyloid beta (1:500, Millipore, CA, USA) antibody and later rinsed with TBS. Afterwards, slices were

incubated with anti-mouse Alexa Fluor-594 (Invitrogen, Carlsbad, CA, USA) at 25 °C for a period of 2 h in dark. Finally, slices were mounted with DAPI flouroshield mounting medium (Sigma Aldrich, USA) and fluorescence intensity was visualized using Leica inverted fluorescent microscope (DMI 6000) and analysed by ImageJ software (NIH, USA).

2.2.14.5. In vitro serum stability:

The serum stability of TNPs was performed in duplicate. Blank rat serum samples (990 µl) taken in two test tubes were pre-incubated in a shaking water bath maintained at 37 ± 0.2°C for 10 min. Next the samples were spiked with 10 µl of TNPs (from 1 mg/ml stock solution) and kept for further incubation under the conditions mentioned above. Next, 80 µl of the sample mixture was taken at 0, 5, 15, 30, 60, 90, and 120 min. Afterwards, 160 µl of acetonitrile was added to precipitate the serum proteins and the samples were subsequently centrifuged for 10 min at 10,000 rpm. Supernatant was subjected to HPLC analysis.

2.2.14.6. Blood brain barrier permeability study:

A pharmacokinetic study was carried out to examine the BBB permeability of TNPs. The NPs (5 mg/kg) were administered intravenously into rats (n=3). The animals were next euthanized at different time intervals (at 0.08, 0.25, 0.5, 1, 2, 4, 6, 8, 12 and 24 h) post dosing. Blood was withdrawn from the retro-orbital plexus of rats and collected into microfuge tubes and brains were isolated from the sacrificed animals. Blood samples were the centrifuged at 12,000 rpm for 10 min for harvesting serum and brain tissue homogenates were prepared in tris buffer (40 mM; pH 7.4) at a ratio of 5:1 (mL:g) and stored at −70±10 °C.

Sample preparation

To extract the TNPs, 100 µL each of serum/brain homogenates samples were taken and 300 µL of cold methanol was added to them. Then the samples were vortexed for 10 min subsequently centrifugation at 10,000 rpm for next 10 min. After centrifugation, supernatants were subjected for further LC-MS/MS analysis.

Instrumentation

HPLC conditions

Sample analysis was carried out by using Shimazdu prominence UPLC with Photodiode array (PDA) detector at 280 nm after separation through Phenomenex column (100 X 4.6 mm, 5.0µm) with a mobile phase comprising of 0.1% acetonitrile and formic acid in 85:15 (v/v) ratio at 0.5 ml/min flow rate.

2.2.14.7. LC-MS/MS estimation of TNPs in rat serum and brain:

LC-MS/MS (ABSciex 4000, Toronto, Canada) having with an API electro-spray ionization (ESI) source was used to estimate the levels of TNPs in tissues. The parameters of instrument: curtain gas (CUR), nebulizer gas (GS1), and heating gas (GS2) were set at 25, 15, and 10 respectively. The collision gas, ion spray voltage and temperature were set at medium, 5500V and 500°C. Compounds parameters: collision energy (CE), collision exit potential (CXP), declustering potential (DP), and entrance potential (EP) were 13, 32 ,56, and 10 V for TNPs. For collision and curtain gas nitrogen was used while for source gas Zero air was used. The mass spectrometer was run at ESI positive ion mode and multiple reaction monitoring (MRM) mode was utilised for the detection of the ions and monitoring the transition of m/z 204.95 precursor ion $[M + H]^+$ to the m/z 187.98 product ion for TNPs. Separation was done

through Agilent Zorbax SB C18 column (150x4.6 mm, 5.0µm) with a mobile phase comprising of methanol: 0.1% formic acid in 75:25 (v/v) ratio at 0.6 ml/min flow rate. Data were analysed and quantified by using analyst software version 1.4.1 (Applied Biosystems, MDS Sciex Toronto, Canada).[55]

2.2.15. Statistical analysis:

Statistical analysis was performed to analyse the difference between the means of subgroups by GraphPad Prism software. One-way analysis of variance (ANOVA) and two way-ANOVA followed by Bonferroni post hoc test, Tukey's multiple comparison and Sidak's multiple comparison test were used to evaluate significant difference. Behavioural significance was analysed by two way-ANOVA and $p<0.05$ was considered as statistically significant.

2.3. Results and Discussion:

2.3.1. Synthesis and characterization of TNPs:

In this study, fluorescent Trp nanoparticles were generated through a simple hydrothermal method (**Scheme** 1) and were further characterized by harnessing different biophysical techniques (**Figure** 1)**.** As presented in **Figure** 1A, an average hydrodynamic diameter of around 210 nm ± 75 nm (SD) with a PDI of 0.324 was observed for the particles in DLS analysis. **Figure** 1B shows the UV-visible spectrum of the TNPs which demonstrated similarity with TrP spectrum (with absorption peaks at 220 nm and 280 nm). The maximum at 280 nm, clearly depicted the presence of TrP.[56]

Next, ATR-FTIR analysis was performed to examine the molecular structure of NPs. The ATR-FTIR spectrum of TNPs showed prominent IR peaks at 1085 cm^{-1}, 1650 cm^{-1}, 3037

cm^{-1}, and 3400 cm^{-1} relating to C-N stretching, C=O stretching, C-H bending and NH stretching vibrations (**Figure**1C).[57]

The TNPs were also characterized using TEM, SEM and AFM. TEM, SEM and AFM pictures of the NPs clearly pointed towards spherical nature. The mean particle size of TNPs were observed to be around 96 nm in TEM, around 121 nm in SEM and around 82 nm in AFM (**Figure** 1D, E, F). Next, the TNPs were analysed using fluorescence spectroscopy. The emission fluorescence spectra of NPs were recorded from 340 to 500 nm after being excited at various wavelengths (**Figure** 1G). The fluorescence emission spectra of TNPs varied according to a change in the excitation wavelength of NPs (from 310 to 470 nm). In addition, it was also noticed that the NPs were capable of emitting blue and green fluorescence which was further verified by confocal microscopy, where bright blue- and green-colored fluorescent NPs were observed as shown in **Figure** 1 H and I**.**

Next, NMR results of synthesised TNPs in comparison with Trp showed the structural integrity of Trp skeleton in the nanoparticles. Both ^{1}H and ^{13}C NMR spectra of TNPs and the control Trp were found to be similar, and this confirmed the synthesis of TNPs (**Figure** 2.2). Further, thermal analysis of Trp and TNPs were also carried out to estimate the thermal stability of both amino acid and its nanostructures. *Thermogravimetric analysis* (TGA) is widely used technique to confirm the thermal stability of various amino acids.[58] From TGA curve, it was clearly observed that Trp was stable to heat for up to 270 ℃, after that its framework started to decompose gradually. Our results were well consistent with the reported literature.[59] More importantly, our synthesized TNPs were also shown to possess good thermal stability and only 4.71% weight loss was found at 200 ℃ (**Figure** 2.3).

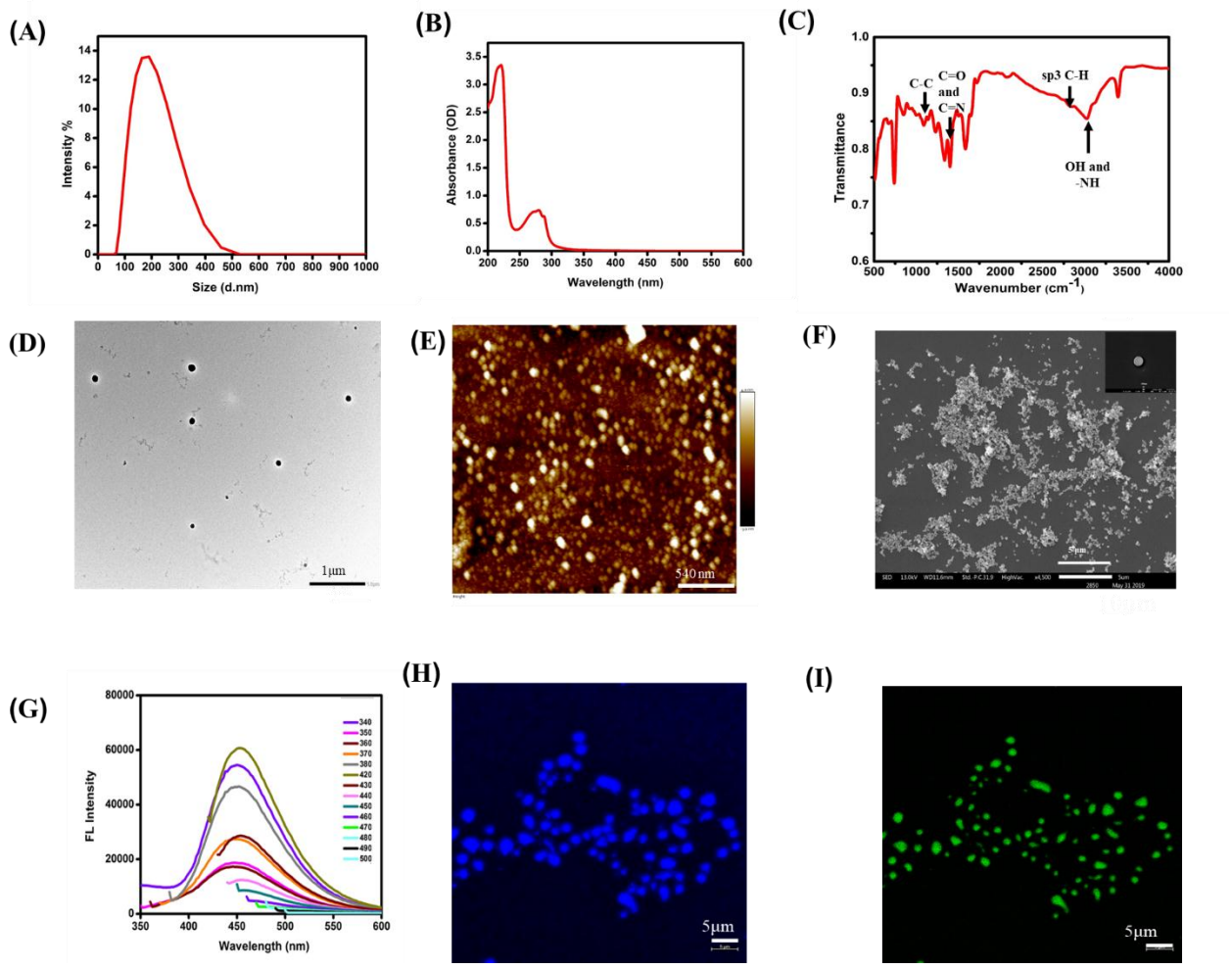

Figure 2.1: (A) DLS profile of TNPs. (B) UV-Vis absorbance spectrum of TNPs**. (**C) ATR-FTIR spectra of TNPs. (D) TEM images of TNPs (scale bar~1 µm). (E) AFM images of TNPs, scale bar is 540 nm. (F) SEM images of TNPs (scale bar~5 µm) (G) Emission spectra of TNPs. (H and I) Confocal images of TNPs (scale bar~5 µm).

(A)

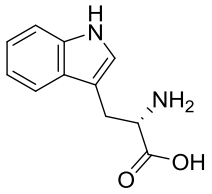

L-tryptophan

(B) **^{1}H of Control** **^{13}C of control**

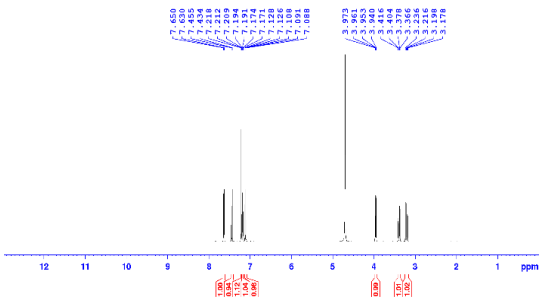

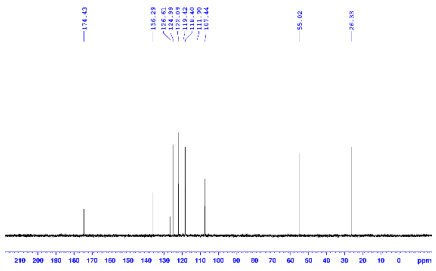

(C) **^{1}H of Nanoparticles** **^{13}C of Nanoparticles**

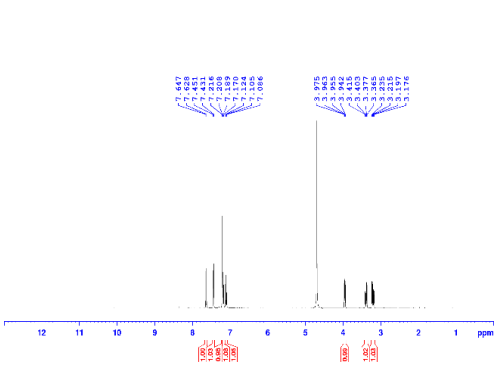

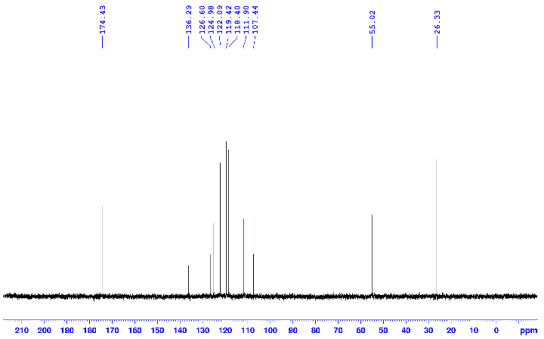

Figure 2.2: (A) Chemical structure of L-Trp. (B) NMR spectrum of Control**:** ^{1}H NMR (400 MHz, D_2O): δ 7.63 (d, J = 7.9 Hz, 1H), 7.44(d, J = 8.1 Hz, 1H), 7.21(s, 1H), 7.21-7.17 (m, 1H), 7.12-7.08 (m, 1H), 3.95(dd, J = 8.1, 4.8 Hz, 1H), 3.38 (dd, J = 15.4, 4.8 Hz, 1H), 3.23-3.17 (m, 1H). ^{13}C NMR (100 MHz, D_2O): δ 174.4, 136.2, 126.6, 124.9, 122.0, 119.4, 118.0, 111.9, 107.4, 55.0, 26.3. (C) NMR spectrum of nanoparticles**:** ^{1}H NMR (400 MHz, D_2O): δ 7.63 (d, J = 7.9 Hz, 1H), 7.44(d, J = 8.1 Hz, 1H), 7.21(s, 1H), 7.20-7.16 (m, 1H), 7.12-7.08 (m, 1H), 3.95(dd, J = 8.0, 4.8 Hz, 1H), 3.38 (dd, J =15.35, 4.8 Hz, 1H), 3.23-3.17 (m, 1H). ^{13}C NMR (100 MHz, D_2O): δ 174.4, 136.2, 126.6, 124.9, 122.0, 119.4, 118.3, 111.8, 107.7, 55.0, 26.3.

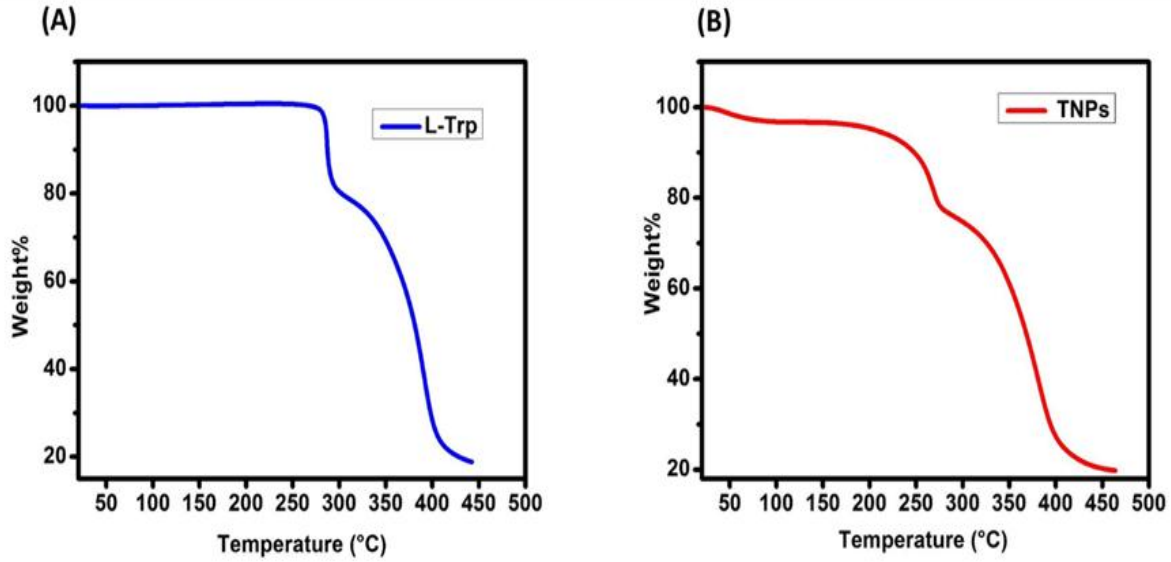

Figure 2.3: TGA plot of (A) L-Tryptophan and (B) TNPs.

2.3.2. In vitro investigation of FF and Aβ42 peptide aggregation:

The Mass spectrum showed the expected mass of synthesized FF was (313 Da) as shown in Figure 2.4. Next, the formation of amyloid-like fibrillar assemblies of both FF and Aβ42 peptide was examined by ThT and electron microscopy. ThT is a well-known fluorescent probe and its extensively utilized for identifying and characterizing amyloid fibrils.[60] Therefore, ThT fluorescence assay was used to investigate the aggregation behaviour of FF. Interestingly, we observed a significant enhancement in the fluorescence intensity of ThT dye with the increasing concentrations of the dipeptide. (**Figure** 2.5A). Thus, ThT results evidently verified the amyloid-like fibrils formation capability of FF. Next, confocal microscopy of FF fibrils was performed to examine the structural and morphological changes of FF at different time points. As depicted in **Figure** 2.5A, the maximum fluorescence intensity of ThT was observed at 12 mM FF. Thus, subsequent characterization experiments for FF were conducted at a concentration of 12 mM. As presented in **Figure** 2.5 C and D, confocal microscopic results showed an enhancement in the amount of FF aggregates with the change in the incubation time of aggregation from 24 h to 48 h. A dense, plaque-like

aggregated mass was observed after incubating the peptide for 48 h (**Figure** 2.5 D), whereas only dense fibrillar structures were observed after an incubation of 24 h (**Figure** 2.5 C).

After demonstrating the in-vitro fibril-forming and aggregation ability of FF, we next investigated the aggregation behaviour of the Aβ42 peptide. First, we formed Aβ42 fibrils as described above and then, their aggregation potential was monitored by carrying out ThT fluorescence assay. We clearly observed an upsurge in the ThT fluorescence intensity with an increase in the concentrations of Aβ42 peptide fibrils (**Figure** 2.5 B). Next, TEM was performed to establish and validate the formation of Aβ42 peptide fibrils. TEM images clearly pointed towards the formation of aggregated fibrils by Aβ42 peptide (**Figure** 2.5 E).

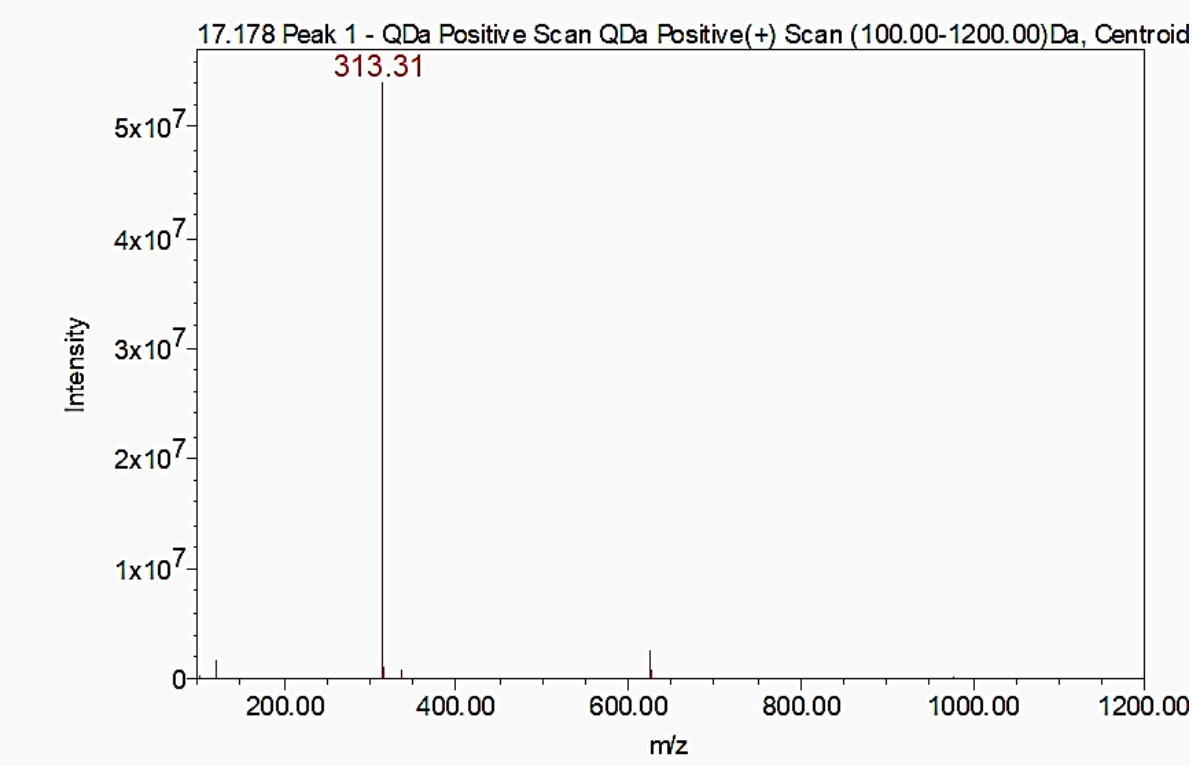

Figure 2.4: Mass spectrum of dipeptide FF.

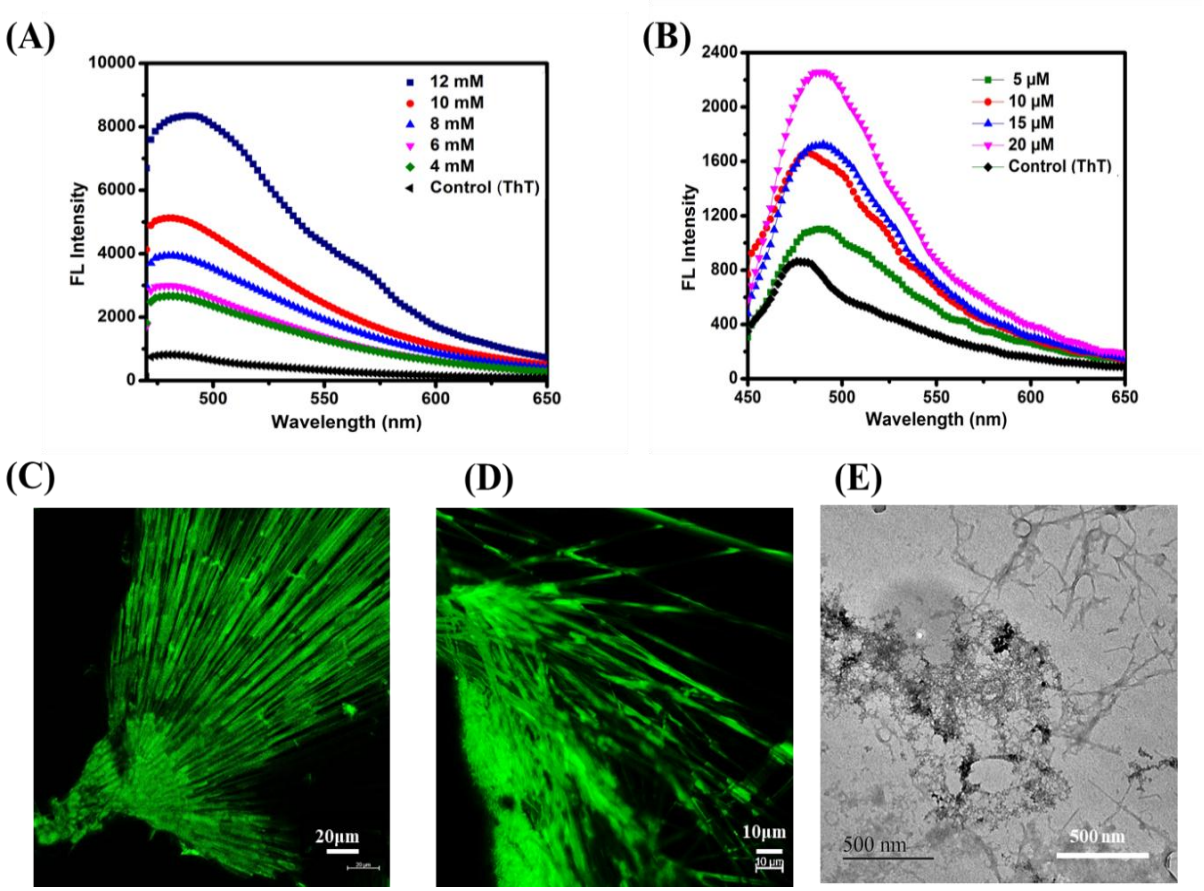

Figure 2.5: ThT fluorescence analysis representing aggregation of (A) FF and (B) Aβ42 peptide in a concentration-dependent manner. Fluorescent images obtained through confocal microscopy representing the structural changes in FF fibrils after (C) 24 h, and (D) 48 h of incubations, respectively at room temperature. (E) TEM image showing Aβ42 peptide fibrils (scale bar~500 nm).

2.3.3. Both disaggregation and inhibition of FF and Aβ42 peptide fibrils by TNPs:

Disaggregation and inhibition experiments in the presence of TNPs were performed using confocal, SEM, TEM and Bis-ANS assay. Firstly, the minimum disaggregating concentrations of TNPs was estimated by using the Bis-ANS assay and it was observed that 100 µg mL^{-1} of TNPs showed optimal disaggregation of FF aggregates in a time dependent manner (**Figure** 2.6), hence we used 100 µg mL^{-1} TNPs for various anti- aggregation and inhibition studies of both FF and Aβ42 peptide.

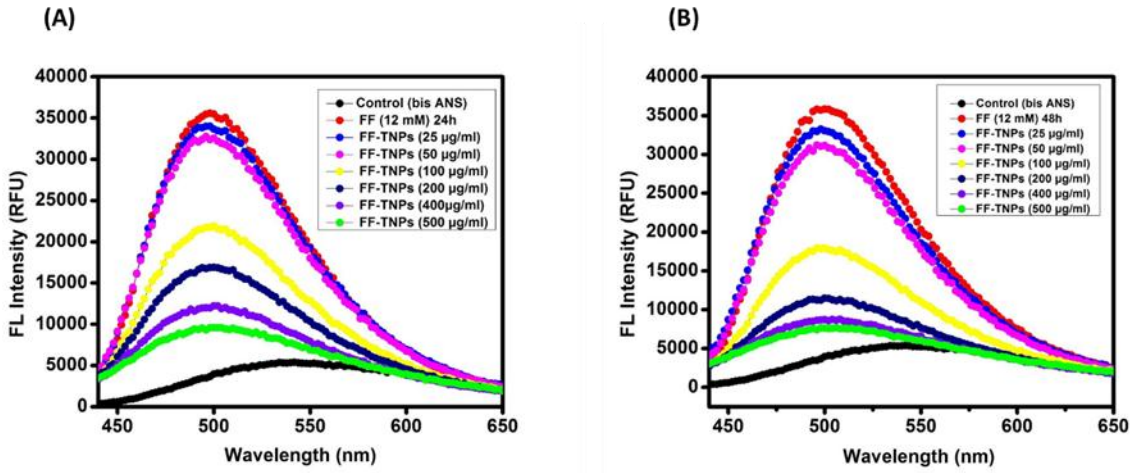

Figure 2.6: Bis-ANS fluorescence assay of FF (12 mM) incubated in the presence of different concentration of TNPs demonstrating a decline in bis-ANS fluorescence intensity after (A) 24h and (B) 48h treatment.

Both confocal and SEM of aggregated FF fibrils indicated the presence of dense fibrillar assemblies (**Figure** 2.7 A, D, and G). However, upon incubating these fibrils with TNPs (100 µg mL^{-1}), time-dependent morphological changes of FF assemblies from aggregated bundle-like fibrils to short unstructured assemblies were examined. Evidently, after an incubation period of 24 h, a few short fibrillar aggregates were evident (**Figure** 2.7 B and E), whereas, after 48 h of TNPs treatment, FF aggregates were almost invisible (**Figure** 2.7 C and F). Similarly, time-dependent decrease in fluorescence intensity of Bis-ANS was observed when FF aggregates were being treated for period of 24 and 48h (**Figure** 2.7 Q). Thus, our confocal microscopic, SEM and Bis-ANS studies results clearly showed that the TNPs could successfully disaggregate FF amyloid fibrils in a time dependent manner which directly confirmed the anti- amyloidogenic nature of these NPs. Likewise, Gazit and group also reported a similar and comparable disassembly of FF fibrils using various polyphenols.[50] Interestingly, we also noticed time dependent inhibition of aggregation of FF fibrils (**Figure** 2.7 H and I) by the TNPs. The time dependent inhibition studies revealed that TNPs remarkably inhibited the self-assembly and aggregation of FF when being treated for 24 and

48 h respectively. Moreover, as presented in **Figure** 2.7 S**,** TNPs also interacted and got tagged with FF fibrils and thus they could additionally serve as a system to identify and recognize FF fibrils.

As the early aggregation intermediates and amyloid fiber-like assemblies of Aβ42 peptide are the major pathological signatures in AD.[61] We therefore investigated the inhibition and disaggregation ability of our NPs toward the Aβ42 peptide assemblies. For this Aβ42 peptide fibrils (20 μM) shown in **Figure** 2.7 J, were incubated with the TNPs (100 μg mL^{-1}) for varying time intervals of 24, and 48 h. As shown in **Figure** 2.7 K and L, after 24 h of incubation with TNPs, many long aggregated Aβ42 peptide fibrils were converted to small fibrillar structures, whereas after 48 h of incubation, degradative products of Aβ42 peptide fibrils were seen in the TEM micrograph. Similarly, we clearly observed time dependent decrease in the Bis-ANS fluorescence intensity when aggregated Aβ42 peptide fibrils were incubated in the presence of the TNPs (**Figure** 2.7 R). Interestingly, we also noticed time dependent inhibition of aggregation of Aβ42 peptide fibrils (**Figure** 2.7 M) by the TNPs. The time dependent inhibition studies revealed that TNPs remarkably inhibited the self-assembly of Aβ42 peptide to dense aggregated fibrils when being treated for periods of 24 (**Figure** 2.7 N), and 72 h (**Figure** 2.7 O) respectively.

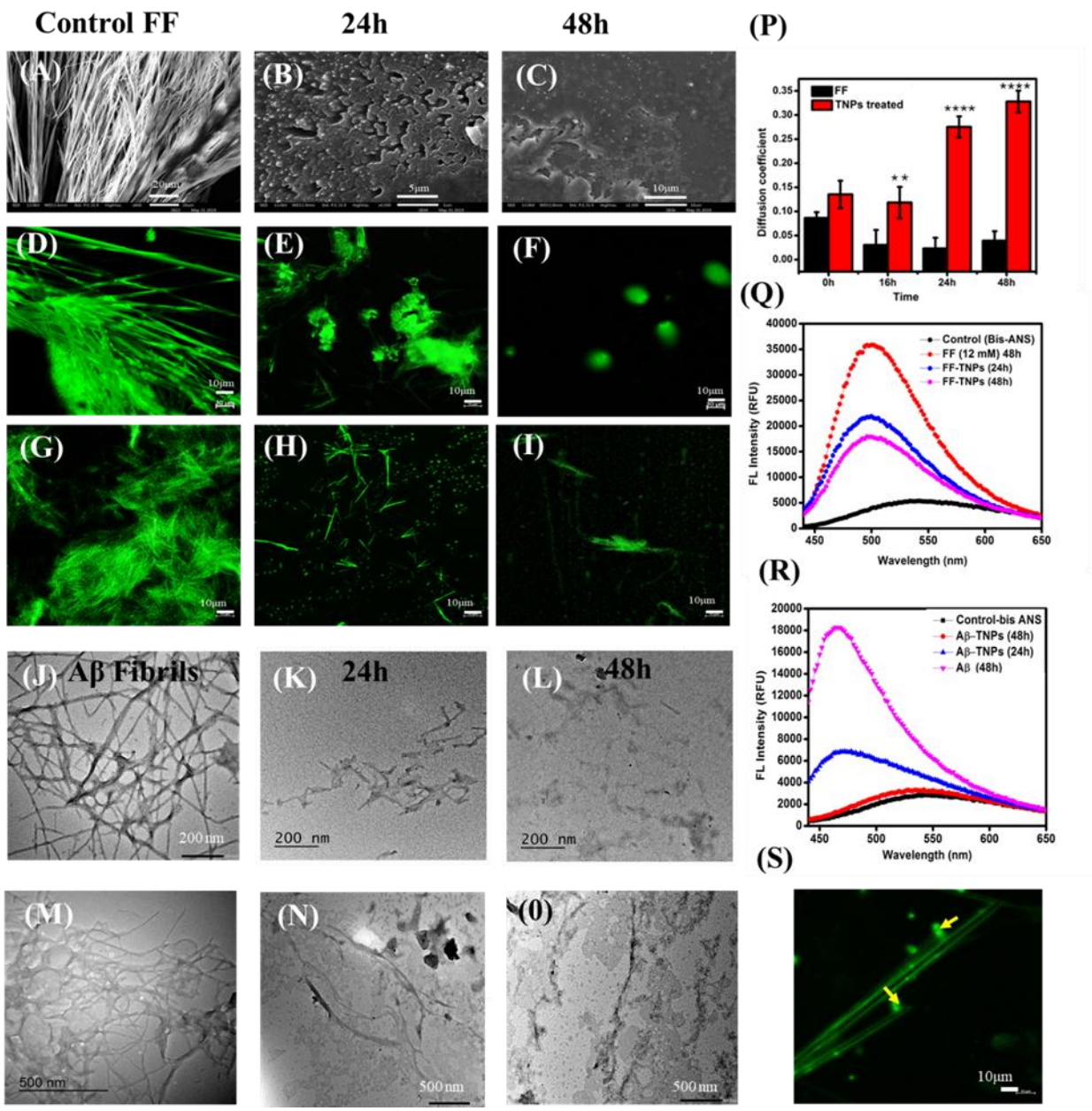

Figure 2.7: SEM images showing FF fibrils formation and their disaggregation, and inhibition by the TNPs. (A) Preformed fibril; (B) Preformed FF fibrils incubated with TNPs for 24 h; (C) Preformed FF fibrils incubated with TNPs for 48 h (Scale bar~10 μm). Confocal microscopic images displaying structural alterations of (D and G) FF fibrils after (E and H) 24 h, (F and I) 48 h of incubation (scale bar~10 μm). TEM images showing inhibition and disaggregation of mature fibrils of Aβ42 by TNPs. (J) Preformed Aβ42 peptide fibrils, (K and L). Disaggregation of Aβ42 peptide fibrillization by TNPs after 24, and 48 h (scale bar~200

nm). (M) Aβ42 peptide fibrils without treatment after 72 h, (N and O) Inhibition of Aβ42 peptide fibrillization by TNPs after 24, and 72 h of incubation. (P) DLS plot showing diffusion coefficient versus time. [Data presented as the mean of three (n = 3) independent samples ± SE]. Data were measured by two-way ANOVA, followed by sidak's multiple comparison test (* $p <$ 0.05; ** $p <$ 0.01; *** $p <$ 0.001; **** $p <$ 0.0001). Bis-ANS fluorescence analysis showing time- dependent disaggregation of (Q) FF and (R) Aβ42 peptide by TNPs. Confocal image of TNPs showing FF fibrils tagging and detection by TNPs (S) (scale bar~5 μm).

Next, fibril dissociation/disaggregation propensity of the TNPs were also supported by both DLS and CD analysis. As shown in **Figure** 2.7 P, the kinetics of disaggregation were evaluated by DLS. DLS provides z-average and particles translational diffusion coefficient,[62](D) that varies directly with the effective hydrodynamic radius of the particles based on the Stokes-Einstein equation 1.[63]

$$D = \frac{K_B T}{6\pi \eta_0 a} \quad (1)$$

where, k_B represents Boltzmann's constant, T represents the absolute temperature and η_0 represents solution viscosity. From the equation, it can be concluded that D values indirectly correlate with the particle or aggregate size and hence an enhancement in the D value would indicate disaggregation of larger aggregates.[64] Our results depicted an enhancement in the D values of the aggregates when being incubated with the TNPs, clearly pointing towards the dissociation of the aggregates into smaller particles. This further confirmed fibril disaggregating potency of the structures. Likewise, CD analysis showed a perturbation in the β-sheet like structure of FF fibrils in a time dependent manner when being treated with the TNPs (**Figure** 2.8**)**.

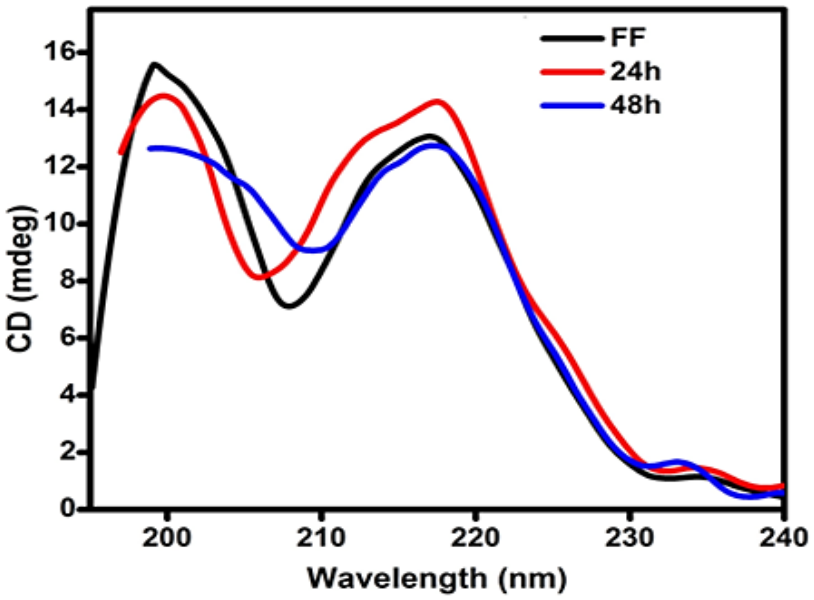

Figure 2.8: CD spectrum of TNPs treated FF fibrils.

2.3.4. Disaggregation potency of L-Trp, D-Trp and TNPs towards FF aggregates:

Disaggregation studies were performed to check the potential disaggregation efficiency of L-Trp, D-Trp and TNPs (100 μg mL^{-1}) towards FF aggregates using confocal and SEM analysis. From confocal and SEM results it was observed that L-Trp showed better disaggregation efficiency towards FF aggregates as compared to D-Trp when being treated for 48 h. Likewise, Malishev et al. demonstrated chiral modulation of Aβ fibrillation by enantiomeric carbon dots of L-Lys and D-Lys, and L-Lys carbon dots exhibited stronger inhibition of A□42 fibrils and mitigated their cytotoxicity as compared to D-Lys .[16] However, upon incubating FF aggregates with TNPs (100 μg mL^{-1}) for 48 h time interval, structural changes of FF aggregates from aggregated mesh-like fibrils to short unstructured remnants were observed. Thus, TNPs (100 μg mL^{-1}) showed remarkable disaggregation potency towards FF aggregates (12mM) as compared to both L-Trp and D-Trp after 48 h of treatment (**Figure** 2.9).

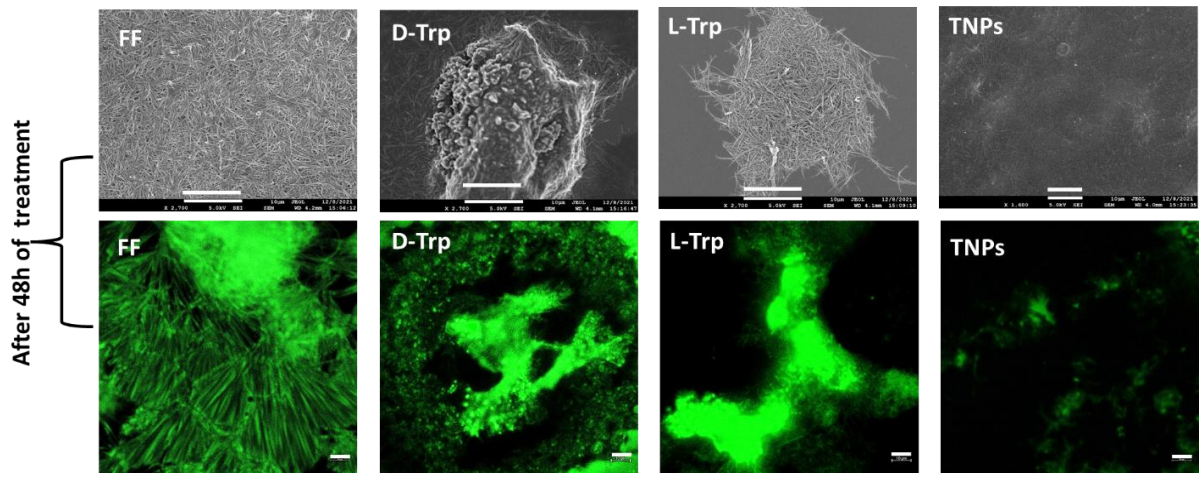

Figure 2.9: SEM and confocal images representing FF fibrils disaggregation by L-Trp, D-Trp and TNPs (100 μg mL^{-1}) after 48h of incubation (scale bar~10μM).

2.3.5. BBB permeation of TNPs by PAMPA:

PAMPA assay serves to be the gold standard to study permeability of molecules across various membranes and exhibits good correlation with the in vivo context. BBB-PAMPA is a non-cellular, fast, high throughput, and 96- well microplate-based assay to predict BBB permeation of molecules by passive diffusion.[65] Though, PAMPA involves testing the permeability of molecules across a membrane coated with phospholipids, mimicking the target membrane and is based on passive diffusion lacking any active transport system,[66] it can be used as the initial screen for determining the permeability of compounds across any biological membrane of interest. Herein, we performed BBB-PAMPA assay to determine the BBB penetrability of the TNPs.[67] Interestingly, TrP can cross the BBB by means of LAT1 transporters [46,47] and, thus, the nanostructures solely prepared from TrP would also show inherent property to traverse across the BBB. Our results depicted a permeability of around 32 % for 500 μg and 52 % for 1mg mL^{-1} of the TNPs when being incubated with PAMPA membrane coated with brain polar lipids for18 h (**Figure** 2.10). Thus, PAMPA results clearly demonstrated that TNPs were capable of traversing through the BBB by following passive diffusion.

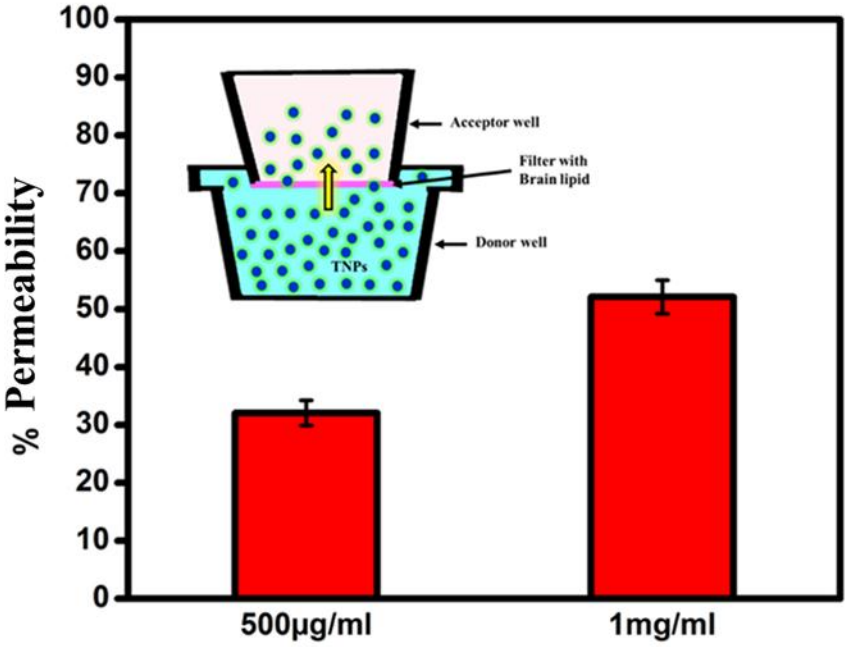

Figure 2.10: Representative bar graph showing percentage permeability of TNPs across the BBB as determined through the BBB-PAMPA model (Data presented as the mean of three (n = 3) independent samples ± SE).

2.3.6. Biocompatibility and cellular uptake studies of TNPs carried out in SH-SY5Y cells:

To monitor the capability of TNPs as a potent imaging agent, we investigated their cellular penetration ability in SH-SY5Y cells by both confocal microscopy and FACS analysis. As shown in the **Figure** 2.11 A-C, the bright blue and green cellular fluorescence detected in the TNPs exposed cells indicated successful cellular intake of these self-fluorescent nanostructures. This exceptional fluorescent property of the TNPs in lighting up the cellular cytoplasm directly proved their ability to serve as a potent imaging and diagnosis agent.

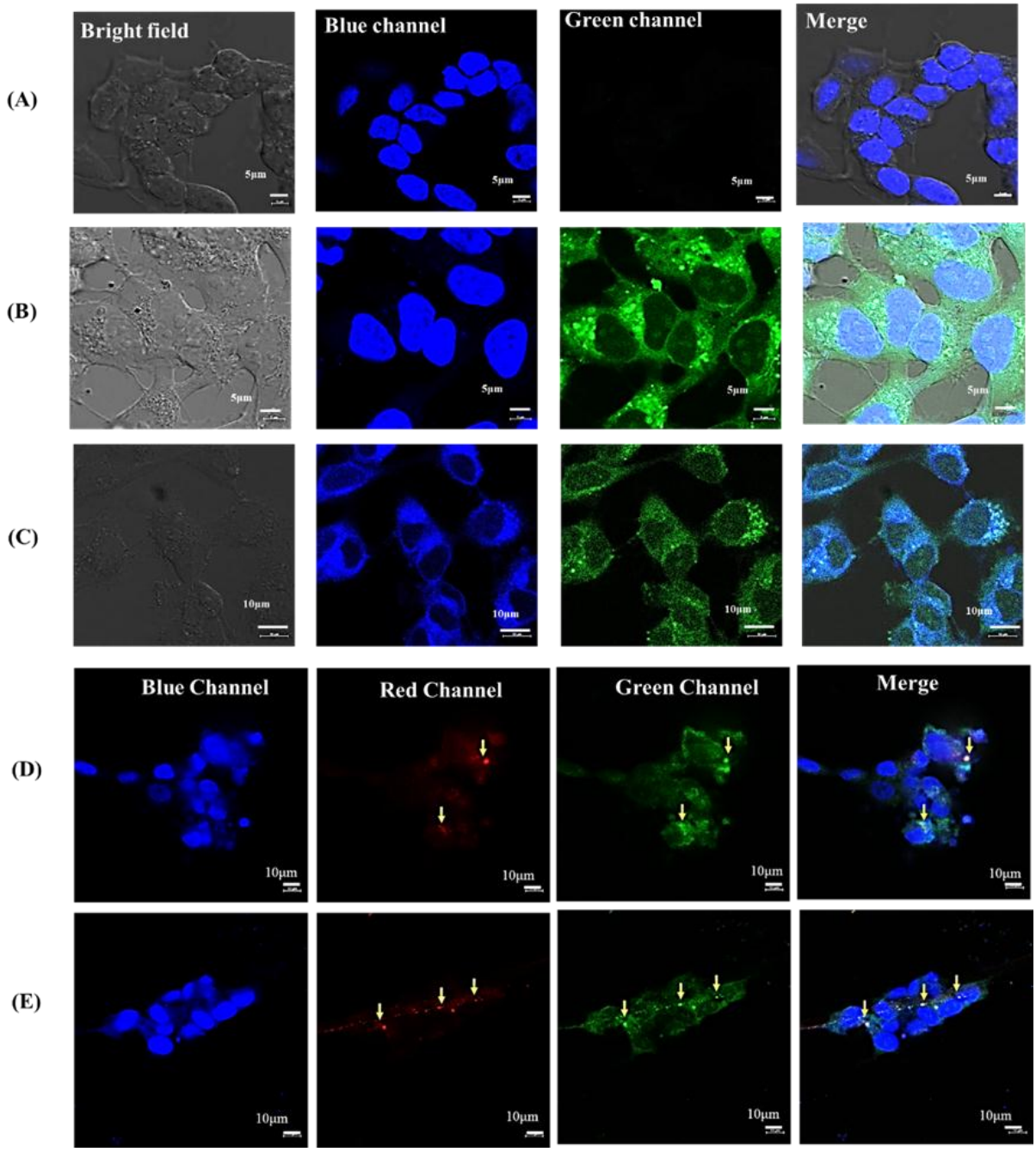

Figure 2.11: Confocal fluorescence images showing the uptake of TNPs in green and blue channel**:** (A) DAPI stained cells, (B) DAPI stained cells incubated with TNPs, (C) TNPs treated without DAPI stained cells (scale bar~5 µm). Confocal images showing interaction of Aβ42 peptide fibrils (red) and TNPs (green) (D); FF fibrils (red) and TNPs (green) (E) in DAPI-stained SH-SY5Y cells (scale bar~10 µm).

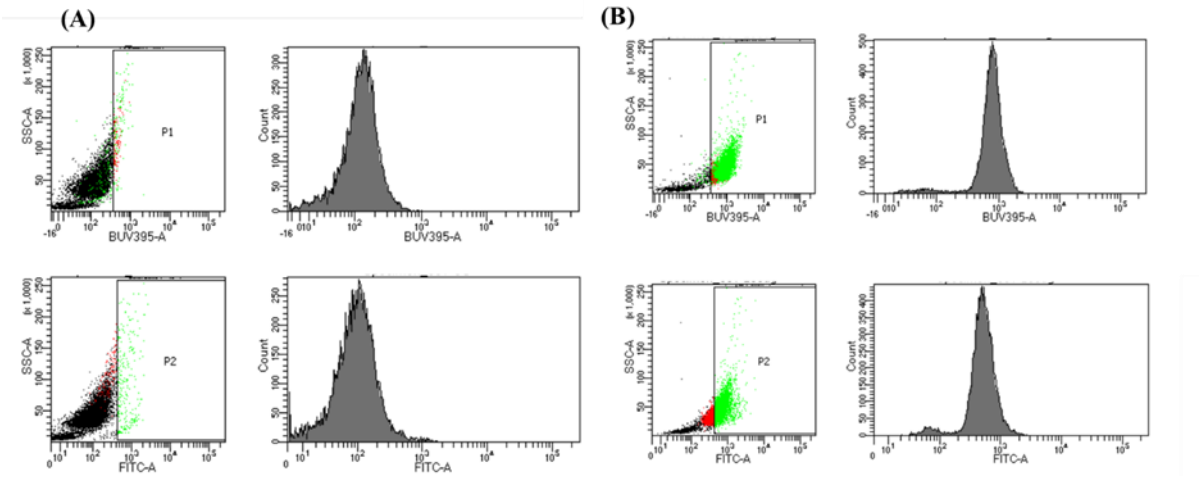

Figure 2.12: Flow cytometric analysis of cellular uptake of TNPs in SH-SY5Y cells after 24 h of incubation. (A) unstained control cells and (B) cells after treatment with TNPs. P1 area represents fluorescence in DAPI region where as P2 represents fluorescence in FITC region.

Likewise, cellular quantitative penetration capability of TNPs was also analysed by FACS. Results demonstrated remarkable green and blue fluorescence in case of TNPs treated cells as compared to unstained cells (**Figure** 2.12). Next, prior to investigating the peripheral clearance of Aβ42 peptide in vivo, we assessed the biocompatibility of TNPs. After incubating various concentrations of TNPs with SH-SY5Y cells for 24 h, cytotoxicity was calculated by standard MTT assay. As shown in **Figure** 2.13 B, the cell viability remained above 90 % even with TNPs concentrations being as high as 300 μg mL^{-1}, suggesting excellent biocompatibility of our TNPs. Further, to check and confirm the potent imaging capability of TNPs, we next assessed intracellular interaction of FF and Aβ42 peptide fibrils by confocal microscopy. TNPs were capable of reaching, detecting and staining the amyloid fibrils of FF as well as Aβ42 peptide (**Figure** 2.11 D and E). Likewise, real time intracellular imaging of amyloid β aggregation was also reported by the Masahiro Kuragano group using quantum dots.[68] Overall, cellular uptake, cell viability and interaction results showed that the TNPs could be utilized as a potential imaging modalities and therapeutic molecule carriers.

2.3.7. Inhibition of FF and Aβ42 peptide induced cytotoxicity by TNPs in SH-SY5Ycells determined by live dead assay:

The neuro protective effect of TNPs against FF and Aβ42 peptide amyloid fibrils caused cytotoxicity in neuronal cells was determined by carrying out live dead assay. Cells were incubated with FF fibrils (12 mM), Aβ42 peptide fibrils (20 μM) and different concentrations of TNPs (50 μg mL^{-1} and 100 μg mL^{-1}) and their viability was evaluated using live dead assay using ZEISS LSM 880 confocal microscope with Airyscan and high content imager. It was noticed that FF and Aβ42 peptide fibrils alone showed toxicity in neuronal cells; however, the cells co-incubated with TNPs and FF fibrils for an interval of 48 h, demonstrated a significantly reduced cell death rate (**Figure** 2.13 A, D). Parallelly, increased level of cell viability was noticed after the cells were treated with different concentrations of TNPs. Similarly, the cells co-incubated with TNPs and Aβ42 peptide fibrils for a period of 48 h, demonstrated reduced cell death rate and dose-dependent enhancement in the cell viability was observed (**Figure** 2.13 B).

2.3.8. Intracellular detection and inhibition of FF and Aβ42 peptide fibrils by TNPs:

As previously described,[69] Aβ42 peptide fibrils can be suitably stained by ThT, enabling the detection and intracellular FF and Aβ42 peptide fibrillations by evaluating the ThT fluorescence intensity. As depicted in **Figure** 2.13 F and H, significant intracellular ThT fluorescence was observed due to the presence of FF and Aβ42 fibrils, whereas a near-complete depletion of ThT fluorescence intensity was examined, when these cells were co-treated with TNPs (**Figure** 2.13 G and I). Likewise, similar and comparable reduction in intracellular ThT fluorescence intensity of Aβ42 peptide fibrillation was also reported earlier.[69,51] Taken together, these results proved that TNPs could effectively inhibit both Aβ42 peptide and FF fibrillations inside the neuronal cells. In addition, we assumed that the

increased cellular uptake of TNPs contributed to its substantially enhanced inhibition of FF and Aβ42 peptide fibrillation in SH-SY5Y cells.

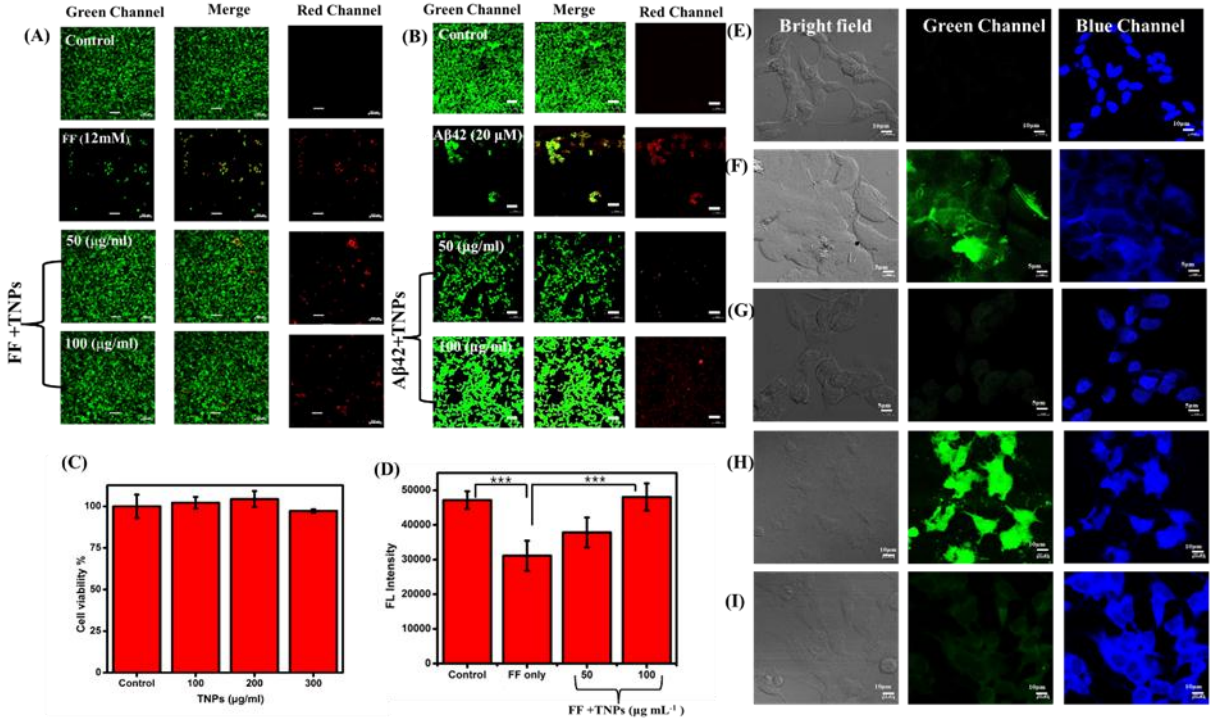

Figure 2.13: Calcein AM/PI staining based confocal images showing neuroprotective effects of TNPs against FF and Aβ42 fibrils mediated cytotoxicity in SH-SY5Y cells after 48 h (scale bar ~100 μm) (A and B). (C) MTT data showing toxicity of TNPs **[**Data presented as the mean of three (n = 3) independent samples ± SE]. (D) Calcein AM assay demonstrating protective effect of TNPs determined using a multimode plate reader. Fluorescence intensity of calcein AM recorded after 48 h. Data were measured by one-way ANOVA and turkey multiple comparison test (* $p < 0.05$; ** $p < 0.01$; *** $p < 0.001$). Confocal microscopic images aimed to detect FF and Aβ42 peptide fibrils in cells. (E) ThT and DAPI-stained control SH-SY5Y cells without treatment (scale bar ~10μm). The intracellular fibrils of FF were assessed by ThT staining in SH-SY5Y cells (F) and (G) in the presence of TNPs (scale bar ~5 μm). (H) The intracellular fibrils of Aβ42 peptide were assessed by ThT staining in SH-SY5Y cells and (I) in the presence of TNPs (scale bar ~10 μm).

2.3.9. TNPs rescued spatial learning and memory deficits in ICV-STZ induced rat model:

To assess the long-term effect of TNPs on the behavioural illnesses (spatial learning/memory) in STZ induced rat amyloid model, we performed MWM assay and observations were analysed as escape latency period and path length between the sessions. Post hoc assessment revealed that the animals treated with ICV-STZ exhibited heightened escape latency time [$F(6,60) = 21.38$]. No comparable variations in the latency time in the subsequent two sessions were observed in case of these animals when being compared to the first one (**Figure** 2.14 A ; $p>0.05$). These results demonstrated the emergence of AD like phenotypes in these animals. The ICV-STZ and TNPs treated rats showed low escape latency time in the second ($p<0.05$) and third ($p<0.05$) sessions when being equated to the first session (**Figure** 2.14 A). This clearly indicated the considerable protective role played by TNPs towards recovery from the behavioural illnesses incurred in the animals due to ICV-STZ administration. Moreover, the TNPs *per se* group exhibited identical learning and memory retention behaviour as noticed in aCSF administered animals (**Figure** 2.14 A). Further, we examined the average path length travelled by rats to get the concealed platform [$F(6,60) = 11.60$]; and observed that ICV STZ treated animals exhibited no considerable variation ($p>0.05$) in path length covered from session 1 to 3 (**Figure** 2.14 B). However, when treated with TNPs, the path length covered by rats to stick out the platform was decreased significantly ($p<0.001$) when being equated to that of session 1 to session 3. On the other hand, we observed no prominent change in swim speed (**Figure** 2.14 C) of rats suggesting that the alteration in escape latency time and path length is solely dependent upon STZ triggered degeneration of neuronal cells. A notable decline in the target quadrant spent time was found in ICV STZ treated rats when being compared to control animals, proving lack in retention memory, which was significantly improved by TNPs treatment (**Figure** 2.14 D, $p<0.001$). ICV STZ treated rats required a

longer time to reach the hidden platform when being matched to aCSF group that could be depicted from **Figure** 2.14 E**,** which represents the path covered by animals in the 3rd session. Our data suggested that TNPs could have a significant influence in attenuating spatial learning and memory retention deficits in AD.

2.3.10. Effect of TNPs on Aβ42 peptide load in ICV-STZ induced rat model of AD-like phenotype:

We also explored the role of TNPs exerted on the reduction of Aβ42 peptide load in the cortex area (**Figure** 2.14 G) and hippocampus (**Figure** 2.14 H) area of rat brain. After ICV administration of STZ, the degree of expression of Aβ42 oligomers increased in both cortex ($p<0.05$) as well as hippocampal region ($p<0.001$) which was monitored by immunohistochemical analysis. Contrarily, on administration of TNPs along with STZ exposure, animals showed progressive downregulation of Aβ42 oligomers expression ($p<0.05$, $p<0.01$), suggesting decreased accretion of the peptide in both brain regions (**Figure** 2.14 F)**.** Interestingly, TNPs *perse* administration group showed the same behaviour as observed in the control group.

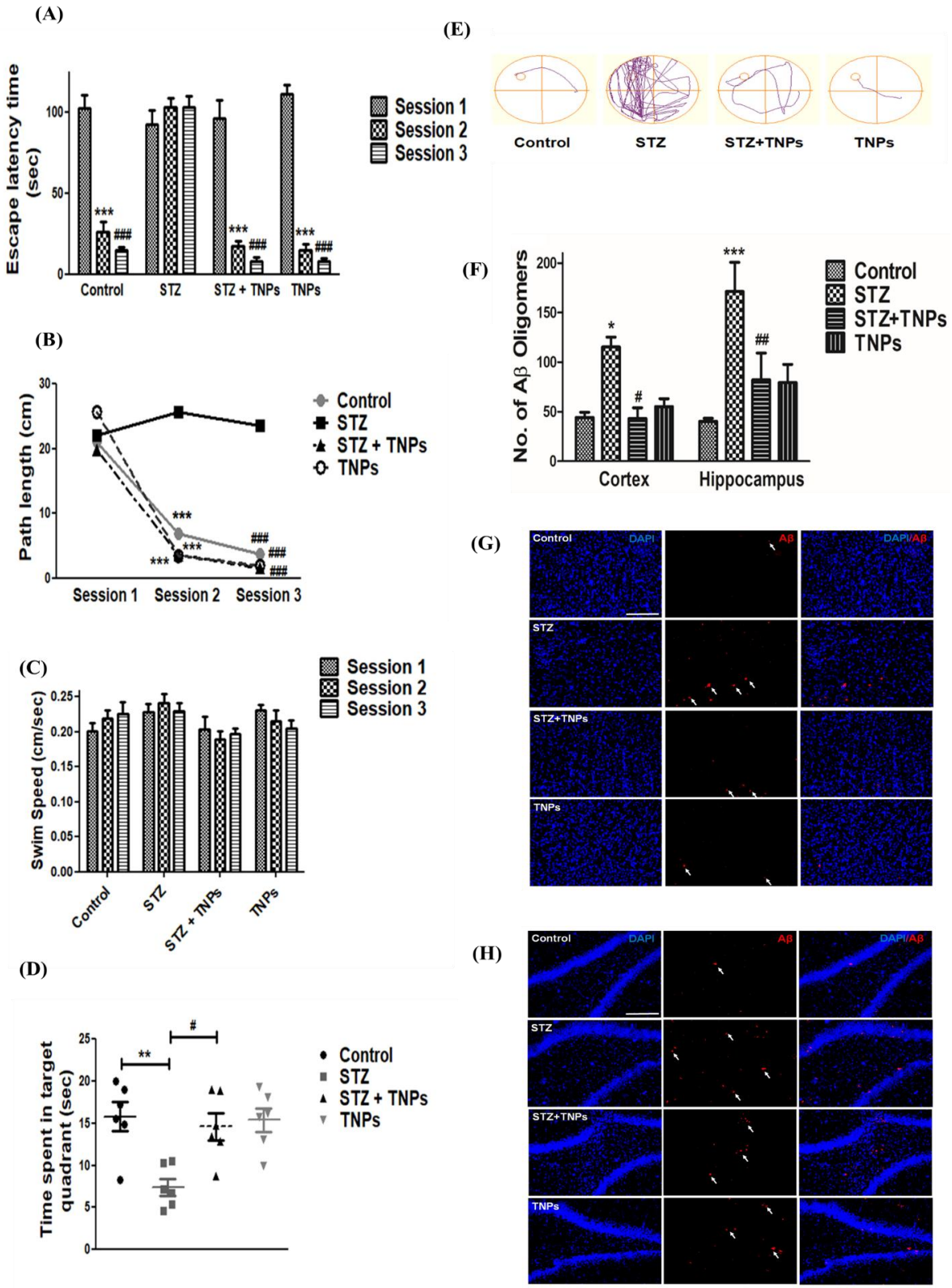

Figure 2.14: Effect of TNPs on behavioural performance of ICV-STZ induced rat model. TNPs treatment improved STZ induced memory and learning deficits in AD rats and also reduced the expression of Aβ42 peptide in both cortex and hippocampus area of rats'

brain. Spatial memory and learning behaviours were determined by using MWM study. (A) Bar graph representing escape latency time (in sec). (B) Bar graph showing average path length represented in cm. (C) Graph showing swim speed (in cm) of the animals after TNPs treatment. (D) Graph showing time spent by the animals in the target quadrant. (E) The track plot representing the path travelled by rat of each group**.** Data are plotted as the mean ± SE of n = 6 animals/group. Data were calculated by repeated-measures two-way ANOVA and bonferroni post hoc analysis [*p < 0.05, **p < 0.01, ***p < 0.001 (* Session 1 vs Session 2, and* control *vs* STZ); #p < 0.05, ##p < 0.01, ###p < 0.001 ($^{\#}$ Session 1 vs Session 3, and $^{\#}$ STZ *vs* STZ+TNPs)]. (F) Bar graph showing numbers of Aβ42 oligomers in both regions. Data were measured by two-way ANOVA and Bonferroni multiple comparison test [*P < 0.05, **P < 0.01, ***P < 0.001 (*Control vs STZ); $^{\#}$P < 0.05, $^{\#\#}$P < 0.01, $^{\#\#\#}$P < 0.001 ($^{\#}$STZ vs STZ+ TNPs)]. (G and H) Immunostaining based photomicrographs displaying expression of Aβ42 oligomers in both cortex and hippocampus areas of the brain.

2.3.11. Serum stability of the TNPs:

The NPs were found to be stable in serum as 80.50±0.27% of the compound was found to be intact after 2 hours of incubation (**Figure** 2.15) depicting their high potential in vivo stability.

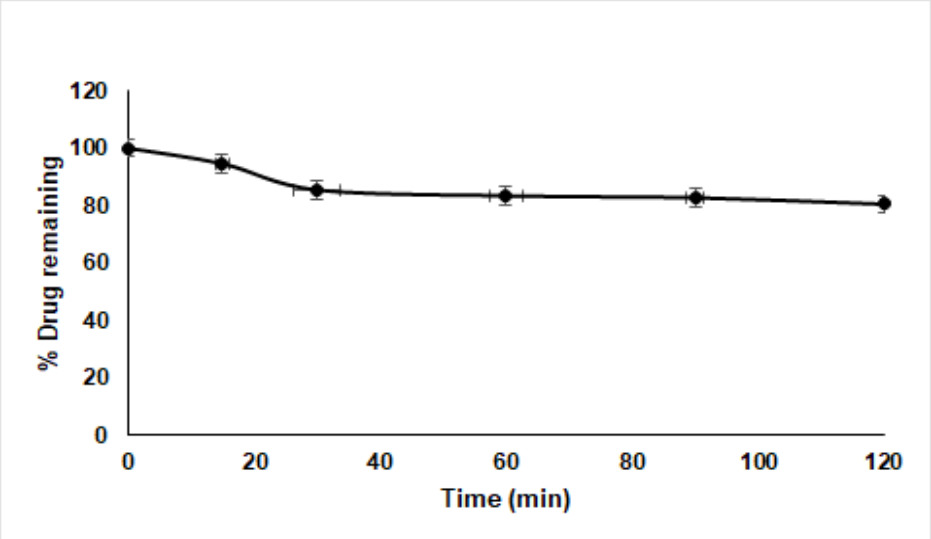

Figure 2.15: *In vitro* serum stability of TNPs after 2 hours of incubation. Data are presented as the mean ± SE of n = 3.

2.3.12. Blood brain barrier permeability determined in animal model:

As previously reported, the serum stability and BBB permeability of any new drug or NP targeting the AD can be determined by their pharmacokinetics pattern.[70] Thus, we performed pharmacokinetic study of TNPs in animal models. The pharmacokinetic profile of TNPs in brain and serum of treated rats could be predicted from **Figure** 2.16 and **Table** 2.1. **Table** 2.2 represents the brain-to-serum concentration ratio after intravenous injection of TNPs (assuming, 1 g of brain tissue is equivalent to 1 mL serum). The brain-to-serum amount ratio of more than 1.5 suggested decent BBB permeabilizing ability of the structures up to 4h, making TNPs a promising drug targeting candidate for brain tissues.

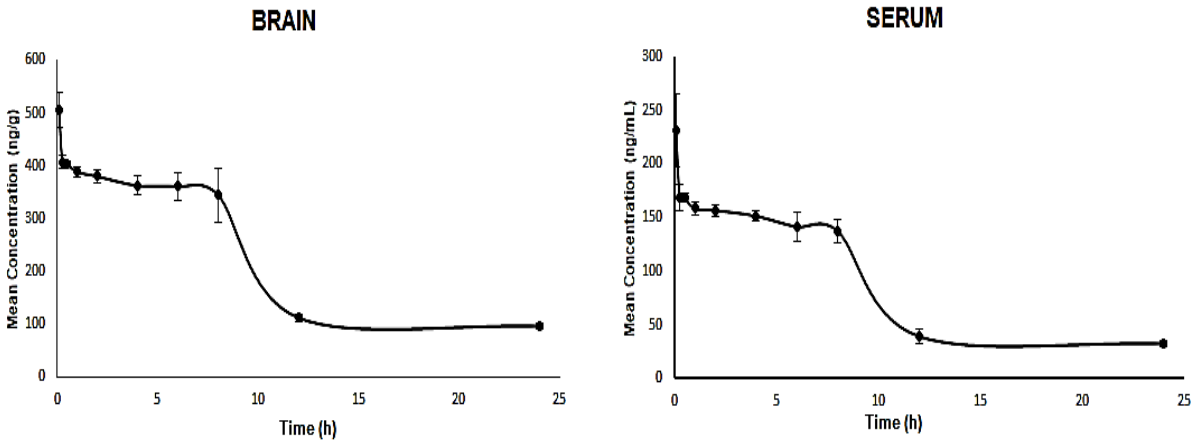

Figure 2.16: The pharmacokinetic profile of TNPs determined in brain and serum after their intravenous administration to SD rats at a dose of 5mg/kg body weight of the animal. Data presented as the mean ± SE of n = 3.

Table 2.1: The pharmacokinetic parameters of TNPs in brain and serum after intravenous administration to SD rats at a dose of 5mg/kg body weight of the animal. Data presented as the mean ± SE of n = 3.

Parameter	Unit	Brain (Mean ± SEM)	Serum (Mean ± SEM)
AUC 0-t	ng/ml*h	3835±159.65	1998±59.84
AUC 0-inf_obs	ng/ml*h	3858.87±159.82	2400.52±63.96
$t_{1/2}$	H	3.25±0.01	8.61±0.17
Tmax	H	0.08±0.0	0.08±0.0
Cmax	ng/ml	505.66±33.57	231.66±34.08

Table 2.2: Brain-to-serum ratio of TNPs determined in SD rats after iv administration at a concentration of 5 mg/kg body weight of the animal (n=3)

Time point (h)	Mean (SEM)
0.08	2.26 (0.28)
0.25	2.43 (0.13)
0.5	2.41 (0.36)
1	2.45 (0.04)
2	2.43 (0.11)
4	2.40 (0.06)

2.4. Conclusion:

In summary, the current work deals with the development of multimodal and solo tryptophan nanoparticles as an armamentarium for the simultaneous imaging, diagnosis and therapy of AD. In this study, the synthesized fluorescent NPs were well capable of disaggregating dipeptide FF fibrils in a time-dependent manner. FF was used as an amyloid reductionist model to investigate anti-amyloidogenic behaviour of self-fluorescent tryptophan nanoparticles. In addition, in vitro assays with Aβ42 peptide further revealed that the nanoparticles could efficiently inhibit the aggregation of preformed Aβ42 peptide aggregates. Moreover, the outstanding neuroprotective effect of these nanoparticles was also tested and validated using live dead cell staining assay. Interestingly, it was noticed that the dipeptide fibrils alone generated toxic effects in neuronal cells; however, when the cells were incubated with tryptophan nanoparticles, the degree of cell death was significantly reduced. The designed tryptophan nanoparticles can further find potential application as bioimaging agents owing to their auto-fluorescent nature. In addition, our synthesized nanostructures have shown remarkable neuroprotective effects in lessening the cognitive deficits and supressing the Aβ42 oligomers accumulation in the brain of ICV-STZ induced AD rat model. Moreover, pharmacokinetics study of the NPs shows that these could breach the BBB to gain access to the neuronal tissues and subsequently serve as a brain delivery agent. Overall, the biocompatible and utterly simple and fluorescent tryptophan nanoparticles synthesized here could serve as potent nanotheranostic agents for treating and diagnosing AD.

2.5. References:

(1) Braak, E.; Griffing, K.; Arai, K.; Bohl, J.; Bratzke, H.; Braak, H. Neuropathology of Alzheimer's Disease: What Is New since A. Alzheimer? *Eur. Arch. Psychiatry Clin. Neurosci.* **1999**, *249 Suppl 3*, 14–22.

(2) Lyketsos, C. G.; Olin, J. Depression in Alzheimer's Disease: Overview and Treatment. *Biol. Psychiatry* **2002**, *52*, 243–252.

(3) Selkoe, D. J. Alzheimer's Disease Is a Synaptic Failure. *Science* **2002**, *298*, 789–791.

(4) Esler, W. P.; Wolfe, M. S. A Portrait of Alzheimer Secretases--New Features and Familiar Faces. *Science* **2001**, *293*, 1449–1454.

(5) Murphy, M. P.; LeVine, H. Alzheimer's Disease and the β-Amyloid Peptide. *J. Alzheimers Dis.* **2010**, *19*, 311.

(6) Umeda, T.; Tomiyama, T.; Sakama, N.; Tanaka, S.; Lambert, M. P.; Klein, W. L.; Mori, H. Intraneuronal Amyloid β Oligomers Cause Cell Death via Endoplasmic Reticulum Stress, Endosomal/Lysosomal Leakage, and Mitochondrial Dysfunction in Vivo. *J. Neurosci. Res.* **2011**, *89*, 1031–1042.

(7) Chen, X.-Q.; Mobley, W. C. Alzheimer Disease Pathogenesis: Insights From Molecular and Cellular Biology Studies of Oligomeric Aβ and Tau Species. *Front Neurosci* **2019**, *13*, 659.

(8) Selkoe, D. J.; Hardy, J. The Amyloid Hypothesis of Alzheimer's Disease at 25 Years. *EMBO Mol Med* **2016**, *8* (6), 595–608.

(9) Bors, L. A.; Erdő, F. Overcoming the Blood–Brain Barrier. Challenges and Tricks for CNS Drug Delivery. *Scientia Pharmaceutica* **2019**, *87* (1), 6.

(10) Ahmad, J.; Akhter, S.; Rizwanullah, M.; Khan, M. A.; Pigeon, L.; Addo, R. T.; Greig, N. H.; Midoux, P.; Pichon, C.; Kamal, M. A. Nanotechnology Based Theranostic Approaches in Alzheimer's Disease Management: Current Status and Future Perspective. *Curr Alzheimer Res* **2017**, *14* (11), 1164–1181.

(11) Gupta, J.; Fatima, M. T.; Islam, Z.; Khan, R. H.; Uversky, V. N.; Salahuddin, P. Nanoparticle Formulations in the Diagnosis and Therapy of Alzheimer's Disease. *Int J Biol Macromol* **2019**, *130*, 515–526.

(12) Shao, X.; Cui, W.; Xie, X.; Ma, W.; Zhan, Y.; Lin, Y. Treatment of Alzheimer's Disease with Framework Nucleic Acids. *Cell Prolif* **2020**, *53* (4), e12787.

(13) Shao, X.; Ma, W.; Xie, X.; Li, Q.; Lin, S.; Zhang, T.; Lin, Y. Neuroprotective Effect of Tetrahedral DNA Nanostructures in a Cell Model of Alzheimer's Disease. *ACS Appl Mater Interfaces* **2018**, *10* (28), 23682–23692.

(14) Zhang, W.; Sigdel, G.; Mintz, K. J.; Seven, E. S.; Zhou, Y.; Wang, C.; Leblanc, R. M. Carbon Dots: A Future Blood-Brain Barrier Penetrating Nanomedicine and Drug Nanocarrier. *Int J Nanomedicine* **2021**, *16*, 5003–5016.

(15) Bai, C.; Lao, Z.; Chen, Y.; Tang, Y.; Wei, G. Pristine and Hydroxylated Fullerenes Prevent the Aggregation of Human Islet Amyloid Polypeptide and Display Different Inhibitory Mechanisms. *Frontiers in Chemistry* **2020**, *8*,**51**.

(16) Malishev, R.; Arad, E.; Bhunia, S. K.; Shaham-Niv, S.; Kolusheva, S.; Gazit, E.; Jelinek, R. Chiral Modulation of Amyloid Beta Fibrillation and Cytotoxicity by Enantiomeric Carbon Dots. *Chem. Commun.* **2018**, *54* (56), 7762–7765.

(17) Xie, L.; Luo, Y.; Lin, D.; Xi, W.; Yang, X.; Wei, G. The Molecular Mechanism of Fullerene-Inhibited Aggregation of Alzheimer's β-Amyloid Peptide Fragment. *Nanoscale* **2014**, *6* (16), 9752–9762.

(18) Kumar, A.; Chaudhary, R. K.; Singh, R.; Singh, S. P.; Wang, S.-Y.; Hoe, Z.-Y.; Pan, C.-T.; Shiue, Y.-L.; Wei, D.-Q.; Kaushik, A. C.; Dai, X. Nanotheranostic Applications for Detection and Targeting Neurodegenerative Diseases. *Frontiers in Neuroscience* **2020**, *14*,**305**.

(19) Moorthy, H.; Govindaraju, T. Dendrimer Architectonics to Treat Cancer and Neurodegenerative Diseases with Implications in Theranostics and Personalized Medicine. *ACS Appl. Bio Mater.* **2021**, *4* (2), 1115–1139.

(20) Du, Z.; Li, M.; Ren, J.; Qu, X. Current Strategies for Modulating Aβ Aggregation with Multifunctional Agents. *Acc. Chem. Res.* **2021**, *54* (9), 2172–2184.

(21) Kása, P.; Rakonczay, Z.; Gulya, K. The Cholinergic System in Alzheimer's Disease. *Prog. Neurobiol.* **1997**, *52*, 511–535.

(22) Butterfield, D. A.; Pocernich, C. B. The Glutamatergic System and Alzheimer's Disease: Therapeutic Implications. *CNS Drugs* **2003**, *17*, 641–652.

(23) Švob Štrac, D.; Pivac, N.; Mück-Šeler, D. The Serotonergic System and Cognitive Function. *Transl. Neurosci.* **2016**, *7*, 35–49.

(24) Rodríguez, J. J.; Noristani, H. N.; Verkhratsky, A. The Serotonergic System in Ageing and Alzheimer's Disease. *Prog. Neurobiol.* **2012**, *99*, 15–41.

(25) Charnay, Y.; Léger, L. Brain Serotonergic Circuitries. *Dialogues Clin. Neurosci.* **2010**, *12*, 471–487.

(26) Nakamura, K. The Role of the Dorsal Raphé Nucleus in Reward-Seeking Behavior. *Front. Integr. Neurosci.* **2013**, *7*,60.

(27) Patthy, Á.; Murai, J.; Hanics, J.; Pintér, A.; Zahola, P.; Hökfelt, T. G. M.; Harkany, T.; Alpár, A. Neuropathology of the Brainstem to Mechanistically Understand and to Treat Alzheimer's Disease. *J. Clin. Med.* **2021**, *10*, 1555.

(28) Mowla, A.; Mosavinasab, M.; Haghshenas, H.; Borhani Haghighi, A. Does Serotonin Augmentation Have Any Effect on Cognition and Activities of Daily Living in Alzheimer's Dementia? A Double-Blind, Placebo-Controlled Clinical Trial. *J. Clin. Psychopharmacol* **2007**, *27*, 484–487.

(29) Cirrito, J. R.; Disabato, B. M.; Restivo, J. L.; Verges, D. K.; Goebel, W. D.; Sathyan, A.; Hayreh, D.; D'Angelo, G.; Benzinger, T.; Yoon, H.; Kim, J.; Morris, J. C.; Mintun, M. A.; Sheline, Y. I. Serotonin Signaling Is Associated with Lower Amyloid-β Levels and Plaques in Transgenic Mice and Humans. *PNAS* **2011**, *108*, 14968–14973.

(30) Robert, S. J.; Zugaza, J. L.; Fischmeister, R.; Gardier, A. M.; Lezoualc'h, F. The Human Serotonin 5-HT4 Receptor Regulates Secretion of Non-Amyloidogenic Precursor Protein *. *J. Biol. Chem.* **2001**, *276*, 44881–44888.

(31) Payton, S.; Cahill, C. M.; Randall, J. D.; Gullans, S. R.; Rogers, J. T. Drug Discovery Targeted to the Alzheimer's APP MRNA 5'-Untranslated Region: The Action of Paroxetine and Dimercaptopropanol. *J. Mol. Neurosci.* **2003**, *20*, 267–275.

(32) Nelson, R. L.; Guo, Z.; Halagappa, V. M.; Pearson, M.; Gray, A. J.; Matsuoka, Y.; Brown, M.; Martin, B.; Iyun, T.; Maudsley, S.; Clark, R. F.; Mattson, M. P. Prophylactic Treatment with Paroxetine Ameliorates Behavioral Deficits and Retards the Development of Amyloid and Tau Pathologies in 3xTgAD Mice. *Exp. Neurol.* **2007**, *205*, 166–176.

(33) Richard, D. M.; Dawes, M. A.; Mathias, C. W.; Acheson, A.; Hill-Kapturczak, N.; Dougherty, D. M. L-Tryptophan: Basic Metabolic Functions, Behavioral Research and Therapeutic Indications. *Int. J. Tryptophan Res.* **2009**, *2*, 45–60.

(34) Noristani, H. N.; Verkhratsky, A.; Rodríguez, J. J. High Tryptophan Diet Reduces CA1 Intraneuronal β-Amyloid in the Triple Transgenic Mouse Model of Alzheimer's Disease. *Aging Cell* **2012**, *11*, 810–822.

(35) Jayamohananan, H.; Manoj Kumar, M. K.; T P, A. 5-HIAA as a Potential Biological Marker for Neurological and Psychiatric Disorders. *Adv. Pharm. Bull.* **2019**, *9*, 374–381.

(36) van der Stelt, H. M.; Broersen, L. M.; Olivier, B.; Westenberg, H. G. M. Effects of Dietary Tryptophan Variations on Extracellular Serotonin in the Dorsal Hippocampus of Rats. *Psychopharmacology* **2004**, *172*, 137–144.

(37) Jenkins, T. A.; Elliott, J. J.; Ardis, T. C.; Cahir, M.; Reynolds, G. P.; Bell, R.; Cooper, S. J. Tryptophan Depletion Impairs Object-Recognition Memory in the Rat: Reversal by Risperidone. *Behav. Brain. Res.* **2010**, *208*, 479–483.

(38) Porter, R. J.; Lunn, B. S.; Walker, L. L.; Gray, J. M.; Ballard, C. G.; O'Brien, J. T. Cognitive Deficit Induced by Acute Tryptophan Depletion in Patients with Alzheimer's Disease. *Am. J. Psychiatry* **2000**, *157*, 638–640.

(39) Haider, S.; Khaliq, S.; Haleem, D. J. Enhanced Serotonergic Neurotransmission in the Hippocampus Following Tryptophan Administration Improves Learning Acquisition and Memory Consolidation in Rats. *Pharmacol. Rep.* **2007**, *59*, 53–57.

(40) Levkovitz, Y.; Richter-Levin, G.; Segal, M. Effect of 5-Hydroxytryptophane on Behavior and Hippocampal Physiology in Young and Old Rats. *Neurobiol. Aging* **1994**, *15*, 635–641.

(41) Miri, A. L.; Hosni, A. P.; Gomes, J. C.; Kerppers, I. I.; Pereira, M. C. d. S. Estudo do L-triptofano na depressao ocorrida pela doenc̃ ą de Alzheimer em modelos experimentais. *J. Phys. Educ.* **2017**, 28, No. e-2839

(42) KrishnaKumar, V. G.; Paul, A.; Gazit, E.; Segal, D. Mechanistic Insights into Remodeled Tau-Derived PHF6 Peptide Fibrils by Naphthoquinone-Tryptophan Hybrids. *Sci. Rep.* **2018**, *8*, 71.

(43) Scherzer-Attali, R.; Pellarin, R.; Convertino, M.; Frydman-Marom, A.; Egoz-Matia, N.; Peled, S.; Levy-Sakin, M.; Shalev, D. E.; Caflisch, A.; Gazit, E.; Segal, D. Complete Phenotypic Recovery of an Alzheimer's Disease Model by a Quinone-Tryptophan Hybrid Aggregation Inhibitor. *PLoS One* **2010**, *5*, e11101.

(44) Paul, A.; Frenkel-Pinter, M.; Escobar Alvarez, D.; Milordini, G.; Gazit, E.; Zacco, E.; Segal, D. Tryptophan-Galactosylamine Conjugates Inhibit and Disaggregate Amyloid Fibrils of Aβ42 and HIAPP Peptides While Reducing Their Toxicity. *Commun. Biol.* **2020**, *3*, 484.

(45) Sharma, M.; Tiwari, V.; Shukla, S.; Panda, J. J. Fluorescent Dopamine-Tryptophan Nanocomposites as Dual-Imaging and Antiaggregation Agents: New Generation of Amyloid Theranostics with Trimeric Effects. *ACS Appl. Mater. Interfaces.* **2020**, *12*, 44180–44194.

(46) Boado, R. J.; Li, J. Y.; Nagaya, M.; Zhang, C.; Pardridge, W. M. Selective Expression of the Large Neutral Amino Acid Transporter at the Blood–Brain Barrier. *Proc. Natl. Acad. Sci. U S A* **1999**, *96* (21), 12079–12084.

(47) Pardridge, W. M. The Role of Blood-Brain Barrier Transport of Tryptophan and Other Neutral Amino Acids in the Regulation of Substrate-Limited Pathways of Brain Amino Acid Metabolism. *J Neural Transm Suppl* **1979**, No. 15, 43–54.

(48) Panda, J. J.; Kaul, A.; Kumar, S.; Alam, S.; Mishra, A. K.; Kundu, G. C.; Chauhan, V. S. Modified Dipeptide-Based Nanoparticles: Vehicles for Targeted Tumor Drug Delivery. *Nanomedicine (Lond)* **2013**, *8*, 1927–1942.

(49) Brahmachari, S.; Arnon, Z. A.; Frydman-Marom, A.; Gazit, E.; Adler-Abramovich, L. Diphenylalanine as a Reductionist Model for the Mechanistic Characterization of β-Amyloid Modulators. *ACS Nano* **2017**, *11*, 5960–5969.

(50) Zhang, J.; Zhou, X.; Yu, Q.; Yang, L.; Sun, D.; Zhou, Y.; Liu, J. Epigallocatechin-3-Gallate (EGCG)-Stabilized Selenium Nanoparticles Coated with Tet-1 Peptide to Reduce Amyloid-β Aggregation and Cytotoxicity. *ACS Appl. Mater. Interfaces.* **2014**, *6*, 8475–8487.

(51) Kour, A.; Dube, T.; Kumar, A.; Panda, J. J. Anti-Amyloidogenic and Fibril-Disaggregating Potency of the Levodopa-Functionalized Gold Nanoroses as Exemplified in a Diphenylalanine-Based Amyloid Model. *Bioconjugate Chem.* **2022**.

(52) Mehla, J.; Pahuja, M.; Gupta, Y. K. Streptozotocin-Induced Sporadic Alzheimer's Disease: Selection of Appropriate Dose. *J. Alzheimers Dis.* **2013**, *33*, 17–21.

(53) Mishra, S. K.; Singh, S.; Shukla, S.; Shukla, R. Intracerebroventricular Streptozotocin Impairs Adult Neurogenesis and Cognitive Functions via Regulating Neuroinflammation and Insulin Signaling in Adult Rats. *Neurochem. Int.* **2018**, *113*, 56–68.

(54) Singh, S.; Mishra, A.; Bharti, S.; Tiwari, V.; Singh, J.; Parul, null; Shukla, S. Glycogen Synthase Kinase-3β Regulates Equilibrium Between Neurogenesis and Gliogenesis in Rat Model of Parkinson's Disease: A Crosstalk with Wnt and Notch Signaling. *Mol. Neurobiol.* **2018**, *55*, 6500–6517.

(55) Wang, L.-S.; Zhang, M.-D.; Tao, X.; Zhou, Y.-F.; Liu, X.-M.; Pan, R.-L.; Liao, Y.-H.; Chang, Q. LC-MS/MS-Based Quantification of Tryptophan Metabolites and Neurotransmitters in the Serum and Brain of Mice. *J Chromatogr B Analyt Technol Biomed Life Sci* **2019**, *1112*, 24–32.

(56) Wiederschain, G. Y. Handbook of Biochemistry and Molecular Biology; Taylor & Francis Group: Boca Raton, FL, **2010, 1098**.

(57) Mintz, K. J.; Mercado, G.; Zhou, Y.; Ji, Y.; Hettiarachchi, S. D.; Liyanage, P. Y.; Pandey, R. R.; Chusuei, C. C.; Dallman, J.; Leblanc, R. M. Tryptophan Carbon Dots and Their Ability to Cross the Blood-Brain Barrier. *Colloids Surf. B Biointerfaces* **2019**, *176*, 488–493.

(58) Weiss, I. M.; Muth, C.; Drumm, R.; Kirchner, H. O. K. Thermal Decomposition of the Amino Acids Glycine, Cysteine, Aspartic Acid, Asparagine, Glutamic Acid, Glutamine, Arginine and Histidine. *BMC Biophysics* **2018**, *11* (1), 2.

(59) da S. Mello, G.; de P. Cardoso, A.; Oliveira, E. W. R. S.; Siqueira, A. B. Tryptophan. *J Therm Anal Calorim* **2015**, *122* (3), 1395–1401.

(60) Krebs, M. R. H.; Bromley, E. H. C.; Donald, A. M. The Binding of Thioflavin-T to Amyloid Fibrils: Localisation and Implications. *J. Struct. Biol.* **2005**, *149*, 30–37.

(61) Ow, S.-Y.; Dunstan, D. E. A Brief Overview of Amyloids and Alzheimer's Disease. *Protein Sci.* **2014**, *23*, 1315–1331.

(62) Pusey, P. N.; Tough, R. J. A. Particle Interactions. In *Dynamic Light Scattering: Applications of Photon Correlation Spectroscopy*; Pecora, R., Ed.; Springer US: Boston, MA, 1985; pp 85–179.

(63) Achuthan, S.; Chung, B. J.; Ghosh, P.; Rangachari, V.; Vaidya, A. A Modified Stokes-Einstein Equation for Aβ Aggregation. *BMC Bioinformatics* **2011**, *12*, S13.

(64) Georgalis, Y.; Starikov, E. B.; Hollenbach, B.; Lurz, R.; Scherzinger, E.; Saenger, W.; Lehrach, H.; Wanker, E. E. Huntingtin Aggregation Monitored by Dynamic Light Scattering. *PNAS* **1998**, *95*, 6118–6121.

(65) Kansy, M.; Avdeef, A.; Fischer, H. Advances in Screening for Membrane Permeability: High-Resolution PAMPA for Medicinal Chemists. *Drug Discov. Today Technol.* **2004**, *1*, 349–355.

(66) Malakoutikhah, M.; Teixidó, M.; Giralt, E. Toward an Optimal Blood−Brain Barrier Shuttle by Synthesis and Evaluation of Peptide Libraries. *J. Med. Chem.* **2008**, *51*, 4881–4889.

(67) Tsinman, O.; Tsinman, K.; Sun, N.; Avdeef, A. Physicochemical Selectivity of the BBB Microenvironment Governing Passive Diffusion--Matching with a Porcine Brain Lipid Extract Artificial Membrane Permeability Model. *Pharm. Res.* **2011**, *28*, 337–363.

(68) Kuragano, M.; Yamashita, R.; Chikai, Y.; Kitamura, R.; Tokuraku, K. Three-Dimensional Real Time Imaging of Amyloid β Aggregation on Living Cells. *Sci. Rep.* **2020**, *10*, 9742.

(69) Yin, T.; Yang, L.; Liu, Y.; Zhou, X.; Sun, J.; Liu, J. Sialic Acid (SA)-Modified Selenium Nanoparticles Coated with a High Blood-Brain Barrier Permeability Peptide-B6 Peptide for Potential Use in Alzheimer's Disease. *Acta Biomater.* **2015**, *25*, 172–183.

(70) Samanta, S.; Rajasekhar, K.; Ramesh, M.; Murugan, N. A.; Alam, S.; Shah, D.; Clement, J. P.; Govindaraju, T. Naphthalene Monoimide Derivative Ameliorates Amyloid Burden and Cognitive Decline in a Transgenic Mouse Model of Alzheimer's Disease. *Advanced Therapeutics* **2021**, *4* (4), 2000225.

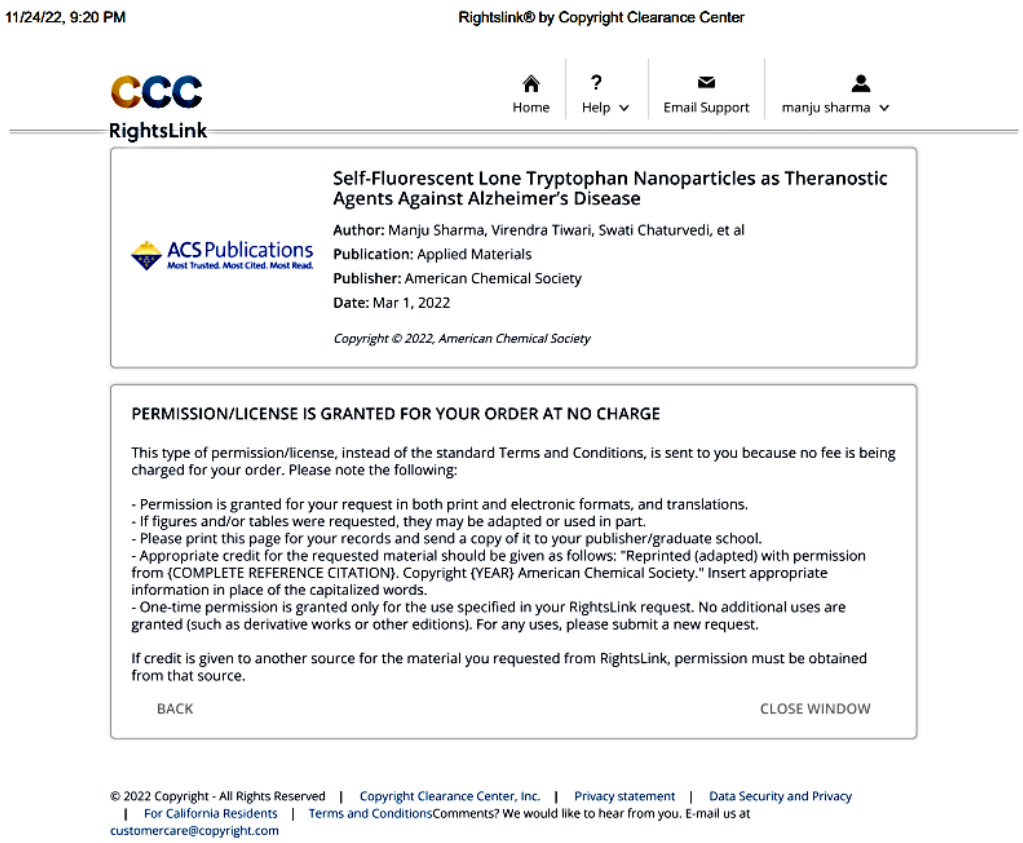

11/24/22, 9:20 PM Rightslink® by Copyright Clearance Center

CCC RightsLink

Home | Help | Email Support | manju sharma

Self-Fluorescent Lone Tryptophan Nanoparticles as Theranostic Agents Against Alzheimer's Disease

Author: Manju Sharma, Virendra Tiwari, Swati Chaturvedi, et al

Publication: Applied Materials

Publisher: American Chemical Society

Date: Mar 1, 2022

Copyright © 2022, American Chemical Society

ACS Publications
Most Trusted. Most Cited. Most Read.

PERMISSION/LICENSE IS GRANTED FOR YOUR ORDER AT NO CHARGE

This type of permission/license, instead of the standard Terms and Conditions, is sent to you because no fee is being charged for your order. Please note the following:

- Permission is granted for your request in both print and electronic formats, and translations.
- If figures and/or tables were requested, they may be adapted or used in part.
- Please print this page for your records and send a copy of it to your publisher/graduate school.
- Appropriate credit for the requested material should be given as follows: "Reprinted (adapted) with permission from {COMPLETE REFERENCE CITATION}. Copyright {YEAR} American Chemical Society." Insert appropriate information in place of the capitalized words.
- One-time permission is granted only for the use specified in your RightsLink request. No additional uses are granted (such as derivative works or other editions). For any uses, please submit a new request.

If credit is given to another source for the material you requested from RightsLink, permission must be obtained from that source.

BACK CLOSE WINDOW

CHAPTER 3

FLUORESCENT DOPAMINE-TRYPTOPHAN NANOCOMPOSITES AS DUAL IMAGING AND ANTI-AGGREGATION AGENTS: NEW GENERATION OF AMYLOID THERANOSTICS WITH TRIMERIC EFFECTS

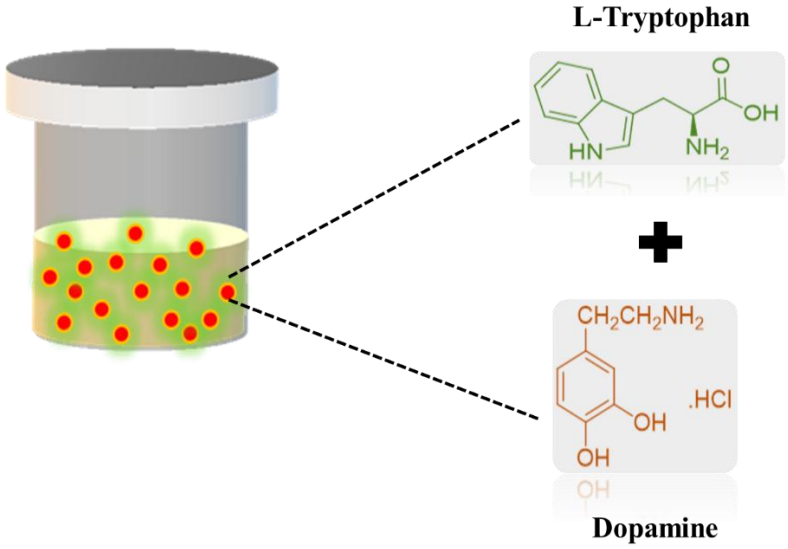

FLUORESCENT DOPAMINE-TRYPTOPHAN NANOCOMPOSITES AS DUAL IMAGING AND ANTI-AGGREGATION AGENTS: NEW GENERATION OF AMYLOID THERANOSTICS WITH TRIMERIC EFFECTS

Abstract:

The aggregation of neurotoxic amyloid-β (Aβ) polypeptides into aberrant extracellular senile plaques is the major neuropathological hallmark of Alzheimer's disease (AD). Inhibiting aggregation of these peptides to control the progression of this deadly disease can serve as a viable therapeutic option. Moving a step ahead in the direction of finding a potent anti-AD therapeutics, in this chapter, we developed inherently fluorescent theranostic dopamine tryptophan-nanocomposites (DTNPs) and investigated their amyloid inhibition propensity along with their ability to act as a cellular bioimaging agent in neuronal cells. The anti-aggregation potency of the nanocomposites was further investigated against an in vitro established reductionist amyloid aggregation model consisting of a mere dipeptide, phenylalanine-phenylalanine (FF). As opposed to large peptide/protein derived robust and high molecular weight amyloid aggregation models of Alzheimer's disease our dipeptide based amyloid model provides an edge over others in terms of the ease of handling, synthesis and cost-effectiveness. Results demonstrated positive anti-aggregation behaviour of the DTNPs towards both FF derived amyloid fibrils and preformed Aβ-peptide fibers by means of electron microscopic and circular dichroism-based studies. Our results further pointed towards the neuroprotective effects of the DTNPs in neuroblastoma cells against FF amyloid fibrils induced toxicity and also significantly suppressed the accumulation of Aβ42 oligomers in both cortex and hippocampus regions and improved cognitive impairment in intracerebroventricular streptozotocin (ICV-STZ) induced animal model of dementia. Besides, DTNPs also exhibited excellent fluorescent properties and light up the cytoplasm of neuroblastoma cells when being co-incubated with cells confirming their ability to serve as an-intracellular bioimaging agent. Overall, these results signify the potency of the DTNPs as promising multifunctional theranostic agents for treating AD.

3.1. Introduction:

Despite many years of intensive research, the available anti-AD drugs targeting in situ Aβ -processing and subsequent aggregation have not gained much success due to their physicochemical nature, limited ability to pass across the blood-brain barrier (BBB), and low bioavailability in the central nervous system (CNS).[1] Thus, there is an unmet need to unearth viable approaches capable of aiding the transport of potent anti-AD therapeutic molecules across the BBB, to treat and reduce the AD-associated features and morbidity. Nanotechnology-based approaches have recently gained considerable attention not only for ferrying potent molecules to the CNS across the BBB but also as efficient brain imaging agents.[2-5] Various nanoparticle (NP) formulations which were commonly used in AD diagnosis and therapy include inorganic NPs, polymeric NPs, protein-based NPs, and carbonaceous nanostructures.[6] Further, various fluorescent nanostructures based on π-conjugated, self-assembled oligomers have been rated to be suitable for theranostic applications in many cases based on their unique photo-physical properties and drug loading capabilities. They possessed well-defined shape and sizes, attained stable architectures in an aqueous environment and sometimes boosted fluorescence quantum yield as well.[7] Thus, NPs carrying inherent theranostic features can offer rapid, real-time and sensitive diagnosis, as well as therapeutic platforms for AD and of late, considerable efforts are being directed towards developing suitable nanotheranostics for AD.

Stepping forward in this direction, in the current study, we tried to develop a multimodal nanotheranostic platform composed of dopamine (DA) and tryptophan by following simple hydrothermal reaction. Dopamine is a vital catecholamine and its secretion in brain plays important roles such as motor control, arousal, cognition, motivation and reward, L-tryptophan is an essential amino acid which has an indole framework and is a precursor of 5-hydroxytryptamine **(**5-HT), an important neurotransmitter which has been reported to

regulate cognitive functions of body. Remarkably, neuroprotective role of tryptophan has been noticed in AD mouse model where intra-neuronal Aβ accumulation was reduced after increased dietary intake of tryptophan.[8] Tryptophan further exhibited beneficial effects on reactive memory in an experimental AD animal model of depression.[9] Dopamine has been shown to exhibit anti-amyloid and fibril disaggregation effects[10] and L-tryptophan also exhibits Aβ-disaggregation properties.[11] Though individually both the molecules exhibited anti-AD effect. However, no study explored their role in combination as an anti-AD drug. Moreover, the role of fluorescent DTNPs as imaging modalities relevant to AD is yet unexplored. Herein, DTNPs were further designed with the added notion of achieving inherent BBB penetration. Tryptophan is an essential amino acid, can pass across the BBB via LAT1 transporters and hence, presence of tryptophan in the nanostructure would impart the nanocomposite with the ability to traverse through the BBB[12,13] This would confiscate the need for additional surface conjugations of the nanocarriers with BBB targeting ligands, which often possess low-yield reactions, and exhibit lesser efficacy in ferrying and delivering adequate quantities of the drugs to brain. Overall, our designed single smart nanocomposite system carrying triple advantages (a) amyloid recognition and binding capacity owing to the aromatic moieties specifically tryptophan and (b) Aβ-polypeptide fibril disaggregation propensity contributed by both the presence of tryptophan and dopamine, (c) inherent BBB permeability by means of tryptophan.

By now, it is well-known that amyloid fibril like assemblies or the early aggregation intermediates of Aβ polypeptide (1-42) are the main pathological determinants in AD.[14,15] However, laborious isolation and purification process of these amyloid-β peptides many a times raise a concern on their role as an ideal in vitro model for performing various preliminary in vitro screening studies of the potential Aβ-aggregation inhibitors.[16] Hence, identifying an alternative, easy to perform small peptide based, platform devoid of the

challenges of tedious protein expression and purification steps that could parallelly mimic amyloid aggregation mechanism and generate reproducible results is of utmost importance. Recently, short amyloidogenic peptide-based models have gained significant attention and have utterly revolutionized the understanding of amyloid formation mechanisms. These short peptide residues contain all the essential molecular and structural information needed for the formation of amyloid fibrils.[17] In 1990, Westermark and co-workers reported about the first short peptide based system, a decapeptide of islet amyloid polypeptide (IAPP) that can form similar kind of amyloid fibrils as generated by the typical full length polypeptide,[18] Similarly, a six amino acid long human IAPP fragment was shown to form highly similar structural and functional amyloid fibrillar assemblies as generated by native 37 amino acid long, full length polypeptide.[19] Later studies from Tycko group had also revealed that a seven amino acid long fragment (*KLVFFAE*) of Aβ polypeptide, formed discrete and well-ordered amyloid assemblies.[20] Interestingly, Gazit and group reported about the smallest amyloidogenic dipeptide fragment phenylalanine-phenylalanine (FF), a core (F19-F20) motif of the 42 amino acid long, Aβ polypeptide as a reductionist model of Aβ polypeptide aggregation which demonstrated excellent ability to form the characteristic amyloid fibrillar assemblies and eventually led to the formation of the plaques.[21]

Thus, in this chapter, we also tried to use FF dipeptide as a reductionist model for establishing Aβ polypeptide aggregation in vitro and further used it to test the potency of DTNPs as potential amyloid inhibitors (**Scheme 3.1**). Further, results obtained with the in vitro dipeptide amyloid model was escalated to the Aβ polypeptide aggregation model. The simplicity of the dipeptide, ease of synthesis and comparatively low cost provides it with many cutting edges over other protein and peptide-based AD models and would definitely make it a researcher's choice in near future. Moreover, the neuroprotective effect of DTNPs both in neuroblastoma cells and in intracerebroventricular streptozotocin (ICV-STZ) animal

model of dementia was also investigated. Our results demonstrate that the DTNPs could act as potential amyloid inhibitors and based on their inherent fluorescent and biocompatible nature as well as the ability to interact with FF tubes, DTNPs can contribute towards AD imaging and diagnosis.

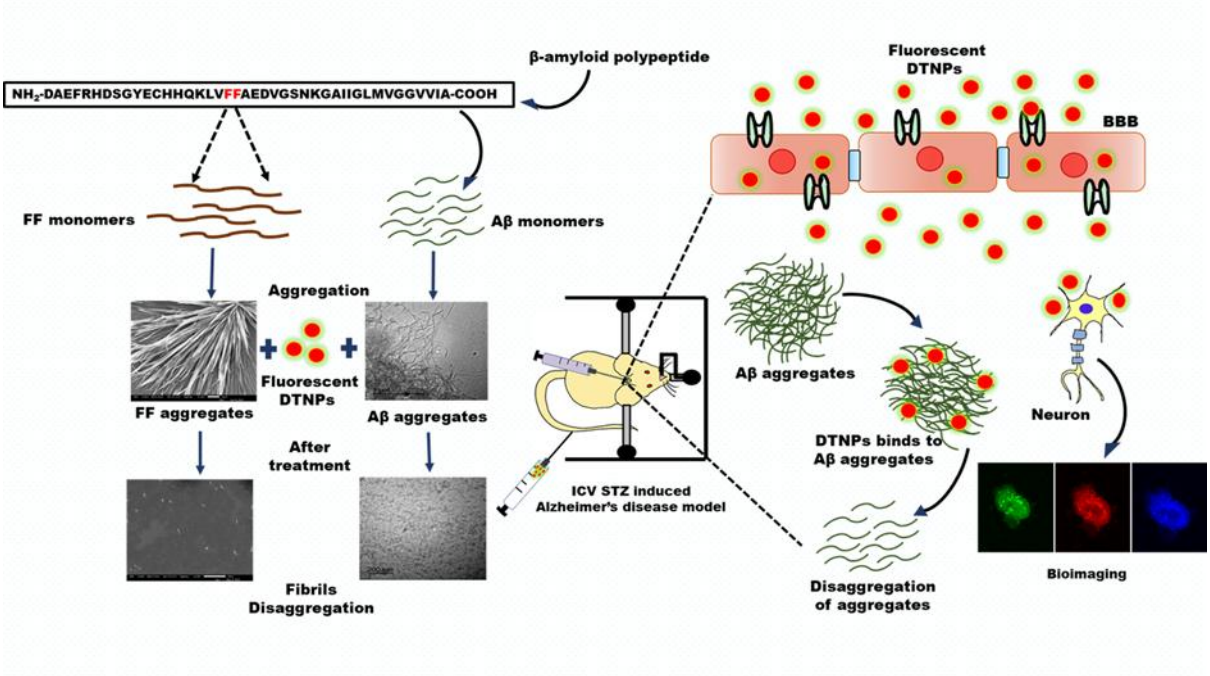

Scheme 3.1: Overall scheme showing self-fluorescent dopamine tryptophan nanocomposites as anti-amyloid theranostic inhibitor and biocompatible neural cell imaging agent for early diagnosis and therapy of AD.

3.2. Materials and Methods:

3.2.1. Materials:

Boc-Phe-OH, L-phenylalanine, isobutyl chloroformate, N-methyl morpholine, sodium chloride, sodium hydroxide, tetrahydrofuran, sodium sulfate, sodium acetate, acetic anhydride, sodium bicarbonate, citric acid, L-tryptophan, 3-(4,5-Dimethyl-2-thiazolyl)-2,5-diphenyltetrazolium bromide (MTT), fluorescein-5-isothiocyanate and 3-hydroxytyramine hydrochloride (Dopamine Hydrochloride) were purchased from TCI Chemicals, Sisco Research Laboratories and HiMedia Laboratories Pvt. Ltd., India. Methanol (MeOH), dichloromethane (DCM), thioflavin-T (ThT), 4′,6-diamidino-2-phenylindole (DAPI),

1,1,1,3,3,3-Hexafluro-2-propanol, quinine hemisulfate salt monohydrate, curcumin and Aβ (1-42) were purchased from Sigma Aldrich Munich Germany.

3.2.2. Synthesis of the dipeptide (FF):

Synthesis of the dipeptide (FF), was performed by solution phase peptide synthesis methods as discussed earlier [22,23] and as also briefly described in the previous chapter.

3.2.3. Synthesis of fluorescent dopamine tryptophan nanoparticles:

The synthesis was initiated by dissolving equal molar ratio of both dopamine salt (20 mM) and L-tryptophan (20 mM) in 10 ml de-ionized (DI) water. The prepared clear solution was then poured into a 25 ml Teflon hydrothermal container and was heated for 2 h at 200 degrees Celsius. After 2h, light orange coloured solution was formed which was then centrifuged for 30 minutes at 14000 rpm (three times) to get rid of debris and obtain pure fluorescent NPs.

3.2.4. UV-Vis spectroscopy of DTNPs:

UV-Visible spectrophotometry was performed to investigate the spectral properties of DTNPs, using a double beam Shimadzu UV-2600 Spectrophotometer. The aqueous solution of DTNPs (1mg/ml) were taken in a cuvette and diluted according to the requirement before carrying out the measurements.

3.2.5. Dynamic light scattering (DLS) analysis of DTNPs:

Hydrodynamic size distribution and the polydispersity index (PDI) of the synthesized nanoparticles were evaluated using dynamic light scattering (DLS) technique which is also called Quasi Elastic Light Scattering (Zetasizer Nano ZSP; Model-ZEN5600; Malvern Instruments Ltd, Worcestershire, UK). The samples were taken in disposable polystyrene cuvettes (Model-DTS0012; Malvern) for measurements. All readings were recorded at an angle of 173^{o}, at room temperature.

3.2.6. Attenuated total reflection-Fourier transform infrared (ATR-FTIR) spectroscopic analysis of DTNPs:

ATR-FTIR spectra of liquid sample of DTNPs (1mg/ml) were recorded on a Bruker VERTEX70 instrument with 20 scans over a range of 4000 − 400 cm^{-1}. Milli Q water was taken for background subtraction.

3.2.7. Atomic force microscopy (AFM) analysis of DTNPs:

The surface morphology of DTNPs were determined by using atomic force microscopy. DTNPs solution (100 μg/ml) was drop casted on to freshly cleaved silicon chip and then kept for 4-5 min at room temperature. Afterward, the silicon chip was rinsed with Milli Q water (50 μl, Millipore) and air-dried before imaging. AFM images were taken with a Bruker Nanoscope-V in tapping mode under ambient conditions.

3.2.8. Determination of photostability of DTNPs:

The photostability of DTNPs suspension in water was tested by exposing them to UV light at 365 nm [24-26] for 30 minutes at room temperature and their fluorescence emission spectra was recorded (390-600 nm) after every 5 minutes using a fluorimeter (FS5 Spectrofluorometer). Photostability of other commercial dyes like fluorescein isothiocyanate (FITC) and biometabolite like curcumin were also determined for drawing a comparison between DTNPs and these fluorophores. For photostability experiments FITC and curcumin were also exposed with 365 nm UV light for 30 minutes and their fluorescence spectra were recorded (390-600 nm) after every 5 minutes.

3.2.9. Determination of the quantum yield (QY) of the DTNPs:

Quantum yield (QY) of DTNPs was determined as per earlier reported method.[24] Quinine sulfate (in 0.1 M H_2SO_4) was chosen as the standard sample (with the reported QY of 54%) as this has been used as a standard for determining the QY of other polydopamine

nanoparticles.[24,25] The optical densities of both standard and sample (OD value between 0.01 and 0.1 nm) were measured at an excitation wavelength 350 nm by using a double beam Shimadzu UV-2600 spectrophotometer and their photoluminescence (PL) emission spectra (380-700 nm) were also recorded at an excitation of 350 nm by using a fluorimeter. Absolute value of QY of the DTNPs was calculated as per following equation:

$$QYs = QY_R \frac{I_S}{I_R} \frac{A_R}{A_S} \frac{n_S^2}{n_R^2}$$

Where subscripts S and R represent sample and reference, QY denotes the quantum yield, I represent the integrated fluorescence intensity, A is the optical density of the fluorophore at λex, n denotes the solvent refractive index.

3.2.10. Formation of fibrillar aggregates of the dipeptide FF:

FF fibres were formed at a concentration of 4 mg/ml, following a protocol mentioned earlier with little modification.[27,21] Typically, 4 mg FF was dissolved in 50 µl of HFIP to remove any preformed aggregated fibrils before the initiation of self-assembly and the sample was diluted to 4 mg/ml in ddH_2O to obtain the fibrils.

3.2.11. Establishment of amyloid-β polypeptide 1-42 (Aβ) aggregation in vitro:

Aβ (1-42) peptide fibrils were prepared as detailed in the literature.[28,29] In brief, powdered Aβ peptide was first monomerized by dissolving it in HFIP at a concentration of 1 mg/ml. Further, the prepared solution was mixed on a shaker for 2 h at 4 °C for proper dissolution of the polypeptide. Before the initiation of fibrillogenesis, HFIP was evaporated on a SpeedVac and a dried and thin clear film of Aβ peptide was obtained. The thin film of peptide was then dissolved in phosphate-buffered saline (PBS; 10 mM, pH 7.4) and briefly sonicated for 1 min. To induce aggregation and formation of fibrils, the Aβ polypeptide solution was kept in incubation at 37 °C for 3 days to obtain higher fibril concentration.

3.2.12. Thioflavin T (ThT) assay to confirm the aggregation and the fibrillization potential of the dipeptide and Aβ-polypeptide:

Thioflavin T dye can selectively bind to matured aggregated protein/peptide fibrils to exhibit an enhancement in its fluorescence intensity and can be used to confirm amyloidogenesis of proteins or peptides.[30] ThT assay was thus performed to check and confirm FF and Aβ-peptide aggregation. FF and Aβ-polypeptide fibrils of different concentrations were prepared as described above. Preformed FF fibrils/ Aβ fibrils were incubated with 20 µM ThT at varying concentrations to monitor their aggregation behaviour. ThT fluorescence excitation at 450 nm and emission at 490 nm was recorded via a multimode plate reader (MPlex 200 pro, Tecan) to study the peptide aggregation.

3.2.13. Scanning electron microscopic (SEM) studies:

Scanning electron microscopy was used to examine morphological details of DTNPs, aggregated amyloid assemblies of FF and subsequent disaggregation of the FF amyloid assemblies by DTNPs. Neat FF fibrils were formed as described above. For disaggregation studies, 100 µl (400 µg) of preformed fibrils of FF (4mg/ml) were incubated with 100 µl of DTNPs solution (100 µg/ml) for different incubation periods (24, 48 and 72 h) at room temperature on a rotary shaker. After incubation, aliquots of 50 µl of each sample were drop casted on cleaned silicon wafers and then air-dried overnight at room temperature following which they were coated with gold before carrying out SEM imaging on a scanning electron microscope (JEOL JEM SEM, Tokyo, Japan).

3.2.14. Laser scanning confocal microscopic studies:

A Zeiss confocal microscope (ZEISS LSM 880 with Airyscan) was employed to further examine FF fibrilization and to ascertain disaggregation potency of DTNPs towards FF fibrils. In order to aid visualization, FF fibrils were first stained with FITC by incubating preformed fibrils (4mg/ml) with 200 µl of FITC (2.5 mg/ml in DMSO) for 1h at room

temperature. After incubation, fibrils were centrifuged and dispersed in water. After FITC staining, 100 µl (400 µg) of prestained fibrils of FF (4mg/ml) were incubated with 100 µl of DTNPs solution (100 µl/ml) for 24, 48 and 72 h at room temperature on a rotary shaker. After 24-72 h of incubation, confocal microscopic images of samples were obtained in the green channel under a laser scanning confocal microscope.

3.2.15. Circular dichroism (CD) of DTNPs treated FF samples:

The secondary structure of FF peptide aggregates was also investigated using CD. FF fibrils were first formed as described above and CD spectra were taken after a dilution of FF stock solution (4mg/ml) to final concentration of 0.04 mg/ml in ddH_2O. For fibril disaggregation assay, preformed peptide aggregates of FF (4 mg/ml) were incubated with DTNPs (100 µg/ml) for 24 h, 48 and 72 h. CD spectra were recorded after diluting all incubated samples to a final concentration of 0.04 mg/ml in the range of 190-290 nm on a JASCO J-1500 CD spectropolarimeter.

3.2.16. Cellular uptake study of DTNPs in SH-SY5Y cells:

SH-SY5Y cells were cultured using DMEM/F12 media supplemented with 10% heat-inactivated fetal bovine serum (FBS), and 1% antibiotics (penicillin/streptomycin) in a 5% CO_2 humidified incubator maintained at 37 °C. Cells were trypsinized at 80% confluency and seeded (20,000 cells) onto 35 mm confocal dishes. Thereafter, cells were incubated for 24 h for spreading and adherence. After incubation, cell culture media were exchanged with serum excluded media containing DTNPs (100 µg/mL) and kept overnight at 37ºC in a 5% CO_2 humidified incubator. After treatment, cells were washed with PBS (three times) and subsequently fixed using 4% (v/v) paraformaldehyde for 10-20 min. Following PBS washes, cells were stained with DAPI (1 µg/ml) for 5 min and washed with chilled PBS (4 °C) thoroughly to remove extra stains. Afterward, confocal dishes were observed under Zeiss

confocal microscope (ZEISS LSM 880 with Airyscan). Cellular uptake images of DTNPs in SH-SY5Y cells were captured and processed using ZEN software.

3.2.17. Cytotoxicity assay of FF aggregates in SH-SY5Y cells:

SH-SY5Y cells (8×10^3 cells/well) were plated in microtiter plates and grown overnight for proper cell adhesion. Cells were then exposed to different concentrations of FF fibrils (4 mM to 12 mM) dispersed in serum free DMEM/F12 media for 24, 48 and 72 h at 37°C. Wells carrying untreated cells were taken as control. After treatment, cell viability was tested by MTT (3-[4,5-dimethylthiazol-3-yl]-2,5-diphenyltetrazolium bromide) assay. For the assay, 20 µl of MTT (from 5 mg/ml solution in PBS) and 180 µl of fresh media was added to each well and kept for 4 h 37°C. Afterward, the medium was discarded and replaced by 100 µl of DMSO. Finally, formazan crystals were dissolved in DMSO and color intensity of the solution was measured using a microplate reader (MPlex Pro 200, Tecan. Ltd.) at 570 nm.

3.2.18. Evaluation of cytotoxicity of FF aggregates towards SH-SY5Y cells when being co-incubated with DTNPs:

SH-SY5Y cells were cultured in 96-well sterile microtiter plates at a density of 8×10^3 cells/ml in complete media and incubated overnight at 37°C. After incubation, cells were incubated with FF aggregates (12 mM dissolved in serum free media) in the presence and absence of various concentrations of DTNPs (100 µg/ml, 300 µg/ml and 500 µg/ml) for different time points (24 h, 48 h, 72 h). Wells carrying untreated cells and incubated with neat media were taken as control. After appropriate incubation time, media were discarded and replaced by 180 µl of fresh media along with 20 µl of MTT (5 mg/ml solution in PBS), and cells were further kept for 4 h incubation at 37 ◦C. Afterward, the media were discarded and 100 µl of DMSO was added to each well to dissolve the formazan crystals. Later, the absorbance was taken at 570 nm using a microplate reader (MPlex Pro 200, Tecan. Ltd.).

3.2.19. Aβ-polypeptide fibril disaggregation assay:

For carrying out Aβ-polypeptide fibril disaggregation study, prepared Aβ-peptide solution in PBS (10 mM, pH 7.4) was kept in incubation at 37 °C for 3 days to obtain enough quantity of amyloid fibrils. DTNPs (50 µg/ml) were added to the preformed Aβ-peptide fibril solutions (20 µM) and incubated for 24, 48 and 72 h. After 24−72 h of incubation periods, samples were drop casted on 200 nm mesh sized carbon coated copper grids and analysed by TEM.

3.2.20. Transmission electron microscopic (TEM) studies:

Transmission electron microscopic analysis was carried out to image the preformed Aβ-peptide fibrils and to investigate the disaggregation process of preformed Aβ fibrils (20 µM) by DTNPs (50 µg/ml). Samples were kept for 24, 48 and 72 h incubations and aliquots of 10 µl were drop casted on 200 nm mesh sized carbon-coated copper grids for 5 min. After 5 min. excess samples were removed followed by rinsing the grids with Milli Q water and subsequent negative staining was carried out with 2% w/v aqueous uranyl acetate solution. Overnight air -dried samples were next examined using JEOL JEM-2100 transmission electron microscope with a tungsten filament at 120 kV (Tokyo, Japan).

3.2.21. In vivo assessment of DTNPs efficacy in rat model with ICV-STZ administration induced memory deficits:

3.2.21.1. Stereotaxic injection of streptozotocin (STZ):

Adult male SD rats were anaesthetized using pentobarbitone sodium (40 mg/kg, *i.p.*) obtained from Sigma-Aldrich USA, followed by fixation in a stereotaxic apparatus (Stoelting Co. USA). Bregma was carefully located, a small burr hole was made using a drill and 10 µl of STZ (1 mg/kg solubilized in artificial cerebrospinal fluid; aCSF) was infused in each lateral ventricle following the coordinates -0.8 mm anteroposterior (AP), ±1.5 mediolateral (ML), -3.6mm dorsoventrally (DV) from bregma using Hamilton syringe (Hamilton company, Switzerland) at a rate of 0.5 µl/min.[31,32] Post-injection, needle was kept at the same place for

5 min to minimize backflow and for complete diffusion. Control group received equal volume of aCSF in lateral ventricles.

3.2.21.2. DTNPs nanocomposite treatment:

Rats were divided into 4 groups randomly each consisting of 5 rats and the time schedule of STZ and DTNPs treatments in rats were represented in **Scheme 3.2**.

Group I: Rats were stereotaxically administered with 10 µl of aCSF in both the lateral ventricle and served as vehicle control group.

Group II: Rats were stereotaxically administered with 10 µl of STZ in each ventricle (1 mg/kg) and assigned as STZ toxin treated rats.

Group III: Rats were stereotaxically administered with 10 µl of STZ in each ventricle (1 mg/kg) and infused with 5 mg/kg (i.v.) of DTNPs 7-day post STZ administration till 21 days on every alternate day.

Group IV: Rats were injected with 5 mg/kg (i.v.) of DTNPs for 21 days on every alternate day and treatment was done parallely with Group III.

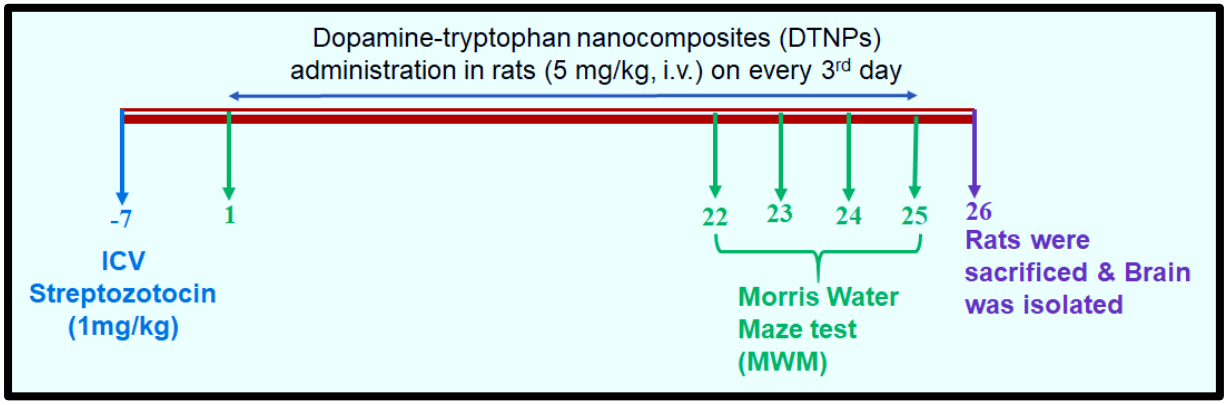

Scheme 3.2: Schematic depiction of study design of in-vivo experiments in rats.

3.2.21.3. Morris Water maze test:

Morris Water Maze (MWM) test was carried out to assess the spatial learning and memory functional alterations, following the method described previously with few minor modifications.[31,32] Briefly, after 3 weeks of STZ lesioning, the rats were trained three times a day in MWM apparatus for three consecutive days/sessions to evaluate the normal cognitive

functions, followed by the probe trial after the last session of training. MWM apparatus contains a black pool (1.32 m diameter and 75 cm height) filled with water maintained at 25 ±2°C temperature. Thereafter, the pool was hypothetically separated into four equal quadrants with a black platform inundated 1 cm below the surface of water at the center of the pre-decided quadrant. Normal learning and memory activities were performed with the rats by carrying out three trials in one session (1, 2, 3 & 4 day), 2 min each. Each trial performed was supposed to be completed when either the animal reached the submerged black platform within 2 min or animals were directed to the platform and allowed to rest for 20 s between each trial. Each test trial was performed to examine learning and memory deficits pre and post exposure to the nanoparticle administration. Behavioral activities of treated rats were captured by a video camera placed above the centre position of the pool and the data was accordingly plotted. The time and distance required to reach the platform position was drawn and calculated in the form of latency time period and the mean path length using ANY-maze video tracking software (ver. 4.73; Stoelting, USA). After carrying out the last session of the training, the platform was taken out from the pool and the probe trial was performed for confirmation of memory retention of animals. The time spent by animals in the target quadrant was calculated using the same software.

3.2.21.4. Immunohistochemical Analysis:

Animals were euthanized by administering sodium pentobarbital (50 mg/kg, *i.p.*) injection and slowly perfused with chilled PBS followed by 4% paraformaldehyde (PFA). Whole brain was extracted and preserved in PFA overnight at 4^0 C, followed by serial dehydration in different concentrations of sucrose (10%, 20%, 30%) for next 3 days. Sections (30 µm thick) encompassing pre-frontal cortex and hippocampus were cut by using cryostat (Thermo Scientific, USA) and free-floating sections were processed for immunohistochemical analysis as described previously.[33] In brief, sections were rinsed with tris buffered saline (TBS) and permeabilization was done by tris buffered saline-Tween 20 (TBST) at normal room temperature and subsequently washing with TBS. Further, to block the nonspecific sites,

sections were blocked with 5% bovine serum albumin (BSA) in TBST for 2 h at room temperature and then incubated with primary antibodies, mouse anti-Aβ (1:500, Millipore, CA, USA). After incubation with primary antibody, sections were rinsed thrice with TBS followed by incubation with anti-mouse Alexa Fluor-594 (Invitrogen, Carlsbad, CA, USA) for 2 h in dark at room temperature. Sections were put on glass slides and incubated with DAPI mounting medium (Sigma Aldrich, USA). An unbiased oligomer quantification method was performed using a 20X objective (total magnification X200) in every third section approximately apart by 120 μm in 1/4 series with a total of four to five sections per rat. Total images for number of Aβ oligomers present were taken by using 20X objective and were analysed by using ImageJ software (NIH). Immunofluorescence was determined separately for each section and averaged for each rat in the cortex or hippocampus region. For quantitative evaluation of immunofluorescence of Aβ oligomers in both cortex and hippocampus region, images of sections were taken in similar settings using 20X objective and analyzed with ImageJ software (NIH) by using a rectangular region of interest (ROI) across the whole image. Mean fluorescence intensity (MFI) was calculated across the ROI. Next, net fluorescent intensity was calculated by subtracting the background intensity from the mean intensity of the selected area, and the the result was represented in terms of arbitrary unit (AU).

3.2.21.5. Statistical analysis:

Statistical analysis was done by using GraphPad Prism software and the data is presented as mean ± SD. One-way analysis of variance (ANOVA) followed by Bonferroni post hoc test and Tukey's multiple comparison was used to compare and calculate the significant difference between the mean values of subgroups. Behavioural significance was measured by two way-ANOVA considering training session as repeated measures of experimentation. $p<0.05$ was considered to be statistically significant.

3.3. Results and Discussion:

3.3.1. Synthesis and characterization of DTNPs:

The fluorescent dopamine tryptophan nanostructures were synthesized via simple hydrothermal method as shown in **Scheme 3.3** and characterized using various biophysical techniques as shown in **Figure 3.1**. DLS results exhibited the mean particle diameter of the NPs to be around 141.7 nm ± 46 nm (SD) with a PDI of 0.09 (**Figure 3.1 A**). Next, the UV-visible absorption spectrum of the DTNPs exhibited two absorption peaks, one at 220 nm corresponding to π- π* transitions due to aromatic groups and another at 280 nm corresponding to n- π* transitions for C=O (**Figure 3.1 B**). The major peak at 280 nm directly indicates the presence of tryptophan in the nanocomposite.[34]

Further, ATR-FTIR spectroscopy was carried out to investigate the possible molecular structure of the DTNPs. The ATR-FTIR spectra of DTNPs exhibited two characteristic major IR peaks, one at 1625 cm^{-1} was due to C=C stretching vibrations and another broad IR band spanning from 3100-3500 cm^{-1} was attributed to O–H stretching vibrations (**Figure 3.1C**). Our ATR-FTIR result of DTNPs was well consistent with earlier reported literature.[35-38]

The morphological and topological analysis of prepared DTNPs were next evaluated by using both SEM and AFM studies. SEM images of the DTNPs clearly demonstrated the formation of uniform sized monodispersed spherical structures with average particle size of 118 nm (**Figure 3.1D**). Further, surface topological analysis of DTNPs was also investigated by using AFM. Similar sphere shaped and densely populated nanoparticles of an average particle size of 73 nm were observed in AFM. (**Figure 3.1 E**). Furthermore, fluorescence spectroscopy was also carried out for the synthesized DTNPs. To do so, particles were excited at different wavelengths and the emission fluorescence spectra of DTNPs were obtained. It was noticed that the fluorescent DTNPs showed diversity in emitted fluorescence intensities when the excitation wavelength of DTNPs changed from 340 to 460 nm, showing its maximum fluorescence intensity when the particles were excited by light with a wavelength of 360 nm (**Figure 3.1F**). Shifts in the emission wavelengths were also observed depending on the

excitation wavelengths. It was observed that the particles were capable of generating fluorescence falling in different regions of the visible spectrum, the most prominent being in the blue, red and green region. The tremendous diversity of red, green and blue fluorescence of DTNPs were also observed by drop casting them on a glass slide followed by imaging on a confocal microscope. Brightly colored particles with blue, green and red fluorescence were observed (**Figures 3.1 G to I**).

The photostability of any nanocomposite can be a major concern in realizing its potential application in the field of bioimaging. Herein, we compared the photostability of DTNPs with a popular commercial fluorophore, FITC and a fluorescent biometabolite, curcumin. We exposed DTNPs, FITC and curcumin with 365 nm excitation light continuously at room temperature for 30 min and their fluorescence emission spectra were recorded after every 5 min. As shown in **Figure 3.1 J**, curcumin showed significant photobleaching within 5 min of excitation and retained only 50% of the initial fluorescence intensity. Fluorescence intensity of FITC also demonstrated a sharp decline within 15 min after being continuously irradiated at 365 nm and retained only 60 % of its initial fluorescence intensity. In contrast, DTNPs showed no significant change in the fluorescence behaviour and preserved more than 90% of their initial fluorescence intensity over a period of 20 min under continuous irradiation at 365 nm which clearly depicts their outstanding photoluminescence nature. Quantum yield, which is a measure of a molecule's photon emission efficiency, is an important fluorophore property.[39,40] Thus, we tried to determine the QY of the DTNPs and compared it with other biometabolite like curcumin. The quantum yields of DTNPs and curcumin were found to be 23.7% and 2.5% using quinine sulphate as a standard respectively. Thus, DTNPs exhibited around 9 fold higher QY than curcumin. Notably, DTNPs also showed higher QY as compared to other reported fluorescent polydopamine based nanoparticles,[24,41,42] organic carbon dots,[43,44] and their QY is even comparable to many other fluorescent biometabolites.[45-47]

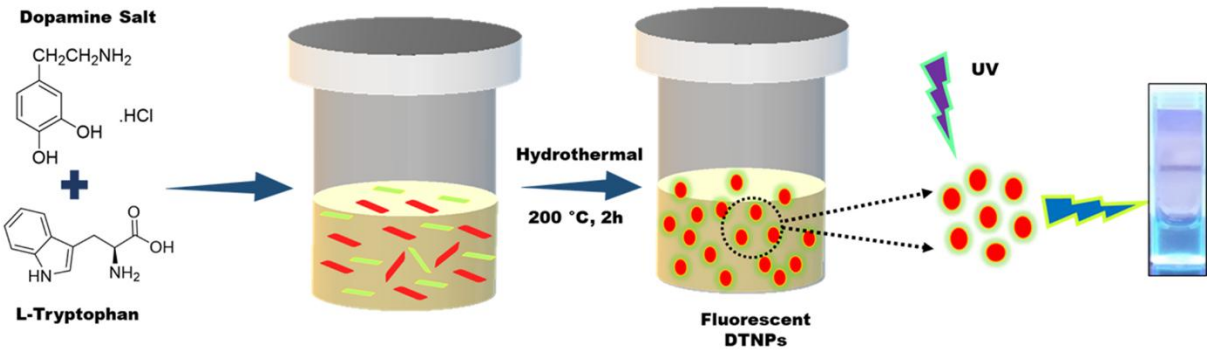

Scheme 3.3: Overall scheme showing hydrothermal synthesis of self-fluorescent dopamine tryptophan nanocomposites (DTNPs).

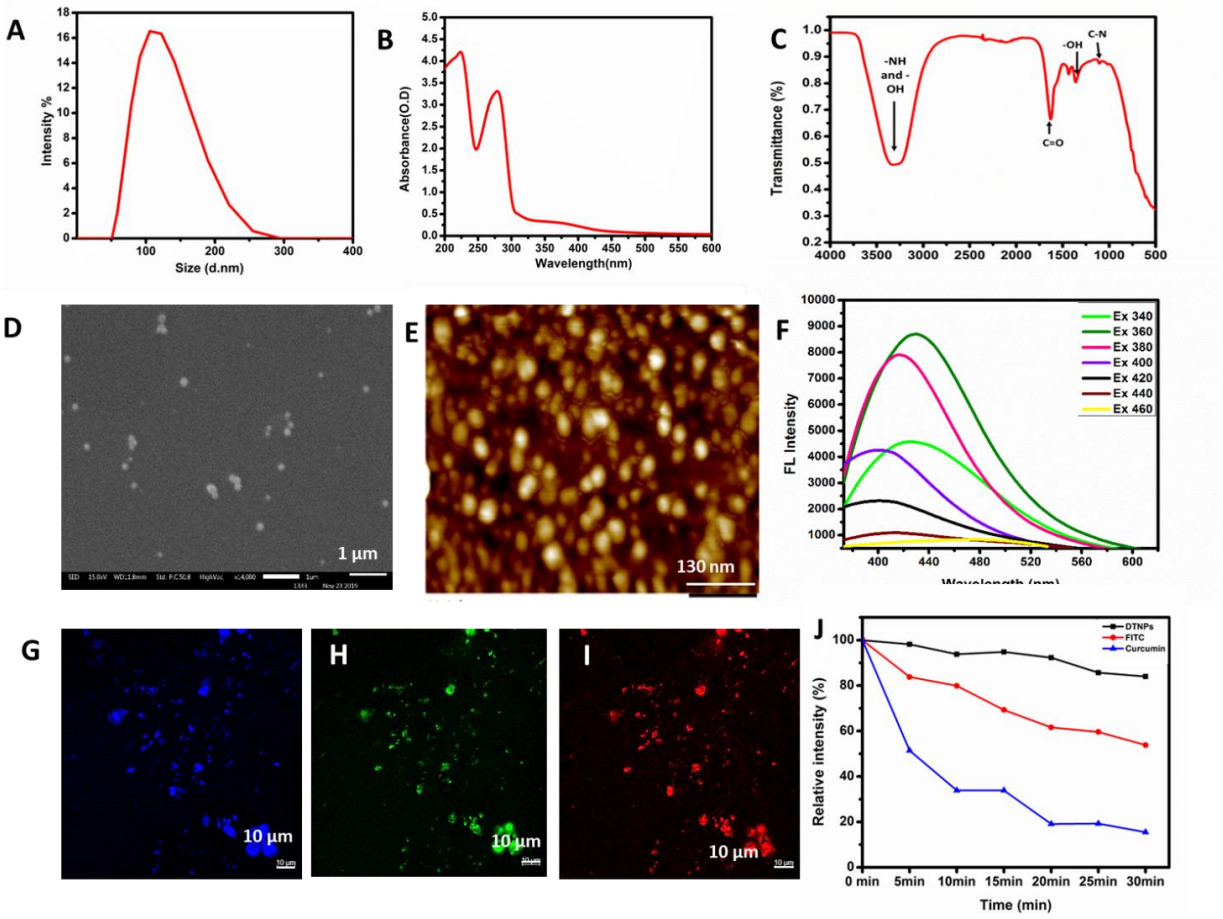

Figure 3.1: (A) DLS size distribution profile of DTNPs. (B) UV absorbance spectra of DTNPs. (C) ATR-FTIR of DTNPs. (D) SEM images of DTNPs. (E) AFM image of DTNPs. (F) Fluorescence emission spectra of DTNPs taken at different excitation wavelengths ranging from 340 nm to 460 nm. (G-I) Confocal images of DTNPs. (J) Photostability of DTNPs, FITC and curcumin irradiated with 365 nm UV light at various time points.

3.3.2. Demonstration of FF and Aβ aggregation in vitro:

The dipeptide, FF was synthesized by using solution phase peptide synthesis method, purified using HPLC and was further analyzed by using mass spectrometric analysis similarly as described in previous chapter. The peptide was allowed to form amyloid-like fibrillar aggregates by adopting the process of molecular self-assembly and was then examined for its aggregation potential by using ThT and electron microscopic assay. ThT is a known protein fibril formation marker and its fluorescence directly correlates with the amount of the presence of proteins or peptide-based aggregates in its vicinity.[48,49] Thus, the aggregation behavior of FF was confirmed by performing ThT fluorescence assay. Interestingly, an enhancement of ThT fluorescence intensity was detected when the dye was being incubated with an increasing concentration of FF (4, 6, 8, 10, and 12 mM) (**Figure 3.2A**). ThT assay clearly demonstrated that the dipeptide FF was capable of forming amyloid-like fibrillar assemblies.

Next, we carried out structural and morphological analysis of FF aggregates by using SEM and confocal microscopy. As ThT fluorescence assay exhibited maximum aggregation of FF at 12 mM concentration, other characterization studies for the dipeptide was also carried out at a concentration of 12 mM. Both SEM and confocal microscopic studies demonstrated an increase in the extent of FF aggregation with an increase in incubation time (**Figures 3.2 C-H**). A densely aggregated or plaque-like mass was detected after 72 h of incubation (**Figures 3.2 E and H**), whereas dense fibrillar structures were seen after 24 and 48 h of incubation (**Figures 3.2 C, D, F, and G**).

After establishing the aggregation and fibril forming ability of FF in vitro, we next embarked onto establishing the aggregation behavior of the amyloidogenic Aβ-polypeptide (Aβ 1-42). To do so, Aβ fibrils were first formed by dissolving thin clear film of the Aβ-polypeptide in PBS (10 mM, pH 7.4) and then the prepared solution of Aβ-polypeptide was incubated at 37

°C for 3 days to obtain higher concentrations of fibrils. The aggregating potential of the Aβ-polypeptide fibrils was also detected by performing ThT fluorescence assay. ThT assay showed an enhancement of ThT fluorescence intensity with a rise in the concentrations of Aβ-polypeptide fibrils (5, 10, 15, 20, and 25 µM) (**Figure 3.2 B**). After ThT analysis, the formation of fibril like aggregates was also confirmed by TEM analysis which clearly revealed the formation of dense fiber like assemblies by the polypeptide. (**Figure 3.2 I**).

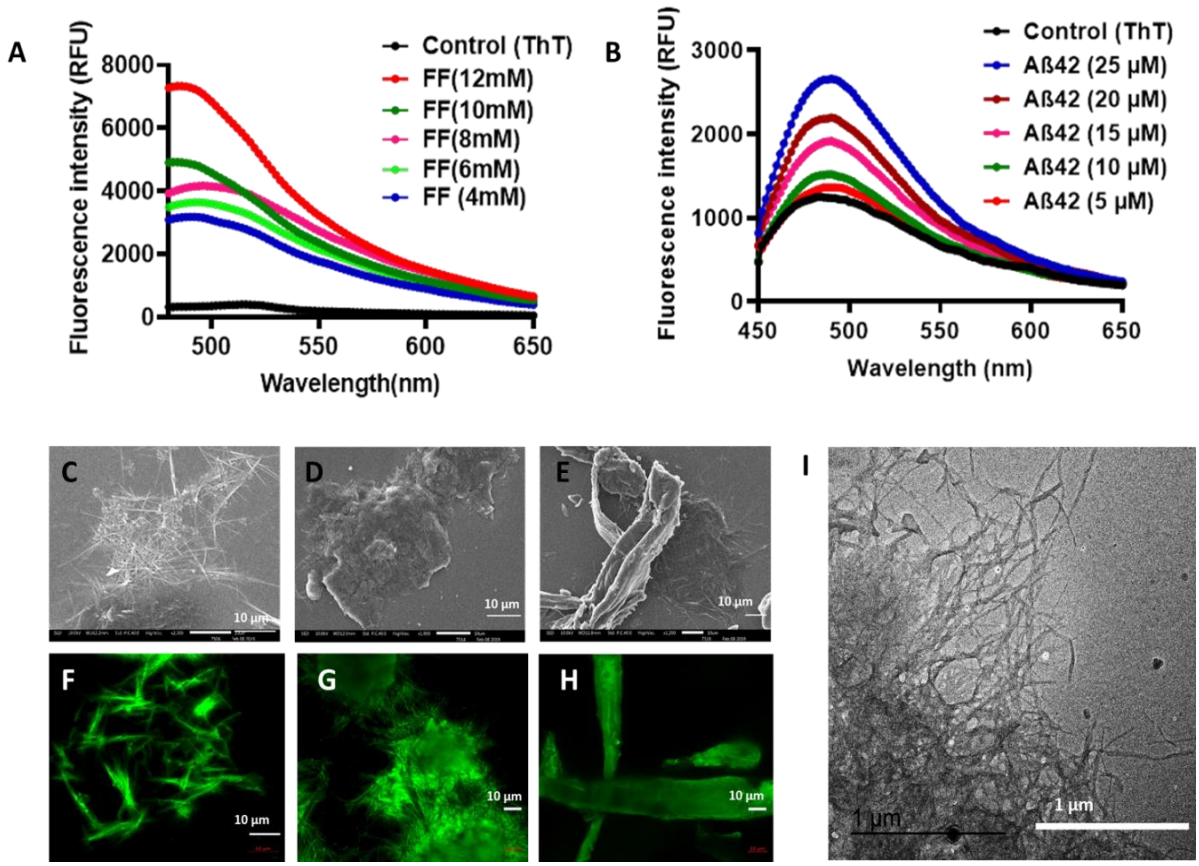

Figure 3.2: ThT assay showing concentration dependent aggregation of (A) FF; (B) Aβ; SEM images showing morphological changes of (C) FF fibrils after 24 h of incubation; (D) FF fibrils after 48 h of incubation; (E) FF fibrils after 72 h of incubation. Confocal microscopic images showing morphological changes of (F) FF fibrils after 24 h of incubation; (G) FF fibrils after 48h of incubation; (H) FF fibrils after 72 h of incubation at the scale of 10 µm ;(I) TEM image of aggregated Aβ-polypeptide fibrils after 3 day of incubation, Scale bar is 1 µm.

3.3.3. Disaggregation of FF dipeptide and Aβ-polypeptide fibrils by DTNPs:

After establishing FF aggregation into fibrillar structures, disaggregation studies in the presence of DTNPs were carried out using microscopic techniques. Confocal microscopy of aggregated FITC-stained FF fibrils (4 mg/ml) demonstrated the existence of dense fibrillar aggregates (**Figure 3.3A**). However, after being treated with DTNPs (100 µg/ml) for different time intervals (24 h, 48 h and 72 h), a time-dependent structural transition of the dipeptide aggregates from dense bundle like aggregated fibrils to small unstructured aggregates were observed. Clearly, after 24 and 48 h of incubations, short fibrillar structures were observed (**Figures 3.3 B and 3.3 C**). Whereas, after 72 h of incubation, a complete inhibition and disappearance of the aggregates were evident (**Figure 3.3 D**). The untreated control FF fibers retained their fibrillar structure and even got thicker and denser with time during the period of the study (**Figures 3.2 F, G, H**). Further, we also validated our confocal results by SEM analysis that showed a similar time dependent disaggregation of FF amyloid fibrils as observed in the confocal studies (**Figures 3.3 E-H**). Additionally, FF fibril recognition and interaction ability of the DTNPs is presented in **Figures 3.4 A-D and F** where the DTNPs can be found recognizing and interacting with the FF fibril, clearly demonstrating that attachment of DTNPs to the fibrils was a crucial step towards initiating the fibril disaggregation process.

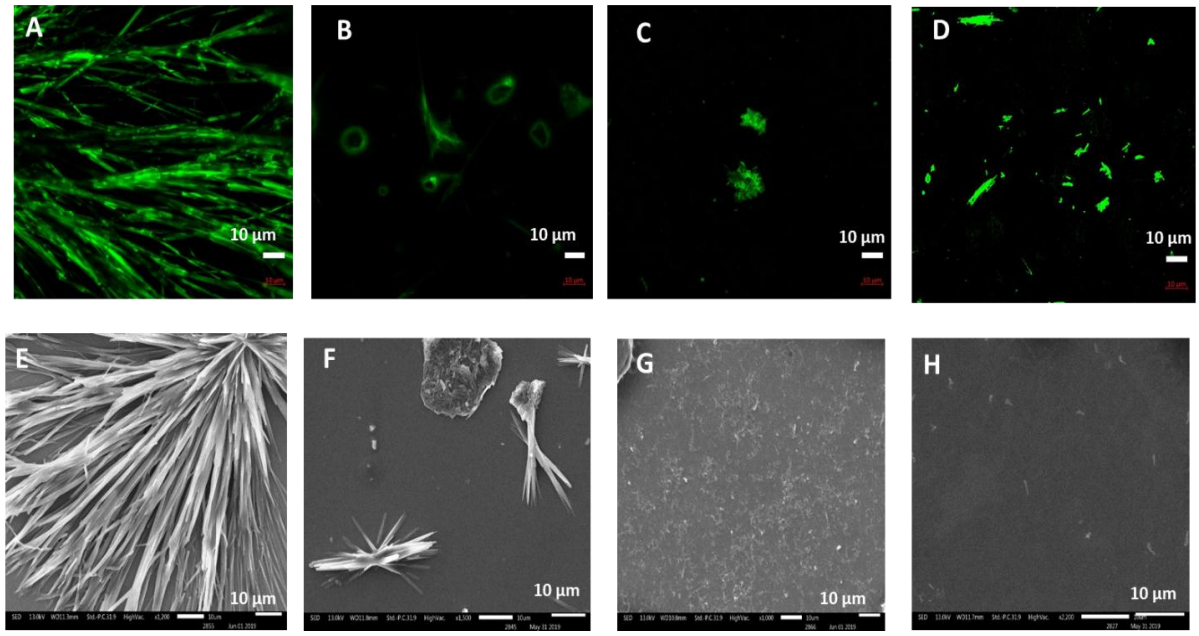

Figure 3.3: Confocal and scanning electron microscopic images depicting the formation of FF fibrils and subsequent disaggregation of the fibrils by the DTNPs. (A and E) Pre-formed FF fibrils; (B and F) Pre-formed FF fibrils treated with DTNPs for a period of 24 h; (C and G) Pre-formed fibrils of FF treated with DTNPs for 48 h and (D and H) Pre formed fibrils of FF treated with DTNPs for 72 h. Scale bar is 10 µm.

Next, CD analysis was done to investigate the conformational transitions in the secondary structure of FF fibrils (12 mM) if any, brought about by the DTNPs. CD spectra of the control dipeptide exhibited two maxima, one at 200 nm corresponding to π- π* transitions and another at 217 nm corresponding to n- π* transitions. The CD signature of the dipeptide resembles that of a β sheet like structure.[50,51]After being treated with the DTNPs the peptide demonstrated a significant loss in its secondary structure. As shown in **Figure 3.4 E**, the peptide plus DTNPs CD spectra showed time dependent decline in both the peaks and a complete loss of peaks was observed after the dipeptide fibrils were incubated with the DTNPs for a period of 72 h.

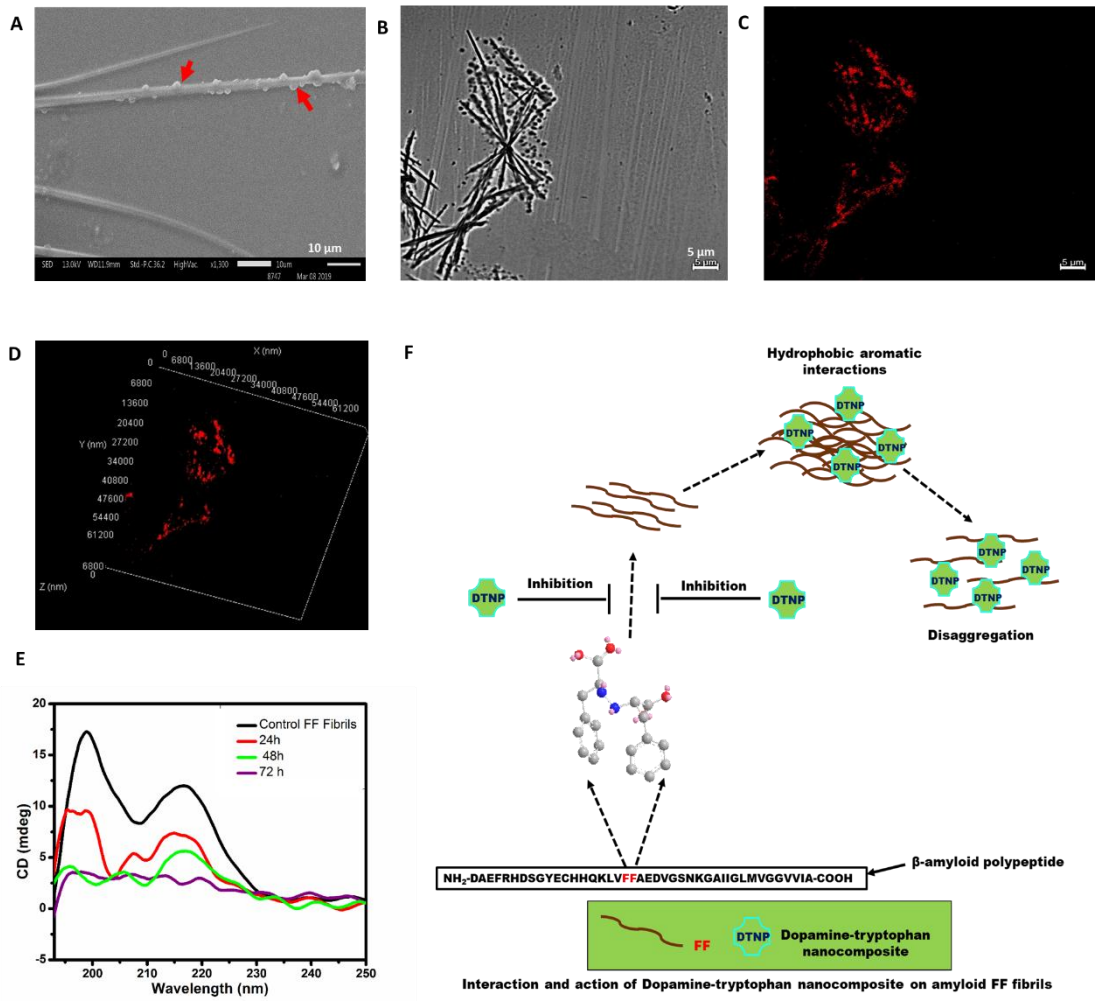

Figure 3.4: SEM and confocal microscopic images showing interaction of DTNPs with FF fibrils. (A) DTNPs interacting with FF fibrils (red arrow) shown by SEM analysis. Scale bar is 10 µm. (B) Brightfield image of DTNPs interacting with FF aggregates. (C) Fluorescent confocal image of DTNPs showing in vitro detection of FF aggregates by DTNPs; scale bar is 5 µm. (D) 3D image of fluorescent DTNPs interacting with FF aggregates. (E) CD spectra of FF fibrils alone and in presence of the DTNPs incubated for a period of 24 - 72 h. (F) Scheme showing interaction of DTNPs with FF fibrils and their subsequent disaggregation by the DTNPs.

We next tried to study the disaggregation potency of the DTNPs towards the Aβ-peptide aggregates. To do so, Aβ-polypeptide fibrils (20 µM) were treated with the DTNPs (50 µg/ml) in PBS (10 mM, pH 7.4) at 37 °C for different time periods (24, 48, and 72 h) and small aliquots of the reaction sample were withdrawn after 24, 48, and 72 h to check the disaggregation of fibrils. As shown in **Figure 3.5**, DTNPs clearly disaggregate many long

Aβ-peptide fibrils to short fibrillar structures after an incubation period of 24 h. After a treatment period of 48 h, we observed degradative products of Aβ-peptide fibrils and only some spherical aggregates were observed in the TEM micrograph. It was interesting to note that, almost all fibrillar Aβ structures were disaggregated and the TEM micrograph did not even show any remnants of the protein aggregates or oligomers after a treatment period of 72 h with the DTNPs. Thus, we observed that the DTNPs were equally effective in disaggregating fibrils formed of either Aβ or FF and considering the ease of synthesis, cost effectiveness and a mere dipeptidic nature, we carried out in vitro cytotoxicity and inhibition studies with FF fibrils only.

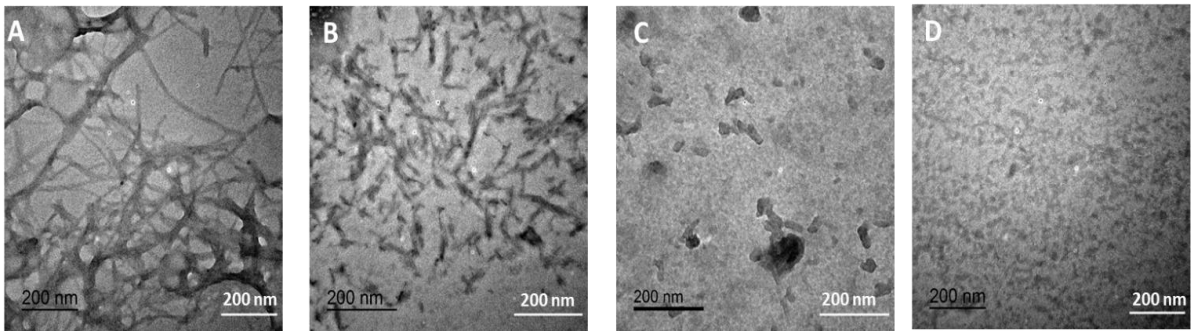

Figure 3.5: TEM images showing mature Aβ-polypeptide fibrils and the disaggregation potential of the DTNPs towards the Aβ-polypeptide fibrils. (A) pre-formed fibrils of Aβ-polypeptide; (B, C and D) inhibition of Aβ-peptide fibrillization when being incubated with DTNPs after 24, 48 and 72 h of incubation. Scale bar is 200 nm.

3.3.4. In vitro cell viability and cellular uptake of DTNPs in neuroblastoma cells:

To evaluate the efficacy of DTNPs as a potential biomolecular imaging agent, we first determined the cellular uptake ability of DTNPs in SH-SY5Y cells using a confocal microscope. The red and green fluorescence observed in the cytoplasm of DTNPs treated cells confirmed successful intracellular uptake and accumulation of self-fluorescent NPs inside them (**Figure 3.6**). This unique ability of the DTNPs in glowing up the cell cytoplasm further confirmed their ability as a biomolecular imaging agent. Cytotoxicity studies based on MTT assay were next carried out to assess the biocompatibility of the DTNPs. Results showed that the cells-maintained viability in the presence of varied concentrations of the NPs even after 24 h of treatment, demonstrating that DTNPs exhibited no cytotoxicity towards the

cultured neural cells (**Figure 3.7).** Thus, cellular uptake and cell viability studies in neuroblastoma cells indicated that the inherently fluorescent nanoparticles could be used as potent imaging and drug delivery vehicles.

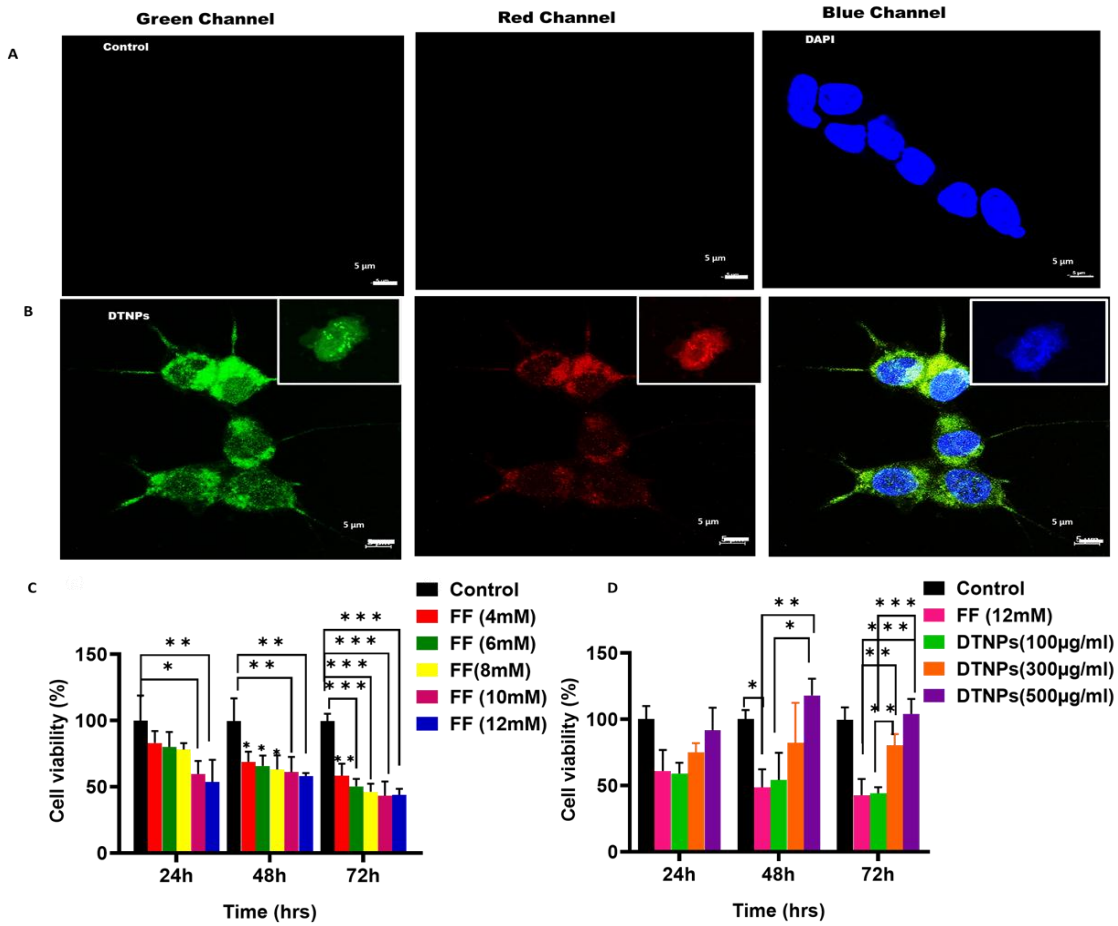

Figure 3.6: Confocal fluorescence images depicting cellular uptake of DTNPs in SH-SY5Y cells. (A) DAPI stained SH-SY5Y cells imaged in green, red and blue channel without DTNPs (B) DAPI stained SH-SY5Y cells treated with DTNPs imaged in green, red, and blue channel; scale bar 5 µm. (C) Cytotoxicity of FF toward SH-SY5Y cells examined by MTT assay, results are presented as mean ±SD. *P < 0.05; **P < 0.01; ***P<0.0001 when aggregated FF treated cells were compared with control groups;(D) Protective effects of DTNPs against FF-induced cytotoxicity in SH-SY5Y cells. Data are presented as mean ± SD. (*P < 0.05; **P < 0.001: ***P<0.0001).

3.3.5. Cytotoxicity of FF fibrils towards SH-SY5Y cells:

To check the neurotoxicity of the amyloid aggregates of FF, we next assessed the cytotoxicity of FF fibrils towards neuroblastoma cells. Elevated concentrations of FF fibrils ranging from

4 to 12 mM were added to cultured SH-SY5Y cells followed by determining their cell viability using MTT assay after different incubation periods. FF fibrils exhibited toxic effects on the SH -SY5Y cells at millimolar concentrations as evaluated by the MTT assay. It was observed that the cell viability of SH-SY5Y cells decreased to 82%, when being treated with 4 mM FF fibrils for a period of 24 h. Further, it was also observed that the cell viability of SH-SY5Y cells declined to approximately 67%, when being treated with 12 mM FF fibrils for a period of 24 h, suggesting a dose-dependent response. Similarly, we also noticed both time and concentration-dependent cytotoxicity in SH-SY5Y cells treated with various concentrations of FF after 48 and 72 h of the treatment period (**Figure 3.6 C**). Furthermore, altered morphology of SH-SY5Y cells due to extracellular deposition of FF fibrillar aggregates was also observed using inverted light microscopy, that clearly indicated towards the cytotoxic effect of these fibrils (**Figure 3.7).**

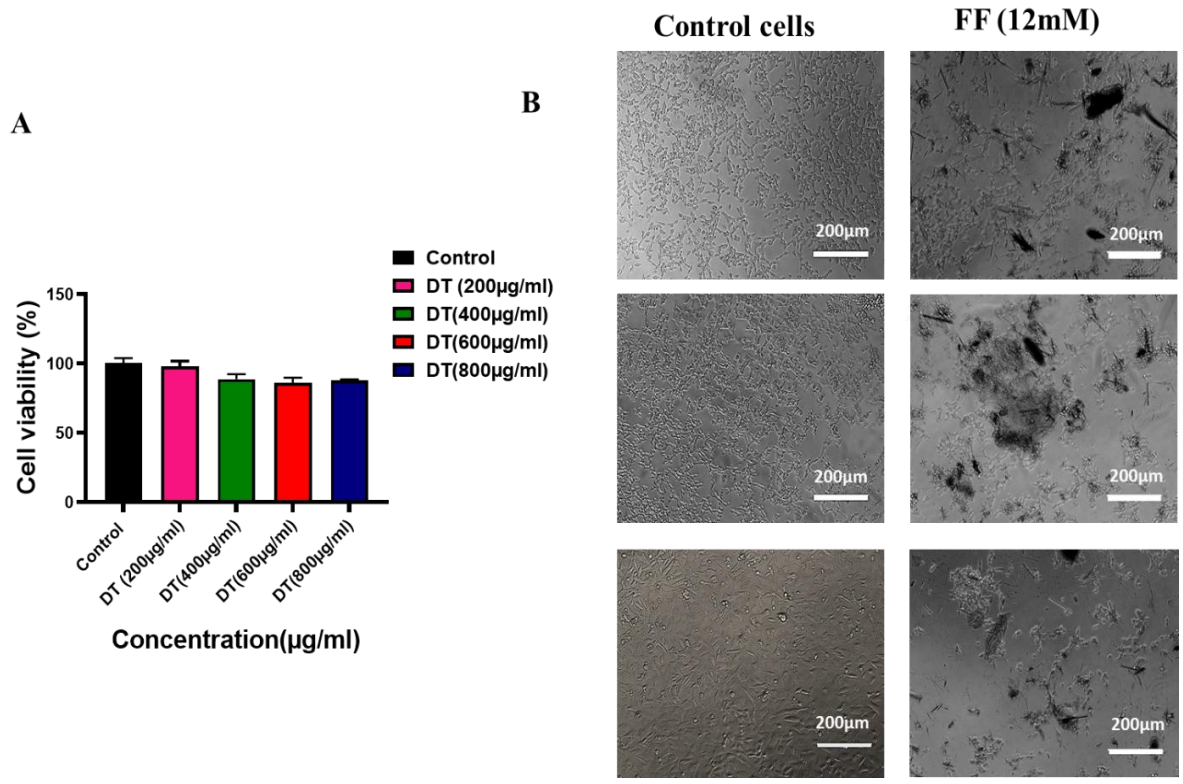

Figure 3.7: Cytotoxicity of DTNPs and FF fibrils toward SH-SY5Y cells. (A) MTT data showing cytotoxicity of DTNPs; (B) cytotoxicity of FF was determined in SH-SY5Y cells and photographed by inverted light microscopy after 24, 48 and 72 h (A-F) at a scale of 200 µm.

3.3.6. Inhibition of FF-Induced Cytotoxicity by DTNPs in neuroblastoma Cells:

After establishing the toxic potential of FF fibers towards the neuroblastoma cells, we next carried out cytotoxicity assay to determine the protective effect of DTNPs towards amyloid FF fibrils mediated cytotoxicity in SH-SY5Y cells. SH-SY5Y cells were treated with amyloid FF aggregates (12 mM) either in the absence of DTNPS or in the presence of increasing concentrations of DTNPs (100 μg/ml, 300 μg/ml and 500 μg/ml) and their viability was evaluated using MTT assay. It was observed that, FF alone caused toxicity towards the human neuroblastoma SH-SY5Y cells, however when these cells were co-treated with DTNPs and FF for a period of 24, 48 and 72 h, the cell death rate was significantly abrogated **(Figure 3.6 D**) and parallelly elevated levels of cell viability was observed in a dose and time-dependent manner. Cell viability results clearly demonstrated that the DTNPs (300 μg/ml) significantly rescued neuroblastoma cells from FF fibril induced cytotoxicity.

3.3.7. In vivo evaluation of DTNPs efficacy in rat model with ICV-STZ induced memory deficits:

3.3.7.1. Spatial learning and memory retention:

As memory deficit is a pathognomonic symptom of AD, MWM assay was performed to examine the potential effect of DTNPs on spatial learning and memory functions in ICV-STZ exposed animals and the observations were recorded in terms of path length and escape latency period between the sessions (**Figure 3.8 A to C**). The statistical analysis of the data set was analyzed using a Two-way ANOVA test followed by Bonferroni multiple comparison test. Post hoc analysis unveiled that the rats exposed to ICV-STZ showed higher escape latency time [$F(2,48) = 21.14$] without any significant differences during the next two sessions when compared to the first session **(Figure 3.8A**; $p>0.05$) indicating the appearance

of AD like phenotypes in rats. Further, DTNPs treatment in ICV-STZ exposed rats reduced the escape latency time by the rats during the second session ($p<0.05$) and third session ($p<0.05$) as compared to the first session **(Figure 3.8A**). This further proved the plausible protective role of DTNPs towards improvement in memory and learning deficits caused by ICV-STZ administration. Further the DTNPs *perse* showed similar learning and memory retention results as that of control group in animals without STZ exposure. Next, we measured the mean path length travelled by the animals to reach the targeted hidden platform [$F(2,48) = 29.52$]; we found that ICV-STZ treated rats showed no significant difference ($p>0.05$) in mean path length travelled from session 1 to session 3. However, DTNPs treatment significantly reduced ($p<0.001$) the path length travelled by the animals to reach the platform when compared to session 1 to session 3.

3.3.7.2. Effect of DTNPs on Aβ burden in ICV-STZ induced rat model:

One of the major hallmark of AD is the aggregation of Aβ42 senile plaques formed due to aberrant processing of amyloidogenic proteins. Protein expression was performed on day 24 after ICV-STZ (1 mg/kg) administration in the cortex (**Figure 3.8 D**) and hippocampus (**Figure 3.8 F**) region of the brain. A remarkable increase in the expression of Aβ42 oligomers was observed in both cortex ($p<0.001$) and hippocampus ($p<0.001$) after ICV-STZ injection as compared to the control group. In contrast, the administration of DTNPs to the STZ injected rats resulted in pronounced curtailment in the deposition of Aβ42 oligomers in cortex (**Figures 3.8 D and E**; $p<0.001$) and hippocampal (**Figures 3.8 F and G**; $p<0.01$) regions. Interestingly, rats administered with DTNPs *per se* exhibited similar behavior as the vehicle control group.

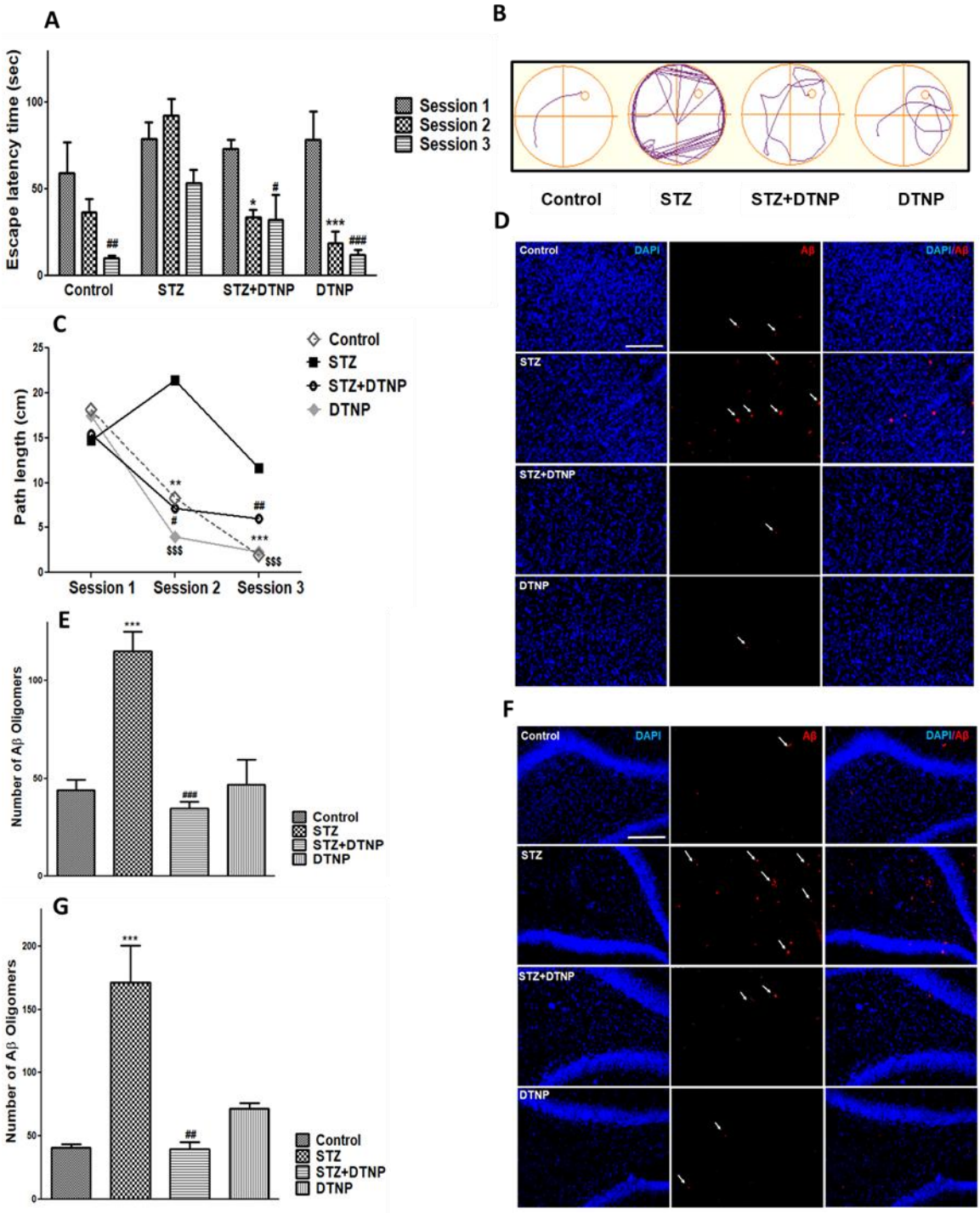

Figure 3.8: Dopamine Tryptophan nanoparticle treatment (5 mg/kg, i.v.) recovered learning and memory impairment in STZ lesioned animals and also subsided the expression of Aβ42 polypeptide in cortex and hippocampus region. Spatial learning and memory activities were evaluated by the MWZ test. (A**)** The bar graph shows escape latency time (in sec), i.e., time taken to reach the targeted hidden platform.; (B**)** Representative track plot for the path traced

by rat of each group; (C**)** The bar graph depicts mean path length (in cm). Data are represented as the mean ± SEM of n = 5 rats/group. Data were evaluated by repeated-measures two-way ANOVA, followed by Newman keuls multiple comparison post hoc test. Values are Mean ±SEM, n=5. *p < 0.05, **p < 0.01, ***p < 0.001. #p < 0.05, ##p < 0.01, ###p < 0.001, $^{\$}$p < 0.05, $^{\$\$}$p < 0.01, $^{\$\$\$}$p < 0.001 * Session 1 vs Session 3, $^{\#}$ Session 1 vs Session 2. * control *vs* STZ, $^{\#}$ STZ *vs* STZ+DTNP, $^{\$}$ STZ *vs* DTNP. Representative photomicrograph shows immunostaining of Aβ42 oligomers in the **(**D**)** cortex and **(**F**)** hippocampus regions. The bar graphs show quantification of the Aβ42 oligomers in **(**E**)** Cortex and **(**G**)** Hippocampus regions. Data were presented and analyzed by one-way ANOVA, followed by Newman-keuls multiple comparison test (*P < 0.05, **P < 0.01, ***P < 0.001; $^{\#}$P < 0.05, $^{\#\#}$P < 0.01, $^{\#\#\#}$P < 0.001). *Control vs STZ; $^{\#}$STZ vs STZ+ DTNP.

Immunohistochemical and DTNPs fluorescence analysis **(Figure 3.9**) further showed that DTNPs were capable of reaching and staining the brain tissues and also co-stained the Aβ42 oligomers in neural tissues (evident from circled merged images).

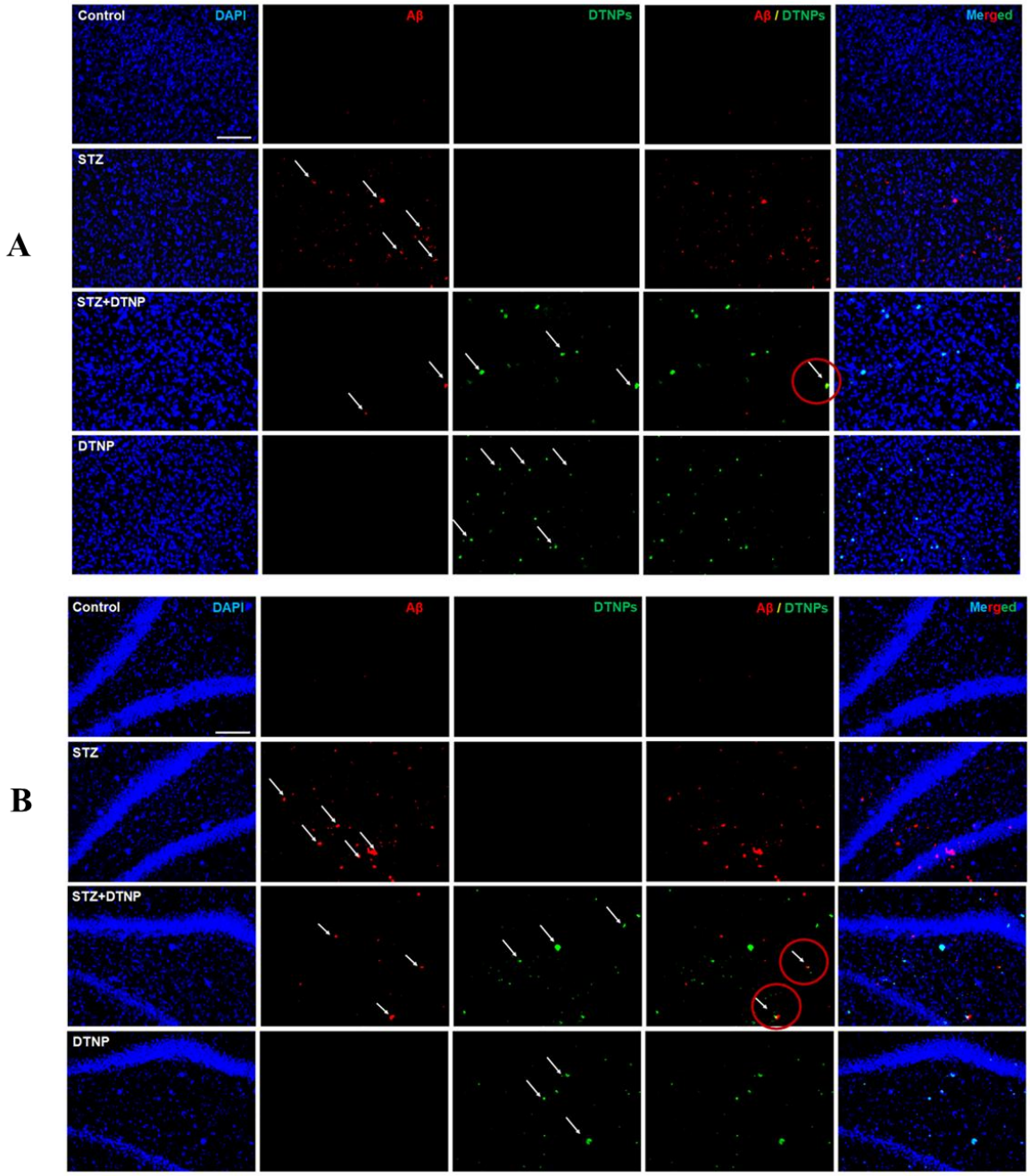

Figure 3.9: Fluorescent images of Cortex (A) and Hippocampal (B) brain region treated with DTNPs. Representative photomicrograph shows immunostaining of Nuclei (DAPI; stained in blue), Aβ (detect beta amyloid; red), and DTNPs (fluorescent nanoparticle; green), on day 28 after STZ injection. scale bar 50 μm.

3.4. Conclusion:

Aggregation of neurotoxic amyloid-beta (Aβ) polypeptide into insoluble self-aggregates is considered to be a crucial event in Alzheimer's disease (AD) and hence amyloid aggregates

constitute to be one of the major viable targets for developing novel therapeutic molecule(s) for early diagnosis, therapy and prevention of AD. As per a disease perspective, it is important to stop amyloid protein accumulation for attenuating the progression rate of AD, as well as to disaggregate the preformed abnormal assemblies thus diminishing the existing amyloid load as well as neurotoxicity. In the present work, using FF dipeptide as an amyloid reductionist model, we tried to examine fibril inhibition properties of self-fluorescent dopamine tryptophan nanocomposites. Our results depicted that; the nanocomposites were well capable of causing disaggregation of preformed fibrils of FF in a time-dependent manner. Moreover, in vitro assays with Aβ polypeptide further depicted that the nanocomposites can also effectively inhibit aggregation of pre-formed Aβ-polypeptide aggregates.

As neuronal cell death caused by insoluble amyloid deposits happens to be a crucial determinant of AD onset and progression, we further tested and validated the cytotoxicity potential of FF-fibrils in neuroblastoma cell line. We observed that FF fibrils alone could induce neuronal cell death in human neuroblastoma cells; however, when these cells were cotreated with the DTNPs for different time periods, the cell death rate was significantly abrogated. Moreover, we also observed the beneficial neuroprotective effect of DTNPs in improving cognitive deficits and suppressing the accumulation of Aβ42 in both cortex and hippocampus regions of the brain in the ICV-STZ rat model of dementia. The designed DTNPs also can be used as efficient bio imaging agents due to their excellent fluorescent properties.

Thus, our results clearly validated and established the dipeptide FF as a reductionist model for amyloid aggregation and neuronal toxicity and proved that multimodal dopamine tryptophan nanocomposite could serve as a potent theranostic agent for drug development towards AD therapy.

3.5. References:

(1) Potschka, H. Targeting the Brain – Surmounting or Bypassing the Blood–Brain Barrier. In *Drug Delivery*; Schäfer-Korting, M., Ed.; Handbook of Experimental Pharmacology; Springer: Berlin, Heidelberg, **2010**; 411–431.

(2) Ahmad, J.; Akhter, S.; Rizwanullah, Md.; Khan, M. A.; Pigeon, L.; Addo, R. T.; Greig, N. H.; Midoux, P.; Pichon, C.; Kamal, M. A. Nanotechnology Based Theranostic Approaches in Alzheimer's Disease Management: Current Status and Future Perspective. *Curr. Alzheimer Res.* **2017**, *14*, 1164–1181.

(3) Ahmad, M. Z.; Akhter, S.; Rahman, Z.; Ahmad, J.; Ahmad, I.; Ahmad, F. J. Nanomedicine Based Drug Targeting in Alzheimer's Disease: High Impact of Small Carter. In *Drug Design and Discovery in Alzheimer's Disease*; Elsevier, **2014**,716–739.

(4) Wong, H. L.; Wu, X. Y.; Bendayan, R. Nanotechnological Advances for the Delivery of CNS Therapeutics. *Adv. Drug Deliv. Rev.* **2012**, *64*, 686–700.

(5) Brambilla, D.; Le Droumaguet, B.; Nicolas, J.; Hashemi, S. H.; Wu, L.-P.; Moghimi, S. M.; Couvreur, P.; Andrieux, K. Nanotechnologies for Alzheimer's Disease: Diagnosis, Therapy, and Safety Issues. *Nanomedicine Nanotechnol. Biol. Med.* **2011**, *7*, 521–540.

(6) Gupta, J.; Fatima, M. T.; Islam, Z.; Khan, R. H.; Uversky, V. N.; Salahuddin, P. Nanoparticle Formulations in the Diagnosis and Therapy of Alzheimer's Disease. *Int. J. Biol. Macromol.* **2019**, *130*, 515–526.

(7) Schill, J.; Schenning, A. P. H. J.; Brunsveld, L. Self-Assembled Fluorescent Nanoparticles from π-Conjugated Small Molecules: En Route to Biological Applications. *Macromol. Rapid Commun.* **2015**, *36*, 1306–1321.

(8) Noristani, H. N.; Verkhratsky, A.; Rodríguez, J. J. High Tryptophan Diet Reduces CA1 Intraneuronal β-Amyloid in the Triple Transgenic Mouse Model of Alzheimer's Disease. *Aging Cell* **2012**, *11*, 810–822.

(9) Miri, A. L.; Hosni, A. P.; Gomes, J. C.; Kerppers, I. I.; Pereira, M. C. da S. Study of L-Tryptophan in Depression Caused by Alzheimer's Disease in Experimental Models. *J. Phys. Educ.* **2017**, *28*, e-2839.

(10) Li, J.; Zhu, M.; Manning-Bog, A. B.; Di Monte, D. A.; Fink, A. L. Dopamine and L-Dopa Disaggregate Amyloid Fibrils: Implications for Parkinson's and Alzheimer's Disease. *FASEB J. Off. Publ. Fed. Am. Soc. Exp. Biol.* **2004**, *18*, 962–964.

(11) Scherzer-Attali, R.; Pellarin, R.; Convertino, M.; Frydman-Marom, A.; Egoz-Matia, N.; Peled, S.; Levy-Sakin, M.; Shalev, D. E.; Caflisch, A.; Gazit, E.; Segal, D. Complete Phenotypic Recovery of an Alzheimer's Disease Model by a Quinone-Tryptophan Hybrid Aggregation Inhibitor. *PLoS ONE* **2010**, *5*.

(12) Boado, R. J.; Li, J. Y.; Nagaya, M.; Zhang, C.; Pardridge, W. M. Selective Expression of the Large Neutral Amino Acid Transporter at the Blood–Brain Barrier. *Proc. Natl. Acad. Sci. U. S. A.* **1999**, *96*, 12079–12084.

(13) Jf, P.; Sk, D.; B, M.; C, M.; C, F.; M, K.; Nl, T. Transcriptional Regulation of the LAT-1/CD98 Light Chain. *Biochem. Biophys. Res. Commun.* **2004**, *318*, 529–534.

(14) Barghorn, S.; Nimmrich, V.; Striebinger, A.; Krantz, C.; Keller, P.; Janson, B.; Bahr, M.; Schmidt, M.; Bitner, R. S.; Harlan, J.; Barlow, E.; Ebert, U.; Hillen, H. Globular Amyloid Beta-Peptide Oligomer - a Homogenous and Stable Neuropathological Protein in Alzheimer's Disease. *J. Neurochem.* **2005**, *95*, 834–847.

(15) Walsh, D. M.; Klyubin, I.; Fadeeva, J. V.; Cullen, W. K.; Anwyl, R.; Wolfe, M. S.; Rowan, M. J.; Selkoe, D. J. Naturally Secreted Oligomers of Amyloid Beta Protein Potently Inhibit Hippocampal Long-Term Potentiation in Vivo. *Nature* **2002**, *416*, 535–539.

(16) Teplow, D. B. Preparation of Amyloid Beta-Protein for Structural and Functional Studies. *Methods Enzymol.* **2006**, *413*, 20–33.

(17) Gazit, E. Mechanisms of Amyloid Fibril Self-Assembly and Inhibition. Model Short Peptides as a Key Research Tool. *FEBS J.* **2005**, *272*, 5971–5978.

(18) Westermark, P.; Engström, U.; Johnson, K. H.; Westermark, G. T.; Betsholtz, C. Islet Amyloid Polypeptide: Pinpointing Amino Acid Residues Linked to Amyloid Fibril Formation. *Proc. Natl. Acad. Sci. U. S. A.* **1990**, *87*, 5036–5040.

(19) Tenidis, K.; Waldner, M.; Bernhagen, J.; Fischle, W.; Bergmann, M.; Weber, M.; Merkle, M. L.; Voelter, W.; Brunner, H.; Kapurniotu, A. Identification of a Penta- and

Hexapeptide of Islet Amyloid Polypeptide (IAPP) with Amyloidogenic and Cytotoxic Properties. *J. Mol. Biol.* **2000**, *295*, 1055–1071.

(20) Balbach, J. J.; Ishii, Y.; Antzutkin, O. N.; Leapman, R. D.; Rizzo, N. W.; Dyda, F.; Reed, J.; Tycko, R. Amyloid Fibril Formation by A Beta 16-22, a Seven-Residue Fragment of the Alzheimer's Beta-Amyloid Peptide, and Structural Characterization by Solid State NMR. *Biochemistry* **2000**, *39*, 13748–13759.

(21) Brahmachari, S.; Arnon, Z. A.; Frydman-Marom, A.; Gazit, E.; Adler-Abramovich, L. Diphenylalanine as a Reductionist Model for the Mechanistic Characterization of β-Amyloid Modulators. *ACS Nano* **2017**, *11*, 5960–5969.

(22) Panda, J. J.; Kaul, A.; Kumar, S.; Alam, S.; Mishra, A. K.; Kundu, G. C.; Chauhan, V. S. Modified Dipeptide-Based Nanoparticles: Vehicles for Targeted Tumor Drug Delivery. *Nanomed.* **2013**, *8*, 1927–1942.

(23) Alam, S.; Panda, J. J.; Mukherjee, T. K.; Chauhan, V. S. Short Peptide Based Nanotubes Capable of Effective Curcumin Delivery for Treating Drug Resistant Malaria. *J. Nanobiotechnology* **2016**, *14*, 26.

(24) Bai, Y.; Zhang, B.; Chen, L.; Lin, Z.; Zhang, X.; Ge, D.; Shi, W.; Sun, Y. Facile One-Pot Synthesis of Polydopamine Carbon Dots for Photothermal Therapy. *Nanoscale Res. Lett.* **2018**, *13*,287.

(25) Zhang, X.; Wang, S.; Xu, L.; Feng, L.; Ji, Y.; Tao, L.; Li, S.; Wei, Y. Biocompatible Polydopamine Fluorescent Organic Nanoparticles: Facile Preparation and Cell Imaging. *Nanoscale* **2012**, *4*, 5581–5584.

(26) Zhao, Y.; Shi, L.; Fang, J.; Feng, X. Bio-Nanoplatforms Based on Carbon Dots Conjugating with F-Substituted Nano-Hydroxyapatite for Cellular Imaging. *Nanoscale* **2015**, *7*, 20033–20041.

(27) Kumaraswamy, P.; Lakshmanan, R.; Sethuraman, S.; Krishnan, U. M. Self-Assembly of Peptides: Influence of Substrate, PH and Medium on the Formation of Supramolecular Assemblies. *Soft Matter* **2011**, *7*, 2744–2754.

(28) Zhang, J.; Zhou, X.; Yu, Q.; Yang, L.; Sun, D.; Zhou, Y.; Liu, J. Epigallocatechin-3-Gallate (EGCG)-Stabilized Selenium Nanoparticles Coated with Tet-1 Peptide to

Reduce Amyloid-β Aggregation and Cytotoxicity. *ACS Appl. Mater. Interfaces* **2014**, *6*, 8475–8487.

(29) Yu, H.; Ren, J.; Qu, X. Different Hydration Changes Accompanying Copper and Zinc Binding to Amyloid Beta-Peptide: Water Contribution to Metal Binding. *Chembiochem Eur. J. Chem. Biol.* **2008**, *9*, 879–882.

(30) LeVine, H. Thioflavine T Interaction with Synthetic Alzheimer's Disease Beta-Amyloid Peptides: Detection of Amyloid Aggregation in Solution. *Protein Sci. Publ. Protein Soc.* **1993**, *2*, 404–410.

(31) Mehla, J.; Pahuja, M.; Gupta, Y. K. Streptozotocin-Induced Sporadic Alzheimer's Disease: Selection of Appropriate Dose. *J. Alzheimers Dis. JAD* **2013**, *33*, 17–21.

(32) Mishra, S. K.; Singh, S.; Shukla, S.; Shukla, R. Intracerebroventricular Streptozotocin Impairs Adult Neurogenesis and Cognitive Functions via Regulating Neuroinflammation and Insulin Signaling in Adult Rats. *Neurochem. Int.* **2018**, *113*, 56–68.

(33) Singh, S.; Mishra, A.; Bharti, S.; Tiwari, V.; Singh, J.; Parul, null; Shukla, S. Glycogen Synthase Kinase-3β Regulates Equilibrium Between Neurogenesis and Gliogenesis in Rat Model of Parkinson's Disease: A Crosstalk with Wnt and Notch Signaling. *Mol. Neurobiol.* **2018**, *55*, 6500–6517.

(34) Wiederschain, G. Ya. Handbook of Biochemistry and Molecular Biology; Taylor & Francis Group, Boca Raton, FL, 2010.

(35) Ju, K.-Y.; Lee, Y.; Lee, S.; Park, S. B.; Lee, J.-K. Bioinspired Polymerization of Dopamine to Generate Melanin-Like Nanoparticles Having an Excellent Free-Radical-Scavenging Property. *Biomacromolecules* **2011**, *12*, 625–632.

(36) Dreyer, D. R.; Miller, D. J.; Freeman, B. D.; Paul, D. R.; Bielawski, C. W. Elucidating the Structure of Poly(Dopamine). *Langmuir* **2012**, *28*, 6428–6435.

(37) Ai, K.; Liu, Y.; Ruan, C.; Lu, L.; Lu, G. M. Sp2 C-Dominant N-Doped Carbon Sub-Micrometer Spheres with a Tunable Size: A Versatile Platform for Highly Efficient Oxygen-Reduction Catalysts. *Adv. Mater.* **2013**, *25*, 998–1003.

(38) Yu, X.; Fan, H.; Liu, Y.; Shi, Z.; Jin, Z. Characterization of Carbonized Polydopamine Nanoparticles Suggests Ordered Supramolecular Structure of Polydopamine. *Langmuir ACS J. Surf. Colloids* **2014**, *30*, 5497–5505.

(39) Wünsch, U. J.; Murphy, K. R.; Stedmon, C. A. Fluorescence Quantum Yields of Natural Organic Matter and Organic Compounds: Implications for the Fluorescence-Based Interpretation of Organic Matter Composition. *Front. Mar. Sci.* **2015**, *2*. 98.

(40) Crosby, G. A.; Demas, J. N. Measurement of Photoluminescence Quantum Yields. Review. *J. Phys. Chem.* **1971**, *75*, 991–1024.

(41) Yin, H.; Zhang, K.; Wang, L.; Zhou, K.; Zeng, J.; Gao, D.; Xia, Z.; Fu, Q. Redox Modulation of Polydopamine Surface Chemistry: A Facile Strategy to Enhance the Intrinsic Fluorescence of Polydopamine Nanoparticles for Sensitive and Selective Detection of Fe3+. *Nanoscale* **2018**, *10*, 18064–18073.

(42) Lin, J.-H.; Yu, C.-J.; Yang, Y.-C.; Tseng, W.-L. Formation of Fluorescent Polydopamine Dots from Hydroxyl Radical-Induced Degradation of Polydopamine Nanoparticles. *Phys. Chem. Chem. Phys.* **2015**, *17*, 15124–15130.

(43) Yang, C.; Ogaki, R.; Hansen, L.; Kjems, J.; Teo, B. M. Theranostic Carbon Dots Derived from Garlic with Efficient Anti-Oxidative Effects towards Macrophages. *RSC Adv.* **2015**, *5*, 97836–97840.

(44) Mintz, K. J.; Mercado, G.; Zhou, Y.; Ji, Y.; Hettiarachchi, S. D.; Liyanage, P. Y.; Pandey, R. R.; Chusuei, C. C.; Dallman, J.; Leblanc, R. M. Tryptophan Carbon Dots and Their Ability to Cross the Blood-Brain Barrier. *Colloids Surf. B Biointerfaces* **2019**, *176*, 488–493.

(45) Zhang, M.; Chi, C.; Yuan, P.; Su, Y.; Shao, M.; Zhou, N. A Hydrothermal Route to Multicolor Luminescent Carbon Dots from Adenosine Disodium Triphosphate for Bioimaging. *Mater. Sci. Eng. C* **2017**, *76*, 1146–1153.

(46) Forster, L. S.; Livingston, R. The Absolute Quantum Yields of the Fluorescence of Chlorophyll Solutions. *J. Chem. Phys.* **1952**, *20*, 1315–1320.

(47) Tao, K.; Fan, Z.; Sun, L.; Makam, P.; Tian, Z.; Ruegsegger, M.; Shaham-Niv, S.; Hansford, D.; Aizen, R.; Pan, Z.; Galster, S.; Ma, J.; Yuan, F.; Si, M.; Qu, S.; Zhang,

M.; Gazit, E.; Li, J. Quantum Confined Peptide Assemblies with Tunable Visible to Near-Infrared Spectral Range. *Nat. Commun.* **2018**, *9*, 3217.

(48) Krebs, M. R. H.; Bromley, E. H. C.; Donald, A. M. The Binding of Thioflavin-T to Amyloid Fibrils: Localisation and Implications. *J. Struct. Biol.* **2005**, *149*, 30–37.

(49) Biancalana, M.; Koide, S. Molecular Mechanism of Thioflavin-T Binding to Amyloid Fibrils. *Biochim. Biophys. Acta* **2010**, *1804*, 1405–1412.

(50) Du, M.; Zhu, P.; Yan, X.; Su, Y.; Song, W.; Li, J. Honeycomb Self-Assembled Peptide Scaffolds by the Breath Figure Method. *Chem. Weinh. Bergstr. Ger.* **2011**, *17*, 4238–4245.

(51) Pang, Y.; Zhang, Q.; Sun, X.; Ji, J.; Pi, F.; Shen, X. Self-Assembled Diphenylalanine Peptide Fibrils with Ultra-High Aspect Ratio: A Platform for Sensitive Electrochemical H2O2 Sensor. *Int J Electrochem Sci* **2018**, *13*, 8518–8529.

CHAPTER 4

DUAL FUNCTIONAL RESVERATROL TRYPTOPHAN NANOPARTICLES LOADED POLYDOPAMINE CORE (RTDNPS) FOR ALZHEIMER'S TREATMENT

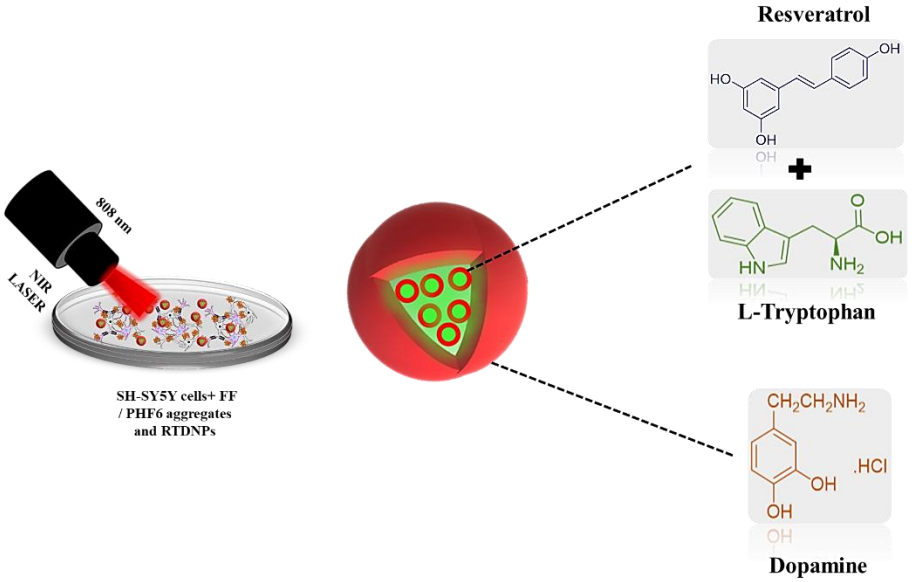

DUAL FUNCTIONAL RESVERATROL TRYPTOPHAN NANOPARTICLES LOADED POLYDOPAMINE CORE (RTDNPS) FOR ALZHEIMER'S TREATMENT

Abstract

Inhibiting the aggregation of neurotoxic amyloid aggregates is one of the most viable approaches to control the progression of Alzheimer's disease (AD). Despite the promising anti-amyloid potency of both solo tryptophan and nanocomposite of tryptophan toward both FF-derived amyloid fibrils and preformed Aβ-peptide fibers as described in our previous chapters, the anti-aggregation property of nanosystems against tau protein were not explored. Tau pathology is also the common cause of neurodegeneration in Alzheimer's disease (AD) and prevention of aggregated form of hyperphosphorylated tau is one of the targets for AD treatment. Thus, in this chapter, we have tried to develop a self–fluorescent dual functional resveratrol and L-tryptophan (Res-Trp) loaded polydopamine core (RTDNPs) nanotheranostic system as a dual targeting anti-amyloid agent. The nanosystem demonstrated dual anti-amyloidogenic activity against both FF amyloid fibrils, and the hexapeptide Ac-PHF6 (VQIVYK) derived from the tau protein. Additionally, RTDNPs exhibited a significant neuroprotective effect in neuroblastoma cells against both FF and Ac-PHF6 fibrils-induced toxicity under the NIR laser irradiation. Moreover, RTDNPs also demonstrated remarkable fluorescent properties and lit up the cytoplasm of neural cells, confirming their capability to serve as bioimaging agents. Overall, the results of this work clearly illustrate that our dual functional nanosystems can serve as a new class of theranostic systems for combating AD.

4.1. Introduction:

Alzheimer's disease (AD), a progressive neurodegenerative disease, is identified as a protein misfolding disorder (proteopathy) taking place due to the abnormal aggregation and accumulation of amyloid beta (Aβ) and tau protein in the brain tissues.[1] The accumulated abnormal extracellular Aβ and intracellular tau protein cause impairment and loss of synapses and neurons which ultimately leads to memory loss, cognitive impairment, and behavioural abnormalities.[2] Thus, both amyloid plaques and tau tangles are two crucial neuropathological hallmarks of AD, and targeting and abrogating their aggregation may be a viable approach for AD treatment.[3]

Resveratrol (RSV) (trans-3,4,5-trihydroxystilbene) is a natural polyphenolic plant compound that is present in grapes, red wine, peanuts, and some berries.[4] RSV exhibits antioxidative, anti-neurodegenerative, and anti-inflammatory properties.[5,6] In recent years, researchers have found that drinking red wine in a moderate amount can help slow down age-related cognitive decline and also lowers the risk of dementia.[7] In addition, there are several studies that claim the inhibitory proficiency of resveratrol against amyloid β-42 peptide aggregates.[8–11]. However, the lower solubility and bioavailability of RSV in water lessen its therapeutic potential.[12] Thus; nano-formulations of RSV with L-tryptophan noticeably improve its absorption, distribution, and bioavailability. Moreover, the synergism between RSV and L-tryptophan (an essential amino-acid that acts as a precursor in the 5-HT synthesis, improves spatial memory and cognition, and also has the ability to disaggregate Aβ aggregates) has a potent neuroprotective effect. In this regard, here we have developed fluorescent resveratrol tryptophan nanocomposite (RTNPs) through a simple hydrothermal synthesis method and tested its ability to inhibit/disrupt the aggregation of amyloid aggregates of FF. Moreover, these nanocomposites can possibly cross the BBB via LAT1 transporters due to the presence of L-tryptophan.

Currently, photothermal therapy has been used to block and regulate Aβ aggregation for the treatment of AD. [13–15] Near-infrared (NIR) light exhibits remarkable deep tissue penetrability and the penetrability of 808 nm NIR light has been verified to reach 10.9 mm across brain tissue.[16,17] Under the irradiation of NIR light, NIR- responsive photothermal nanoparticles convert light energy into heat for enabling inhibitions and disaggregation of amyloid aggregates.[18,19].It is well-studied that inhibiting the aggregation of neurotoxic amyloid aggregates is one of the most viable approach to control the progression of Alzheimer's disease (AD).[20] However, molecules that target a single protein are unable to considerably alter the progression of AD due to the complex multifactorial nature of this disease.[21] Thus, like Aβ aggregates, inhibition, and prevention of aggregated form of hyperphosphorylated tau protein is also one of the therapeutic targets for AD treatment.[22] In this regard, to achieve this goal, herein we fabricated a dual functional fluorescent resveratrol tryptophan nanoparticles loaded polydopamine Core (RTDNPs) nanostructure that consists of NIR light-responsive photothermal polydopamine core for disaggregating tau fibrils because of photothermal conversion ability of polydopamine[23–26], and RTNPs for recognizing, binding and disaggregating amyloid aggregates.

In addition, short amyloidogenic peptide-based models have been widely used to screen the potent anti-amyloid therapeutics as compared to large polypeptides or full-length proteins because of their tedious preparation, isolation, purification and self-assembly processes that are generally associated with many errors and often yields inconsistent and irreproducible results.[27] Moreover, various small fragments of peptides such as pentapeptide of calcitonin, hexapeptide of the islet amyloid polypeptide,[28,29] and heptapeptide of amyloid beta[30] have been exemplified to encompass all the crucial molecular and structural information necessary for the formation of amyloid fibrils.[31] Likewise, Gazit *et al*. reported a very short sequence of only two amino acidsm the diphenylalanine, FF, a core residue placed at positions 19 and 20

of the Aβ polypeptide to carry characteristics features of Aβ42 polypeptide aggregates.[32] In our previous reports, we have validated and used FF as in vitro model for screening potent anti-amyloidogenic nanostructures.[33,34]

Similarly, hexapeptide ^{306}VQIVYK^{311} (PHF6), located in the third repeat of the microtubule binding region of tau protein mediates the aggregation of tau protein and is also responsible for the oligomerization of neurotoxic tau. [35,36] Additionally, it is widely used as an in vitro model system for studying aggregation process of tau and to screen various anti-amyloidogenic molecules.[37,38] Thus, considering this, we tried to explore the dual anti-amyloidogenic activity of fluorescent RTDNPs towards both FF and Ac-PHF6 based amyloid aggregation models **(Scheme 4.1)**.

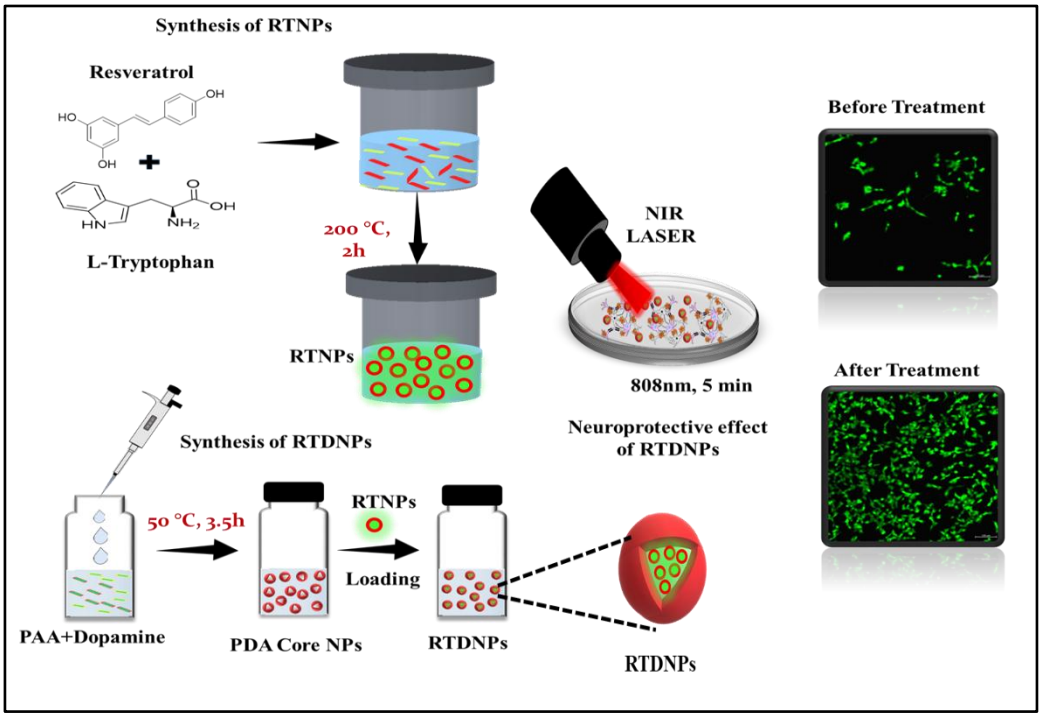

Scheme 4.1: Overall scheme showing the synthesis of self–fluorescent dual functional resveratrol and L-tryptophan (Res-Trp) loaded polydopamine core (RTDNPs) theranostic nanoparticles and their neuroprotective effect in neuroblastoma cells against both FF amyloid fibrils and hexapeptide Ac-PHF6 fibrils-induced toxicity under the NIR laser irradiation.

4.2. Materials and Methods:

4.2.1. Materials:

L-tryptophan (99%), D-tryptophan (99%), L-phenylalanine (99%), Boc-Phe-OH, isobutyl chloroformate (>99.8%), sodium chloride (99.9%), sodium sulfate (>99.0%), N-methyl morpholine (99%), tetrahydrofuran (>99.9%), sodium hydroxide, sodium acetate (>99%), acetic anhydride (98%), citric acid (>99.5%), sodium bicarbonate, and 3-(4,5-Dimethyl-2-thiazolyl)-2,5-diphenyltetrazolium bromide (MTT) were obtained from Sisco Research Laboratories, TCI Chemicals, and HiMedia Laboratories Pvt. Ltd., India. Thioflavin-T (ThT), 1,1,1,3,3,3-Hexafluro-2-propanol (HFIP) (> 99%), Aβ42 peptide (>95%), Methanol (MeOH) (99.8%), 4′,6-diamidino-2-phenylindole (DAPI)(>98%), and dichloromethane (DCM) (>99.8%), 4,4′-Dianilino-1,1′-binaphthyl-5,5′-disulfonic acid dipotassium salt (Bis-ANS), resveratrol (Sigma Aldrich Munich Germany), fetal bovine serum (FBS), *Calcein AM*, dulbecco's modified eagle medium (DMEM/F12), Phosphate buffer saline (PBS), trypsin EDTA solution (1X), and antibiotic antimycotic solution (100×) were obtained from Gibco, Thermo Fisher Scientific Inc., NY, USA.

4.2.2. Synthesis of fluorescent RTDNPs:

RTNPs were prepared by first dissolving 5mM of RSV and L-Trp in ethanol: water solvent mixture in 1:20 ratios. Next, the prepared mixture was added into a hydrothermal container and kept for 2 h at 200 degrees Celsius (°C). After 2 h, the obtained light orange coloured crude solution was obtained and to obtain pure solution of only RTNPs, the crude solution was centrifuged for 25 min at 14000 rpm (thrice) to eliminate large nanoparticles and other debris.

For fabricating a NIR responsive photothermal nanostructure, polydopamine-core nanostructures were formed following a similar protocol mentioned earlier.[39] Next, the

Fluorescent RTNPs nanoparticles and hollow core nanostructure of polydopamine were mixed in 1:1 ratio and were incubated for 24 h for the formation of RTDNPs loaded nanoparticles.

4.2.3. Characterization of RTDNPs:

The RTDNPs were characterized by using different spectroscopic and microscopic techniques. Briefly, the size of RTNPs, Polydopamine core nanostructures, and RTDNPs were measured by using a Malvern Zetasizer Nano ZSP Instrument. For measurement, sample solutions (1 mg mL^{-1}) were diluted with ultrapure water.

Further, UV-vis spectral properties of NPs were monitored by a double beam Shimadzu UV-2600 Spectrophotometer. For spectral measurement, sample solution of 1 mg mL^{-1} was diluted with ultrapure water.

Next, morphological details of RTDNPs were determined by using Scanning electron microscopic **(**SEM) studies. For SEM samples, 10 µL of sample solution (100 µg mL^{-1}) was drop casted onto silicon wafers. Afterwards, wafers were air-dried until sample analysis.

Moreover, intracellular uptake of the prepared fluorescent nanostructures was determined by using a confocal microscope (ZEISS LSM 880 with Airyscan).

4.2.4. Measurement of Photothermal Effect:

To determine the photothermal effect, prepared RTDNPs were exposed to an 808 nm NIR laser (2 W cm^{-2}, 10 min.). The rise in temperature of the NPs solutions was measured by a thermometer.

4.2.5. Demonstration of FF and tau-derived peptide aggregation in vitro:

The dipeptide (FF) was synthesized following a similar protocol mentioned earlier.[33,34] Ac-PHF6 (Ac-VQIVYK-amide) was synthesized using a Liberty Blue CEM Microwave

Automated Peptide Synthesizer (Matthews, NC, USA) by a similar protocol reported earlier.[40]After synthesis, the peptide was characterized by using HPLC and mass spectrometry.

FF fibrils were formed as described in our previous reports. Ac-PHF6 fibrils were formed as previously described in the literature. [41] Briefly, fibrils were generated by incubating 3 mg/mL of peptides at 70°C for 3 days. Both the fibrils were assessed for their aggregation by using SEM, TEM, AFM and confocal microscopy.

4.2.6. Disaggregation studies of FF and Ac-PHF6 fibrils by RTDNPs:

In order to investigate the anti amyloidogenic potential of RTDNPs against FF and Ac-PHF6 fibrils, the NPs were coincubated with FF fibrils (12 mM) in 1:1 ratio and were irradiated with NIR 808 laser for 10 min. After treatments, samples (90 μL) were incubated with 10 μL of ThT solution (1 mM) for 30 min. After incubation, disaggregation of fibrils was determined by ThT assay and morphological changes were visualized under confocal microscope.

4.2.7. Biocompatibility and cellular uptake study of RTDNPs carried out in SH-SY5Y cells:

For biocompatibility and cellular uptake assay, SH-SY5Y cells at a density of 1×10^4 cells were plated in 5% CO_2 incubator maintained at 37 °C with DMEM/F12 media (with 10% FBS, and 1% Pen-Strep) for 24 h. For biocompatibility studies, different concentrations of NPs (50, 100, 200 μg mL^{-1}) were incubated for 24 h in serum free cell culture media and cellular viability was measured by standard MTT assay by following similar protocols reported earlier.[33,34] For cellular uptake assay, NPs (100 μg mL^{-1}) were incubated overnight in serum free cell culture media. After incubation, cells were fixed with 4% (v/v) paraformaldehyde (PFA) for few minutes. Afterward, cells were stained with DAPI (1 μg

mL^{-1}) for 6 min and washed with cold PBS (3 times) to eliminate extra stain. Next, cellular uptake of NPs were observed under ZEISS LSM 880.

4.2.8. Calcein AM assay to determine the neuroprotective effect of RTDNPs against FF and Ac-PHF6 induced cytotoxicity:

SH-SY5Y cells at a density of 1×10^4 cells were plated for 24 h. After incubation, cells were cotreated with RTDNPs (50, 100 and 200 μg mL^{-1}) and FF (12 mM) and Ac-PHF6 (100 μM) fibrils for 48 h. After treatment, cells were irradiated with 808 NIR laser (1 W cm-2, 5 min) and incubated for next 24 h. After incubation, cells were carefully washed with PBS two times and stained with 2 μL mL^{-1} of calcein AM (1mg mL^{-1}) for 15 min at 37 °C in the dark. Afterward, extra stain was removed by PBS washing and calcein AM stained viable cells were analyzed by a ZEISS LSM 880 confocal microscope with Airyscan to determine the neuroprotective effect of RTDNPs.

4.3. Results and Discussion:

4.3.1. Synthesis and characterization of RTDNPs:

RTNPs synthesis process is shown in **Figure 4.1 A**. The Fluorescent RTNPs were prepared through a simple hydrothermal process by heating an aqueous solution of RSV and L Trp at 200 °C for 2h. The morphology and fluorescence of the prepared NPs were further characterized via SEM and confocal microscopy. Before hydrothermal treatment, the SEM images of an aqueous solution of RSV and L Trp showed fibrillar-like structure as shown in **Figure 4.1B** whereas the spherical structure of RTNPs was formed after hydrothermal treatment **(Figure 4.1C)**. The DLS graph showed an average diameter of ≈400 nm and 0.2 PDI **(Figure 4.1D)**. Further, confocal microscopy of the prepared NPs displayed the formation of blue, green, and red color fluorescent NPs as shown in **Figure 4.1(E-G)**. The NPs were also excited at different wavelengths and varied fluorescence emission spectra were observed according to change in the excitation wavelength of NPs **(Figure 4.1H)**

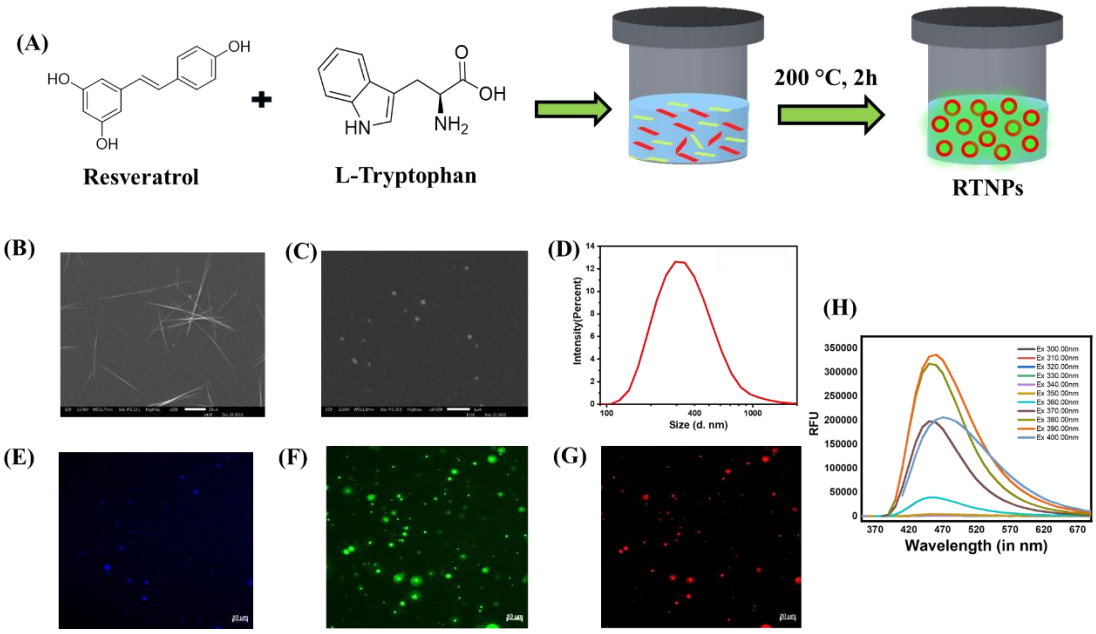

Figure 4.1: Scheme showing synthesis process of RTNPs (A); SEM images of RSV and L-Trp solution before (B); scale bar is 10µm and after hydrothermal treatment (C); scale bar is 1µm; DLS of RTNPs (D); confocal images of fluorescent RTNPs in all green, blue and red channels (E-G); scale bar is 10µm; Fluorescence emission spectra of RTNPs (H).

Next, polydopamine core nanoparticles were formed by a similar method as reported earlier [39] as shown in **Figure 4.2(A)**. The DLS results showed an average diameter of ≈800nm with a PDI of 0.2 **(Figure 4.2 B)** and SEM images revealed the core-like structure of prepared nanostructures (**Figure 4.2 C)**. The hollow core of the prepared nanostructures was employed for the high-loading of fluorescent RTNPs. The morphology and fluorescence of loaded nanostructures (RTDNPs) were further characterized by SEM and confocal microscopy. SEM images depicted the successful loading of RTNPs on polydopamine core structures (**Figure 4.2 D)**. and their fluorescence was further monitored by confocal microscopy. The loaded nanoparticles also displayed blue, green, and red fluorescence in confocal microscopy (**Figure 4.2 E-G)**.

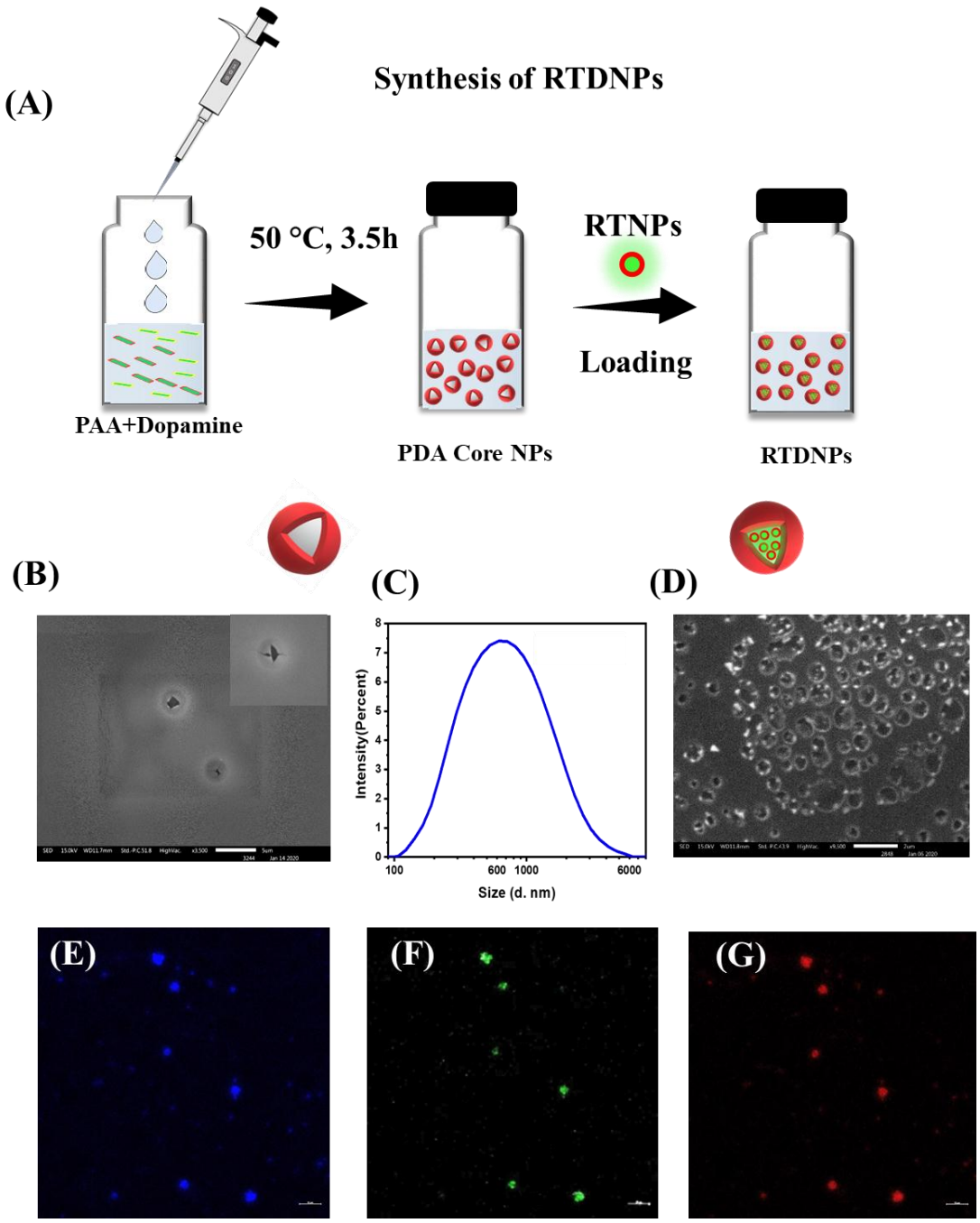

Figure 4.2: Scheme showing synthesis process of RTDNPs (A); SEM image of polydopamine core nanostructure (B); DLS of polydopamine core nanostructures (C); SEM image of RTNPs loaded polydopamine core nanostructures (RTDNPs) (D); scale bar is 5 and 2µm; confocal images of fluorescent RTDNPs in all green, blue and red channels (E-G). scale bar is 10 µm.

4.3.2. In vitro aggregation of FF and Ac-PHF6 (VQIVYK):

The in vitro fibril formation and aggregation potential of both FF and Ac-PHF6 peptide was examined by SEM, TEM, AFM, and confocal microscopy. The mass spectrum showed an expected mass of 790 Da for AcPHF6 (Ac-VQIVYK-NH2) (**Figure 4.3).**

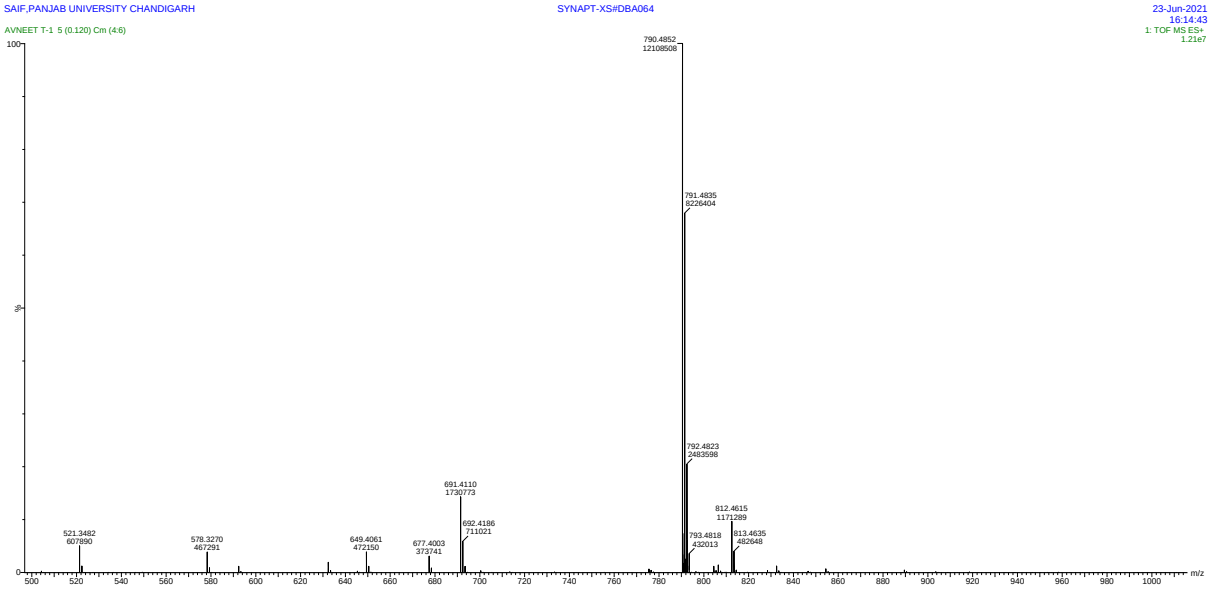

Figure 4.3: The mass spectrum of AcPHF6 peptide.

As shown in **Figure 4.4 A**, the SEM image revealed that dense aggregated forms of fibril-like structures were formed by the dipeptide. As it is well studied that ThT is a very sensitive fluorescent marker of amyloid fibrils and is widely used for in vitro aggregation detection assay.[42] Thus, we further used ThT dye to detect the aggregation of FF by using confocal microscopy. Confocal microscopic images also depicted the presence of bundles of FF fibrils (**Figure 4.4 B**). Similarly, aggregation and fibril formation potential of Ac-PHF6, tau peptide was also monitored by TEM, AFM, and confocal microscopy. Both AFM and TEM images revealed the formation of densely aggregated fibrils by tau peptide (**Figure 4.4 C and D**). ThT-stained tau aggregates were also visualized using confocal microscopy which further confirmed the in vitro aggregation potential of Ac-PHF6, tau peptide (**Figure 4.4E**). Thus, the in vitro fibrillation capability of tau-derived Ac-PHF6 peptide was observed to be similar to the full-length tau protein signifying its utility as a promising in vitro tau aggregation model. [43,44]

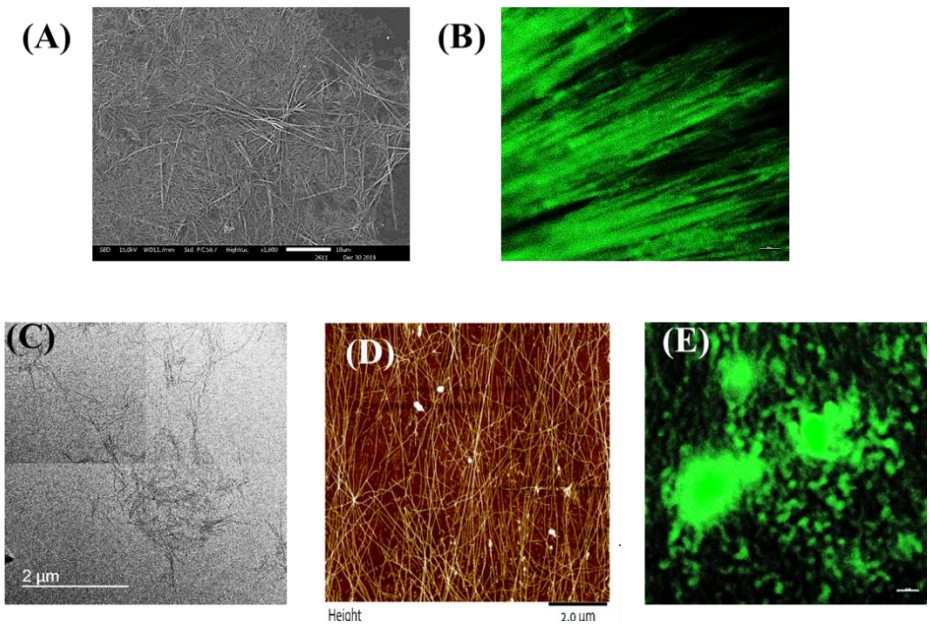

Figure 4.4: SEM and confocal images showing in vitro aggregation of FF fibrils (A and B); scale bar is 10µm; TEM, AFM and confocal microscopic images showing in vitro aggregation of Ac-PHF6 fibrils (C-E); scale bar is 2µm.

4.3.3. FF and Ac-PHF6 fibrils disaggregation studies:

To examine the effect of NPs on the disaggregation of FF and Ac-PHF6 fibrils, microscopic analysis was carried out to investigate the changes in the morphology of FF and Ac-PHF6 aggregates after disaggregation. Firstly, we have examined the disaggregation potency of lone RTNPs against FF aggregates by using SEM. As shown in **Figure 4.5A**, FF exhibited the formation of a large number of aggregated fibrils at 0 h. When these fibrils were incubated with RTNPs, their number and length gradually decreased after 24 h of the incubation period. However, when FF fibrils were incubated with RTDNPs (**Figure 4.5B**) and irradiated with an 808 nm laser for 10 minutes, the number and length of fibrils decreased significantly which clearly demonstrated that RTDNPs were more effective as compared to RTNPs in the disaggregation of FF fibrils to smaller fragments in lesser time due to the synergistic effect of NIR light-responsive photothermal polydopamine (**Figure 4.5 C**) and antiamyloidogenic activity of RSV and L-Trp. In addition, RTDNPs also showed

remarkable disaggregation efficiency against Ac-PHF6 peptide (**Figure 4.5 D)** and can be used as a dual anti-amyloid agent. The nanosystem demonstrated dual anti-amyloidogenic activity against both FF amyloid fibrils, and the hexapeptide Ac-PHF6 (VQIVYK) derived from the tau protein.

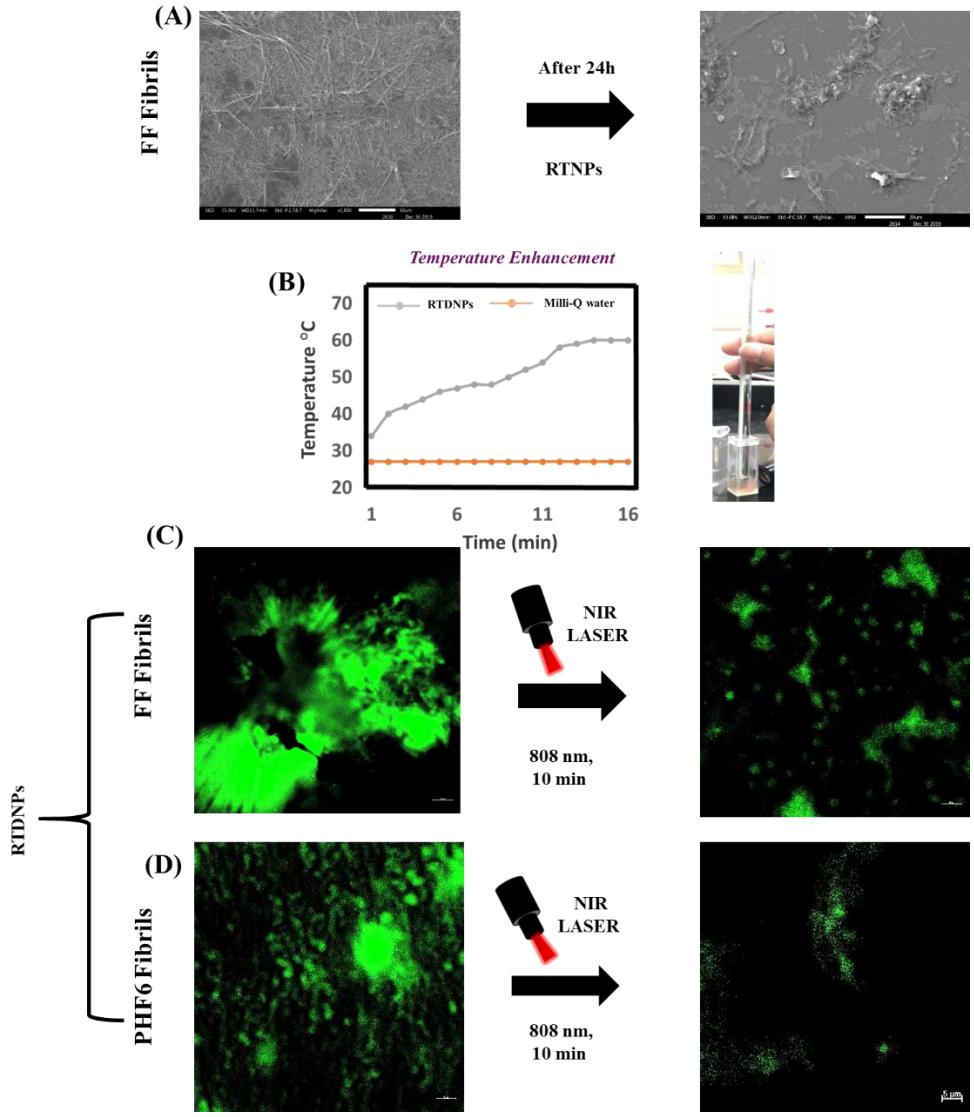

Figure 4.5: SEM images showing in vitro disaggregation of FF fibrils by RTNPs (A); scale bar is 10µm; Graph showing rise in temperature of NPs solutions after 808 nm laser irradiation (B); confocal images showing ThT stained in vitro disaggregation of FF (C) and Ac-PHF6 fibrils **(**D**)** by RTDNPs; scale bar is 5µm. The laser irradiation wavelength used was at 808 nm.

4.3.4. Biocompatibility and cellular uptake studies of RTDNPs:

To be used as a potent neurotherapeutic agent, we investigated the biocompatibility of RTDNPs in SH-SY5Y cells by MTT assay. As shown in **Figure 4.6 A**, after incubating different concentrations of RTDNPs (50, 100, 200, and 400 µg/ mL) with SH-SY5Y cells for 24 h, it was observed that the cell viability remained above 80 % even with RTDNPs concentrations being as high as 400 µg mL^{-1}, confirming their biocompatible and non-cytotoxic nature towards the neuronal cells. Next, potent bioimaging property of fluorescent RTDNPs was investigated in neuronal cells. The green and red fluorescence observed in the cytoplasm of RTDNPs treated cells directly confirmed the successful uptake of these fluorescent nanostructures inside the neuronal cells (**Figure 4.6 B)**. Thus, cell viability and cellular uptake results showed that our inherently fluorescent NPs could be used as potent neurotherapeutic and bioimaging agent.

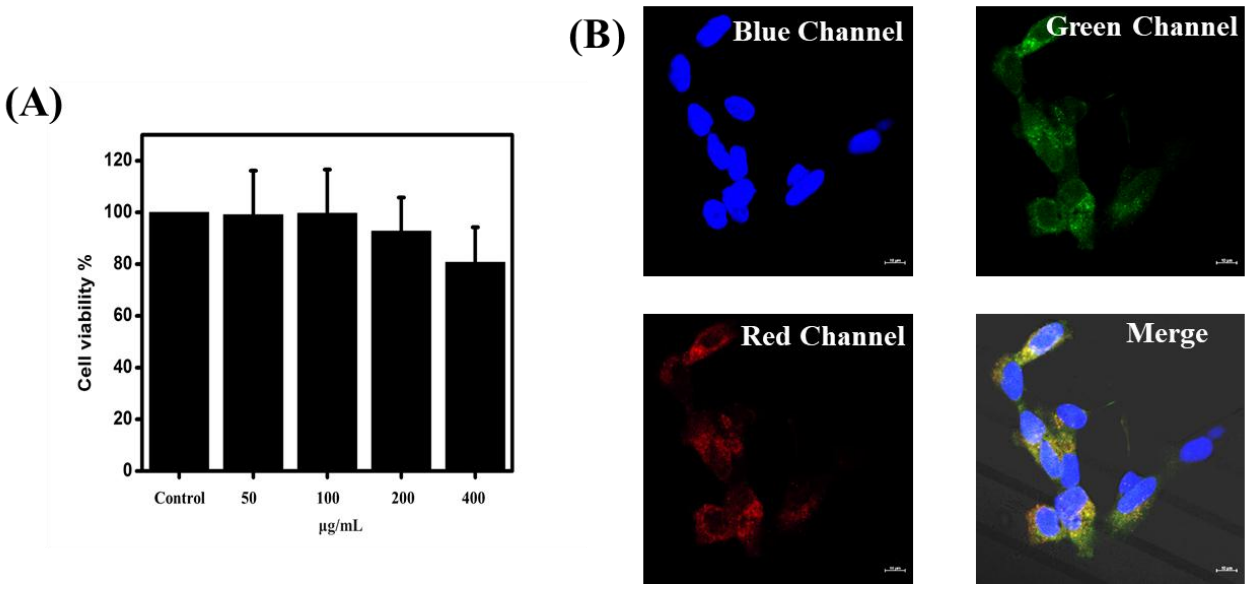

Figure 4.6: MTT data showing RTDNPs cytotoxicity (A); confocal images showing cellular uptake of RTDNPs (B); scale bar is 10µm.

4.3.5. Neuroprotective effect of RTDNPs:

As previously reported, accumulation and aggregation of β-amyloid (Aβ) peptides and microtubule-associated tau protein results in neuron cell death, leading to cognitive dysfunction in Alzheimer's disease.[45] Thus, we also tried to determine the neuroprotective effect of RTDNPs against FF and Ac-PHF6 fibrils-induced cytotoxicity by calcein AM assay. SH-SY5Y cells were incubated with FF fibrils (12 mM) and Ac-PHF6 fibrils (100 μM), and various concentrations of RTDNPs (50 μg mL^{-1}, 100 μg $mL^{-1,}$ and 200 μg mL^{-1}) for 24 h. It was observed that upon irradiation with laser, FF and Ac-PHF6 fibrils alone exhibited cytotoxic effects in SH-SY5Y cells as compared to control non-treated cells. However, when these cells co-incubated with RTDNPs and FF fibrils and were irradiated with laser showed evidently fewer cell death. Moreover, dose-dependent enhancement was observed in the cell viability of RTDNPs treated cells. Similarly, irradiation of Ac-PHF6 fibrils (100 μM) and RTDNPs co-incubated cells, a substantial decline in cell death rate and a dose dependent enhancement in the 7cell viability were observed (**Figure 4.7**). Thus, our results demonstrated that RTDNPs were able to protect the cells from both toxic peptide aggregates of FF and Ac-PHF6 fibrils.

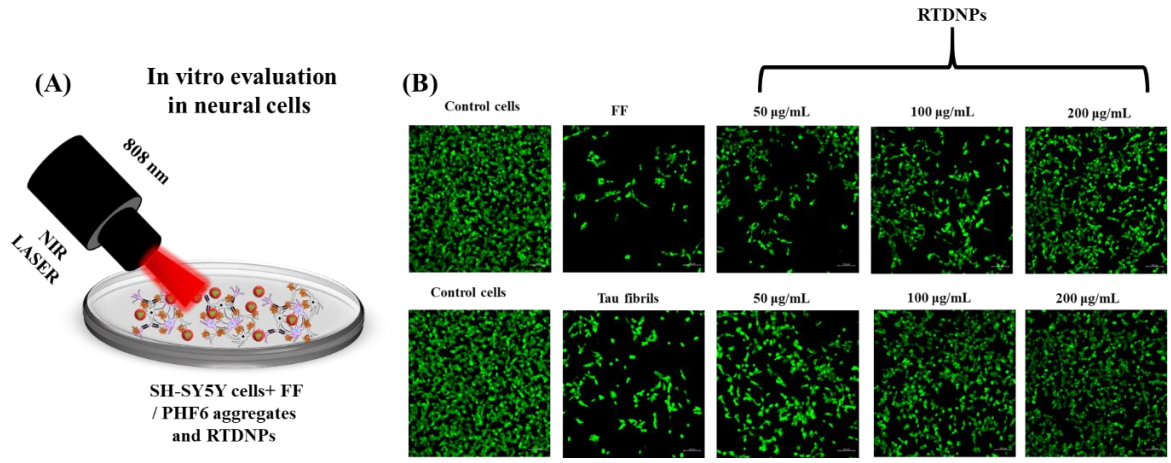

Figure 4.7: Illustration showing in vitro evaluation of RTDNPs and fibril treated cells in neuronal cells (A); confocal images showing calcein AM stained viable cells in green channel and neuroprotective effect of different concentrations of RTDNPs against FF and Ac-PHF6 fibrils in neuronal cells after irradiation with 808 nm laser (B); scale bar is 50μm.

4.4. Conclusion:

In summary, we fabricated RTNPs with NIR- responsive photothermal polyddopamine core structures to bind, and disaggregate both FF and Ac-PHF6 fibrils. More importantly, FF and Ac-PHF6 were used as in vitro aggregation model to examine anti-amyloidogenic behaviour of self-fluorescent NPs. The NPs showed significant disaggregation of both aggregated fibrils of FF and Ac-PHF6 peptides after irradiation with 808 nm laser due to the potent antiamyloidogenic and photothermal property of RTDNPs. Moreover, the designed NPs can also use as potent bioimaging agents because of tremendous auto-fluorescent nature of these nanoparticles. Furthermore, the RTDNPs efficiently eased both FF and Ac-PHF6 fibrils-induced neurotoxicity in SH-SY5Y cells after NIR light irradiation. Hence, the NIR light-responsive RTDNPs provide a novel disease modifying material and approach for the treatment of AD.

4.5. References:

(1) Hashimoto, M.; Rockenstein, E.; Crews, L.; Masliah, E. Role of Protein Aggregation in Mitochondrial Dysfunction and Neurodegeneration in Alzheimer's and Parkinson's Diseases. *Neuromolecular medicine* **2003**, *4* (1), 21–35.

(2) Rajmohan, R.; Reddy, P. H. Amyloid-Beta and Phosphorylated Tau Accumulations Cause Abnormalities at Synapses of Alzheimer's Disease Neurons. *Journal of Alzheimer's Disease* **2017**, *57* (4), 975–999.

(3) Serrano-Pozo, A.; Frosch, M. P.; Masliah, E.; Hyman, B. T. Neuropathological Alterations in Alzheimer Disease. *Cold Spring Harbor perspectives in medicine* **2011**, *1* (1), a006189.

(4) Burns, J.; Yokota, T.; Ashihara, H.; Lean, M. E.; Crozier, A. Plant Foods and Herbal Sources of Resveratrol. *Journal of agricultural and food chemistry* **2002**, *50* (11), 3337–3340.

(5) Oomen, C. A.; Farkas, E.; Roman, V.; Van Der Beek, E. M.; Luiten, P. G.; Meerlo, P. Resveratrol Preserves Cerebrovascular Density and Cognitive Function in Aging Mice. *Frontiers in aging neuroscience* **2009**, *1*, 4.

(6) Abedini, E.; Khodadadi, E.; Zeinalzadeh, E.; Moaddab, S. R.; Asgharzadeh, M.; Mehramouz, B.; Dao, S.; Samadi Kafil, H. A Comprehensive Study on the Antimicrobial Properties of Resveratrol as an Alternative Therapy. *Evidence-Based Complementary and Alternative Medicine* **2021**, *2021*.

(7) Reale, M.; Costantini, E.; Jagarlapoodi, S.; Khan, H.; Belwal, T.; Cichelli, A. Relationship of Wine Consumption with Alzheimer's Disease. *Nutrients* **2020**, *12* (1), 206.

(8) Al-Edresi, S.; Alsalahat, I.; Freeman, S.; Aojula, H.; Penny, J. Resveratrol-Mediated Cleavage of Amyloid B1–42 Peptide: Potential Relevance to Alzheimer's Disease. *Neurobiology of Aging* **2020**, *94*, 24–33.

(9) Li, F.; Zhan, C.; Dong, X.; Wei, G. Molecular Mechanisms of Resveratrol and EGCG in the Inhibition of Aβ 42 Aggregation and Disruption of Aβ 42 Protofibril: Similarities and Differences. *Physical Chemistry Chemical Physics* **2021**, *23* (34), 18843–18854.

(10) Jiang, P.; Li, W.; Shea, J.-E.; Mu, Y. Resveratrol Inhibits the Formation of Multiple-Layered β-Sheet Oligomers of the Human Islet Amyloid Polypeptide Segment 22–27. *Biophysical journal* **2011**, *100* (6), 1550–1558.

(11) Al-Edresi, S.; Alsalahat, I.; Freeman, S.; Aojula, H.; Penny, J. Resveratrol-Mediated Cleavage of Amyloid B1–42 Peptide: Potential Relevance to Alzheimer's Disease. *Neurobiology of Aging* **2020**, *94*, 24–33.

(12) Intagliata, S.; Modica, M. N.; Santagati, L. M.; Montenegro, L. Strategies to Improve Resveratrol Systemic and Topical Bioavailability: An Update. *Antioxidants* **2019**, *8* (8), 244.

(13) Li, M.; Yang, X.; Ren, J.; Qu, K.; Qu, X. Using Graphene Oxide High Near-Infrared Absorbance for Photothermal Treatment of Alzheimer's Disease. *Advanced Materials* **2012**, *24* (13), 1722–1728.

(14) Yin, T.; Xie, W.; Sun, J.; Yang, L.; Liu, J. Penetratin Peptide-Functionalized Gold Nanostars: Enhanced BBB Permeability and NIR Photothermal Treatment of Alzheimer's Disease Using Ultralow Irradiance. *ACS applied materials & interfaces* **2016**, *8* (30), 19291–19302.

(15) Ma, M.; Gao, N.; Li, X.; Liu, Z.; Pi, Z.; Du, X.; Ren, J.; Qu, X. A Biocompatible Second Near-Infrared Nanozyme for Spatiotemporal and Non-Invasive Attenuation of Amyloid Deposition through Scalp and Skull. *ACS nano* **2020**, *14* (8), 9894–9903.

(16) Deng, K.; Li, C.; Huang, S.; Xing, B.; Jin, D.; Zeng, Q.; Hou, Z.; Lin, J. Recent Progress in near Infrared Light Triggered Photodynamic Therapy. *Small* **2017**, *13* (44), 1702299.

(17) Heo, Y.; Kim, K.; Kim, J.; Jang, J.; Park, C. B. Near-Infrared-Active Copper Bismuth Oxide Electrodes for Targeted Dissociation of Alzheimer's β-Amyloid Aggregates. *ACS applied materials & interfaces* **2020**, *12* (21), 23667–23676.

(18) Geng, H.; Pan, Y.; Zhang, R.; Gao, D.; Wang, Z.; Li, B.; Li, N.; Guo, D.; Xing, C. Binding to Amyloid- β Protein by Photothermal Blood- Brain Barrier- Penetrating Nanoparticles for Inhibition and Disaggregation of Fibrillation. *Advanced Functional Materials* **2021**, *31* (41), 2102953.

(19) Geng, H.; Yuan, H.; Qiu, L.; Gao, D.; Cheng, Y.; Xing, C. Inhibition and Disaggregation of Amyloid β Protein Fibrils through Conjugated Polymer–Core Thermoresponsive Micelles. *Journal of Materials Chemistry B* **2020**, *8* (44), 10126–10135.

(20) Bharadwaj, P. R.; Dubey, A. K.; Masters, C. L.; Martins, R. N.; Macreadie, I. G. Aβ Aggregation and Possible Implications in Alzheimer's Disease Pathogenesis. *Journal of cellular and molecular medicine* **2009**, *13* (3), 412–421.

(21) Samanta, S.; Ramesh, M.; Govindaraju, T. Alzheimer's Is a Multifactorial Disease. **2022**.

(22) Takashima, A. Tau Aggregation Is a Therapeutic Target for Alzheimer's Disease. *Current Alzheimer Research* **2010**, *7* (8), 665–669.

(23) Liu, Y.; Ai, K.; Liu, J.; Deng, M.; He, Y.; Lu, L. Dopamine- melanin Colloidal Nanospheres: An Efficient Near- infrared Photothermal Therapeutic Agent for in Vivo Cancer Therapy. *Advanced materials* **2013**, *25* (9), 1353–1359.

(24) Liu, Y.; Zhang, Y.; Wang, J.; Yang, H.; Zhou, J.; Zhao, W. Doxorubicin-Loaded Walnut-Shaped Polydopamine Nanomotor for Photothermal-Chemotherapy of Cancer. *Bioconjugate Chemistry* **2022**, *33* (4), 726–735.

(25) Tas, C. E.; Berksun, E.; Koken, D.; Unal, S.; Unal, H. Photothermal Waterborne Polydopamine/Polyurethanes with Light-to-Heat Conversion Properties. *ACS Applied Polymer Materials* **2021**, *3* (8), 3929–3940.

(26) Cao, H.; Yang, Y.; Liang, M.; Ma, Y.; Sun, N.; Gao, X.; Li, J. Pt@ Polydopamine Nanoparticles as Nanozymes for Enhanced Photodynamic and Photothermal Therapy. *Chemical Communications* **2021**, *57* (2), 255–258.

(27) Teplow, D. B. Preparation of Amyloid B- protein for Structural and Functional Studies. *Methods in enzymology* **2006**, *413*, 20–33.

(28) Tenidis, K.; Waldner, M.; Bernhagen, J.; Fischle, W.; Bergmann, M.; Weber, M.; Merkle, M.-L.; Voelter, W.; Brunner, H.; Kapurniotu, A. Identification of a Penta-and Hexapeptide of Islet Amyloid Polypeptide (IAPP) with Amyloidogenic and Cytotoxic Properties. *Journal of molecular biology* **2000**, *295* (4), 1055–1071.

(29) Reches, M.; Porat, Y.; Gazit, E. Amyloid Fibril Formation by Pentapeptide and Tetrapeptide Fragments of Human Calcitonin. *Journal of Biological Chemistry* **2002**, *277* (38), 35475–35480.

(30) Balbach, J. J.; Ishii, Y.; Antzutkin, O. N.; Leapman, R. D.; Rizzo, N. W.; Dyda, F.; Reed, J.; Tycko, R. Amyloid Fibril Formation by Aβ16-22, a Seven-Residue Fragment of the Alzheimer's β-Amyloid Peptide, and Structural Characterization by Solid State NMR. *Biochemistry* **2000**, *39* (45), 13748–13759.

(31) Gazit, E. Mechanisms of Amyloid Fibril Self- assembly and Inhibition: Model Short Peptides as a Key Research Tool. *The FEBS journal* **2005**, *272* (23), 5971–5978.

(32) Brahmachari, S.; Arnon, Z. A.; Frydman-Marom, A.; Gazit, E.; Adler-Abramovich, L. Diphenylalanine as a Reductionist Model for the Mechanistic Characterization of β-Amyloid Modulators. *ACS nano* **2017**, *11* (6), 5960–5969.

(33) Sharma, M.; Tiwari, V.; Chaturvedi, S.; Wahajuddin, M.; Shukla, S.; Panda, J. J. Self-Fluorescent Lone Tryptophan Nanoparticles as Theranostic Agents Against Alzheimer's Disease. *ACS Applied Materials & Interfaces* **2022**, *14* (11), 13079–13093.

(34) Sharma, M.; Tiwari, V.; Shukla, S.; Panda, J. J. Fluorescent Dopamine–Tryptophan Nanocomposites as Dual-Imaging and Antiaggregation Agents: New Generation of Amyloid Theranostics with Trimeric Effects. *ACS Applied Materials & Interfaces* **2020**, *12* (39), 44180–44194.

(35) Von Bergen, M.; Friedhoff, P.; Biernat, J.; Heberle, J.; Mandelkow, E.-M.; Mandelkow, E. Assembly of τ Protein into Alzheimer Paired Helical Filaments Depends on a Local Sequence Motif (306VQIVYK311) Forming β Structure. *Proceedings of the National Academy of Sciences* **2000**, *97* (10), 5129–5134.

(36) von Bergen, M.; Barghorn, S.; Li, L.; Marx, A.; Biernat, J.; Mandelkow, E.-M.; Mandelkow, E. Mutations of Tau Protein in Frontotemporal Dementia Promote Aggregation of Paired Helical Filaments by Enhancing Local β-Structure. *Journal of Biological Chemistry* **2001**, *276* (51), 48165–48174.

(37) Frenkel-Pinter, M.; Tal, S.; Scherzer-Attali, R.; Abu-Hussien, M.; Alyagor, I.; Eisenbaum, T.; Gazit, E.; Segal, D. Naphthoquinone-Tryptophan Hybrid Inhibits

Aggregation of the Tau-Derived Peptide PHF6 and Reduces Neurotoxicity. *Journal of Alzheimer's Disease* **2016**, *51* (1), 165–178.

(38) Frenkel-Pinter, M.; Tal, S.; Scherzer-Attali, R.; Abu-Hussien, M.; Alyagor, I.; Eisenbaum, T.; Gazit, E.; Segal, D. Cl-NQTrp Alleviates Tauopathy Symptoms in a Model Organism through the Inhibition of Tau Aggregation-Engendered Toxicity. *Neurodegenerative Diseases* **2017**, *17* (2–3), 73–82.

(39) Zhang, M.; Zhang, L.; Chen, Y.; Li, L.; Su, Z.; Wang, C. Precise Synthesis of Unique Polydopamine/Mesoporous Calcium Phosphate Hollow Janus Nanoparticles for Imaging-Guided Chemo-Photothermal Synergistic Therapy. *Chemical science* **2017**, *8* (12), 8067–8077.

(40) Belostozky, A.; Richman, M.; Lisniansky, E.; Tovchygrechko, A.; Chill, J. H.; Rahimipour, S. Inhibition of Tau-Derived Hexapeptide Aggregation and Toxicity by a Self-Assembled Cyclic d, l-α-Peptide Conformational Inhibitor. *Chemical Communications* **2018**, *54* (47), 5980–5983.

(41) Fanni, A. M.; Vander Zanden, C. M.; Majewska, P. V.; Majewski, J.; Chi, E. Y. Membrane-Mediated Fibrillation and Toxicity of the Tau Hexapeptide PHF6. *Journal of Biological Chemistry* **2019**, *294* (42), 15304–15317.

(42) Freire, S.; de Araujo, M. H.; Al-Soufi, W.; Novo, M. Photophysical Study of Thioflavin T as Fluorescence Marker of Amyloid Fibrils. *Dyes and Pigments* **2014**, *110*, 97–105.

(43) Goux, W. J.; Kopplin, L.; Nguyen, A. D.; Leak, K.; Rutkofsky, M.; Shanmuganandam, V. D.; Sharma, D.; Inouye, H.; Kirschner, D. A. The Formation of Straight and Twisted Filaments from Short Tau Peptides. *Journal of Biological Chemistry* **2004**, *279* (26), 26868–26875.

(44) Lunven, L.; Bonnet, H.; Yahiaoui, S.; Yi, W.; Da Costa, L.; Peuchmaur, M.; Boumendjel, A.; Chierici, S. Disruption of Fibers from the Tau Model AcPHF6 by Naturally Occurring Aurones and Synthetic Analogues. *ACS chemical neuroscience* **2016**, *7* (7), 995–1003.

(45) Bloom, G. S. Amyloid-β and Tau: The Trigger and Bullet in Alzheimer Disease Pathogenesis. *JAMA neurology* **2014**, *71* (4), 505–508.

CHAPTER 5

ANTI-AMYLOIDOGENIC POTENCY OF ACOUSTIC STIMULUS ACTIVATED PIEZOELECTRIC POLYDOPAMINE-PVDF NANOSPHERES, A FUTURISTIC APPROACH TOWARDS ALZHEIMER'S THERAPY

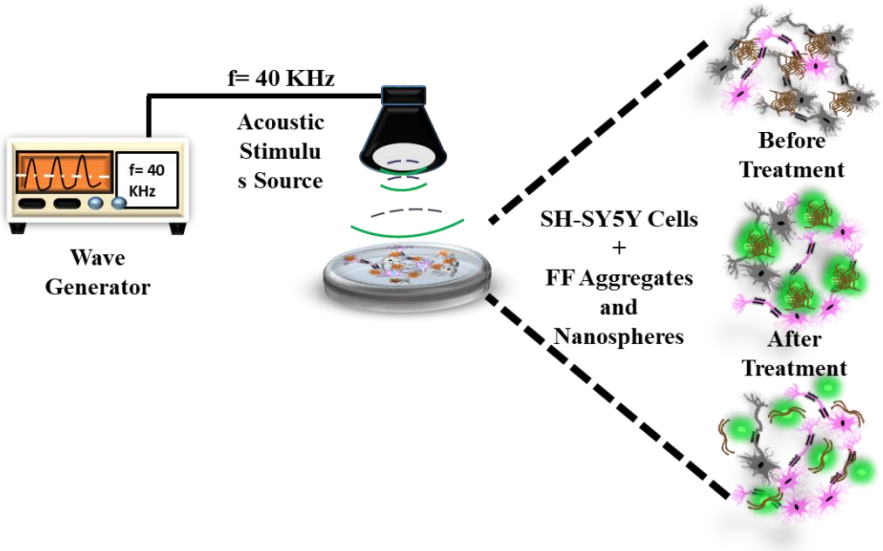

ANTI-AMYLOIDOGENIC POTENCY OF ACOUSTIC STIMULUS ACTIVATED PIEZOELECTRIC POLYDOPAMINE-PVDF NANOSPHERES, A FUTURISTIC APPROACH TOWARDS ALZHEIMER'S THERAPY

Abstract

The degeneration of neurons due to the accumulation of misfolded amyloid aggregates in the central nervous system (CNS) is a fundamental neuropathology of Alzheimer's disease (AD). Dislodging/clearing these amyloid aggregates from the neuronal tissues is considered a viable strategy for finding a potential cure for AD. In the present chapter, we explored biocompatible polydopamine-coated piezoelectric polyvinylidene fluoride (DPVDF) nanospheres as acoustic stimulus-triggered anti-fibrillating agents against two model amyloidogenic peptides, which includes the reductionist model-based amyloidogenic dipeptide, diphenylalanine, and the amyloid polypeptide, Aβ42. Our results revealed that DPVDF nanospheres could effectively disassemble the model peptide-derived amyloid fibrils, under suitable acoustic stimulation. In vitro studies also revealed that the stimulus-activated DPVDF nanospheres could efficiently alleviate the neurotoxicity of FF fibrils as exemplified in neuroblastoma, SHSY5Y cells. Thus, these acoustic stimuli-activated nanospheres could serve as a novel class of disease-modifying nanomaterials for non-invasive electro-chemotherapy of Alzheimer's disease.

5.1. Introduction:

Alzheimer's disease (AD) is a neurological disorder, majorly characterized by an irreversible decline in cognitive ability and memory-related functions in older adults.[1] Numerous studies have shown that abnormal extracellular deposition of self-assembled Aβ assemblies (i.e., Aβ oligomers, fibrils, and plaques) is the main pathological hallmark of AD.[2-4] According to the amyloid hypothesis,[2] the extracellular accumulation of these neurotoxic amyloid assemblies

activates inflammatory responses towards neurons and synapses, eventually causing their improper functioning during neuronal ionic homeostasis, ultimately leading to cognitive decline and other associated AD symptoms.[5,6] It is well known that Aβ42 polypeptide aggregates are the critical pathological determinant of AD and these widely serve as in vitro models for the screening of potent anti-amyloid drugs.[7,8] As we have already discussed in our previous chapters that purification, isolation, and self-assembly of the amyloid-β peptides generally involve arduous processes, and are often associated with several errors, which ultimately raise a concern about using these peptides as ideal in vitro amyloid models.[9] Hence, it is important to find an alternative, promising, convenient, short peptide-based model, which could mimic amyloid aggregation under in vitro conditions. It is further desirable that the model should not contain tedious protein isolation and purification procedures and can yield consistent and reproducible results is of paramount importance. Recently, amyloid aggregates generated by small amyloidogenic peptides such as a hexapeptide (NFGAIL) of human islet amyloid polypeptide (hIAPP), [10] heptapeptide (KLVFFAE) derived from Aβ42 polypeptide,[11]and the dipeptide, diphenylalanine (FF),[12] a core residue (F19-F20) of Aβ42 polypeptide have revolutionized the understanding of amyloid formation mechanisms. Among these peptides, the dipeptide FF, a fragment derived from the Aβ42 polypeptide, as reported by Gazit and group, is labeled as the smallest amyloidogenic peptide fragment endowed with many characteristics features of Aβ42 polypeptide aggregates, which include mechanical rigidity, photoluminescence and typical amyloid like structural and conformational features such as β-sheet like organization.[12] Thus, FF, a short and much simpler dipeptide, can be used as a surrogate amyloid model to mimic Aβ42 polypeptide aggregation, [13,14] and in the current study, we have tried to utilize FF fibrils as a reductionist model for exploring and establishing the potential amyloid inhibition propensity of DPVDF nanospheres.

Up to now, many anti-amyloidogenic agents have been reported to efficiently clear Aβ42 aggregates and also to destabilize their fibrils.[15] However, most of these agents exhibit weak disaggregation propensity against the Aβ42 aggregates. This happens due to the presence of strong intermolecular interactions between the Aβ42 monomers,[16] which promote the formation of robust fibrillar peptide aggregates under various physical,[17,18] chemical,[19,20] and biochemical conditions.[21] Thus, to dissolve/dislodge these comparatively robust fibrillar aggregates, it is highly desirable to look for more promising and innovative approaches for finding potential and viable therapeutic solutions for AD.

Piezoelectric materials can stimulate electrochemical reactions by enabling charge transfer to reactants under the influence of mechanical stimulus and are abundant in nature including live bio-physiological systems.[22] These carry significant utility in the field of material fabrication and in the field of the development of intelligent self-powered devices.[23,24] Several studies have demonstrated that piezoelectric materials are effective in generating electric stimulation-induced bio-effects with broad application potential.[25] In this regard, a biodegradable triboelectric nanogenerator (BD-TENG) has been designed by Zheng et al, which was capable of converting biomechanical energy into electric power that could be used to power implantable medical devices under in vivo conditions. The nanogenerator was found to be biocompatible and did not exhibit any adverse effects.[26] Furthermore, Liu et al. developed an implantable self-powered optogenetic system (SOS) for blood glucose control. The SOS system harvested energy from body movement and power from the far-red light (FRL) source.[27] Zhang et al. developed a biomechanical-energy-driven shape memory piezoelectric nanogenerator (sm-PENG) that was integrated with a fixation splint to promote osteogenic differentiation. The pulsed direct current (DC) generated from the sm-PENG effectively promoted MC3T3-E1 preosteoblast cell proliferation, orientation and increased the level of intracellular calcium ions.[28]

PVDF is a piezoelectric polymer extensively used in electro-optical, electromechanical, and biomedical applications. It is biocompatible in nature, exhibit high piezoelectric coefficient, and is cost-effective.[29] It is a semicrystalline polymer consisting of mainly four different polymorphic phases such as α, β, γ and δ.[30] Among them, α-phase is non-electroactive, β is the most electroactive phase, and γ is semi-electroactive. It is notable to mention that the δ phase remains less explored since its theoretical prediction. At the same time there are sparse reports which indicate that the δ phase has nearly comparable electroactive properties as that of the β phase.[31,32] Many fundamental properties of the piezoelectric δ-phase of PVDF nanospheres have been recently studied and reported by Mandal and co-workers.[33]

So far, various processing techniques are being harnessed to obtain different morphologies and electroactive phases of PVDF.[34] Micro/ nanosphere of PVDF can be synthesized by adopting various approaches, which include versatile techniques such as electrospraying, non-solvent induced phase separation, microdroplets formation, emulsion, and dispersion polymerization, gas atomization, oil-water emulsion and coacervation techniques.[35-41] In these reported studies, the fabrication of micro/nanospheres was primarily done using β, γ, and mixed electroactive phases, depending on the processing conditions and methodology. However, it is noteworthy that in this work, we have reported on the fabrication of PVDF nanospheres from pure δ-phase of the polymer, using a single-step processing technique. The obtained δ-PVDF nanospheres were demonstrated to exhibit piezo and ferro-electric properties as expected for the δ-phase of PVDF.

In the recent past, PVDF micro/nanostructures have been explored for various applications that include tissue engineering, in vivo implantable nanogenerators, etc.[42,43] We, thus in the current work, present a polydopamine coated piezoelectric PVDF (DPVDF) nanosphere-based system that is capable of disrupting amyloid fibrils merely under the influence of acoustic stimulus. Herein, due to the polar electroactive nature of the nanospheres, their

activation under acoustic stimulus led to the generation of electro-chemical and ROS mediated anti-amyloid effect (**Scheme 5.1**).[44-48] The potency of DPVDF nanospheres as anti-amyloidogenic agents was established by testing and validating their fibril dissociating ability towards the reductionist model-based amyloidogenic FF and Aβ42 polypeptide aggregates. It is interesting to note here that dopamine was used as a coating agent for PVDF nanospheres because under alkaline conditions, dopamine can self-polymerize (due to the oxidation of catechol) and generate polydopamine (PDA).[49,50] It can form a hydrophilic coating that firmly attaches to bulk materials of different surface properties and shapes.[51] Dopamine additionally has high adhesive properties [52] and hence it can strongly adsorb onto the spheres. Furthermore, the remarkable physicochemical, biocompatible and fluorescent properties of PDA render it suitable to be used as bioimaging agent, besides being used as a coating material.[53,54] In addition, we hypothesized that as dopamine has inherent anti-amyloid activity, [55] its presence would ultimately impart higher anti-fibrillating properties to the coated PVDF nanospheres.

The arena of piezoelectric-based disruption of AD is an emerging and pressing field with just one report showcasing the anti-amyloidogenic propensity of piezoelectric materials based on bismuth oxychloride (BiOCl) nanosheets.[44] We believe that the piezoelectric material triggered disruption of amyloid fibrils can be a potential and practical approach towards tackling the debilitating neurodegenerative disorder, AD. The process would open a huge possibility to be explored further to generate new and potent anti-amyloid and disease modifying therapeutics for AD.

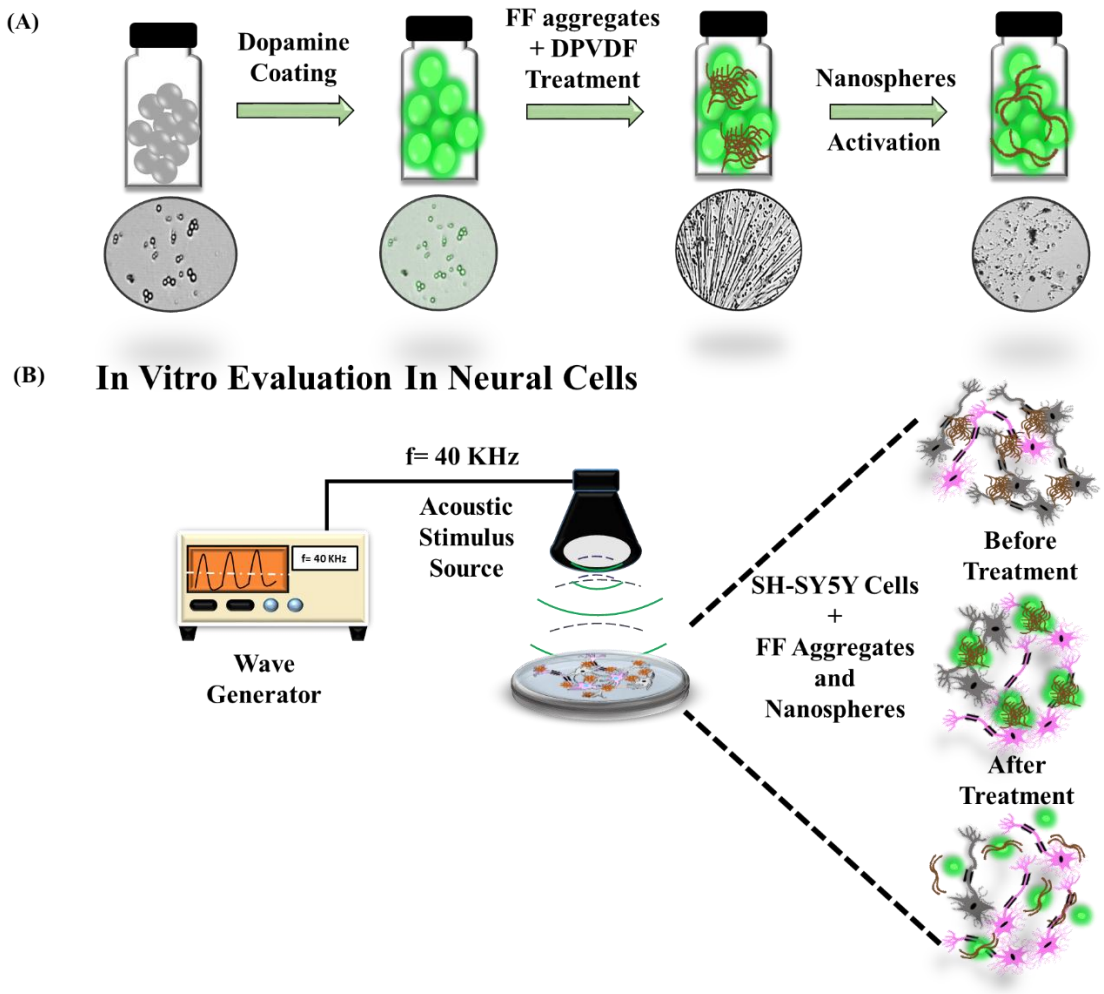

Scheme 5.1: (A) Overall schematic representation showing the formation of dopamine coated PVDF nanospheres. (B) Amyloid fibril disaggregation ability and neuroprotective effects exhibited by the coated nanospheres demonstrated in neural cells, on being activated by an acoustic stimulus.

5.2. Methods:

5.2.1. Preparation of PVDF nanospheres and their surface coating with polydopamine:

PVDF pellets (Mw~1,80,000) were procured from Sigma-Aldrich. Dimethylformamide (DMF) and acetone were procured from Merck chemicals. All the chemicals were used without any purification. PVDF pellets were dissolved in DMF: acetone solvent mixture in 6:4 ratios and a transparent solution was obtained after stirring the sample at 60 °C.

Electrospraying of the polymeric solution was carried out at 14 kV, keeping the constant 'tip to collector' distance as 12 cm. A 0.3 ml/h flow rate was employed for the synthesis of the nanospheres at an ambient temperature of 25 °C. 45 % humidity was maintained throughout the experiment. The produced δ-PVDF nanospheres were collected on an aluminium foil wrapped over the plate collector.

For fabricating a piezoelectric nanogenerator (PNG), 0.1 % (w/v) polydopamine-coated δ-PVDF nanospheres were blended in polydimethylsiloxane (PDMS) solution. The composite solution was cast on a clean glass slide (3 x 2.5 cm^2) and the slide was heated to 70 °C for three h. After heating, the composite film was peeled off from the glass slide and copper electrodes were adhered in a planar geometry on the composite film (**Figure 5.3**) named D-PNG (device-based PNG).

The PVDF nanospheres were coated with different concentrations of dopamine solutions (2, 4 and, 6 mg/mL), following a protocol mentioned earlier wherein, PVDF membrane was coated with dopamine.[56] The dopamine solution was formed by dissolving dopamine hydrochloride in tris-HCl buffer (15 mM, pH 8.8). The nanospheres (1mg) were then added to the prepared solution of dopamine and were incubated for 24 h on a rotary shaker. After 24 h, the mixture was centrifuged and rinsed with Milli-Q water several times at 14000 rpm to get rid of the loosely attached polydopamine particles and to obtain polydopamine coated PVDF nanospheres (DPVDF). The sample was subsequently dried and lyophilised using freeze drier to obtain dry powder. After rinsing, the nanospheres were probe sonicated for 10 min to get uniform PVDF nanosphere dispersion. As the coating was carried out under alkaline conditions, the self-polymerization of dopamine into polydopamine could not be overruled here and what we obtained finally could be the polydopamine coated PVDF nanospheres, henceforth named as DPVDF nanospheres.[57-60]

5.2.2. Characterization of PVDF and DPVDF nanospheres:

PVDF and DPVDF nanospheres were characterized by using different spectroscopic and microscopic techniques. The size and shape of δ-PVDF and DPVDF nanospheres were characterized by using Dynamic light scattering (DLS) and field emission scanning electron microscopy (FESEM). For DLS analysis, samples (1 mg mL^{-1}) were dispersed in milli Q water and their particle size were characterized by using a Malvern Zetasizer Nano ZSP Instrument.

For FESEM, samples (100 μg mL^{-1}) were drop casted onto silicon wafers and were air dried at 25 °C (RT). Thereafter, samples were gold coated for 90 s and were analysed by using FESEM (JSM-7610FPlus).

The polydopamine coating on the nanospheres was confirmed by using UV−visible (UV-Vis) spectroscopy, attenuated total reflection-fourier transform infrared (ATR-FTIR) spectroscopy and confocal microscopic, based studies.

A confocal microscope (ZEISS LSM 880) was also used to examine the fluorescent nature of the DPVDF nanospheres and also to monitor their intracellular uptake in SH-SY5Y cells.

Further, spectral properties of nanospheres were determined by a double beam Shimadzu UV-2600 spectrophotometer. Spectral measurements were carried out after suitably diluting the nanospheres dispersion (1 mg mL^{-1}) with milli Q water. ATR-FTIR (Attenuated total reflection-Fourier transform infrared) spectra of both PVDF and DPVDF nanospheres were also recorded using a Bruker VERTEX70 instrument (32 scans, from 4000− 400 cm^{-1}).

Surface potential determination and piezoelectric characterization of the nanospheres were done using kelvin probe force microscopy (KPFM) and piezo-response force microscopy (PFM) respectively. KPFM and PFM were performed using an AFM instrument, Nanosurf and Bruker Multimode-8 system, using Pt/Ir coated conducting probe, with spring constant of

3 Nm^{-1} and resonance frequency of 75 kHz. The KPFM measurements were performed in non-contact mode, while the PFM measurements were performed in contact mode. Samples for these measurements were prepared by using spin coating technique, in which uncoated and polydopamine coated PVDF nanospheres were drop casted on ITO coated glass substrates (5 mm × 5 mm) at 1500 rpm for 30 s. Furthermore, Finite element analysis-based simulation of PVDF nanospheres was performed by applying uniform external mechanical stimuli to the nanospheres assumed to be fixed at the base.

Moreover, the chemical similarity between PVDF and polydopamine coated PVDF nanospheres was examined using X-ray photoelectron spectroscopy (XPS). For the study, samples were drop cast on silicon wafers and loaded in UHV equipped X-ray photoelectron spectroscopy (XPS) (Kα, Thermo Fisher Scientific, USA) system, having Al-K_α energy source of 1486.5 eV. The XPS spectra for PVDF and DPVDF samples were recorded under the similar conditions.

5.2.3. Synthesis of FF and optimization of fibril formation by Aβ42 polypeptide and FF in vitro:

Boc-Phe-OH and L-phenylalanine were used for the synthesis of the dipeptide, FF, by using solution-phase peptide synthesis method as described in previous reports and thoroughly discussed in our previous chapters.[53,61,62]

In vitro fibrils formation by both FF and Aβ42 polypeptide was achieved by adopting similar protocols as reported earlier.[53,63] In brief, fibrils formation by FF was achieved by first dissolving 4 mg of the dipeptide in 50 μL of HFIP. The solution was then diluted in 950 μL of milli Q water to obtain fibrils. Aβ42 polypeptide fibrils were formed by dissolving 100 μg of Aβ42 polypeptide powder in 100 μL of HFIP solution to obtain monomeric form of Aβ42 polypeptide. For fibrillization initiation, HFIP was evaporated from the peptide solution to

attain a thin clear film of Aβ42 polypeptide and then the sample was resuspended in 100 μL of 10 mM phosphate-buffered saline (PBS, pH 7.4) and incubated for 3 days at 37 °C to obtain the fibrils.

5.2.4. Determination of the disaggregation propensity of PVDF nanospheres, DPVDF nanospheres and dopamine solution towards FF fibrils:

Light microscopy (ZEISS LSM 880) was used to establish and confirm FF fibrils formation and to determine the disaggregation potency of PVDF nanospheres, DPVDF nanospheres and dopamine solution towards FF fibrils. For disaggregation studies, FF fibrils (12 mM) were ultra-sonicated (at 40 kHz) for half an hour in the presence of PVDF nanospheres (1mg/mL), DPVDF nanospheres (2, 4 and 6 mg/mL) and dopamine solution (2, 4 and 6 mg/mL). After incubation, 50 μL dispersions from each sample (both control and treated) were drop casted onto cleaned glass slides and the samples were air dried at 25 °C (RT). Subsequently, coverslips were mounted onto glass slides and then analyzed using bright field microscopy.

5.2.5. Performing Bis-ANS assay to monitor fibril disaggregation propensity of DPVDF nanospheres:

The disaggregation potency of DPVDF nanospheres was also determined by Bis-ANS assay (50 μM). In brief, FF fibrils (12 mM) were ultrasonicated (at 40 kHz) with DPVDF nanospheres for half an hour. After treatment, 50 μM of Bis-ANS solution was added to all the control and treated samples and the samples were further incubated for the next 30 min at RT. After incubation, fluorescence intensity of the samples (Ex 405 and Em-440 nm) was determined using a Tecan, multimode plate reader.

5.2.6. Determination of disaggregation potency of PVDF and DPVDF nanospheres towards Aβ42 polypeptide fibrils

To evaluate the disaggregation potency of PVDF and DPVDF nanospheres towards Aβ42 polypeptide fibrils, Aβ42 polypeptide fibrils (20 μM) were prepared by adopting a similar protocol as mentioned earlier.[13] In disaggregation studies, PVDF and DPVDF nanospheres (800 μg/mL) were added to the prepared Aβ42 polypeptide fibrils. Samples were then ultra-sonicated (at 40 kHz) for half an hour. After treatment, samples were cast on carbon-coated copper grids (200 nm mesh size) and observed under the TEM, JEOL JEM-2100 transmission electron microscope at 120 kV (Tokyo, Japan).

5.2.7. Biocompatibility studies of PVDF and DPVDF nanospheres performed in L929 and SH-SY5Y cells both in the presence and absence of the acoustic stimulus:

Our in vitro disaggregation studies involved activation of the nanospheres by using a sonication frequency of around 40 kHz. However, in the case of cellular studies it is not practically feasible to use sonication as the medium for nanosphere activation. Hence, for cellular studies we used acoustic stimulus of similar frequency (40 kHz) to activate the nanospheres. A customised acoustic chamber of dimensions 16×27×24 cm^3 (capable of providing 2 W of acoustic power at 40 kHz frequency) was used for the studies **(Figure 5.1**). The biocompatibility of both acoustic stimuli activated and non-activated nanospheres of DPVDF and PVDF were determined in mouse L929 fibroblastic cell line (L929) and human neuroblastoma cell line (SH-SY5Y). For the study, L929 cells were cultured in fresh Dulbecco's modified Eagle's medium (DMEM) whereas SH-SY5Y cells were cultured in (DMEM)/F12 containing 10% fetal bovine serum (FBS), and 100 U/mL Pen-Strep at 37 °C with 5% CO_2 in a humidified incubator. Cells were trypsinized after achieving 80% confluency and then seeded in 96 well plates at a density of 10000 cells/well. After seeding, cells were incubated for 24 h for proper adherence and spreading. Thereafter, cells were treated with various concentrations of both PVDF and DPVDF nanospheres (0.4, 0.6 and 0.8 mg/mL) overnight. A customised acoustic chamber of dimensions 16×27×24 cm^3 (capable of

providing 2 W of acoustic power at 40 kHz frequency) was used to apply acoustic stimulus to the cells for a duration of 5 min after every one hour till 8 h to activate the nanospheres. Cells incubated with the nanospheres under identical cell culture conditions but without any stimulation were taken as non-activated control. Later on, both activated (exposed to acoustic stimulus) and non-activated (without stimulus) PVDF and DPVDF nanospheres treated cells were kept overnight in a humidified incubator and their viability was evaluated using MTT as well as live dead cell viability assay. For MTT assay, exhausted cell culture media (after treatment) were replaced by fresh culture media (180 µL) supplemented with 20 µL of MTT (5 mg/mL) and the sample was incubated further for 4 h. Afterwards, media were removed followed by DMSO (100 µL) addition to solubilize the formazan crystals. Sample absorbance was recorded using a multimode plate reader at a wavelength of 570 nm (MPlex Pro 200, Tecan Ltd.).

For the live/dead assay, cells were gently rinsed with PBS twice following treatment and subsequently stained with 2 µL mL^{-1} of calcein AM and PI (1 mg mL^{-1}) for 15 min. Afterwards, cells were rinsed with PBS gently to remove extra stains and were analyzed by confocal microscopy.

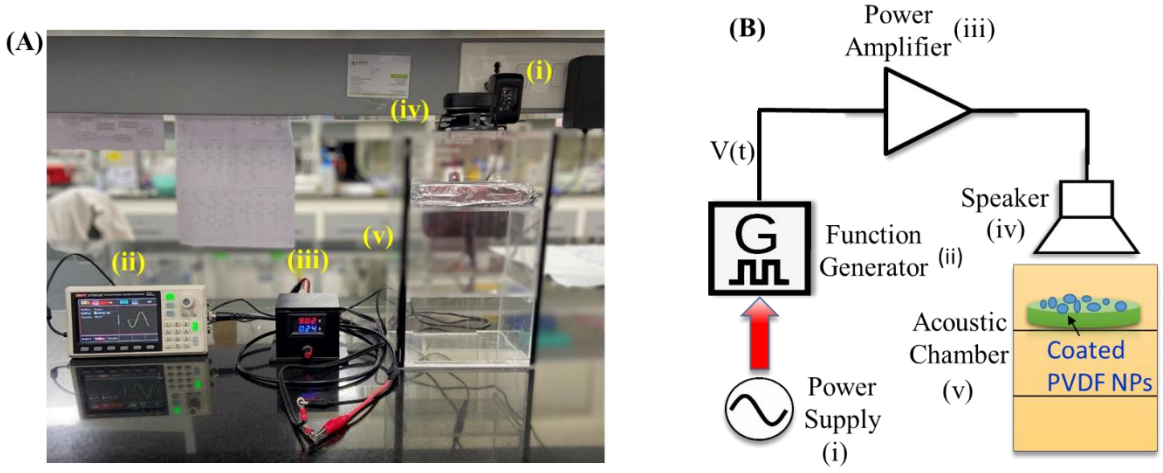

Figure 5.1: (A) Image showing the acoustic chamber used in the study for achieving acoustic stimulation-based activation of the nanospheres. (B) Equivalent circuit diagram consisting of (i) power supply, (ii) function generator, (iii) power amplifier and (iv) speaker for the mechanical stimulation to the acoustic chamber (iv) where the 'specimen of study' was placed.

5.2.8. Cellular uptake studies of DPVDF nanospheres performed in SH-SY5Y cells:

Cellular uptake studies of DPVDF nanospheres in SH-SY5Y cells were performed following protocol as reported in one of our earlier study.[53] In brief, SH-SY5Y cells were cultured in fresh DMEM/F12 containing 10% FBS, and 100 U/mL Pen-Strep at 37 °C with 5% CO_2 in a humidified incubator. Cells were then trypsinized after achieving 80% confluency followed by seeding in cell culture dishes (35 mm) at a density of 20000 cells/dish. After seeding, cells were incubated for 24 h for adherence and spreading. Next, cells were treated with DPVDF nanospheres (0.8 mg /mL) overnight. Afterward, treated cells were rinsed with PBS and fixed with 4% (v/v) paraformaldehyde (PFA) for 15 min. Fixed cells were stained with 1 μg/mL solution of 4',6-diamidino-2-phenylindole (DAPI) for 5 min, followed by rinsing with PBS to remove extra stains. Following this, cells were visualised under a confocal microscope (ZEISS LSM 880).[13]

5.2.9. Determination of cytotoxic effect of FF fibrils toward SH-SY5Y cells observed in the presence of acoustic stimulus activated or non-activated PVDF and DPVDF nanospheres:

The cytotoxicity of FF fibrils towards SH-SY5Y cells was determined using MTT assay. The protective effects exerted by different concentrations of PVDF and DPVDF nanospheres (0.4, 0.6 and 0.8 mg/mL) on neural cells against FF fibrils induced cytotoxicity, under both intermittent acoustic stimulus (5 min. after every one hour till 8h) and non-stimulus conditions, was also evaluated by MTT assay.[13] Briefly, 10×10^3 cells per well were plated in sterile 96-well microtiter plates in (DMEM)/F12 complete media and maintained overnight at 37 °C. Thereafter, cells were treated with fibrillar aggregates of FF (12 mM) in the presence as well as absence of different concentrations of PVDF and DPVDF nanospheres (0.4, 0.6 and 0.8 mg/mL) under both intermittent acoustic stimulus and non-stimulus conditions. After treatments, the exhausted culture media were replaced by fresh culture media (180 μL) supplemented with 20 μL of MTT (5 mg/mL) and the plate was further incubated for 4 h.

Afterward, media were removed followed by DMSO (100 μL) addition. Sample absorbance was recorded using a multimode plate reader at 570 nm (MPlex Pro 200, Tecan Ltd.).

5.2.10. Detection of the intracellular reactive oxygen species (ROS) generated by the PVDF nanospheres inside cells, both in the presence and absence of the acoustic stimulus:

To determine the ROS generating ability of the nanospheres, dichlorodihydrofluorescein diacetate (DCFH-DA) dye, was used as a fluorescent probe to measure the redox state of the cells exposed to the spheres both under activating and non-activating conditions.[64] Briefly, SH-SY5Y cells were incubated with various concentrations of PVDF nanospheres (0.4, 0.6 and 0.8 mg/mL) under both intermittent acoustic stimulus and non-stimulus conditions. Afterward, cells were treated with DCFH-DA (30 μM) for 45 min. After incubation, cells were gently washed with phenol free medium and were observed under a confocal microscope.

5.2.11. Determination of ROS generating ability of the nanospheres under non-cellular conditions:

To detect the ROS species generating ability of the nanospheres, Nitroblue tetrazolium test (NBT) and 3,3',5,5'-tetramethylbenzidine (TMB) assays were performed. NBT assay is generally used to detect the generation of superoxide ion in various samples.[65] NBT solution gets reduced by free oxygen radicals and blue color formazan product is formed. To monitor the generation of superoxide ion by the PVDF nanospheres, NBT solution (500 μM) carrying PVDF nanospheres (1mg/mL) was stimulated by acoustic stimuli for 30 min and 1 h. The relative amount of superoxide ion produced was further monitored by measuring sample absorbance at 560 nm. Furthermore, TMB assay was performed to detect the generation of hydroxyl radicals (•OH) by the decomposition of hydrogen peroxide (H_2O_2), by the nanospheres. [66,67] For •OH detection, PVDF nanospheres (1mg/mL) were treated with 1:1 ratio of TMB (20 mg/ml) and H_2O_2 (3%) for 30 min and 1h under both acoustic stimuli and

non-acoustic stimuli conditions. The relative amount of •OH radical produced in each sample was evaluated by measuring the sample absorbance at 655 nm using a spectrophotometer.

5.2.12. Biodistribution of DPVDF nanospheres in mice:

In order to examine the biodistribution of the DPVDF nanospheres in mice, the particles were first labelled with the near infrared active dye, indocysanine green and fluorescence imaging of the dosed animals was performed by using an *in vivo* fluorescence imaging system (IVIS Spectrum, PerkinElmer, U.S.) carrying IVIS live imaging 3.0 software at λex = 780 nm, λem = 850 nm. For *in-vivo* imaging, 50 μL of ICG-labeled nanospheres were administered through the intranasal route to mice, and fluorescent images of whole mice were taken at 1, 2,3, and 4 h, and isoflurane anesthetization (3% for induction and 1% for maintenance). Animal experiments were carried out ethically and humanely.

5.2.13. Statistical analysis:

Statistical analysis was performed using GraphPad Prism software and the data was plotted as mean ± standard deviation (SD). One-way and two-way analysis of variance (ANOVA) followed by Tukey's multiple comparison test were used to analyse the significant difference between the mean values of controls and nanospheres treated samples. Data were plotted as the mean of three (n = 3) independent samples ± SE and $p<0.05$ was considered to be statistically significant.

5.3. Results and discussion:

5.3.1. Polydopamine coating on PVDF nanospheres:

Dopamine coating on the nanospheres was achieved by dispersing PVDF nanospheres in dopamine solution (6 mg/mL) overnight as described above (methods). The biomolecule coating on the surface of PVDF nanospheres was confirmed through various biophysical techniques as shown in **Figure** 5.2. **Figure 5.2** (**A)** shows PVDF nanospheres before (left side) and after 6 mg/mL of dopamine coating (right side). The coated nanospheres were black in color compared to the white color of the uncoated nanospheres. DPVDF nanospheres were

further probe sonicated to obtain a better dispersed sample. DLS results showed that the PVDF nanostructures exhibited a mean hydrodynamic diameter of around 601 nm with a high polydispersity index (PDI) of 0.52. The high PDI of PVDF nanospheres could be attributed to the hydrophobic nature of non-dispersed nanospheres in water. DPVDF nanospheres however exhibited a mean hydrodynamic diameter of 941 nm with the PDI of 0.039 nm. Such a small PDI of the nanospheres reveal their monodisperse nature **(Figure 5.2 B, and C)**. Further, the fluorescence property of polydopamine coated nanospheres was also determined by confocal microscopy. Images demonstrated green-colored fluorescence on the particles after coating [**Figure 5.2 (D-F)].** As several earlier studies have reported that in an alkaline environment or oxidative stress, catechol group of dopamine gets oxidized to form quinone derivatives, and then the molecule auto polymerizes into fluorescent polydopamine structures at room temperature.[57-60] Therefore, it could be hypothesized here that under alkaline conditions or oxidative stress, dopamine polymerised on the nanospheres forming poly-dopamine layers which have been shown to carry fluorescence properties. The UV−Vis absorption spectrum of DPVDF exhibited strong absorption in the UV region, with an extending tail in the visible range. DPVDF nanospheres were also studied using fluorescence spectroscopy. The broad emission spectrum obtained for DPVDF in the visible range directly indicated the presence of fluorescent polydopamine coating (**Figure 5.2 G**).[54] However, it was observed that bare PVDF was non-emissive in the visible range. Furthermore, ATR-FTIR spectra also confirmed polydopamine coating on PVDF nanospheres. The IR absorption spectra of polydopamine coated PVDF nanospheres showed the presence of peaks that could be attributed to various functional groups present on dopamine. A broad absorption peak from 3100 to 3600 cm^{-1} can be assigned to the stretching vibration of -NH and -OH groups of dopamine catechol. In addition, the new absorption band at 1508 cm^{-1} corresponded to the vibrational bending of N-H bond in the indole group and 1595 cm^{-1} band corresponded to the C=C stretching vibrations of the aromatic ring respectively (**Figure 5.2 H**).

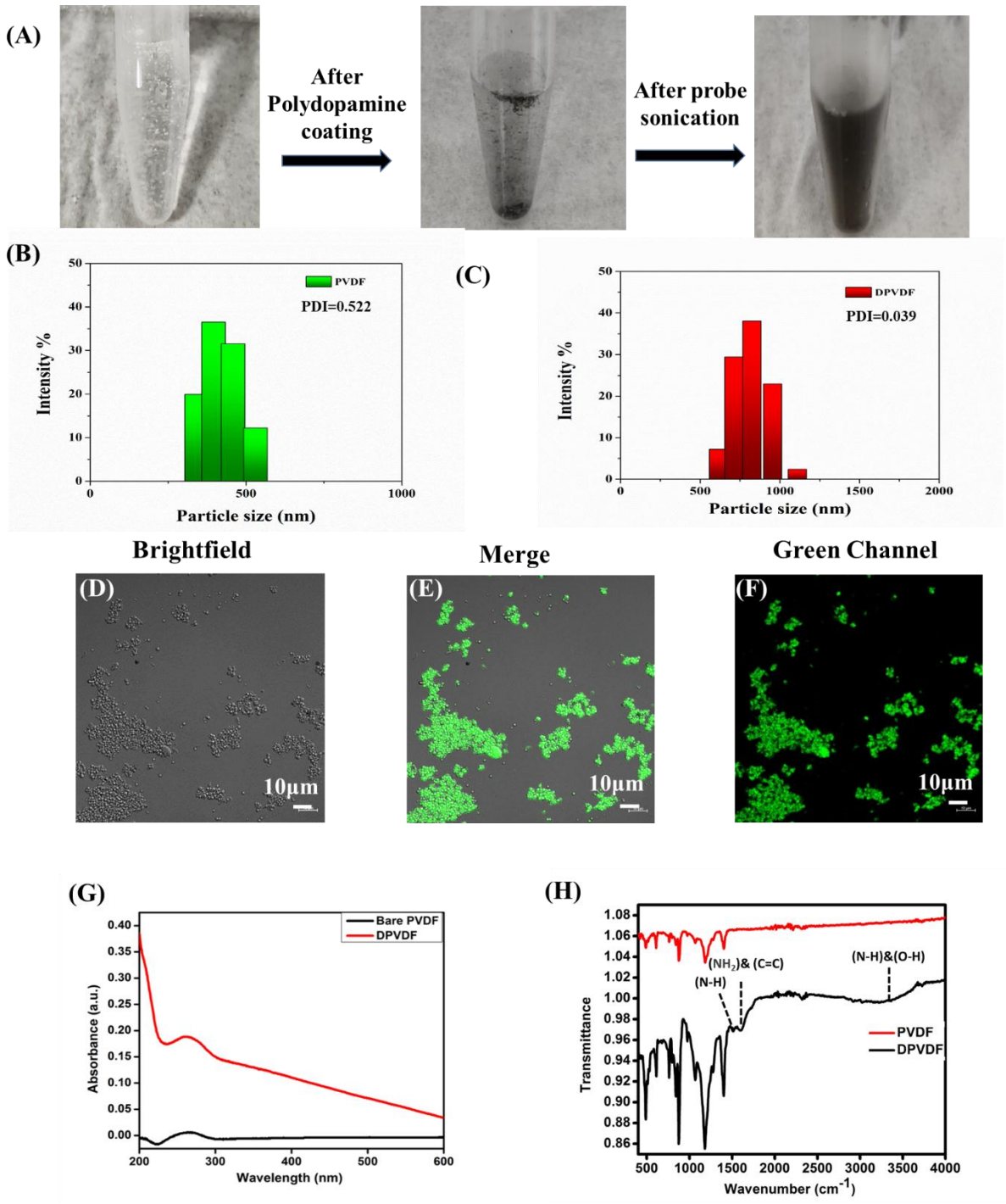

Figure 5.2: (A) Images showing PVDF nanospheres before and after getting coated with polydopamine, (B) DLS data of PVDF nanospheres, (C) DLS data of DPVDF nanospheres, (D) brightfield, (E) merge, and (F) green channel confocal images of polydopamine-coated PVDF nanospheres (scale bar~10 µm), (G) UV-Vis absorbance spectra of DPVDF and PVDF nanospheres, (H) ATR-FTIR spectra of DPVDF and PVDF nanospheres.

Furthermore, nanospheres were also characterised by using FESEM, KPFM, and XPS analysis (**Figure 5.3 and 5.4**). The FE-SEM images [**Figure 5.3 and 5.4 (A and B)]** of the PVDF and DPVDF nanospheres demonstrated a particle size of approx. 912 nm for PVDF nanospheres and approx. 963 nm for DPVDF nanospheres.

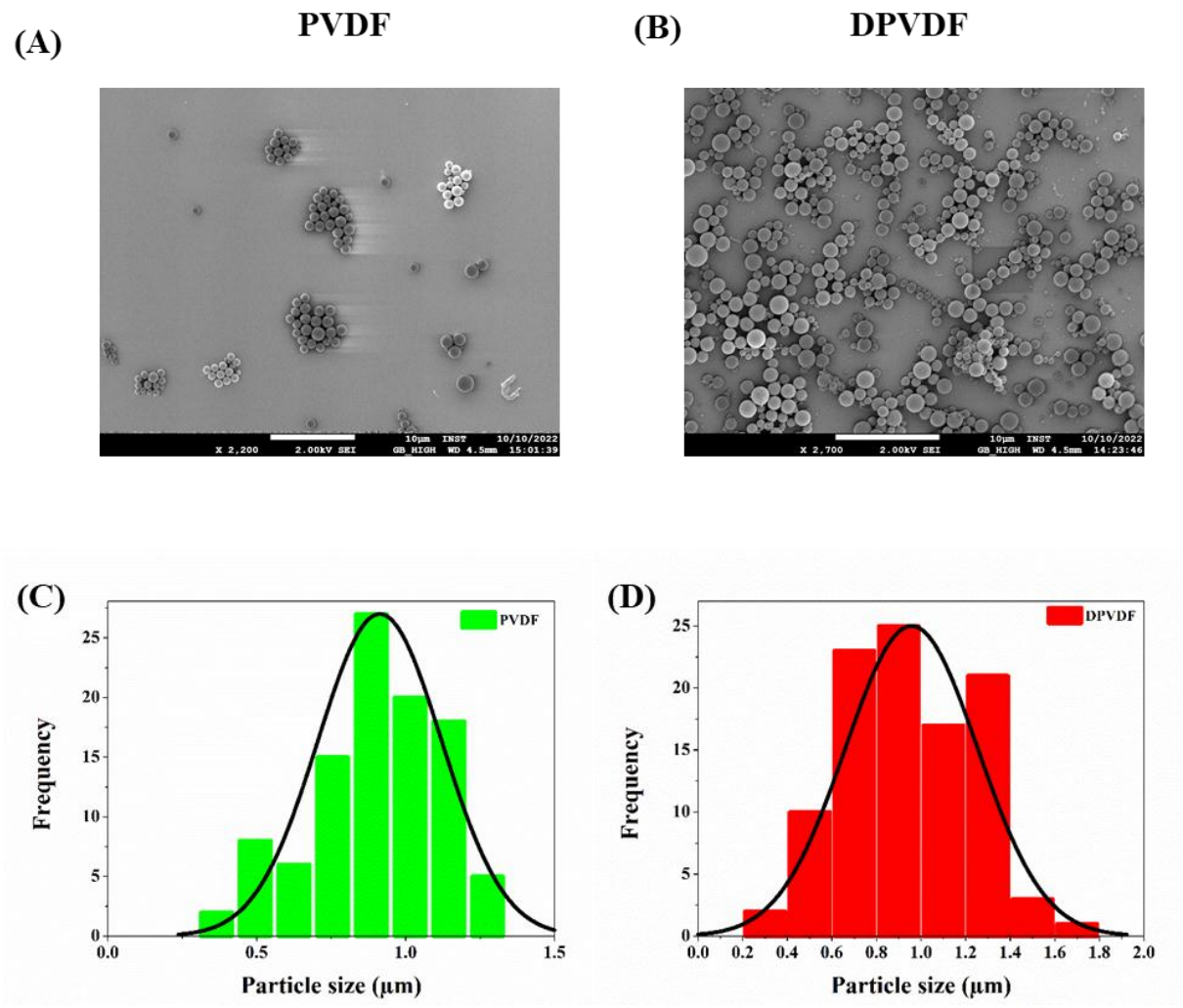

Figure 5.3: FESEM images of PVDF and DPVDF nanospheres (A and B), histogram showing the size distribution profile of PVDF (C) and DPVDF nanospheres (D) based on FESEM data (N=100).

Further, AFM topography and kelvin probe force microscopy (KPFM) were also performed to determine the surface potential of the nanospheres. **Figure 5.4 C** and **E** shows topography of nanospheres whereas, **Figure 5.4 D** and **F** shows surface potential of the nanospheres.

From KPFM images, the surface potential of PVDF nanospheres was found to be ~-25 mV (**Figure 5.4 D)**, while after the polydopamine coating it changed to ~45 mV (**Figure 5.4 F)**. This also confirmed positive surface modification of PVDF nanospheres with polydopamine. Moreover, to study the chemical composition and to strike any resemblance between PVDF and DPVDF nanospheres, X-ray photoelectron spectroscopy (XPS) was performed. In case of neat PVDF nanospheres [**Figure 5.4 G**, (upper panel)], for C 1s window, the two peaks at 286.6 eV and 291 eV, were attributed to -CH_2- and -CF_2- moieties of PVDF, respectively. These two peaks of C 1s, that could be ascribed as characteristic peaks of PVDF, had similar intensity (1:1), due to equal contributions emanating from both the groups. The XPS spectrum of DPVDF nanospheres (**Figure 5.4 G)**, (lower panel) as shown in the deconvoluted C 1s window, could be attributed to contributions emanating from carbon species of polydopamine. For instances, the presence of peaks corresponding to -C=O, -C-N, C-NH_2 groups (the signature peaks of dopamine) and the existence of low intensity peaks of -CH_2 and -CF_2 groups gave a clear indication of polydopamine coating on the PVDF nanospheres. [68,69] XPS spectrum of F 1s was also recorded for neat PVDF [**Figure 5.4 H**, (upper panel)] and for DPVDF [**Figure 5.4 H**, (lower panel)] at ~ 688.2 eV. The spectra showed that fluorine atoms were not affected by the presence of polydopamine. Further, we also obtained N 1s (**Figure 5.4 I)**, and O 1s (**Figure 5.4 J)**, spectra for DPVDF nanospheres, which verified uniform coating of polydopamine on PVDF nanospheres. Deconvoluted peaks of N 1s and O 1s demonstrated the existence of possible contributions from the polydopamine coating present over PVDF.

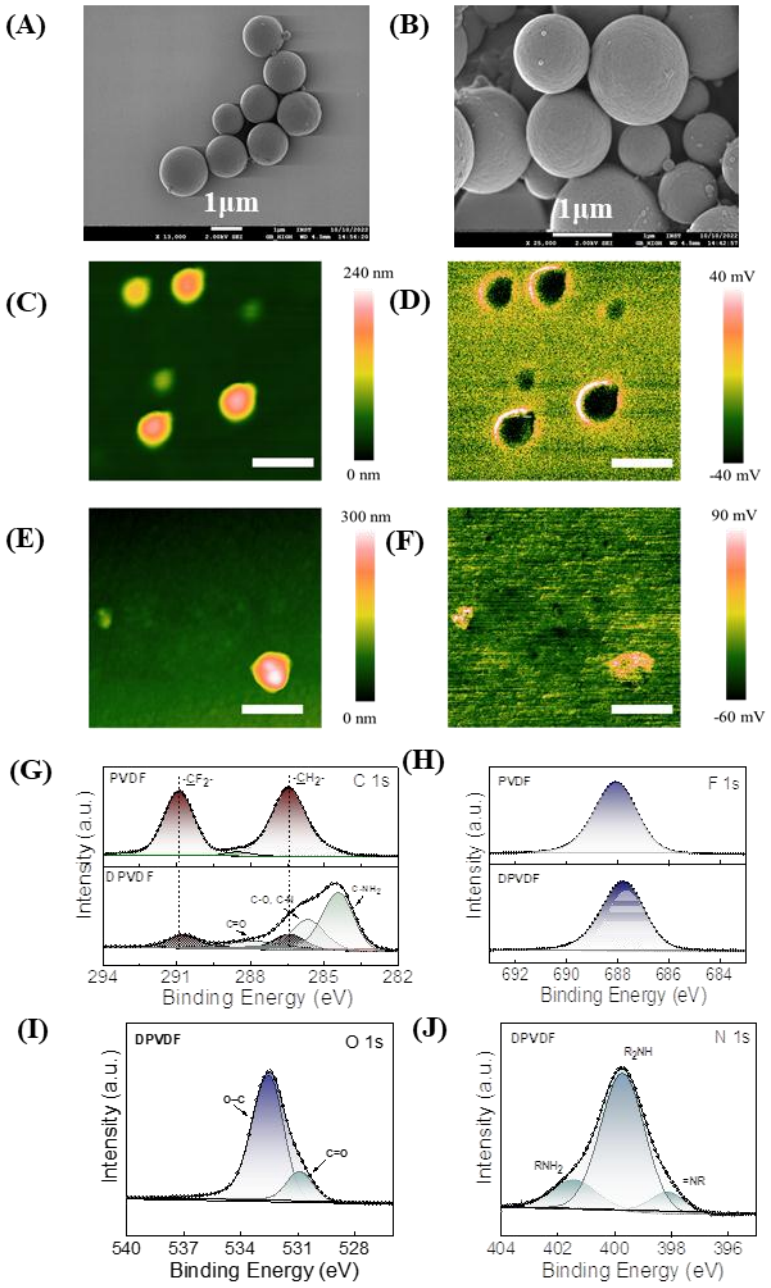

Figure 5.4: FESEM images showing spherical structure of (A) PVDF and (B) DPVDF (Scale bar is 1 µm). Surface potential characterization of nanospheres. Morphology and surface potential images of uncoated PVDF nanospheres as shown in (C), (D), and polydopamine coated nanospheres (DPVDF) as shown in (E), (F), respectively (Scale bar is 1 µm). Chemical resemblance of PVDF and DPVDF nanospheres as represented by XPS spectra. C 1s (G) and F 1s (H) XPS spectra of PVDF (upper panel)] nanospheres and (I) N 1s and (J) O 1s XPS spectra of DPVDF nanospheres (lower panel).

5.3.2. Determination of the Piezoelectric behaviour of DPVDF nanospheres:

To further ensure the piezoelectric nature of the DPVDF nanospheres, we fabricated a piezoelectric nanogenerator device (D-PNG) and successively studied the piezoelectric response of the coated nanospheres. The schematic of D-PNG fabrication is illustrated in **Figure 5.5 A**. Different periodic uniaxial bending strains were employed to determine the piezoelectric behaviour of D-PNG. It is evident from **Figure 5.5 B** that as the bending strain was increased, the voltage response of D-PNG also increased and reached up to 50 mV at 12 % of the bending strain.

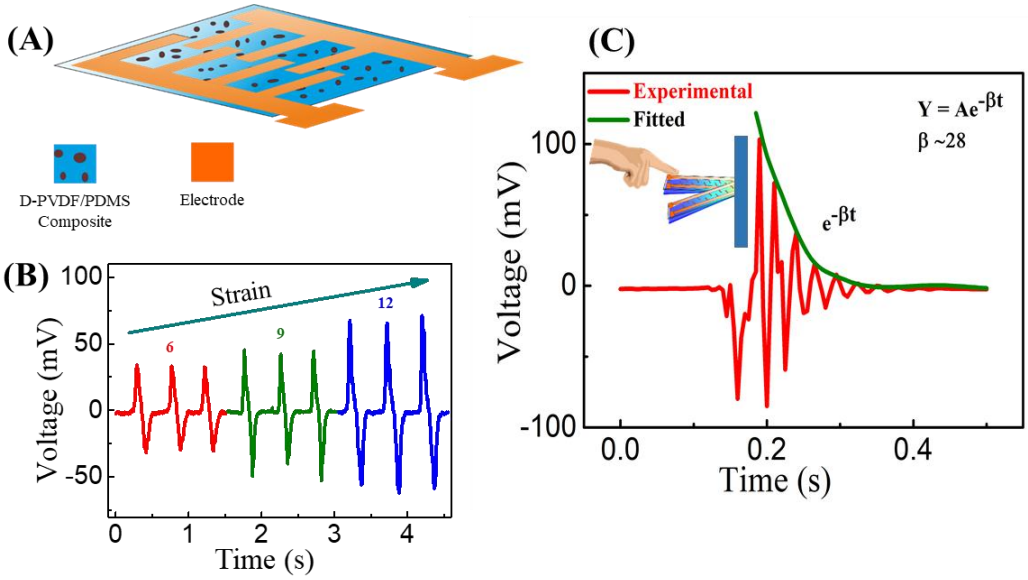

Figure 5.5: (A) Schematic diagram of D-PNG. (B) Voltage response of D-PNG obtained at different bending strains. (C) Output response of D-PNG as a vibration sensor. Inset shows the schematic of the measurement and the fitted equation with a damping coefficient of 28.

The exerted bending strain was calculated by following the given Equation (1).[70]

$$\varepsilon = \frac{h}{2r} \quad (1)$$

Where, h is the thickness of the D-PNG and r is the bending radius. Further, we investigated the ultrasensitive nature of D-PNG. It acted like a vibrational sensor [71,72] (**Figure 5.5 C),** after being mounted in a cantilever arrangement. It allowed the D-PNG to move freely under finger striking from 2 cm height. The damping behaviour of D-PNG

under finger imparting further confirmed its piezoelectric behaviour.[73] The D-PNG produced up to 100 mV of voltage response. After fitting, the equation to exponential function ($e^{-\beta t}$), a damping factor of 28 was obtained.

Next, finite element analysis (FEA) based simulation study was carried out for gaining a detailed insight into the piezoelectric nature of the PVDF nanospheres. Here, PVDF nanosphere was considered to be hinged at the base, and input mechanical stimuli of 100 $\frac{kN}{m^2}$ was applied (kindly note that here the nanosphere was considered to be hinged at the base to strike an analogy with the cellular experimentation studies) as shown in **Figure 5.6 (A)**, which gave rise to the internal strain within the PVDF nanosphere [**Figure 5.6 (B)**]. Due to the electroactive nature of PVDF nanosphere mechanical agitation led to the generation of piezoelectric potential as illustrated in **Figure 5.6 (C)**.

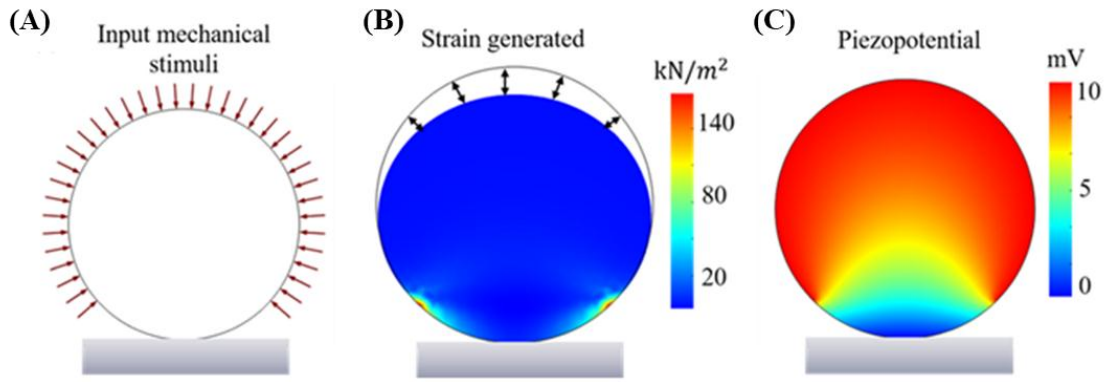

Figure 5.6: (A) Schematic demonstrating the input mechanical stimuli (shown by arrows) of 100 $\frac{kN}{m^2}$ provided to the PVDF nanosphere. (B) Strain generation within the nanosphere (as per FEA analysis) as a result of the input mechanical agitation (double headed arrows indicate the mechanical deformation caused due to the stimuli). (C) Piezoelectric potential generated in PVDF nanospheres due to strain generation under the mechanical stimuli.

Moreover, piezoelectric behaviour of the PVDF nanospheres was also demonstrated by using PFM. The butterfly (amplitude) loop and hysteresis (phase) loop from as prepared PVDF (**Figure 5.7 A** and **B)** and DPVDF (**Figure 5.7 C** and **D)** nanospheres were obtained. Butterfly (amplitude) loops in piezoelectric materials arise due the converse piezoelectric effect. In this case, when we applied the external electrical bias between the sample and the

AFM probe, we obtained an amplitude change as a local piezoelectric response manifested in terms of compression/expansion of the PVDF nanospheres.[74] Further, the obtained hysteresis loops response as shown in **Figure 5.7 A** and **C** were related to the ferroelectric response of the nanospheres for PVDF and DPVDF, respectively. As an external bias of -18 V to +18 V was applied, dipoles switching took place within the PVDF nanospheres, as 180□ phase shift, for both forward and reverse bias, resulting in the phase change under the electric field (**Figure 5.7 A** and **C)** as expected from a ferroelectric sample. Hence, from PFM results, it can be concluded that PVDF nanospheres were piezoelectric and ferroelectric in nature.

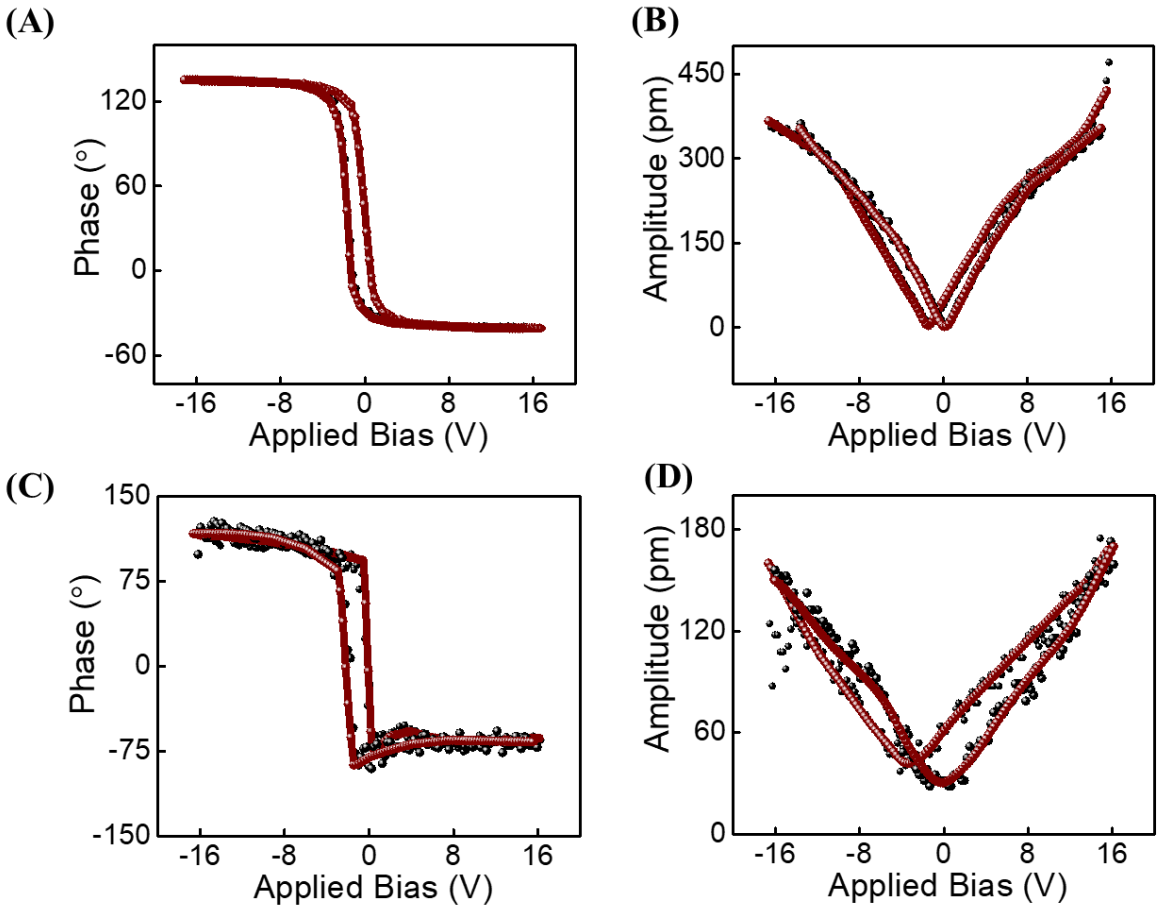

Figure 5.7: PFM (A) phase (hysteresis) and (B) amplitude (butterfly) response of neat PVDF nanospheres. PFM phase response (C) and amplitude response (D) of the DPVDF nanospheres.

5.3.3. Disaggregation of FF fibrils mediated by the polydopamine coated PVDF nanospheres:

We first synthesized the dipeptide, FF, using solution phase peptide synthesis methods.[53] Then, FF fibrils were formed by following a similar protocol as described earlier.[13] To examine the structure and morphology of FF fibrils, we performed bright field microscopic analysis (**Figure 5.8**). As depicted in **Figure 5.8 A**, fibril-like structures were observed for the peptide aggregates. After confirming the aggregation of FF fibrils, disaggregation studies were performed in the presence of DPVDF nanospheres by using bright-field microscopy. FF, an aromatic dipeptide derived from Aβ-polypeptide self-assembles to form amyloid aggregates. The dipeptide self-assembly is being propelled by various non-covalent interactions, that includes electrostatic, hydrophobic, hydrogen bonding, van der Waals and π-π stacking interactions.[75] The peptide assemblies carry specific alignment of dipoles based on their directional hydrogen-bonding and aromatic interaction-networks which may produce directed electrical polarization.[76,77] We would like to hypothesize here that the internal electric potential produced by activated piezoelectric DPVDF nanospheres upon mechanical perturbation such as ultrasonication [44] may interact with the polarised peptide assemblies and would interfere with their aggregating behaviour, thus serving as potential anti-amyloids. Hence, effects of activated nanospheres on the morphology of FF fibrils were examined using bright-field microscopy. Microscopic images of FF fibrils (1 mg/mL) confirmed the presence of dense fibrillar aggregates (**Figure 5.8 A** and **E)**. However, a morphological and structural transition of these aggregates from dense aggregated fibrils to unstructured small aggregates was evident, when the fibrils were treated with different concentrations of polydopamine coated activated nanospheres (2, 4 and 6 mg/mL for half an hour) [**Figure 5.8 (B-D)]**.

Whereas, these nanospheres did not show significant disaggregation of the fibrils in the absence of the mechanical perturbations [**Figure 5.8 (F-H)]**. Maximum disaggregation was observed in the case of 6 mg/mL polydopamine coated (DPVDF) and activated nanospheres as compared to 2 and 4 mg/mL samples.

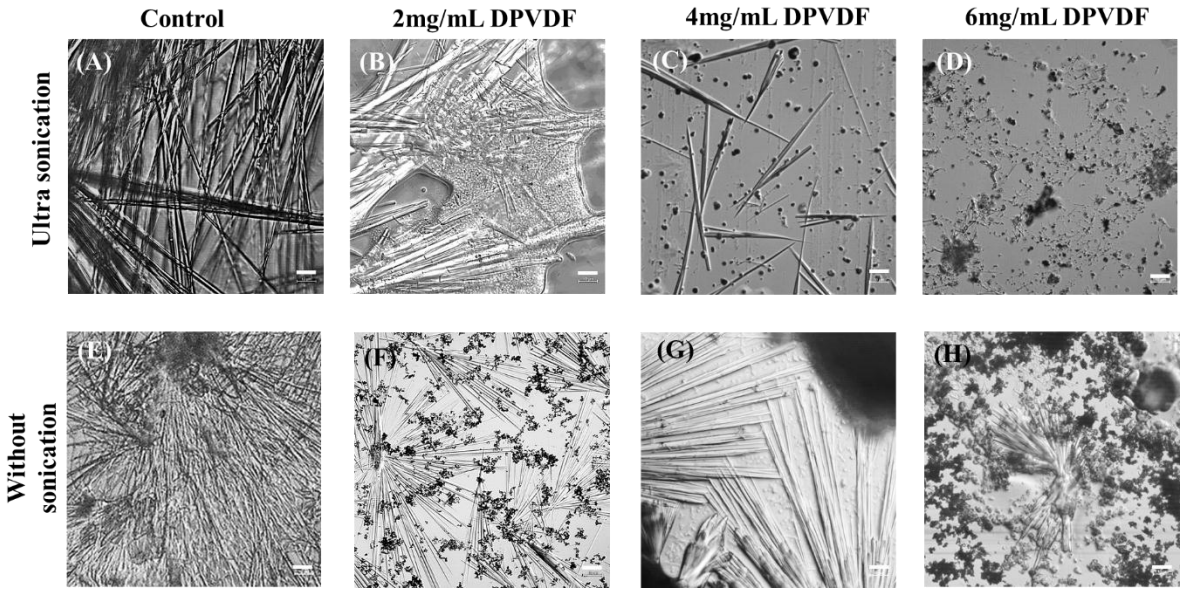

Figure 5.8: Brightfield microscopic images showing the structural and morphological transitions of FF fibrils [as shown in (A) and (E)] after being treated with different concentration of DPVDF nanospheres (2, 4 and 6 mg/mL) in the presence [as shown in (B-D)] and absence [as shown in (F-H)] of mechanical perturbations (ultra-sonication for 30 min). Scale bar is 10 μm.

Next, we also studied the quantitative disaggregation potential of DPVDF (6 mg/mL) nanospheres towards FF fibrils by Bis-ANS assay and a decline in the fluorescence intensity of the dye was detected when the fibrils were treated with the nanospheres (**Figure 5.9**). Thus, light microscopic and Bis-ANS results revealed that DPVDF nanospheres could effectively disaggregate FF amyloid fibrils which ultimately indicated the anti-amyloidogenic property of these nanospheres.

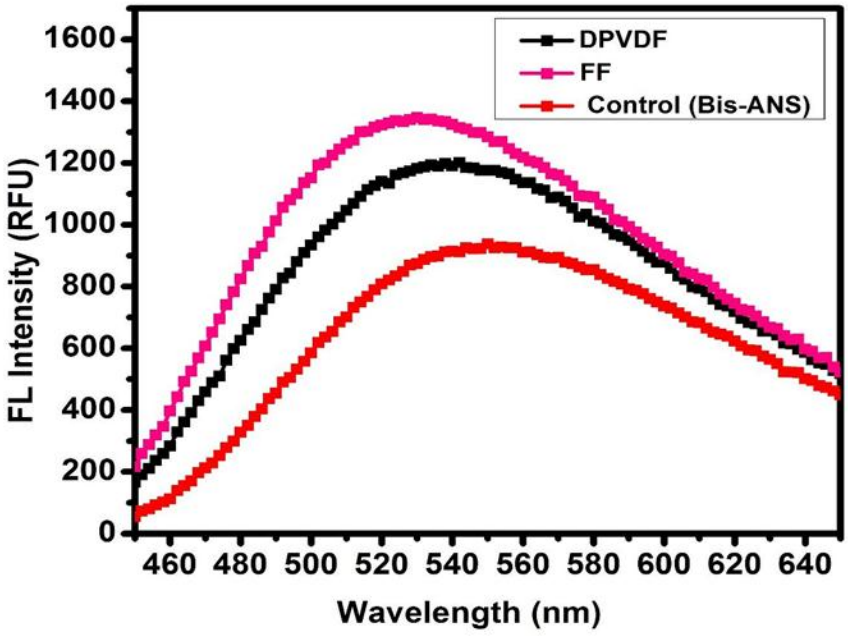

Figure 5.9: Bis-ANS assay showing disaggregation of FF fibrils in presence of activated DPVDF nanospheres.

5.3.4. Disaggregation of FF fibrils by DPVDF nanospheres, dopamine solution and PVDF nanospheres:

Disaggregation studies were carried out to determine the FF fibril dislodging behaviour of the coated and non-coated nanospheres towards FF fibrils**.** Maximum disaggregation was observed in case of activated DPVDF nanospheres, whereas only activated PVDF nanospheres and dopamine solution (6 mg/mL) under similar conditions did not show much disaggregation propensity [**Figure 5.10 (B-D)]**. Moreover, it was observed that DPVDF nanospheres without mechanical perturbation showed very limited disaggregation potency towards FF fibrils (**Figure 5.10 F)**. The potential anti-fibrillizing effect of the DPVDF nanospheres observed here could be attributed to the summation of inherent anti-amyloid activity of dopamine [55] along with the peizocatalysis triggered anti-amyloid effect presented by the PVDF nanospheres. It was further worth noticing that uncoated nanospheres (**Figure 5.10 C** and **D)** and only dopamine solution (**Figure 5.10 G** and **H)** did not show any significant disaggregation of the peptide-fibrils in the presence or absence of the mechanical perturbations (ultra-sonication).

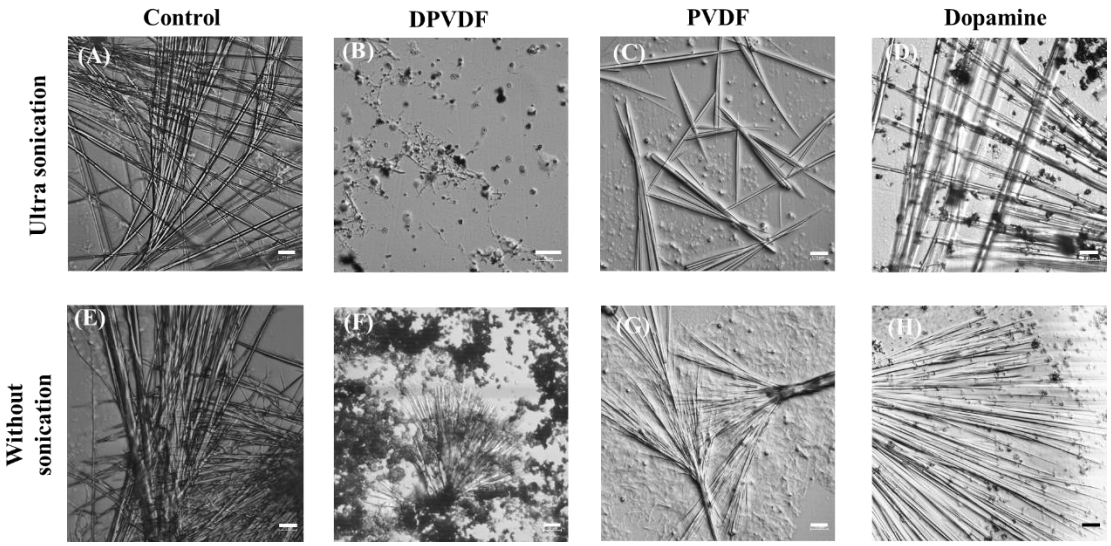

Figure 510: Microscopic images showing the structural and morphological transitions occurring in FF fibrils [as shown in (A) and (E)], after being treated with DPVDF nanospheres [demonstrated in (B) and (F)], PVDF nanospheres [as shown in (C) and (G)], and dopamine solution; [as shown in (D) and (H)]. Experiments were done in the presence and absence of mechanical perturbations (Sonicating power; 40 kHz for half an hour). Scale bar is 10 μm.

We next explored the disaggregating potency of the nanospheres towards Aβ42 polypeptide fibrils. For the study, Aβ42 polypeptide fibrils (20 μM) were incubated with activated DPVDF nanospheres (0.8 mg/mL) and PVDF nanospheres (0.8 mg/mL) for a period of half an hour. As shown in **Figure 5.11 A**, structural transition of Aβ42 polypeptide fibrils from dense aggregates (**Figure 5.11 A** and **B)** to small unstructured morphologies was observed in the presence of PVDF nanospheres (**Figure 5.11 C**). However, interestingly almost all Aβ42 polypeptide fibrils got disaggregated (**Figure 5.11 D)** in the presence of DPVDF nanospheres under activating conditions. Hence, it can be assumed here that the piezoelectric properties of the nanospheres also contributed to the anti-amyloidogenic activities of dopamine. Similar anti-fibrillation activities have also been earlier obtained in case of piezoelectric bismuth oxychloride nanosheets, where they have been shown to disaggregate Aβ42 polypeptide fibrils.[44] The anti-fibrillation effect of these piezo-active nanostructures could be attributed to their ability to generate ROS response. Such observation can be supported by earlier studies

which demonstrated that oxidation of methionine (Met-35) in Aβ polypeptide not only altered the morphology of amyloid fibrils but also prevented their formation.[45-47] ROS species generated disaggregation of Aβ aggregates has also been earlier observed in case of photoactivated bPEI@CDs.[48]

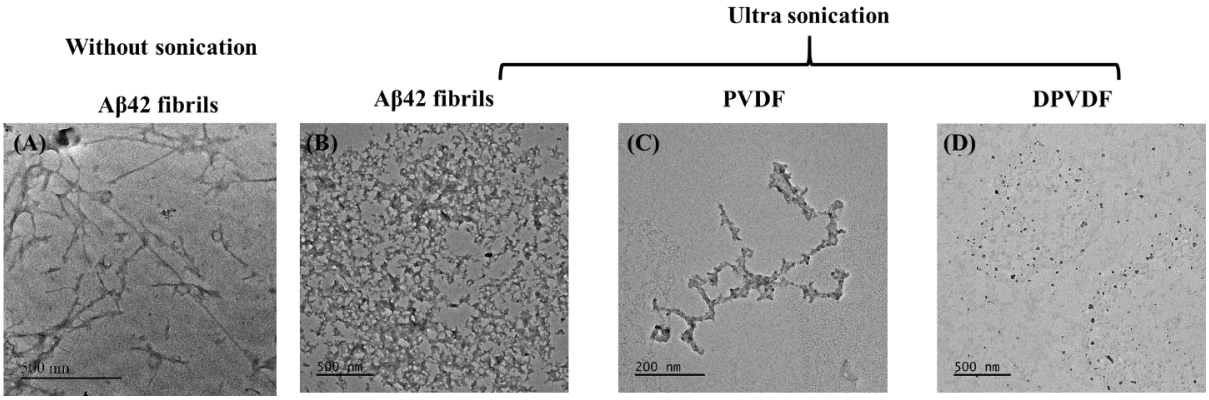

Figure 5.11: TEM images showing the morphological changes occurring in Aβ42 polypeptide fibrils in presence of the activated nanospheres. (A) Aβ42 polypeptide fibrils and (B), Aβ42 polypeptide fibrils exposed to sonication. (C)Aβ42 polypeptide fibrils after being treated with sonication activated PVDF nanospheres. (D) Aβ42 polypeptide fibrils after being treated with sonication activated DPVDF nanospheres.

5.3.5. Biocompatibility studies of PVDF and DPVDF nanospheres performed in L929 and SH-SY5Y cells in both the presence and absence of acoustic stimulus:

Biocompatibility of both the coated and uncoated nanospheres under acoustic stimulus and non-stimulus conditions were performed in fibroblast (L929) and neuroblastoma (SH-SY5Y) cells and their cellular viability was determined by MTT and live dead assays. As shown in **Figure 5.12 (A-H),** the nanospheres were found to be non-cytotoxic in nature under both activating and non-activating conditions. Moreover, it has been observed that DPVDF nanospheres exhibited higher biocompatibility when being compared to activated PVDF nanospheres in both cell lines. This could be attributed towards their higher water dispersibility and the presence of the more biocompatible polydopamine coating. Thus, these nanoparticles were safe to be used for further biomedical applications.

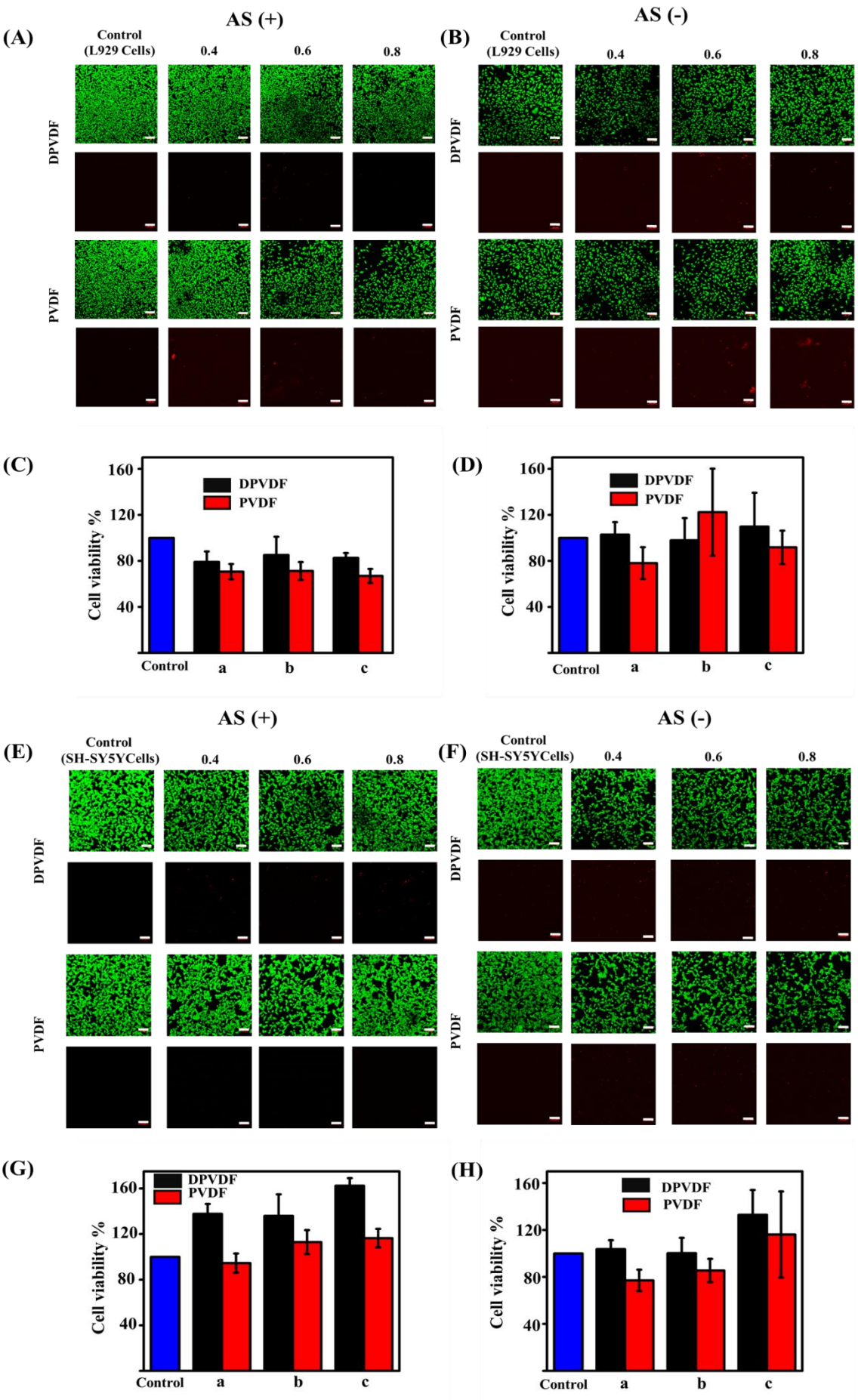
(A)
AS (+)
Control (L929 Cells)
0.4
0.6
0.8
DPVDF
PVDF
(B)
AS (-)
Control (L929 Cells)
0.4
0.6
0.8
DPVDF
PVDF
(C)
Cell viability %
160
120
80
40
DPVDF
PVDF
Control
a
b
c
(D)
Cell viability %
160
120
80
40
DPVDF
PVDF
Control
a
b
c
(E)
AS (+)
Control (SH-SY5YCells)
0.4
0.6
0.8
DPVDF
PVDF
(F)
AS (-)
Control (SH-SY5YCells)
0.4
0.6
0.8
DPVDF
PVDF
(G)
Cell viability %
160
120
80
40
DPVDF
PVDF
Control
a
b
c
(H)
Cell viability %
160
120
80
40
DPVDF
PVDF
Control
a
b
c

Figure 5.12: Calcien AM/PI and MTT results showing biocompatibility of PVDF and DPVDF nanospheres determined in the presence (AS +) or absence (AS -) of acoustic stimulus. (A and B) Confocal microscopic images showing biocompatibility of activated and non-activated PVDF and DPVDF nanospheres towards L929 cells determined by live dead assay (Calcien AM/PI staining) at the scale of 100 μm; (C and D) Biocompatibility of PVDF and DPVDF nanospheres towards L929 cells determined by MTT assay (a = 0.4 mg/mL, b = 0.6 mg/mL, c = 0.8 mg/mL). (E and F) Confocal images showing biocompatibility of PVDF and DPVDF nanospheres towards SH-SY5Y cells examined by live-dead assay (Calcien AM/PI staining). Scale bar: 100 μm. (G and H) Biocompatibility of nanospheres towards SH-SY5Y cells determined by MTT assay (a = 0.4 mg/mL, b = 0.6 mg/mL, c = 0.8 mg/mL).

5.3.6. Cellular uptake studies of DPVDF nanospheres performed in SH-SY5Y cells:

In order to target the cellular amyloids, it is expected that the nanospheres should possess a decent ability to enter the neural cells. Thus, we next tried to determine the intracellular uptake of DPVDF nanospheres in SH-SY5Y cells using confocal microscopy. The inherent fluorescence imparted to the structures by the polydopamine coating aided in tracking the particles inside the cells without any further labelling.[78,79] The green fluorescence detected in the cytoplasm of DPVDF nanospheres treated cells confirmed successful uptake of these nanospheres and accumulation of the self-fluorescent DPVDF nanospheres inside them (**Figure 5.13 A)**.

5.3.7. Neuroprotective effect exhibited by DPVDF nanospheres against FF-induced cytotoxicity in SH-SY5Y cells:

To examine whether PVDF and DPVDF nanospheres could alleviate the neurotoxicity of FF fibrils towards SH-SY5Y cells, we incubated the cells with amyloid aggregates of FF (12 mM) in the presence of different concentrations of PVDF and DPVDF nanospheres (0.4, 0.6 and 0.8 mg/mL) under both intermittent acoustic stimulus (5 min. after every one hour till 8 h) and non-stimulus conditions. Cellular viability was next determined by using MTT assay. Cells incubated with only FF aggregates were taken as control. The mechanical perturbations experienced by the polydopamine-coated spheres under acoustic stimulus triggered their piezoelectric properties

generate heightened anti-amyloid activities. This led to enhanced protection of the neuronal cells from the FF fiber mediated toxicity as compared to PVDF nanospheres. It was further detected that FF fibrils alone caused toxicity to the cells; however, when these cells were simultaneously treated with DPVDF nanospheres and FF fibrils, the cell death rate and death percentage was significantly abrogated (**Figure 5.13 C** and **D)**. A parallel elevation in the levels of cell viability was also noticed when the neural cells were treated with an increasing concentration of polydopamine coated nanospheres (DPVDF) vs similar concentrations of PVDF nanospheres under both acoustic stimulus as well as non-acoustic stimulus conditions.

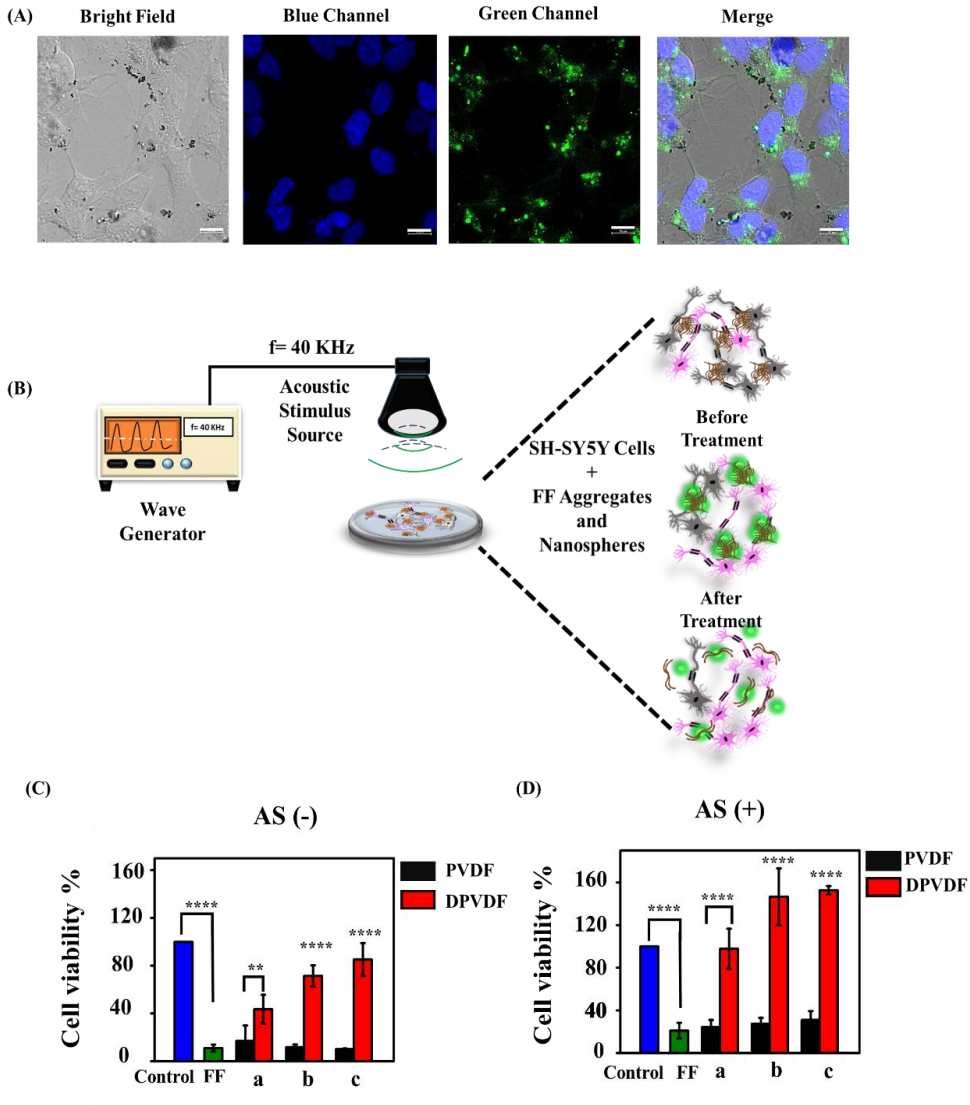

Figure 5.13: (A) Confocal microscopic images depicting cellular uptake of polydopamine coated nanospheres in SH-SY5Y cells (scale bar~10 μm). (B) Schematic representation

showing the neuroprotective effects exhibited by the coated nanospheres demonstrated in neural cells, on being activated by an acoustic stimulus. (C) MTT results showing neuroprotective effects of non-activated (without exposure to acoustic stimulus) PVDF and DPVDF nanospheres (a = 0.4 mg/mL, b = 0.6 mg/mL, c = 0.8 mg/mL) against FF fibrils (12mM) induced toxicity in SH-SY5Y cells. (D) MTT results showing neuroprotective effects of sono-activated (placed under acoustic stimulus) PVDF and DPVDF (a = 0.4 mg/mL, b = 0.6 mg/mL, c = 0.8 mg/mL) nanospheres against FF fibrils (12mM) induced toxicity in SH-SY5Y cells. One-way analysis of variance (ANOVA) followed by Tukey's multiple comparison test were used to analyse the significant difference between the mean values of controls and treated samples; results are presented as mean ± SD. *$p < 0.05$, **$p < 0.01$, ***$p < 0.001$, and ****$p < 0.0001$ when nanospheres treated cells were compared with control groups.

5.3.8. Determination of ROS generation ability of piezoelectric PVDF nanospheres under in vitro conditions and in SH-SY5Y cells:

Piezoelectric materials create a built-in electric field that can separate electrons and holes.[22] In an aqueous medium, these charge carriers promote the generation of reactive oxygen species (ROS) like superoxide radicals (•O2−), and hydroxyl radicals (•OH). Though ROS generate harmful effects on cellular components like proteins, nucleic acids, lipids,[80] these can have numerous applications in the field of medical science, pollution control etc.[81] Additionally, various studies have reported that at low or moderate concentrations, free radicals play several beneficial roles in living organisms. For example, they are required to synthesize many cellular structures and are used by the host defence system to fight pathogens. Newer models describing the role of ROS in cell, suggest that a moderate elevation in ROS can be favourable to an organism, conceivably through the activation of cellular stress response signalling pathways.[82,83] In fact, phagocytes synthesize and store free radicals, in order to be able to release them when they aim towards destroying invading pathogenic microbes.[84,85] Free radicals are also involved in a number of cellular signaling

pathways.[86-88] Additionally, in one report by Chung et. al, branched polyethylenimine coated carbon nanodots (bPEI@CDs), have been shown to disintegrate Aβ aggregates by ROS-mediated photooxidation of Aβ peptides.[48] Thus, the ability of peizoelectric materials to generate ROS species, may in turn cause oxidation of the Aβ residues, thus lessening the peptide aggregation and fibril formation propensity. A report by Jang et al, suggested that piezoelectric materials like bismuth oxychloride (BiOCl) nanosheets were capable of dissociating Aβ fibrils due to the piezocatalytic induced generation of reactive oxidative species mediated by the sono-activated nanosheets.[44] Thus, we further investigated the ROS generation ability of the PVDF nanospheres by using NBT, TMB dye under in vitro conditions and by using the fluorescence probe, DCFH-DA, in neuroblastoma cells. NBT assay, is being used to detect the generation of superoxide ions in different samples.[65] As shown in **Figure 5.14 A**, the generation of superoxide ion was evident when NBT solution was treated with activated PVDF nanospheres as compared to non-activated nanospheres. Furthermore, TMB assay was performed to detect the generation of hydroxyl radicals (•OH), by the decomposition of H_2O_2, by the nanospheres. TMB, a chromophoric substrate usually chosen in nano-peroxidase mimetic experiments, was selected as a substrate to be oxidized and to detect ROS radicals (•OH) in the present study.[66,67] In presence of H_2O_2, the nanospheres catalyzed H_2O_2 to generate hydroxyl radicals. For •OH detection, each sample containing PVDF nanospheres, TMB and hydrogen peroxide was incubated for a period of either 30 min or 1 h under both acoustic stimulus activation and non-stimulus conditions. It was clearly observed that the activated PVDF nanospheres catalysed the oxidation of TMB and produced blue color in the presence of •OH as compared to non-activated PVDF nanospheres. Control reactions performed in the absence of PVDF nanospheres displayed negligible color changes over similar time duration as the nanosphere groups, indicating that our nanospheres, like natural oxidase and peroxidase, were responsible for TMB oxidation (**Figure 5.14 B**). In addition, we further explored the ROS generating ability of the PVDF nanospheres by using a fluorescence probe, DCFH-DA, in neuroblastoma cells**.** As shown in

Figure 5.14 C, we observed that the cells treated with PVDF nanospheres under acoustic stimulus conditions, generated a strong green colored fluorescence which directly correlated with the generation of efficient ROS whereas, those treated with PVDF nanospheres under non acoustic stimulus conditions showed no fluorescence indicating that the absence of the production of any ROS species. Thus, our in vitro results clearly confirmed that the nanospheres were capable of generating reactive oxygen species under activating conditions which ultimately caused the ROS mediated disaggregation of amyloid polypeptide fibrils as reported earlier.[45-48]

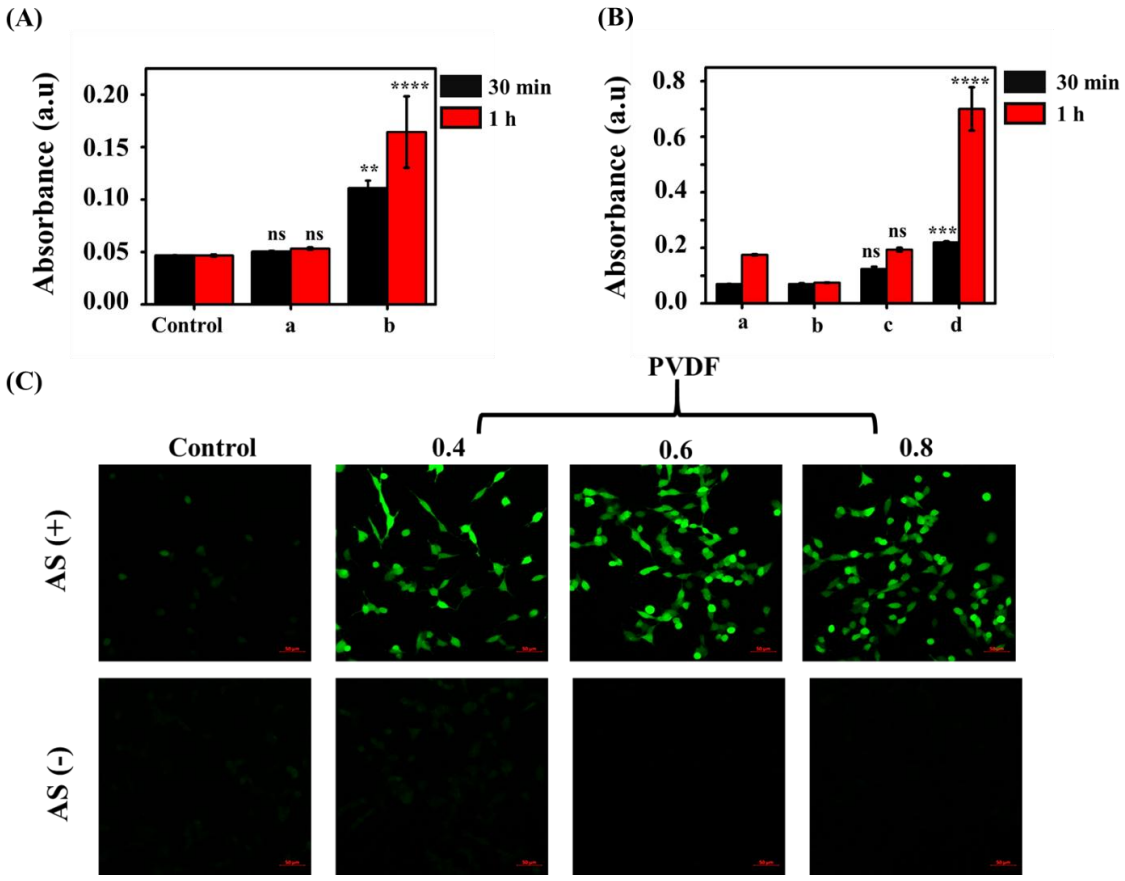

Figure 5.14: (A) Data showing generation of ROS using NBT assay, where 'a' represents the ROS generated by non-activated nanospheres after 30 min and 1 h and 'b' represents ROS generated by activated nanospheres after 30 min and 1 h of exposure to the acoustic stimuli. (B) TMB assay results, where 'a' represents ROS generated by TMB and H_2O_2 solution without nanospheres, 'b' represents ROS generated by only TMB solution and nanospheres, 'c; represents

ROS generated by TMB, H_2O_2 solution and nanospheres in the absence of acoustic stimulus, and 'd' represents ROS generated by TMB, H_2O_2 solution and nanospheres after 30 min and 1h exposure of the acoustic stimulus. (C) Confocal images showing ROS produced by different concentrations of PVDF nanospheres under acoustic stimulus and non-stimulus conditions (scale bar 50 μm). Two-way analysis of variance (ANOVA) followed by Tukey's multiple comparisons were used to analyse the significant difference between the mean values of controls and treated samples; results are presented as mean ± SD. *$p < 0.05$, **$p < 0.01$, ***$p < 0.001$, and ****$p < 0.0001$ when treated samples were compared with control groups.

Overall, our current work embodies the potential disaggregation of amyloid peptide fibrils by means of mechanically activated DPVDF nanospheres. These mechanical stimulus-activated DPVDF nanospheres exhibited piezocatalysis properties upon being stimulated by sonication power (40 kHz). The nanospheres effectively dissociated fibrils formed by the model amyloid peptides, FF and Aβ42, into very short globular debris. We propose the probable mechanism of the disaggregation of these fibrils to involve piezocatalysis induced electrochemical interactions, ROS generation (by the mechanical stimulus-activated peizo-active nanospheres) along with the fibril disaggregating effect mediated by the coated polydopamine molecule. Based on the in vitro results we expect a fruitful translation of these systems as anti-amyloid agents under in vivo conditions. For in vivo applications, the piezoelectric materials could be activated by various mechanical stimulation sources, including vibration plates, sounds, and ultrasounds (USs) as well as by the mechanical energy produced by our body movements.[89-91] Using mechanical energy scavenging, sufficient power can be provided to ensure long-term autonomy for self-powered systems.[92,93] For example, around 10 mW power can be harvested from the motion of the upper limbs, 1 mW can be obtained from a typing motion, breathing generates around 100 mW power and, by walking, we generate a power of up to 1W.[94]

In the current work, we have demonstrated the generation of piezoelectric response by the polydopamine-coated nanospheres under acoustic stimuli. We can very well assume that the appropriate activating frequency generated from various bodily motions would trigger the initiation of a desirable piezoelectric effect by the nanospheres inside our body. Additionally, the subjects can also be exposed to specific acoustic stimulus to generate the desirable response. This will enable the purposeful utility of our systems as potential therapeutic modalities specially in combating Alzheimer's disease as exemplified by us in the current work.

5.3.9. Determination of in vivo biodistribution of DPVDF nanospheres in mice brain:

As previously reported that the intranasal route of drug administration offers numerous advantages, such as bypassing the blood-brain barrier and providing a direct entrance to the brain through the olfactory and trigeminal neurons and the route can be used for the delivery of different micro- and nanoscale nose-to-brain drug-delivery systems for the treatment of Alzheimer's and Parkinson's disease.[95] Thus, we used the intranasal route for the administration of the near active dye, indocyanine green loaded particles (ICG-labeled DPVDF nanospheres) in mice and performed fluorescence *in-vivo* imaging analysis to determine their ability to reach the brain tissues. Fluorescence images of the animals administered with ICG-labeled DPVDF nanospheres were taken at different time points utilizing IVIS. As shown in **Figure 5.15**, we got positive fluorescent signals captured in the brain areas of treated mice which were retained in the brain tissues for the tested duration, confirming the successful penetration of ICG-labeled DPVDF nanospheres in the brain tissues. Thus, the nanospheres showed significant delivery and retention in brain tissues as directly evident from the IVIS images of the animals.

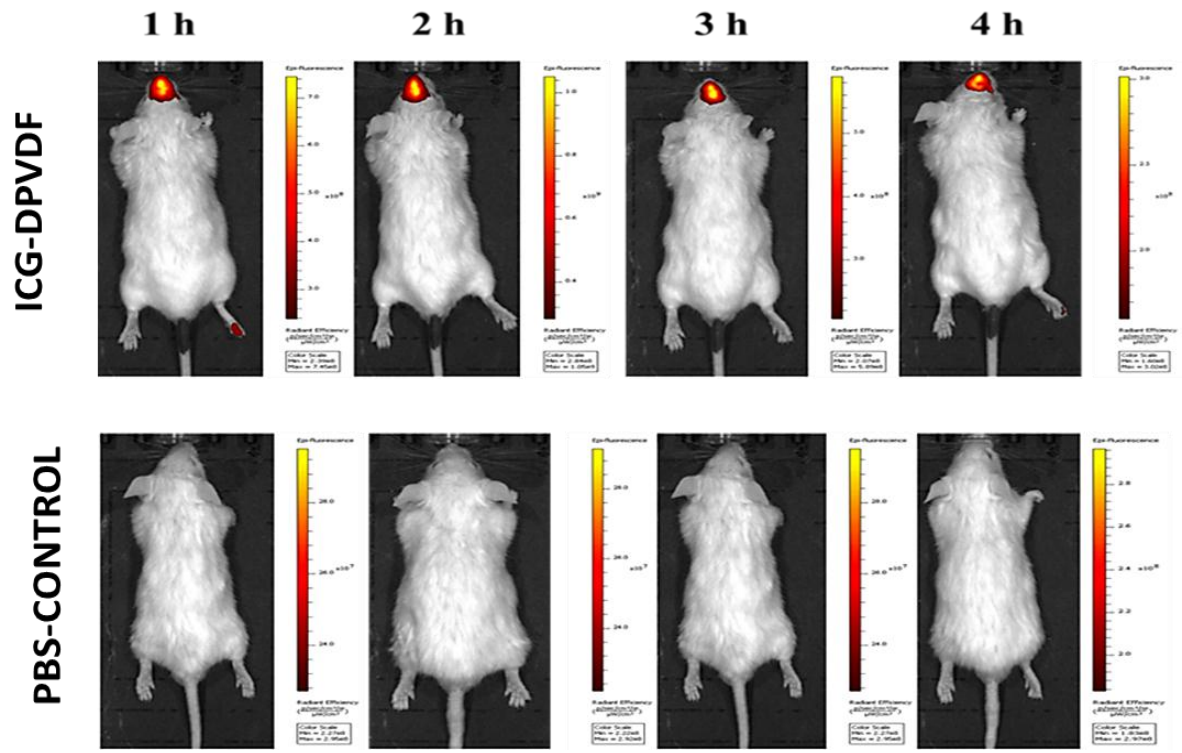

Figure 5.15: *In vivo* fluorescence images of ICG-labeled DPVDF nanospheres obtained in Balb/c mice. (A) *In-vivo* fluorescence imaging of ICG- DPVDF nanospheres-treated mice demonstrated that the particles can reach and stay in the brain tissues from the nasal cavity after 1,2, 3, and 4h of nanospheres administration. (B) *In-vivo* fluorescence imaging of PBS treated mice.

5.4. Conclusion

The current work embodies the potential disaggregation of amyloid peptide fibrils by using mechanically activated DPVDF nanospheres and presents the nanospheres as potential anti-amyloid agents. According to our studies, mechanical stimulus-activated DPVDF nanospheres exhibit piezocatalysis properties upon being stimulated by sonication power (40 kHz). The nanospheres effectively dissociated fibrils formed by the model amyloid peptides, FF and Aβ42, into very short globular debris. We propose the probable mechanism of the disaggregation of these fibrils to involve piezocatalysis induced electrochemical interactions, ROS generation (by the mechanical stimulus-activated peizo-active nanospheres) along with

the fibril disaggregating effect mediated by the polydopamine coating. We also observed that the acoustic stimulus activated DPVDF nanospheres were not only biocompatible but also displayed excellent fluorescent properties and can be used as potent bioimaging agents. Moreover, we further observed that the activated and polydopamine coated nanospheres generated significant and effective neuroprotective effects towards the neural cells and guarded them against the cytotoxic effects exhibited by FF fibrils. Thus, this study directly hints at the potential use of these biocompatible and self-fluorescent simple mechanical stimulus-activated DPVDF nanospheres for future drug development and for electro-chemo-therapy of AD.

5.5 References:

(1) Deture, M. A.; Dickson, D. W. The Neuropathological Diagnosis of Alzheimer's Disease. *Mol. Neurodegener. 2019 141* **2019**, *14* (1), 1–18. https://doi.org/10.1186/S13024-019-0333-5.

(2) Selkoe, D. J.; Hardy, J. The Amyloid Hypothesis of Alzheimer's Disease at 25 Years. *EMBO Mol. Med.* **2016**, *8* (6), 595–608. https://doi.org/10.15252/EMMM.201606210.

(3) Haass, C.; Selkoe, D. J. Soluble Protein Oligomers in Neurodegeneration: Lessons from the Alzheimer's Amyloid Beta-Peptide. *Nat. Rev. Mol. Cell Biol.* **2007**, *8* (2), 101–112. https://doi.org/10.1038/NRM2101.

(4) Palmqvist, S.; Schöll, M.; Strandberg, O.; Mattsson, N.; Stomrud, E.; Zetterberg, H.; Blennow, K.; Landau, S.; Jagust, W.; Hansson, O. Earliest Accumulation of β-Amyloid Occurs within the Default-Mode Network and Concurrently Affects Brain Connectivity. *Nat. Commun.* **2017**, *8* (1), 1214. https://doi.org/10.1038/s41467-017-01150-x.

(5) Terry, R. D.; Masliah, E.; Salmon, D. P.; Butters, N.; DeTeresa, R.; Hill, R.; Hansen, L. A.; Katzman, R. Physical Basis of Cognitive Alterations in Alzheimer's Disease: Synapse Loss Is the Major Correlate of Cognitive Impairment. *Ann. Neurol.* **1991**, *30* (4), 572–580. https://doi.org/10.1002/ANA.410300410.

(6) DeKosky, S. T.; Scheff, S. W. Synapse Loss in Frontal Cortex Biopsies in Alzheimer's Disease: Correlation with Cognitive Severity. *Ann. Neurol.* **1990**, *27* (5), 457–464. https://doi.org/10.1002/ANA.410270502.

(7) Barghorn, S.; Nimmrich, V.; Striebinger, A.; Krantz, G.; Keller, P.; Janson, B.; Bahr, M.; Schmidt, M.; Bitner, R. S.; Harlan, J.; Barlow, E.; Ebert, U.; Hillen, H. Globular Amyloid Beta-Peptide Oligomer - a Homogenous and Stable Neuropathological Protein in Alzheimer's Disease. *J. Neurochem.* **2005**, *95* (3), 834–847. https://doi.org/10.1111/J.1471-4159.2005.03407.X.

(8) Walsh, D. M.; Klyubin, I.; Fadeeva, J. V.; Cullen, W. K.; Anwyl, R.; Wolfe, M. S.; Rowan, M. J.; Selkoe, D. J. Naturally Secreted Oligomers of Amyloid Beta Protein Potently Inhibit Hippocampal Long-Term Potentiation in Vivo. *Nature* **2002**, *416* (6880), 535–539. https://doi.org/10.1038/416535A.

(9) Teplow, D. B. Preparation of Amyloid B- Protein for Structural and Functional Studies. In *Methods in enzymology*; Methods Enzymol, 2006; Vol. 413, pp 20–33. https://doi.org/10.1016/S0076-6879(06)13002-5.

(10) Tenidis, K.; Waldner, M.; Bernhagen, J.; Fischle, W.; Bergmann, M.; Weber, M.; Merkle, M. L.; Voelter, W.; Brunner, H.; Kapurniotu, A. Identification of a Penta- and Hexapeptide of Islet Amyloid Polypeptide (IAPP) with Amyloidogenic and Cytotoxic Properties. *J. Mol. Biol.* **2000**, *295* (4), 1055–1071. https://doi.org/ 10.1006/JMBI.1999.3422.

(11) Balbach, J. J.; Ishii, Y.; Antzutkin, O. N.; Leapman, R. D.; Rizzo, N. W.; Dyda, F.; Reed, J.; Tycko, R. Amyloid Fibril Formation by A Beta 16-22, a Seven-Residue Fragment of the Alzheimer's Beta-Amyloid Peptide, and Structural Characterization by Solid State NMR. *Biochemistry* **2000**, *39* (45), 13748–13759. https://doi.org/10.1021/BI0011330.

(12) Brahmachari, S.; Arnon, Z. A.; Frydman-Marom, A.; Gazit, E.; Adler-Abramovich, L. Diphenylalanine as a Reductionist Model for the Mechanistic Characterization of β-Amyloid Modulators. *ACS Nano* **2017**, *11* (6), 5960–5969. https://doi.org/ 10.1021/ACSNANO.7B01662.

(13) Sharma, M.; Tiwari, V.; Shukla, S.; Panda, J. J. Fluorescent Dopamine−tryptophan Nanocomposites as Dual-Imaging and Antiaggregation Agents: New Generation of Amyloid Theranostics with Trimeric Effects. *ACS Appl. Mater. Interfaces* **2020**, *12* (39), 44180–44194. https://doi.org/10.1021/ACSAMI.0C13223/ SUPPL_FILE/ AM0C13223_SI_001.PDF.

(14) Kour, A.; Dube, T.; Kumar, A.; Panda, J. J. Anti-Amyloidogenic and Fibril-Disaggregating Potency of the Levodopa-Functionalized Gold Nanoroses as Exemplified in a Diphenylalanine-Based Amyloid Model. *Bioconjug. Chem.* **2022**, *33* (2), 397–410. https://doi.org/10.1021/ACS.BIOCONJCHEM.2C00007.

(15) Graham, W. V.; Bonito-Oliva, A.; Sakmar, T. P. Update on Alzheimer's Disease Therapy and Prevention Strategies. *Annu. Rev. Med.* **2017**, *68* (1), 413–430. https://doi.org/10.1146/annurev-med-042915-103753.

(16) Wang, J.; Liu, K.; Xing, R.; Yan, X. Peptide Self-Assembly: Thermodynamics and Kinetics. *Chem. Soc. Rev.* **2016**, *45* (20), 5589–5604. https://doi.org/ 10.1039/ C6CS00176A.

(17) Meersman, F.; Dobson, C. M.; Heremans, K. Protein Unfolding, Amyloid Fibril Formation and Configurational Energy Landscapes under High Pressure Conditions. *Chem. Soc. Rev.* **2006**, *35* (10), 908–917. https://doi.org/10.1039/B517761H.

(18) Yoshimura, Y.; Lin, Y.; Yagi, H.; Lee, Y. H.; Kitayama, H.; Sakurai, K.; So, M.; Ogi, H.; Naiki, H.; Goto, Y. Distinguishing Crystal-like Amyloid Fibrils and Glass-like

Amorphous Aggregates from Their Kinetics of Formation. *Proc. Natl. Acad. Sci. U. S. A.* **2012**, *109* (36), 14446–14451. https://doi.org/10.1073/PNAS.1208228109/-/DCSUPPLEMENTAL/PNAS.1208228109_SI.PDF.

(19) Hamada, D.; Dobson, C. M. A Kinetic Study of β-Lactoglobulin Amyloid Fibril Formation Promoted by Urea. *Protein Sci.* **2002**, *11* (10), 2417. https://doi.org/10.1110/PS.0217702.

(20) Su, Y.; Chang, P. T. Acidic PH Promotes the Formation of Toxic Fibrils from Beta-Amyloid Peptide. *Brain Res.* **2001**, *893* (1–2), 287–291. https://doi.org/10.1016/S0006-8993(00)03322-9.

(21) Liu, L.; Komatsu, H.; Murray, I. V. J.; Axelsen, P. H. Promotion of Amyloid Beta Protein Misfolding and Fibrillogenesis by a Lipid Oxidation Product. *J. Mol. Biol.* **2008**, *377* (4), 1236–1250. https://doi.org/10.1016/J.JMB.2008.01.057.

(22) Qian, W.; Yang, W.; Zhang, Y.; Bowen, C. R.; Yang, Y. Piezoelectric Materials for Controlling Electro-Chemical Processes. *Nano-Micro Lett. 2020 121* **2020**, *12* (1), 1–39. https://doi.org/10.1007/S40820-020-00489-Z.

(23) Zhao, Z.; Dai, Y.; Dou, S. X.; Liang, J. Flexible Nanogenerators for Wearable Electronic Applications Based on Piezoelectric Materials. *Mater. Today Energy* **2021**, *20*, 100690. https://doi.org/10.1016/J.MTENER.2021.100690.

(24) Qiu, J.; Ji, H. Research on Applications of Piezoelectric Materials in Smart Structures. *Front. Mech. Eng. 2011 61* **2011**, *6* (1), 99–117. https://doi.org/10.1007/S11465-011-0212-4.

(25) Xu, Q.; Gao, X.; Zhao, S.; Liu, Y.-N.; Zhang, D.; Zhou, K.; Khanbareh, H.; Chen, W.; Zhang, Y.; Bowen, C.; Xu, Q.; Gao, X.; Zhao, S.; Liu, Y.-N.; Chen, W.; Zhang, D.; Zhang, Y.; Zhou, K.; Khanbareh, H.; Bowen, C. Construction of Bio-Piezoelectric Platforms: From Structures and Synthesis to Applications. *Adv. Mater.* **2021**, *33* (27), 2008452. https://doi.org/10.1002/ADMA.202008452.

(26) Zheng, Q.; Zou, Y.; Zhang, Y.; Liu, Z.; Shi, B.; Wang, X.; Jin, Y.; Ouyang, H.; Li, Z.; Wang, Z. L. Biodegradable Triboelectric Nanogenerator as a Life-Time Designed Implantable Power Source. *Sci. Adv.* **2016**, *2* (3). https://doi.org/10.1126/SCIADV.1501478/SUPPL_FILE/1501478_SM.PDF.

(27) Liu, Z.; Zhou, Y.; Qu, X.; Xu, L.; Zou, Y.; Shan, Y.; Shao, J.; Wang, C.; Liu, Y.; Xue, J.; Jiang, D.; Fan, Y.; Li, Z.; Ye, H. A Self-Powered Optogenetic System for Implantable Blood Glucose Control. *Research* **2022**, *2022*, 1–13. https://doi.org/10.34133/2022/9864734.

(28) Zhang, Y.; Xu, L.; Liu, Z.; Cui, X.; Xiang, Z.; Bai, J.; Jiang, D.; Xue, J.; Wang, C.; Lin, Y.; Li, Z.; Shan, Y.; Yang, Y.; Bo, L.; Li, Z.; Zhou, X. Self-Powered Pulsed Direct Current Stimulation System for Enhancing Osteogenesis in MC3T3-E1. *Nano Energy* **2021**, *85*, 106009. https://doi.org/10.1016/J.NANOEN.2021.106009.

(29) Xie, L.; Wang, G.; Jiang, C.; Yu, F.; Zhao, X. Properties and Applications of Flexible Poly(Vinylidene Fluoride)-Based Piezoelectric Materials. *Cryst. 2021, Vol. 11, Page 644* **2021**, *11* (6), 644. https://doi.org/10.3390/CRYST11060644.

(30) Lovinger, A. J. Ferroelectric Polymers. *Science* **1983**, *220* (4602), 1115–1121. https://doi.org/10.1126/SCIENCE.220.4602.1115.

(31) Li, M.; Wondergem, H. J.; Spijkman, M. J.; Asadi, K.; Katsouras, I.; Blom, P. W. M.; De Leeuw, D. M. Revisiting the Delta-Phase of Poly(Vinylidene Fluoride) for Solution-Processed Ferroelectric Thin Films. *Nat. Mater.* **2013**, *12* (5), 433–438. https://doi.org/10.1038/NMAT3577.

(32) Martín, J.; Zhao, D.; Lenz, T.; Katsouras, I.; De Leeuw, D. M.; Stingelin, N. Solid-State-Processing of δ-PVDF. *Mater. Horizons* **2017**, *4* (3), 408–414. https://doi.org/10.1039/C7MH00007C.

(33) Gupta, V.; Babu, A.; Ghosh, S. K.; Mallick, Z.; Mishra, H. K.; Saini, D.; Mandal, D. Revisiting δ-PVDF Based Piezoelectric Nanogenerator for Self-Powered Pressure Mapping Sensor. *Appl. Phys. Lett.* **2021**, *119* (25), 252902. https://doi.org/10.1063/5.0071625.

(34) Martins, P.; Lopes, A. C.; Lanceros-Mendez, S. Electroactive Phases of Poly(Vinylidene Fluoride): Determination, Processing and Applications. *Prog. Polym. Sci.* **2014**, *39* (4), 683–706. https://doi.org/10.1016/J.PROGPOLYMSCI.2013.07.006.

(35) Ribeiro, C.; Costa, C. M.; Correia, D. M.; Nunes-Pereira, J.; Oliveira, J.; Martins, P.; Gonçalves, R.; Cardoso, V. F.; Lanceros-Méndez, S. Electroactive Poly(Vinylidene Fluoride)-Based Structures for Advanced Applications. *Nat. Protoc.* **2018**, *13* (4), 681–704. https://doi.org/10.1038/NPROT.2017.157.

(36) Zhu, J.; Zhu, Y.; Wang, X. A Hybrid Piezoelectric and Triboelectric Nanogenerator with PVDF Nanoparticles and Leaf-Shaped Microstructure PTFE Film for Scavenging Mechanical Energy. *Adv. Mater. Interfaces* **2018**, *5* (2), 1700750. https://doi.org/10.1002/ADMI.201700750.

(37) Fu, C.; Zhu, H.; Hoshino, N.; Akutagawa, T.; Mitsuishi, M. Interfacial Nanostructuring of Poly(Vinylidene Fluoride) Homopolymer with Predominant Ferroelectric Phases. *Langmuir* **2020**, *36* (46), 14083–14091. https://doi.org/10.1021/

ACS.LANGMUIR.0C02667.

(38) Okada, D.; Kaneko, H.; Kato, K.; Furumi, S.; Takeguchi, M.; Yamamoto, Y. Colloidal Crystallization and Ionic Liquid Induced Partial β-Phase Transformation of Poly(Vinylidene Fluoride) Nanoparticles. *Macromolecules* **2015**, *48* (8), 2570–2575. https://doi.org/10.1021/ACS.MACROMOL.5B00337/ASSET/IMAGES/MEDIUM/MA-2015-00337B_0010.GIF.

(39) Joaquim, A.; Paul, O.; Ibezim, M.; Johnson, D.; Falconer, A.; Wu, Y.; Williams, F.; Mu, R. Electrospray Deposition of Polyvinylidene Fluoride (PVDF) Microparticles: Impact of Solvents and Flow Rate. *Polym. 2022, Vol. 14, Page 2702* **2022**, *14* (13), 2702. https://doi.org/10.3390/POLYM14132702.

(40) Xiao, Z.; Dong, Q.; Sharma, P.; Yuan, Y.; Mao, B.; Tian, W.; Gruverman, A.; Huang, J. Synthesis and Application of Ferroelectric P(VDF-TrFE) Nanoparticles in Organic Photovoltaic Devices for High Efficiency. *Adv. Energy Mater.* **2013**, *3* (12), 1581–1588. https://doi.org/10.1002/AENM.201300396.

(41) Ribeiro, C.; Sencadas, V.; Correia, D. M.; Lanceros-Méndez, S. Piezoelectric Polymers as Biomaterials for Tissue Engineering Applications. *Colloids Surf. B. Biointerfaces* **2015**, *136*, 46–55. https://doi.org/10.1016/J.COLSURFB.2015.08.043.

(42) Yu, Y.; Sun, H.; Orbay, H.; Chen, F.; England, C. G.; Cai, W.; Wang, X. Biocompatibility and in Vivo Operation of Implantable Mesoporous PVDF-Based Nanogenerators. *Nano Energy* **2016**, *27*, 275–281. https://doi.org/10.1016/J.NANOEN.2016.07.015.

(43) Correia, D. M.; Gonçalves, R.; Ribeiro, C.; Sencadas, V.; Botelho, G.; Ribelles, J. L. G.; Lanceros-Méndez, S. Electrosprayed Poly(Vinylidene Fluoride) Microparticles for Tissue Engineering Applications. *RSC Adv.* **2014**, *4* (62), 33013–33021. https://doi.org/10.1039/C4RA04581E.

(44) Binger, K. J.; Griffin, M. D. W.; Howlett, G. J. Methionine Oxidation Inhibits Assembly and Promotes Disassembly of Apolipoprotein C-II Amyloid Fibrils. *Biochemistry* **2008**, *47* (38), 10208–10217. https://doi.org/10.1021/BI8009339.

(45) Yan, Y.; McCallum, S. A.; Wang, C. M35 Oxidation Induces Aβ40-like Structural and Dynamical Changes in Aβ42. *J. Am. Chem. Soc.* **2008**, *130* (16), 5394–5395. https://doi.org/10.1021/JA711189C/SUPPL_FILE/JA711189C-FILE002.PDF.

(46) Hou, L.; Kang, I.; Marchant, R. E.; Zagorski, M. G. Methionine 35 Oxidation Reduces Fibril Assembly of the Amyloid Abeta-(1-42) Peptide of Alzheimer's Disease. *J. Biol. Chem.* **2002**, *277* (43), 40173–40176. https://doi.org/10.1074/JBC.C200338200.

(47) Chung, Y. J.; Kim, K.; Lee, B. Il; Park, C. B. Carbon Nanodot-Sensitized Modulation of Alzheimer's β-Amyloid Self-Assembly, Disassembly, and Toxicity. *Small* **2017**, *13* (34). https://doi.org/10.1002/SMLL.201700983.

(48) Lynge, M. E.; Van Der Westen, R.; Postma, A.; Städler, B. Polydopamine—a Nature-Inspired Polymer Coating for Biomedical Science. *Nanoscale* **2011**, *3* (12), 4916–4928. https://doi.org/10.1039/C1NR10969C.

(49) Lee, H.; Dellatore, S. M.; Miller, W. M.; Messersmith, P. B. Mussel-Inspired Surface Chemistry for Multifunctional Coatings. *Science (80-.).* **2007**, *318* (5849), 426–430. https://doi.org/10.1126/SCIENCE.1147241/SUPPL_FILE/LEE.SOM.PDF.

(50) Lee, H.; Lee, Y.; Statz, A. R.; Rho, J.; Park, T. G.; Messersmith, P. B. Substrate-Independent Layer-by-Layer Assembly by Using Mussel-Adhesive-Inspired Polymers. *Adv. Mater.* **2008**, *20* (9), 1619–1623. https://doi.org/10.1002/ADMA.200702378.

(51) Yang, F. K.; Zhao, B. Adhesion Properties of Self-Polymerized Dopamine Thin Film. *Open Surf. Sci. J.* **2014**, *3* (1), 115–122. https://doi.org/10.2174/ 18765319 01103010115.

(52) Sharma, M.; Tiwari, V.; Shukla, S.; Panda, J. J. Fluorescent Dopamine−tryptophan Nanocomposites as Dual-Imaging and Antiaggregation Agents: New Generation of Amyloid Theranostics with Trimeric Effects. *ACS Appl. Mater. Interfaces* **2020**, *12* (39), 44180–44194. https://doi.org/10.1021/ACSAMI.0C13223/SUPPL_FILE/ AM0C13223_SI_001.PDF.

(53) Gu, G. E.; Park, C. S.; Cho, H. J.; Ha, T. H.; Bae, J.; Kwon, O. S.; Lee, J. S.; Lee, C. S. Fluorescent Polydopamine Nanoparticles as a Probe for Zebrafish Sensory Hair Cells Targeted in Vivo Imaging. *Sci. Reports 2018 81* **2018**, *8* (1), 1–8. https://doi.org/ 10.1038/ s41598-018-22828-2.

(54) Li, J.; Zhu, M.; Manning-Bog, A. B.; Di Monte, D. A.; Fink, A. L. Dopamine and L-Dopa Disaggregate Amyloid Fibrils: Implications for Parkinson's and Alzheimer's Disease. *FASEB J.* **2004**, *18* (9), 962–964. https://doi.org/10.1096/FJ.03-0770FJE.

(55) Jang, J.; Kim, K.; Yoon, J.; Park, C. B. Piezoelectric Materials for Ultrasound-Driven Dissociation of Alzheimer's β-Amyloid Aggregate Structure. *Biomaterials* **2020**, *255*, 120165. https://doi.org/10.1016/j.biomaterials.2020.120165.

(56) Muchtar, S.; Wahab, M. Y.; Fang, L. F.; Jeon, S.; Rajabzadeh, S.; Takagi, R.; Mulyati, S.; Arahman, N.; Riza, M.; Matsuyama, H. Polydopamine-Coated Poly(Vinylidene Fluoride) Membranes with High Ultraviolet Resistance and Antifouling Properties for a Photocatalytic Membrane Reactor. *J. Appl. Polym. Sci.* **2019**, *136* (14), 47312.

https://doi.org/ 10.1002/APP.47312.

(57) Yang, P.; Zhang, S.; Chen, X.; Liu, X.; Wang, Z.; Li, Y. Recent Developments in Polydopamine Fluorescent Nanomaterials. *Mater. Horizons* **2020**, *7* (3), 746–761. https://doi.org/10.1039/C9MH01197H.

(58) Lin, L.; Zheng, Q.; Chen, Q.; Fang, M.; Lai, Q.; He, X.; Qin, J.; Lin, Z.; Lin, R. Preparation of Fluorescent Organic Nanoparticles via Self-Polymerization for Tartrazine Detection in Food Samples. *New J. Chem.* **2022**, *46* (10), 4756–4761. https://doi.org/10.1039/D1NJ05176H.

(59) Chen, X.; Yan, Y.; Müllner, M.; Van Koeverden, M. P.; Noi, K. F.; Zhu, W.; Caruso, F. Engineering Fluorescent Poly(Dopamine) Capsules. *Langmuir* **2014**, *30* (10), 2921–2925. https://doi.org/10.1021/LA4049133.

(60) Yildirim, A.; Bayindir, M. Turn-on Fluorescent Dopamine Sensing Based on in Situ Formation of Visible Light Emitting Polydopamine Nanoparticles. *Anal. Chem.* **2014**, *86* (11), 5508–5512. https://doi.org/10.1021/AC500771Q/SUPPL_FILE/AC 500771Q _SI_001.PDF.

(61) Panda, J. J.; Kaul, A.; Kumar, S.; Alam, S.; Mishra, A. K.; Kundu, G. C.; Chauhan, V. S. Modified Dipeptide-Based Nanoparticles: Vehicles for Targeted Tumor Drug Delivery. *Nanomedicine (Lond).* **2013**, *8* (12), 1927–1942. https://doi.org/10.2217/ NNM.12.201.

(62) Alam, S.; Panda, J. J.; Mukherjee, T. K.; Chauhan, V. S. Short Peptide Based Nanotubes Capable of Effective Curcumin Delivery for Treating Drug Resistant Malaria. *J. Nanobiotechnology* **2016**, *14* (1), 26. https://doi.org/10.1186/s12951-016-0179-8.

(63) Kumaraswamy, P.; Lakshmanan, R.; Sethuraman, S.; Krishnan, U. M. Self-Assembly of Peptides: Influence of Substrate, PH and Medium on the Formation of Supramolecular Assemblies. *Soft Matter* **2011**, *7* (6), 2744–2754. https://doi.org/ 10.1039/ C0SM00897D.

(64) Eruslanov, E.; Kusmartsev, S. Identification of ROS Using Oxidized DCFDA and Flow-Cytometry. In *Methods in molecular biology (Clifton, N.J.)*; Methods Mol Biol, 2010; Vol. 594, pp 57–72. https://doi.org/10.1007/978-1-60761-411-1_4.

(65) Bielski, B. H. J.; Shiue, G. G.; Bajuk, S. Reduction of Nitro Blue Tetrazolium by CO2- and O2- Radicals. *J. Phys. Chem.* **1980**, *84* (8), 830–833. https://doi.org/10.1021/J 100445A006/ ASSET/J100445A006.FP.PNG_V03.

(66) Feng, B.; Zhao, D.; Peng, Y.; Wang, F. Cytochrome-c Aptamer Functionalized Pt

Nanoclusters for Enhanced Chemodynamic Therapy. *J. Innov. Opt. Health Sci.* **2021**, *14* (4). https://doi.org/10.1142/S1793545821410042/ASSET/IMAGES/LARGE /S1793545821410042FIGF9.JPEG.

(67) Chen, C.; Wang, Y.; Zhang, D. Peroxidase-like Activity of Vanadium Tetrasulfide Submicrospheres and Its Application to the Colorimetric Detection of Hydrogen Peroxide and L-Cysteine. *Microchim. Acta 2019 18612* **2019**, *186* (12), 1–8. https://doi.org/10.1007/S00604-019-3942-3.

(68) Zangmeister, R. A.; Morris, T. A.; Tarlov, M. J. Characterization of Polydopamine Thin Films Deposited at Short Times by Autoxidation of Dopamine. *Langmuir* **2013**, *29* (27), 8619–8628. https://doi.org/10.1021/LA400587J.

(69) Ding, Y.; Weng, L.-T.; Yang, M.; Yang, Z.; Lu, X.; Huang, N.; Leng, Y. Insights into the Aggregation/Deposition and Structure of a Polydopamine Film. *Langmuir* **2014**, *30* (41), 12258–12269. https://doi.org/10.1021/LA5026608.

(70) Park, K. Il; Xu, S.; Liu, Y.; Hwang, G. T.; Kang, S. J. L.; Wang, Z. L.; Lee, K. J. Piezoelectric $BaTiO_3$ Thin Film Nanogenerator on Plastic Substrates. *Nano Lett.* **2010**, *10* (12), 4939–4943. https://doi.org/10.1021/NL102959K.

(71) Yu, A.; Song, M.; Zhang, Y.; Zhang, Y.; Chen, L.; Zhai, J.; Wang, Z. L. Self-Powered Acoustic Source Locator in Underwater Environment Based on Organic Film Triboelectric Nanogenerator. *Nano Res. 2015 83* **2014**, *8* (3), 765–773. https://doi.org/10.1007/S12274-014-0559-Z.

(72) Ghosh, S. K.; Mandal, D. High-Performance Bio-Piezoelectric Nanogenerator Made with Fish Scale. *Appl. Phys. Lett.* **2016**, *109* (10), 103701. https://doi.org/10.1063/1.4961623.

(73) Ghosh, S. K.; Mandal, D. Efficient Natural Piezoelectric Nanogenerator: Electricity Generation from Fish Swim Bladder. *Nano Energy* **2016**, *28*, 356–365. https://doi.org/10.1016/j.nanoen.2016.08.030.

(74) Choi, Y. Y.; Sharma, P.; Phatak, C.; Gosztola, D. J.; Liu, Y.; Lee, J.; Lee, B.; Li, J.; Gruverman, A.; Ducharme, S.; Hong, S. Enhancement of Local Piezoresponse in Polymer Ferroelectrics via Nanoscale Control of Microstructure. *ACS Nano* **2015**, *9* (2), 1809–1819. https://doi.org/10.1021/NN5067232/SUPPL_FILE/NN5067232_SI_001.PDF.

(75) Yan, X.; Zhu, P.; Li, J. Self-Assembly and Application of Diphenylalanine-Based Nanostructures. *Chem. Soc. Rev.* **2010**, *39* (6), 1877–1890. https://doi.org/10.1039/B915765B.

(76) Tao, K.; Makam, P.; Aizen, R.; Gazit, E. Self-Assembling Peptide Semiconductors. *Science* **2017**, *358* (6365). https://doi.org/10.1126/SCIENCE.AAM9756.

(77) Kholkin, A.; Amdursky, N.; Bdikin, I.; Gazit, E.; Rosenman, G. Strong Piezoelectricity in Bioinspired Peptide Nanotubes. *ACS Nano* **2010**, *4* (2), 610–614. https://doi.org/10.1021/NN901327V/SUPPL_FILE/NN901327V_SI_001.PDF.

(78) Zhang, X.; Wang, S.; Xu, L.; Feng, L.; Ji, Y.; Tao, L.; Li, S.; Wei, Y. Biocompatible Polydopamine Fluorescent Organic Nanoparticles: Facile Preparation and Cell Imaging. *Nanoscale* **2012**, *4* (18), 5581–5584. https://doi.org/10.1039/C2NR31281F.

(79) Quignard, S.; D'Ischia, M.; Chen, Y.; Fattaccioli, J. Ultraviolet-Induced Fluorescence of Polydopamine-Coated Emulsion Droplets. *Chempluschem* **2014**, *79* (9), 1254–1257. https://doi.org/10.1002/CPLU.201402157.

(80) Juan, C. A.; de la Lastra, J. M. P.; Plou, F. J.; Pérez-Lebeña, E. The Chemistry of Reactive Oxygen Species (ROS) Revisited: Outlining Their Role in Biological Macromolecules (DNA, Lipids and Proteins) and Induced Pathologies. *Int. J. Mol. Sci. 2021, Vol. 22, Page 4642* **2021**, *22* (9), 4642. https://doi.org/10.3390/IJMS22094642.

(81) Yang, B.; Chen, Y.; Shi, J. Reactive Oxygen Species (ROS)-Based Nanomedicine. *Chem. Rev.* **2019**, *119* (8), 4881–4985. https://doi.org/10.1021/ACS.CHEMREV.8B00626.

(82) Hekimi, S.; Lapointe, J.; Wen, Y. Taking a "Good" Look at Free Radicals in the Aging Process. *Trends Cell Biol.* **2011**, *21* (10), 569–576. https://doi.org/10.1016/J.TCB.2011.06.008.

(83) Heidler, T.; Hartwig, K.; Daniel, H.; Wenzel, U. Caenorhabditis Elegans Lifespan Extension Caused by Treatment with an Orally Active ROS-Generator Is Dependent on DAF-16 and SIR-2.1. *Biogerontology* **2010**, *11* (2), 183–195. https://doi.org/10.1007/S10522-009-9239-X.

(84) Dröge, W. Free Radicals in the Physiological Control of Cell Function. *Physiol. Rev.* **2002**, *82* (1), 47–95. https://doi.org/10.1152/PHYSREV.00018.2001.

(85) Young, I. S.; Woodside, J. V. Antioxidants in Health and Disease. *J. Clin. Pathol.* **2001**, *54* (3), 176–186. https://doi.org/10.1136/JCP.54.3.176.

(86) Pacher, P.; Beckman, J. S.; Liaudet, L. Nitric Oxide and Peroxynitrite in Health and Disease. *Physiol. Rev.* **2007**, *87* (1), 315–424. https://doi.org/10.1152/ PHYSREV.00029.2006.

(87) Genestra, M. Oxyl Radicals, Redox-Sensitive Signalling Cascades and Antioxidants. *Cell. Signal.* **2007**, *19* (9), 1807–1819. https://doi.org/10.1016/ J.CELLSIG.2007.04.009.

(88) Harwell, B. Biochemistry of Oxidative Stress. *Biochem. Soc. Trans.* **2007**, *35* (Pt 5), 1147–1150. https://doi.org/10.1042/BST0351147.

(89) Royo-Gascon, N.; Wininger, M.; Scheinbeim, J. I.; Firestein, B. L.; Craelius, W. Piezoelectric Substrates Promote Neurite Growth in Rat Spinal Cord Neurons. *Ann. Biomed. Eng.* **2013**, *41* (1), 112–122. https://doi.org/10.1007/S10439-012-0628-Y.

(90) Inaoka, T.; Shintaku, H.; Nakagawa, T.; Kawano, S.; Ogita, H.; Sakamoto, T.; Hamanishi, S.; Wada, H.; Ito, J. Piezoelectric Materials Mimic the Function of the Cochlear Sensory Epithelium. *Proc. Natl. Acad. Sci. U. S. A.* **2011**, *108* (45), 18390–18395. https://doi.org/10.1073/PNAS.1110036108.

(91) Wang, X.; Song, J.; Liu, J.; Zhong, L. W. Direct-Current Nanogenerator Driven by Ultrasonic Waves. *Science* **2007**, *316* (5821), 102–105. https://doi.org/10.1126/SCIENCE.1139366.

(92) Yoon, H. J.; Kim, S. W. Nanogenerators to Power Implantable Medical Systems. *Joule* **2020**, *4* (7), 1398–1407. https://doi.org/10.1016/J.JOULE.2020.05.003.

(93) Rjafallah, A.; Hajjaji, A.; Guyomar, D.; Kandoussi, K.; Belhora, F.; Boughaleb, Y. Modeling of Polyurethane/Lead Zirconate Titanate Composites for Vibration Energy Harvesting. *https://doi.org/10.1177/0021998318788604* **2018**, *53* (5), 613–623. https://doi.org/10.1177/0021998318788604.

(94) Caliò, R.; Rongala, U. B.; Camboni, D.; Milazzo, M.; Stefanini, C.; de Petris, G.; Oddo, C. M. Piezoelectric Energy Harvesting Solutions. *Sensors 2014, Vol. 14, Pages 4755-4790* **2014**, *14* (3), 4755–4790.

(95) Boyuklieva, R.; Pilicheva, B. Micro- and Nanosized Carriers for Nose-to-Brain Drug Delivery in Neurodegenerative Disorders. *Biomedicines* **2022**, *10* (7), 1706.

CONCLUSIONS AND FUTURE PERSPECTIVES

6.1. Conclusions:

Use of new-generation theranostic nanomedicines, a modern treatment approach indulging the applicability of nanotechnology in healthcare have provided safer solutions by opening cutting-edge platforms in terms of real-time, rapid, and sensitive diagnosis as well as treatment for AD. Researchers are continuously working for improving the sensitivity and precision in screening/diagnosis as well as in achieving effective treatment strategies for AD, an approach to develop a drug delivery system, carrying both imaging and therapeutic function within a single nanomedicine platform. Hence, developing an ultrasmall multimodal nanotheranostics system that can precisely diagnose as well as treat AD is the dire need of the hour.

Moving in this direction, the present thesis work provides a set of contributions to the field of nanomedicine which are based on the potential of different small molecule-derived nanotheranostic systems for simultaneous detection and treatment of AD. Small molecule-derived nanotheranostic systems that carry both therapeutic and diagnostic moieties in a single nanosystem have garnered notable research interest with tremendous focus because of the real-time monitoring of disease progression as well as enhanced biodistribution of the loaded therapeutic and diagnostic moieties at the target tissues. This has increased drug efficacy along with lessening toxicity due to reduced non-specific biodistribution. Overall, this thesis consists of mainly six chapters.

The introductory chapter gives an overview of AD, its global health impact, fundamental pathogenesis hypotheses, currently available treatments with their drawbacks, importance of nanotheranostic systems for realizing solutions for diagnosis as well as therapy of AD.

Salient features of fluorescent nanostructures and their utility for rapid, real-time, and sensitive diagnosis, as well as treatment of AD, are also being discussed.

Overall, exploiting a minimalistic approach, we demonstrated the development of different small molecule-derived nanotheranostic systems, capable of transversing the BBB to serve as simultaneous amyloid inhibitors and aggregate detecting agents under one roof.

The second chapter focuses on the development of self-fluorescent solo tryptophan nanoparticles (TNPs) from a single amino acid, L-tryptophan, and explores and investigates their efficacies as anti-amyloid and aggregate detecting agents in *in-vitro* and *in-vivo* studies. The self-fluorescent solo tryptophan nanoparticles showed anti-amyloid activity against both FF and Aβ42 aggregates in vitro as well as also protected the neurons from Aβ42 peptide and FF aggregates-induced cytotoxicity. Additionally, these nanostructures exhibited remarkable neuroprotective effects in lessening the cognitive deficits and suppressing the Aβ42 oligomers accumulation in the brain of ICV-STZ induced AD rat model. Moreover, the pharmacokinetics study of the nanoparticles further demonstrated that these could breach the BBB to gain access to the neuronal tissues and subsequently serve as a brain delivery agent. The Inherent excellent fluorescent properties of these nanoparticles were also exploited to use them as imaging modalities for tagging and detecting FF and Aβ42 peptide fibrils. Thus, overall the biocompatible and utterly simple fluorescent tryptophan nanoparticles synthesized here could serve as potent nanotheranostic agents for treating and diagnosing AD.

In the third chapter, we have discussed about the synthesis of autofluorescent nanocomposite of tryptophan and the neuroactive molecule, dopamine and explored their anti-amyloidogenic and neuroprotective properties. The designed multimodal theranostic system exhibited triple advantages: (a) amyloid recognition and binding capacity owing to the presence of the aromatic moiety specifically tryptophan, (b) Aβ-polypeptide fibril disaggregation propensity

contributed by the presence of both tryptophan and dopamine, and (c) inherent BBB permeability by means of tryptophan. The nanocomposite showed synergistic neuroprotective effects against fibril induced toxicity in both neuroblastoma cells and in animal model (ICV-STZ) of dementia. In addition, nanocomposite exhibited excellent fluorescent properties and light up the cytoplasm of neuroblastoma cells when being incubated with cells, confirming their ability to serve as an intracellular bioimaging agent.

In the fourth chapter, we have described the synthesis of a dual functional fluorescent resveratrol and L-tryptophan (ResTrp) loaded dopamine (dopa) core nanotheranostic system (RTDNPs) as a dual functional anti-amyloid agent. The nanosystem demonstrated dual anti-amyloidogenic activity against both aggregated fibrils of FF and hexapeptide Ac-PHF6 (VQIVYK) derived from tau protein after irradiation with 808 nm laser due to the potent anti-amyloidogenic and photothermal property of nanosystem. Additionally, Res-Trp loaded Dopamine core showed a remarkable neuroprotective effect in neuroblastoma cells against both FF amyloid fibrils and hexapeptide Ac-PHF6 fibrils induced toxicity under the NIR laser irradiation. Moreover, the designed dual-functional nanosystem exhibited auto-fluorescent property and can also be used as a potent bioimaging agents.

The last chapter reports the synthesis and application of dopamine-coated piezoelectric polyvinylidene fluoride nanospheres as acoustic stimulus (sonication) triggered anti-fibrillizing agents towards FF, as well as Aβ42-polypeptide fibrils. In addition to simple small molecule-based nanotheranostic systems for treating and diagnosing AD, the dopamine-coated piezoelectric polyvinylidene fluoride nanospheres represent a class of biocompatible piezoelectric materials with piezo-catalytic property triggered in response to an acoustic stimulus. The acoustic stimulus-activated DPVDF nanospheres produced piezo-induced oxidative stress, under both in vitro and in cellular conditions, which successfully

destabilized FF and Aβ42 fibrils. The stimulus-activated coated nanospheres also exhibited neuroprotective properties and efficiently alleviated the neuro-toxicity of FF fibrils as exemplified in the neuroblastoma, SHSY5Y cells. Thus, these acoustic stimuli-activated nanospheres can serve as a novel class of disease-modifying nanomaterials for non-invasive electro-chemotherapy of AD.

6.2. Future Perspectives:

The work presented in this thesis provides comprehensive information about how small molecules can be utilized for designing novel fluorescent nanotheranostic agents which can be utilized further for the simultaneous diagnosis and treatment of AD. However, multidisciplinary efforts are further essential for the fruitful translation of these research outcomes into medical practices to benefit humanity.

The designed auto-fluorescent multifunctional nanosystems can be helpful to understand the utilization and importance of an efficacious single nanomedicine platform for biomedical imaging and disease therapy. Further, the results will help in designing cost-effective, sensitive, biocompatible, and affordable nanotheranostics to facilitate inexpensive diagnostic tests and increase therapeutic efficacy for AD therapy.

Moreover, dual anti-amyloid nanostructures will also help in fabricating a newer generation of amyloid inhibitors that have the dual anti-amyloidogenic capability for treating complex multifactorial diseases. Additionally, the acoustic stimulus-activated nanostructures will definitely open the window to a new class of disease-modifying nanomaterials with enhanced therapeutic efficacy for the non-invasive electro-chemotherapy of AD.

LIST OF PUBLICATIONS

Included in Thesis

1. Nanotheranostics, a future remedy of neurological disorders: **Sharma, M**., Dube, T., Chibh, S., Kour, A., Mishra, J., & Panda, J. J. (2019). *Expert opinion on drug delivery*, *16*(2), 113-128

2. Self-Fluorescent Lone Tryptophan Nanoparticles as Theranostic Agents Against Alzheimer's Disease; **Sharma, Manju**; Tiwari, Virendra; Chaturvedi, Swati; Wahajuddin, Muhammad; Shukla, Shubha; Panda, Jiban; ***ACS Appl. Mater. Interfaces*** **2022**, 14, 11, 13079–13093.

3. Fluorescent dopamine–tryptophan nanocomposites as dual-imaging and antiaggregation agents: new generation of amyloid theranostics with trimeric effects: **Sharma, M**., Tiwari, V., Shukla, S., & Panda, J. J. (2020). ***ACS Applied Materials & Interfaces***, *12*(39), 44180-44194.

4. Anti-amyloidogenic potency of acoustic stimulus activated piezoelectric polydopamine-PVDF nanospheres, a futuristic approach towards Alzheimer's therapy; **Manju Sharma**, Samraggi Choudhury, Dipanjan Sengupta, Anand Babu, Varun Gupta, Dipankar Mandal and Jiban Jyoti Panda; (Under Revision 2022)

5. Dual functional resveratrol tryptophan nanoparticles loaded polydopamine core nanoparticles for Alzheimer's treatment; **Manju Sharma** and Jiban Jyoti Panda (Communicated 2022)

6. Current therapeutic strategies for reverting neurological deficit with a special emphasis on oxidative damage, protein aggregation and DNA damage-based impairment in neuroglia; **Manju Sharma**, Nidhi Aggarwal, Jiban Anand Mishra, and Jiban Jyoti Panda (Communicated 2022)

Not a part of Thesis

7. Carrier-free self-built aspirin nanorods as anti-aggregation agents towards alpha-crystallin-derived peptide aggregates: potential implications in non-invasive cataract therapy: Bisht, A., Sharma, **M., Sharma,** S., Ali, M. E., & Panda, J. J. (2019). ***Journal of Materials Chemistry B***, *7*(44), 6945-6954. **(Equal first author)**

8. Microflow synthesis and enhanced photocatalytic dye degradation performance of antibacterial Bi 2 O 3 nanoparticles: Katoch, V., Sharma, N., **Sharma, M**., Baghoria, M., Panda, J. J., Singh, M., & Prakash, B. (2021). ***Environmental Science and Pollution Research,*** *28*(15), 19155-19165.

9. Continuous Flow Reactor for the Controlled Synthesis and Inline Photocatalysis of Antibacterial Ag2S Nanoparticles: Prakash B, Katoch V, Shah A, **Sharma M**, Devi MM, Panda JJ, Sharma J, Ganguli AK, **Photochemistry and Photobiology, 2020,** 96 (6), 1273-1282.

10. l-3, 4-Dihydroxyphenylalanine templated anisotropic gold nano/micro-roses as potential disrupters/inhibitors of α-crystallin protein and its gleaned model peptide aggregates: Kour, A., Sharma, S., Dube, T., Bisht, A., **Sharma, M**., Mishra, J., ... & Panda, J. J. (2020). ***International Journal of Biological Macromolecules***, *163*, 2374-2391.

11. Kaur, H., Shorie, M., **Sharma, M**., Ganguli, A. K., & Sabherwal, P. (2017). Bridged Rebar Graphene functionalized aptasensor for pathogenic E. coli O78: K80: H11 detection. ***Biosensors and Bioelectronics***, *98*, 486-49

CONFERENCES AND AWARDS

1. Received "'**Best Poster Award with Cash Prize**" in "National Biomedical Competition organized by SYBS", **2021**.
2. Attended 6th International on Nanoscience and Nanotechnology (Virtual Conference**), ICONN 2021**.
3. Poster Presentation at Conference conducted in **Chemical Biology Unit** in INST Mohali, **2021.**
4. Poster Presentation at Conference conducted in **Chemical Biology Unit** in INST Mohali, **2022**.
5. Poster Presentation in Conference in **12th Bengaluru India Nano, 2022.**
6. Oral Presentation in International Conference **APA, Nanoforum**, **2022**.
7. Poster Presentation in 8 International Symposium on Current Trends in Drug Discovery Research "**CTDDR-2022**".